

---

Search for Dark Matter in association  
with a Higgs boson decaying into  $b$ -quarks  
with the ATLAS detector

Andrea Matic

---



München 2020



---

**Search for Dark Matter in association  
with a Higgs boson decaying into  $b$ -quarks  
with the ATLAS detector**

Andrea Matic

---

Dissertation  
an der Fakultät für Physik  
der Ludwig-Maximilians-Universität  
München

vorgelegt von  
Andrea Matic  
aus München

München, den 9. November 2020

Erstgutachterin: PD Dr. Jeanette Lorenz

Zweitgutachter: Prof. Dr. Wolfgang Dünneberger

Tag der mündlichen Prüfung: 15. Dezember 2020

# Contents

<b>1</b>	<b>Introduction</b>	<b>1</b>
<b>2</b>	<b>Theoretical background</b>	<b>3</b>
2.1	The Standard Model of particle physics	3
2.1.1	Particle content and interactions	3
2.1.2	The Standard Model as a gauge theory	4
2.1.3	Quantum Chromodynamics	6
2.1.4	Electroweak interactions	7
2.1.5	Spontaneous symmetry breaking and the Higgs field	8
2.1.6	Feynman diagrams and renormalisation	10
2.2	Dark Matter	12
2.3	Two Higgs doublet models	15
2.4	Signal models in the mono- $h(b\bar{b})$ analysis	18
2.4.1	$Z'$ -2HDM	19
2.4.2	2HDM+ $a$	21
<b>3</b>	<b>Experiment</b>	<b>27</b>
3.1	The Large Hadron Collider	27
3.2	The ATLAS detector	30
3.2.1	The coordinate system	30
3.2.2	Magnet system	31
3.2.3	Inner Detector	32
3.2.4	Calorimeter system	34
3.2.5	Muon Spectrometer	36
3.2.6	Forward detectors	38
3.2.7	Trigger system	38
3.2.8	Data preparation and computing	38
3.2.9	Simulation	39
<b>4</b>	<b>Object reconstruction and identification</b>	<b>43</b>
4.1	Track reconstruction and primary vertex	43
4.2	Small-radius jets	44
4.3	Large-radius jets	46
4.4	Variable-radius track jets	48
4.5	$b$ -tagging	48
4.6	Electrons and photons	50

4.7	Muons	51
4.8	$\tau$ -leptons	53
4.9	Overlap removal	54
4.10	Missing transverse momentum	54
4.11	Object-based $E_T^{\text{miss}}$ significance	55
<b>5</b>	<b>Introduction to the mono-<math>h(b\bar{b})</math> analysis</b>	<b>57</b>
5.1	Signature and analysis strategy	57
5.2	SM background processes	60
5.3	Simulated samples	62
5.4	Trigger strategy and efficiency calibration	65
5.4.1	Trigger strategy	65
5.4.2	Nomenclature and reconstruction algorithms	66
5.4.3	Trigger efficiency calibration	68
5.5	Event cleaning	72
<b>6</b>	<b>The 79.8 fb<math>^{-1}</math> analysis</b>	<b>75</b>
6.1	Object definitions	75
6.2	Event selection	76
6.2.1	Common selection	77
6.2.2	Resolved SR	78
6.2.3	Merged SR	81
6.3	Background estimation	83
6.3.1	1 $\mu$ -CR	85
6.3.2	2 $\ell$ -CR	86
6.3.3	Multijet background and $E_T^{\text{miss}}$ significance	87
6.4	Statistical analysis	89
6.4.1	Mathematical concepts	90
6.4.2	Fit setup of the analysis	93
6.5	Uncertainties	95
6.5.1	Experimental uncertainties	95
6.5.2	Theory uncertainties	95
6.5.3	Breakdown of dominant uncertainties	96
6.6	Results	96
<b>7</b>	<b>The 139 fb<math>^{-1}</math> analysis</b>	<b>103</b>
7.1	Motivation and improvements	103
7.2	Object definitions	104
7.3	Signal region optimisation	106
7.3.1	Event preselection	106
7.3.2	Kinematic properties of the 2HDM+ $a$ signals	107
7.3.3	Optimisation of the resolved SR	109
7.3.4	Event selection in the merged SR	123
7.4	Background estimation	125
7.4.1	1 $\mu$ -CR	125

7.4.2	2 $\ell$ -CR	128
7.5	Statistical analysis	132
7.6	Uncertainties	134
7.6.1	Experimental uncertainties	134
7.6.2	Theory uncertainties	134
7.6.3	Impact of uncertainties	135
7.7	Results	136
<b>8</b>	<b>Future prospects</b>	<b>145</b>
8.1	Analysis strategy	145
8.2	Axion-like particles	146
8.3	Combinations	147
<b>9</b>	<b>Conclusion</b>	<b>149</b>
<b>A</b>	<b>Additional information on <math>E_T^{\text{miss}}</math> trigger efficiency calibration</b>	<b>155</b>
A.1	Strategy in the 79.8 fb <sup>-1</sup> analysis	155
A.2	Event selection in the 139 fb <sup>-1</sup> analysis	157
A.3	Efficiencies and scale factors in the 139 fb <sup>-1</sup> analysis	158
<b>B</b>	<b>Signal acceptance and efficiency</b>	<b>163</b>



# Zusammenfassung

In dieser Arbeit werden zwei Suchen nach Dunkler Materie in Assoziation mit einem Higgs-Boson vorgestellt. Die Suchen basieren auf Daten, die vom ATLAS-Detektor in Proton-Proton-Kollisionen am LHC mit einer Schwerpunktsenergie von 13 TeV aufgenommen wurden. Es werden Endzustände mit fehlendem Transversalimpuls und einem Higgs-Boson, das in zwei  $b$ -Quarks zerfällt, untersucht. Abhängig vom Impuls des Higgs-Bosons wird zwischen zwei Signaturen unterschieden. Bei niedrigen Impulsen führen die  $h \rightarrow b\bar{b}$  Zerfallsprodukte zu zwei getrennten Jets mit kleinen Radiusparameter im Kalorimeter, während sie bei hohen Impulsen in einem einzelnen Jet mit großen Radiusparameter kollimiert sind. Mithilfe von Unterstrukturinformationen wird ausgewertet, ob ein Jet mit großem Radiusparameter von zwei  $b$ -Quarks initiiert wurde. Die Suche wird in Signalregionen durchgeführt, die aus Ereignissen ohne Leptonen bestehen. Lepton-basierte Kontrollregionen werden verwendet, um die dominanten Untergründe zu bestimmen, die aus  $t\bar{t}$ ,  $W$ +jets and  $Z$ +jets Prozessen bestehen. Die Ergebnisse werden mit einem simultanen Fit evaluiert, welcher Informationen aus den Signal- und Kontrollregionen berücksichtigt. Die wichtigsten Fitvariablen sind die Masse des rekonstruierten Higgs-Boson-Kandidaten und der fehlende Transversalimpuls.

Die erste Suche verwendet den vom 2015 bis 2017 aufgezeichneten Datensatz, der einer integrierten Luminosität von  $79.8 \text{ fb}^{-1}$  entspricht. In dieser werden neuartige Rekonstruktionsmethoden verwendet, um den Multijetuntergrund zu reduzieren und die Identifikation von Higgs-Bosonen mit sehr hohen Impulsen zu verbessern. Die zweite Suche basiert auf den von 2015 bis 2018 aufgezeichneten Daten, welche einer integrierten Luminosität von  $139 \text{ fb}^{-1}$  entsprechen. Diese beinhaltet Verbesserungen in der Ereignisselektion wie auch in der statistischen Analyse, wodurch der  $t\bar{t}$  Untergrund weiter unterdrückt und die Sensitivität auf Dunkle-Materie-Signale in unterschiedlichen kinematischen Bereichen gesteigert werden kann.

In keiner der Suchen ist ein signifikanter Überschuss an Daten im Vergleich zu den Standardmodellvorhersagen vorhanden. Beide Suchen werden in einem vereinfachten Modell, dem  $Z'$ -2HDM, für einen bestimmten Parameterbereich interpretiert. Dabei werden unterschiedliche Massen des  $Z'$ -Bosons und des pseudoskalaren Higgs-Bosons  $A$  getestet. In der Suche mit einem Datensatz von  $139 \text{ fb}^{-1}$  können  $Z'$ -Bosonen bis zu einer Masse von 3.2 TeV auf einem Konfidenzniveau von 95% ausgeschlossen werden. Für die  $A$ -Masse reichen die Ausschlussgrenzen bis 700 GeV. Zusätzlich wird die Suche in einem anderen vereinfachten Modell, dem 2HDM+ $a$ , für zwei verschiedene Parameterbereiche interpretiert, die sich in ihrem dominanten Produktionsmechanismus unterscheiden. Für von Gluon-Gluon-Fusion initiierte Prozesse können  $A$ -Massen bis zu 1.6 TeV und Massen vom pseudoskalaren  $a$  bis zu 520 GeV ausgeschlossen werden. Für Produktion aus  $b$ -Quark-Paarvernichtung reichen die Ausschlussgrenzen für die Massen vom  $A$  und  $a$  bis zu 1 TeV bzw. 300 GeV.



# Abstract

This thesis presents two searches for Dark Matter in association with a Higgs boson. The searches analyse the data recorded by the ATLAS detector in proton-proton collisions at the LHC with a centre-of-mass energy of 13 TeV. In these, final states with missing transverse momentum and a Higgs boson decaying into a pair of  $b$ -quarks are studied. Two different final state signatures are considered, which depend on the momentum of the Higgs boson. For low momenta, the  $h \rightarrow b\bar{b}$  decay products lead to two well separated small-radius jets in the calorimeter, while for high momenta, they are collimated into a single large-radius jet. Additionally, jet substructure information is used to determine, whether the large-radius jet is compatible with originating from two  $b$ -quarks. The search is performed in signal regions consisting of events with no leptons in the final state. Control regions with leptons are used to constrain the dominant backgrounds, coming from  $t\bar{t}$ ,  $W$ +jets and  $Z$ +jets processes. The results are evaluated with a simultaneous fit, which takes into account information from the different signal and control regions. The main fit variables are the mass of the reconstructed Higgs boson candidate and the missing transverse momentum.

The first search is based on the dataset collected from 2015 to 2017, which corresponds to an integrated luminosity of  $79.8 \text{ fb}^{-1}$ . This uses novel reconstruction methods to reduce the multijet background and improve the identification of Higgs bosons with very large momenta. The second search uses the dataset recorded from 2015 to 2018, corresponding to an integrated luminosity of  $139 \text{ fb}^{-1}$ . In this, several optimisations in the event selection and the statistical analysis are introduced. These allow for a better rejection of the  $t\bar{t}$  background and enhance the sensitivity to Dark Matter signals in different kinematic regimes.

In both searches, no significant excess of data with respect to the Standard Model expectations is seen. The results of the searches are interpreted for a certain parameter subset of the  $Z'$ -2HDM benchmark model, in which different masses of the  $Z'$ -boson and the pseudoscalar Higgs boson  $A$  are tested. In the search with  $139 \text{ fb}^{-1}$  of data, masses of the  $Z'$ -boson and  $A$  are excluded up to 3.2 TeV and 700 GeV at 95% confidence level, respectively. The results are additionally interpreted within the 2HDM+ $a$  benchmark model for two parameter regions, which differ in their dominant production mechanisms. For processes induced by gluon-gluon fusion, masses of  $A$  and of the pseudoscalar mediator  $a$  are excluded up to 1.6 TeV and 520 GeV, respectively. For signals from  $b\bar{b}$ -induced production, the mass limits on  $A$  and  $a$  reach up to 1 TeV and 300 GeV, respectively.



# Chapter 1

## Introduction

The aim of particles physics is to explain, what the fundamental constituents of matter are and how they interact with each other. The elementary particles observed so far and all their interactions, except gravity, are successfully described by the Standard Model of particle physics. However, the particle content of the Standard Model accounts only for a small part of the total matter density in the universe. With a fraction of about 85% [1], most of it consists of *Dark Matter*. The existence of Dark Matter was inferred from various astrophysical observations. As an example, the velocity of stars within a galaxy cannot be explained, if only luminous objects contribute to the total galaxy mass [2]. Compelling evidence for Dark Matter also comes from the collisions of galaxy clusters, such as in the Bullet Cluster. In this, the visible hot gas was decelerated due to electromagnetic interactions. On the other hand, gravitational lensing showed, that most of the mass in the clusters passed through each other practically collisionless [2–4]. Therefore, there must be a large amount of non-luminous Dark Matter, which hardly interacts with ordinary matter and also with itself.

However, it is still an open question what Dark Matter actually consists of. A possible explanation could be, that it is made of elementary particles which interact only weakly with the particles of the Standard Model. Such Dark Matter particles could be produced in the proton-proton collisions at the Large Hadron Collider (LHC), which is currently the largest particle accelerator in the world, located near Geneva at the European Organization for Nuclear Research (CERN, from the French *Conseil Européen pour la Recherche Nucléaire*). The collisions delivered by the LHC are recorded and analysed by four big experiments. One of them is the ATLAS detector and the search for Dark Matter represents a substantial part of its research field. Since they do not interact with the detector material, Dark Matter particles would traverse it without a measurable signal. Thus, a final state consisting of Dark Matter particles alone cannot be measured. However, their presence can be inferred, if they are produced in association with a detectable Standard Model particle  $X$ , which recoils against the DM particles. Since the latter are “invisible”, this leads to a momentum imbalance in the collision which can be measured. Such final states are commonly referred to as “mono- $X$ ” signatures. Typically, these arise from initial state radiation, i.e. a particle  $X$  is radiated off the colliding quarks or gluons, which are the constituents of the protons. This is illustrated in Figure 1.1. However, if  $X$  is a Higgs boson, initial state radiation is highly suppressed due to the size of the Yukawa couplings. Therefore, in mono-Higgs final states, the Higgs boson originates from the same production mechanism as the Dark Matter particles, which allows to probe the effective coupling of Dark Matter to Standard Model particles [5].

The Higgs boson decays almost immediately after its production, so that only its decay

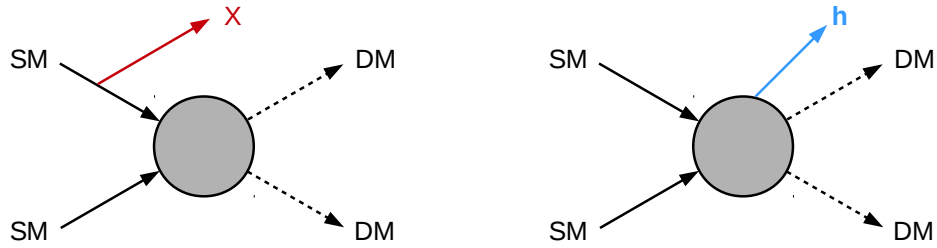


**Figure 1.1:** The left figure shows a typical mono- $X$  production mechanism, in which the particle  $X$  arises from initial state radiation of the colliding Standard Model particles (quarks or gluons). If  $X$  is a Higgs boson  $h$ , initial state radiation is suppressed. Therefore, in mono- $h$  signatures the Higgs boson originates from the same mechanism as the Dark Matter particles, as shown in the right plot. The Dark Matter particles are invisible in the detector, which is indicated by the dashed lines.

products can be detected. With a branching ratio of 58% [6], it decays predominantly into a pair of  $b$ -quarks. Compared to other decay modes, this channel thus allows to also test very rare processes with a mono-Higgs topology. Therefore, it is sensitive to a large variety of possible Dark Matter models.

At the ATLAS experiment, mono- $h(b\bar{b})$  final states have already been probed before in proton-proton collisions at the LHC [7–9]. There, no significant excess of data with respect to the Standard Model expectations was seen. Nevertheless, for many potential Dark Matter models the previous searches were not sensitive enough to find a possible signal among the Standard Model background. This makes it necessary to introduce more sophisticated analysis strategies. In this thesis, two searches are presented which, by using novel reconstruction techniques and optimised analysis methods, achieve a significantly higher sensitivity to Dark Matter models in various kinematic regimes. The first search is based on an integrated luminosity of  $79.8 \text{ fb}^{-1}$ , which corresponds to the data recorded in 2015-2017 with a centre-of-mass energy of 13 TeV. This uses e.g. a new approach to reconstruct  $h \rightarrow b\bar{b}$  decays, which considerably enhances the identification efficiency for Higgs bosons with high momenta. The second search uses the dataset collected in 2015-2018, corresponding to an integrated luminosity of  $139 \text{ fb}^{-1}$ . It contains numerous additional improvements, e.g. an optimised event selection. In this, better background rejection methods are introduced, which allow for a sensitivity increase to a broad class of Dark Matter models. The development and description of this new event selection, together with its impact on the sensitivity, represents the focus of this thesis.

The structure of the thesis is the following: Chapter 2 gives an introduction to the Standard Model and the Dark Matter models analysed in this work. The LHC, the ATLAS detector and the generation of simulations are explained in Chapter 3. The reconstruction and identification of the different physics objects is described in Chapter 4. Chapter 5.1 gives an introduction to the mono- $h(b\bar{b})$  analysis strategy and discusses common aspects of the  $79.8 \text{ fb}^{-1}$  and  $139 \text{ fb}^{-1}$  searches, which are presented in Chapter 6 and Chapter 7, respectively. An overview of future prospects for the mono- $h(b\bar{b})$  search is given in Chapter 8, followed by the conclusion in Chapter 9.

# Chapter 2

## Theoretical background

### 2.1 The Standard Model of particle physics

The Standard Model (SM) of particle physics is a theory which successfully describes the elementary particles of nature and, except gravity, their interactions with each other. This section gives an overview of the particle content of the SM and its mathematical formulation. The information presented is mostly taken from Ref. [10–12] and follows the notation convention of Ref. [12].

#### 2.1.1 Particle content and interactions

The particles of the SM are classified into fermions with spin  $\pm 1/2$  and bosons with integer spin. An overview of all fermions and bosons in the SM is given in Table 2.1 and Table 2.2, respectively<sup>1</sup>.

The fermions in the SM are divided into leptons and quarks. Leptons consist of the electron ( $e^-$ ), muon ( $\mu^-$ ) and the  $\tau$ -lepton ( $\tau^-$ ), which have an electric charge of  $-1$  (expressed in terms of the elementary charge), and their associated electrically neutral neutrinos  $\nu_e$ ,  $\nu_\mu$  and  $\nu_\tau$ . Quarks occur in six different *flavours*, namely as up ( $u$ ), down ( $d$ ), charm ( $c$ ), strange ( $s$ ), top ( $t$ ) and bottom ( $b$ ) quarks. The up, charm and top quark have an electric charge of  $+2/3$  and are therefore collectively referred to as up-type quarks. The other three quark flavours are called down-type quarks and have an electric charge of  $-1/3$ . Each quark also carries one of the three possible colour charges, denoted as red, green and blue. Fermions are further grouped into three generations. A lepton generation consists of a charged lepton and its associated neutrino, while in the case of quarks, a generation contains an up-type and a down-type quark. Moreover, each fermion has a corresponding anti-particle with the same mass, but with opposite charges. For example, the anti-particle of the electron is a positron with an electric charge of  $+1$ . If not explicitly stated, in this thesis anti-particles are always included when a certain fermion type is mentioned, e.g. the term “muon” denotes the actual muon as well as its positively charged anti-particle.

Bosons with spin 1 are so-called force carrier particles. These mediate electromagnetic, weak or strong interactions, which constitute the three fundamental interactions of particle physics. The photon is the mediator of the electromagnetic force. It is massless and couples to all particles which have an electric charge. Weak interactions are mediated by the three massive  $W^\pm$  and  $Z$ -bosons. The force carriers of strong interactions are eight gluons, which

---

<sup>1</sup>Throughout this work, natural units ( $\hbar = c = 1$ ) are used. Energies, masses and momenta are therefore always given in units of GeV.

are massless and have colour charges. They only couple to particles with colour charge, i.e. to quarks and other gluons. Furthermore, the SM contains a massive spin-0 boson, which is electrically neutral: The Higgs boson. It is a product of the Higgs mechanism, through which the  $W$  and  $Z$ -bosons acquire their masses.

Generation	Quarks			Leptons		
	Quark	$Q$ [ $e$ ]	Mass	Lepton	$Q$ [ $e$ ]	Mass
1	$u$	+2/3	2.2 MeV	$\nu_e$	0	$\approx 0$
	$d$	-1/3	4.7 MeV	$e$	-1	0.511 MeV
2	$c$	+2/3	1.28 GeV	$\nu_\mu$	0	$\approx 0$
	$s$	-1/3	95 MeV	$\mu$	-1	106 MeV
3	$t$	+2/3	173 GeV	$\nu_\tau$	0	$\approx 0$
	$b$	-1/3	4.18 GeV	$\tau$	-1	1.78 GeV

**Table 2.1:** The fermions of the SM with their electric charges  $Q$  and masses. The mass values are taken from Ref. [2] and are rounded to three significant digits, if known to this precision. Neutrinos also have masses, though they are very small. In the SM they are treated as completely massless.

Boson	Spin	$Q$ [ $e$ ]	Mass [GeV]
$\gamma$	1	0	0
$g$	1	0	0
$W^\pm$	1	$\pm 1$	80.4
$Z$	1	0	91.2
$H$	0	0	125

**Table 2.2:** The bosons of the SM with their spins, electric charges  $Q$  and masses. The mass values are taken from Ref. [2] and are rounded to three significant digits.

### 2.1.2 The Standard Model as a gauge theory

The mathematical formulation of the SM is based on Quantum Field Theories (QFT). This allows to describe processes at very small, i.e. quantum mechanical scales, which at the same time occur at relativistic energies. In QFT particles are not treated as discrete objects in three-dimensional space, but instead they represent modes of quantised fields. The field approach is necessary, because classical Quantum Mechanics cannot describe processes, in which the particle type and multiplicity changes, as for example in particle decays. The tools established by QFT are used to calculate decay rates as well as scattering cross sections.

The dynamics of fields is given by the action  $S$  [11], which is defined as the space-time integral of the Lagrangian density  $\mathcal{L}$ :

$$S = \int \mathcal{L}(\phi, \partial_\mu \phi) d^4x. \quad (2.1)$$

$\mathcal{L}$  is a function of one or more fields  $\phi$  and their derivatives  $\partial_\mu$ . In the following, the Lagrangian density is abbreviated simply as *Lagrangian*. Imposing  $\delta S = 0$ , which is referred

to as principle of least action, yields the Euler-Lagrange equation:

$$\partial_\mu \left( \frac{\partial \mathcal{L}}{\partial(\partial_\mu \phi)} \right) - \frac{\partial \mathcal{L}}{\partial \phi} = 0. \quad (2.2)$$

As in classical mechanics, the Euler-Lagrange equation leads to the equations of motion of a system. The formulation in terms of the Lagrangian has the advantage that all resulting expressions are Lorentz invariant. According to Noether's theorem, the invariance of physics laws under a continuous transformation is related to a conservation law [10]. For example, the symmetry under translations in time results in the conservation of energy. Similarly, the conservation of electric charges originates from the invariance of Quantum Electrodynamics (QED) under gauge transformations, which are described in the following.

The Lagrangian for a fermion field  $\psi$  with mass  $m$  is given by [10–12]:

$$\mathcal{L} = \bar{\psi}(i\gamma^\mu \partial_\mu - m)\psi, \quad (2.3)$$

where  $\gamma^\mu$  denotes the four Dirac matrices  $\gamma^0, \gamma^1, \gamma^2$  and  $\gamma^3$ . Furthermore,  $\bar{\psi}$  is defined as  $\bar{\psi} = \psi^\dagger \gamma^0$ , with  $\psi^\dagger$  indicating the hermitian adjoint of the field  $\psi$ .  $\mathcal{L}$  has a global  $U(1)$  symmetry under transformations of the form:

$$\psi(x) \rightarrow e^{-iQ\alpha} \psi(x), \quad (2.4)$$

where  $Q$  is the fermion charge and  $\alpha$  an arbitrary real number. However,  $\mathcal{L}$  is not invariant under local transformations with a space-time dependent  $\alpha(x)$ , i.e. it is not *gauge invariant*. To achieve this,  $\partial_\mu$  in Equation 2.3 needs to be replaced by the covariant derivative  $D_\mu$ :

$$D_\mu = \partial_\mu + iQA_\mu(x). \quad (2.5)$$

Here, a massless vector field  $A_\mu$  is introduced, which interacts with the fermion field. The strength of this interaction is proportional to  $Q$ . The field  $A_\mu$  transforms like:

$$A_\mu(x) \rightarrow A_\mu(x) - \frac{1}{Q} \partial_\mu \alpha(x), \quad (2.6)$$

thereby  $\mathcal{L}$  becomes the Lagrangian of QED:

$$\mathcal{L}_{\text{QED}} = \bar{\psi}(i\gamma^\mu D_\mu - m)\psi - \frac{1}{4} F_{\mu\nu} F^{\mu\nu}. \quad (2.7)$$

The second term in  $\mathcal{L}_{\text{QED}}$  is the kinetic term of the free vector field  $A_\mu$ , expressed by the field strength tensor  $F_{\mu\nu}$ :

$$F_{\mu\nu} = \partial_\mu A_\nu - \partial_\nu A_\mu. \quad (2.8)$$

which is invariant under transformations of  $A_\mu$ . The latter represents the photon field obeying the Maxwell equations.

QED is based on a  $U(1)$  symmetry group, which is a one-dimensional unitary group with abelian, i.e. commuting generators. The steps to achieve gauge invariance in QED can be generalised to non-abelian gauge groups like  $SU(N)$ , which describe special unitary matrices of dimension  $N$  with unit determinant. This is referred to as Yang-Mills theory [12, 13]. Since

it is based on a  $U(1)$  symmetry group, the QED formalism leads to a single vector field, while a Yang-Mills theory has as many gauge bosons as there are generators in the underlying group. The symmetry group  $SU(N)$  has  $N^2 - 1$  generators. Therefore, a Yang-Mills theory based e.g. on the group  $SU(2)$  has three, while for  $SU(3)$  there are eight associated gauge fields. In addition to the coupling to fermions, Yang-Mills theories also allow for self-interactions of gauge fields with triple and quartic couplings.

The full SM can be described as a combination of three gauge groups:

$$SU(3)_c \times SU(2)_L \times U(1)_Y. \quad (2.9)$$

The following sections will explain the different symmetry groups and their impact on the SM particles and interactions.

### 2.1.3 Quantum Chromodynamics

Quantum Chromodynamics (QCD) describes the interaction of quarks and gluons. It is based on a  $SU(3)_C$  symmetry group, where the subscript  $C$  indicates that the strong force only acts on particles with colour charge. As QCD is a Yang-Mills theory, it contains eight gauge fields, corresponding to the massless gluon fields. The covariant derivative of QCD is defined by:

$$D_\mu = \partial_\mu - ig_s \frac{\lambda^a}{2} G_\mu^a, \quad (2.10)$$

in which  $g_s$  denotes the strong coupling constant and  $\lambda^a$  the Gell-Mann matrices [12]. Commonly,  $g_s$  is expressed through  $\alpha_s = g_s^2/4\pi$ . The second term in Equation 2.10 describes the interaction of quarks with gluon fields  $G_\mu^a$ , where  $a \in [1, 8]$ . The gluon field strength tensor  $G_{\mu\nu}^a$  is given by:

$$G_{\mu\nu}^a = \partial_\mu G_\nu^a - \partial_\nu G_\mu^a + g_s f^{abc} G_\mu^b G_\nu^c, \quad (2.11)$$

where  $f^{abc}$  are the structure constants of  $SU(3)$ . With Equation 2.10 and 2.11, the Lagrangian of QCD is obtained as:

$$\mathcal{L}_{QCD} = \sum_q \bar{q}(i\gamma^\mu D_\mu - m)q - \frac{1}{4} G_{\mu\nu}^a G^{a,\mu\nu}. \quad (2.12)$$

Here,  $q$  and  $\bar{q}$  denote a quark field and the corresponding adjoint, respectively. The sum runs over the six different quark flavours. The second term in Equation 2.12 represents the kinetic term of the gluon fields. Apart from quark-gluon interactions, the gluon fields can also undergo self-interactions with triple and quartic vertices.

A substantial aspect of QCD is *asymptotic freedom*, which comes from the fact that  $\alpha_s$  decreases with increasing momentum scales. Consequently, quarks and gluons act as free particles at short distances. In this regime, QCD processes can be calculated with the use of perturbation theory. However, at large distances QCD becomes non-perturbative and quarks and gluons are confined in colour-neutral states, which is thus referred to as colour confinement [10, 13]. For this reason, quarks and gluons cannot be observed as free particles in nature. Instead, they occur as bound states of quarks and anti-quarks (mesons) carrying a

given colour and the associated anti-colour, or three quarks or three anti-quarks (baryons) with the three colours red, green and blue, which are cancelling each other. Bound states of quarks are collectively denoted as hadrons<sup>1</sup>. Due to colour confinement, quarks and gluons created in the proton-proton ( $pp$ ) collisions at the LHC appear in the detector as collimated showers of hadrons, called *jets*.

#### 2.1.4 Electroweak interactions

The electromagnetic and weak interactions are described in a common theory of electroweak interactions, which is based on the symmetry group  $SU(2)_L \times U(1)_Y$ . Transformations of this group act differently on left and right-handed fermion fields, denoted by  $\psi_L$  and  $\psi_R$ , respectively. These are obtained from the standard fermion field  $\psi$  through the projections [12]:

$$\psi_L = \frac{1 - \gamma_5}{2} \psi, \quad \psi_R = \frac{1 + \gamma_5}{2} \psi, \quad (2.13)$$

with  $\gamma_5 = -i\gamma^0\gamma^1\gamma^2\gamma^3$ .  $SU(2)_L$  is called the weak isospin group. It has the quantum numbers  $I$  and  $I_3$ , with  $I_3$  being the  $z$ -component of  $I$ , and acts only on left-handed fermion fields. Hence, the subscript  $L$  is appended to the group name. All left-handed fermion fields have  $I = 1/2$ . They form doublets consisting either of a charged lepton and its associated neutrino or of an up-type and a down-type quark:

$$\begin{pmatrix} \nu_e \\ e^- \end{pmatrix}_L, \quad \begin{pmatrix} u \\ d' \end{pmatrix}_L, \quad \begin{pmatrix} \nu_\mu \\ \mu^- \end{pmatrix}_L, \quad \begin{pmatrix} c \\ s' \end{pmatrix}_L, \quad \begin{pmatrix} \nu_\tau \\ \tau^- \end{pmatrix}_L, \quad \begin{pmatrix} t \\ b' \end{pmatrix}_L.$$

The particles in the top doublet entries have  $I_3 = +1/2$  and the ones in the bottom  $I_3 = -1/2$ . Transformations of the weak isospin group proceed always within the same doublet. For leptons, the doublets are identical to the mass eigenstates of a given generation. However, this is not the case for quarks, hence a prime symbol is appended to the down-type quarks in the definition above. An up-type (down-type) quark will still predominantly transform into the corresponding down-type (up-type) quark of its generation. It is also possible, though with a much smaller probability, that it goes into a down-type (up-type) quark of another generation. For example, charm-quarks decay mostly into strange-quarks, but transformations into a down or bottom quark can occur, too. This is indicated by  $s'$ . The different quark-transition probabilities are given by the magnitude squared elements of the Cabibbo-Kobayashi-Maskawa (CKM) matrix.

Right-handed fermion fields have  $I = 0$  and are therefore singlets under  $SU(2)_L$ . A  $SU(2)_L$  singlet consist only of a quark or a charged lepton, as there are no right-handed neutrinos in the SM.

The group  $U(1)_Y$  acts on both left and right-handed fermion fields. It couples to the weak hypercharge  $Y$ , which is defined by the Gell-Mann-Nishijima relation:

$$Y = \frac{Q - I_3}{2}. \quad (2.14)$$

<sup>1</sup>There exist also more exotic hadronic states, like pentaquarks or tetraquarks. However, these are produced very rarely compared to mesons and baryons.

$U(1)_Y$  has an associated vector field  $B_\mu$  with the field strength tensor  $B_{\mu\nu}$ :

$$B_{\mu\nu} = \partial_\mu B_\nu - \partial_\nu B_\mu. \quad (2.15)$$

The group  $SU(2)_L$  has three gauge fields  $W_\mu^a$  and the field strength tensor  $W_{\mu\nu}^a$ :

$$W_{\mu\nu}^a = \partial_\mu W_\nu^a - \partial_\nu W_\mu^a + g_2 \epsilon^{abc} W_\mu^b W_\nu^c, \quad (2.16)$$

with  $a = 1, 2, 3$ . Here,  $g_2$  is the coupling constant of  $SU(2)_L$  and  $\epsilon^{abc}$  is the structure constant of  $SU(2)$ . The Lagrangian of electroweak interactions is given by:

$$\mathcal{L}_{\text{EW}} = \sum_f \bar{\psi}_L^f i \gamma^\mu D_\mu^L \psi_L^f + \sum_f \bar{\psi}_R^f i \gamma^\mu D_\mu^R \psi_R^f - \frac{1}{4} W_{\mu\nu}^a W^{a,\mu\nu} - \frac{1}{4} B_{\mu\nu} W^{\mu\nu}, \quad (2.17)$$

where the first sum runs over all left-handed fermion doublets and the second sum over the right-handed fermion singlets. The covariant derivatives for left and right-handed fermion fields are:

$$D_\mu^L = \partial_\mu - i g_2 \frac{\sigma^a}{2} W_\mu^a + i g_1 \frac{Y}{2} B_\mu, \quad (2.18)$$

$$D_\mu^R = \partial_\mu + i g_1 \frac{Y}{2} B_\mu, \quad (2.19)$$

with  $\sigma^a$  being the Pauli matrices and  $g_1$  the coupling constant of  $U(1)_Y$ . At this stage all gauge and fermion fields are massless. In the SM, mass terms are obtained by introducing a Higgs field and the concept of spontaneous symmetry breaking to the theory.

### 2.1.5 Spontaneous symmetry breaking and the Higgs field

The Higgs sector in the SM is composed of an isospin doublet of complex scalar fields:

$$\phi = \begin{pmatrix} \phi^+ \\ \phi^0 \end{pmatrix}, \quad (2.20)$$

where  $\phi^+$  has an electric charge of +1 and  $\phi^0$  is electrically neutral [12]. The field  $\phi$  has  $I = 1/2$  and  $Y = 1$ . Therefore, the same covariant derivative as for left-handed fermion fields (c.f. Equation is 2.18) is applied to  $\phi$ , too. The corresponding Lagrangian is given by:

$$\mathcal{L}_H = (D_\mu \phi)^\dagger (D_\mu \phi) - V(\phi), \quad (2.21)$$

with a rotationally symmetric potential  $V(\phi)$  of the form:

$$V(\phi) = -\mu^2 \phi^\dagger \phi + \frac{\lambda}{4} (\phi^\dagger \phi)^2. \quad (2.22)$$

In the vacuum, i.e. in the ground state of the theory,  $V(\phi)$  must be minimal. Taking e.g.  $\mu^2$  to be negative and  $\lambda$  positive, the potential has only a single minimum at  $\phi = 0$ . However, if

both  $\mu^2$  and  $\lambda$  are positive,  $V(\phi)$  has a minimum for all values of  $\phi$  which satisfy  $\phi^\dagger\phi = 2\mu^2/\lambda$ . These minima describe a circle in the complex plane. The minimum is chosen as:

$$\langle\phi\rangle = \frac{1}{\sqrt{2}} \begin{pmatrix} 0 \\ v \end{pmatrix} \quad \text{with} \quad v = \frac{2\mu}{\sqrt{\lambda}}. \quad (2.23)$$

The brackets  $\langle \ \rangle$  around  $\phi$  denote the expectation value. By selecting a minimum, the initial symmetry of  $\mathcal{L}_H$  is broken, which is referred to as spontaneous symmetry breaking. It was found that  $v \approx 246$  GeV, which is determined from  $v = (\sqrt{2}G_F)^{-1/2}$ . Here,  $G_F$  denotes the Fermi constant. This describes the effective coupling constant of the four-fermion interaction in Fermi's theory of weak decays, which is obtained from measurements of the muon lifetime.

The field  $\phi$  can be expressed as an expansion around the vacuum expectation value:

$$\phi = \frac{1}{\sqrt{2}} \begin{pmatrix} \phi_1(x) + i\phi_2(x) \\ v + H(x) + i\chi(x) \end{pmatrix}, \quad (2.24)$$

in which the real scalar fields  $\phi_1$ ,  $\phi_2$ ,  $\chi$  and  $H$  are introduced. After inserting this into  $V_H$  of Equation 2.22 and evaluating with that  $\mathcal{L}_H$  of Equation 2.21, one finds that the electrically neutral field  $H$  has a mass of:

$$m_H = \sqrt{2}\mu. \quad (2.25)$$

The field  $H$  represents the Higgs boson, which has a measured mass  $m_H = 125$  GeV [2]. On the other hand, the fields  $\phi_1$ ,  $\phi_2$  and  $\chi$  remain massless and can be removed from  $\mathcal{L}_H$  by a suitable gauge transformation. The term  $(D_\mu\phi)^\dagger(D_\mu\phi)$  in Equation 2.21 leads to a coupling of  $H$  with the gauge fields  $B_\mu$  and  $W_\mu^a$ , through which they acquire mass terms. The physically observable states of  $B_\mu$  and  $W_\mu^a$ , i.e. the photon, the  $W$  and the  $Z$ -bosons, are obtained by the following linear combinations:

$$A_\mu = -\sin\theta_W W_\mu^3 + \cos\theta_W B_\mu, \quad (2.26)$$

$$W_\mu^\pm = \frac{1}{\sqrt{2}} (W_\mu^1 \mp iW_\mu^2), \quad (2.27)$$

$$Z_\mu = \cos\theta_W W_\mu^3 + \sin\theta_W B_\mu. \quad (2.28)$$

Here,  $\theta_W$  is the weak mixing angle, also referred to as Weinberg angle. The masses of the bosons are given by:

$$m_A = 0, \quad m_W = \frac{g_2}{2}v, \quad m_Z = \frac{\sqrt{g_1^2 + g_2^2}}{2}v. \quad (2.29)$$

Moreover,  $A_\mu$  stays massless and therefore corresponds to the photon field of the electromagnetic symmetry group  $U(1)_{\text{em}}$ . The masses of the  $W$  and  $Z$ -boson, the electroweak coupling constants and  $\theta_W$  are connected with each other through the relation:

$$\cos\theta_W = \frac{g_2}{\sqrt{g_1^2 + g_2^2}} = \frac{m_W}{m_Z}. \quad (2.30)$$

In summary, the bosons of the weak interaction acquire their masses through the Higgs mechanism, in which the  $SU(1)_L \times U(1)_Y$  symmetry gets broken with a non-zero vacuum expectation value.

Fermion masses are connected to the so-called Yukawa interactions of the Higgs field with the fermion fields. The Lagrangian describing these Yukawa interactions is given by:

$$\mathcal{L}_{Yukawa} = -Y_\ell \bar{L}_L \phi \ell_R - Y_d \bar{Q}_L \phi d_R - Y_u \bar{Q}_L \phi^c u_R + \text{h.c.} \quad (2.31)$$

where  $L_L$  and  $Q_L$  indicate left-handed lepton and quark doublets, respectively. The right-handed fields for the charged leptons are denoted by  $\ell_R$ , while  $u_R$  and  $d_R$  denote the right-handed up-type and down-type quarks, respectively. The coupling constants for the corresponding fermion type are given by  $Y_\ell$ ,  $Y_d$  and  $Y_u$ . In the third term,  $\phi^c$  specifies the charge conjugate of the Higgs field. The last term represents the hermitian conjugate of the preceding three terms. The mass of a fermion is given by:

$$m_f = Y_f \frac{v}{\sqrt{2}}, \quad (2.32)$$

which means that the higher the mass of the fermion is, the stronger also its coupling strength to the Higgs field.

The Higgs boson was discovered in 2012 by the ATLAS and CMS experiments [14, 15], which was mainly achieved through its decay modes into two photons or four leptons. With a branching ratio of 58% [6], the Higgs boson decays mostly into a pair of  $b$ -quarks. However, due to the large QCD background, the Higgs boson reconstruction is very challenging in this channel. Thus, it took another six years until also the observation of this decay mode could be claimed [16, 17].

### 2.1.6 Feynman diagrams and renormalisation

The mathematical expressions describing the interaction of elementary particles, which are based on perturbation theory, can be graphically represented through Feynman diagrams. Two examples are shown in Figure 2.1. All Feynman diagrams presented in this thesis have a horizontal time axis going from left to right, i.e. the particles on the left-hand side of the diagram constitute the initial and the ones on the right the final state of a certain interaction. Fermions are conventionally drawn as solid lines with arrows. An arrow pointing along the time axis indicates a fermion, while an arrow pointing backwards in time denotes an anti-fermion. Spin-1 bosons are drawn as wavy and gluons as curled lines. A dashed line represents a spin-0 boson, which in the SM can only be the Higgs boson.

The Feynman diagrams in Figure 2.1 illustrate so-called  $s$ -channel and  $t$ -channel processes, named after the Mandelstam variables  $s$  and  $t$ <sup>1</sup>. These are used to calculate scattering processes of a pair of two initial and two final state particles. Besides that, the variable  $s$  has an important meaning: Its square root,  $\sqrt{s}$ , yields the centre-of-mass energy of the particle system. In an  $s$ -channel process the initial two particles annihilate to form an intermediate particle, which eventually decays into another pair of particles. An example for this is the

<sup>1</sup>Apart from  $s$  and  $t$ , there is also a third Mandelstam variable  $u$ . It represents  $t$ -channel diagrams in which the two final state particles are interchanged.

process  $e^+e^- \rightarrow \mu^+\mu^-$  via an intermediate photon or  $Z$ -boson, as shown in the left diagram of Figure 2.1. For intermediate particles, one discriminates between on-shell and off-shell propagators. On-shell particles satisfy the relativistic energy-momentum relation, while off-shell particles do not [18]. Therefore, if a reaction proceeds via a  $W$ ,  $Z$  or Higgs boson, the invariant mass of its decay products does not necessarily have to be equal to the rest mass of the boson. The right Feynman diagram in Figure 2.1 is a  $t$ -channel process illustrating the scattering of two quarks through the exchange of a gluon. Feynman diagrams as in Figure 2.1 are so-called *tree-level* diagrams. In these, the initial and final state particles interact through a single propagator.

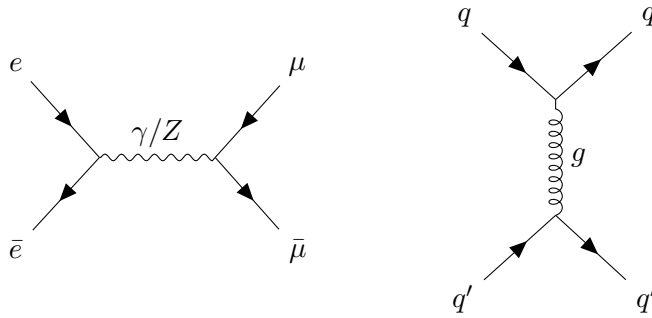


**Figure 2.1:** Illustration of an  $s$ -channel (left) and a  $t$ -channel diagram (right).

Diagrams with the minimum number of vertices and internal lines required to describe a certain process are called leading order (LO) diagrams. They can be viewed as the lowest order of a perturbation series. Higher-order diagrams of this series describe interactions with internal loops, as shown for example in Figure 2.2. Such processes are termed next-to-leading order (NLO) diagrams. With a loop more, they are referred to as NNLO diagrams, and so on.

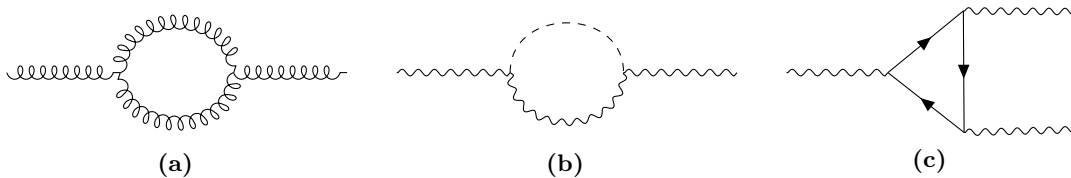


**Figure 2.2:** Examples for loop diagrams affecting a gluon propagator (a), a  $W$  or  $Z$ -boson propagator (b) or the vertex between three spin-1 bosons (c). Figure adapted from Ref. [12].

To determine the decay rate or the production cross section of a certain process, one needs to calculate its amplitude, which describes the dynamics of the process. For this, it is necessary to include all possible diagrams into the amplitude calculation which can mediate the interaction between a given initial and final state. For each vertex, the value of the corresponding coupling constant goes as an additional factor into the amplitude calculation. All coupling constants in the SM have values of less than unity (excluding values of  $\alpha_s > 1$ , for which perturbation theory breaks down). Therefore, the higher the order of a diagram, the less it contributes to the total amplitude.

For LO diagrams, the propagator momentum is fixed by the momenta of the incoming and outgoing particles. However, for diagrams with loops the momenta of internal lines cannot be inferred by momentum conservation, so that an integration over all possible momenta, i.e. up to infinity, must be performed. This would result in divergences in the process amplitude. To eliminate these, one needs to first *regularise* the integral. That is done by introducing a suitable procedure through which the integral can converge again. After that, a *renormalisation* scheme is applied. Thereby the divergences are absorbed into the quantities of the Lagrangian, e.g. the couplings and the masses. The physically observable couplings and masses correspond to the values obtained after renormalisation [10, 12]. All processes in the SM are renormalisable. If one wants to add effects beyond the SM in a theoretically consistent way, it is important to ensure the renormalisability of all interactions.

## 2.2 Dark Matter

The SM successfully describes the known elementary particles and their electromagnetic, weak and strong interactions. Nevertheless, the SM has various shortcomings, which makes it necessary to find a suitable *beyond-the-Standard-Model* (BSM) theory. For example, the SM does not include gravitational interactions and cannot explain the matter-anti-matter asymmetry in the universe. Furthermore, it treats neutrinos as massless, although the observation of neutrino oscillations proves that they indeed do have a mass [4, 10].

One major open question is the nature of Dark Matter (DM). Its existence is inferred from different astrophysical observations, e.g. from the measurement of galactic rotation curves. These describe the orbital velocity  $v(r)$  of stars as a function of their distance  $r$  from the galactic center. Using Newtonian mechanics and assuming that galaxies consist only of luminous matter,  $v(r)$  should scale as  $v(r) \propto 1/\sqrt{r}$  for sufficiently large  $r$ . However, it was found that  $v(r)$  is typically relatively flat, as can be seen in the rotation curve in Figure 2.3. This indicates that there is an additional halo of non-luminous (*dark*) matter. Another important example for the existence of DM comes from the collisions of galaxy clusters, for example the Bullet Cluster (1E0657-558). As most of the baryonic matter in a cluster consists of hot gas, one would expect the gravitational potential of the total mass, which can be derived from gravitational lensing, to follow the distribution of the hot gas. In the collision of the two clusters, the hot gas was decelerated through electromagnetic interactions. However, most of the total mass passed through each other practically collisionless [2–4]. Consequently, interactions of DM must be much weaker than of baryonic matter.

Another substantial method to investigate DM is the analysis of anisotropies in the cosmic microwave background. These anisotropies are well described by the so-called  $\Lambda$  Cold Dark Matter ( $\Lambda$ CDM) model [2]. The  $\Lambda$ CDM model parametrises the evolution and composition of the universe, for which it postulates *cold*, i.e. non-relativistic, DM and a cosmological constant  $\Lambda$  associated to Dark Energy. Introducing this form of energy makes it possible to explain the observed accelerated expansion of the universe. The ultimate fate of the universe depends on its curvature  $k$ . One distinguishes between  $k < 0$ ,  $k = 0$  and  $k > 0$ , for which the universe is considered to be closed, flat or open, respectively. If the universe is closed, it will eventually stop expanding and collapse afterwards, while a flat or open universe will infinitely expand. The most recent data from the Planck satellite is, within its experimental

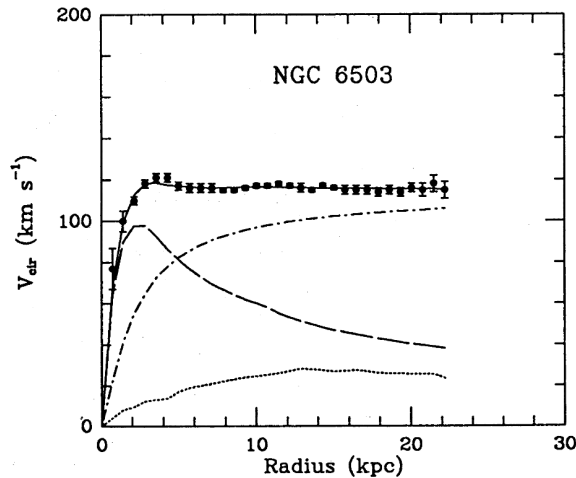


**Figure 2.3:** Rotation curve for the galaxy NGC 6503 [19]. The dots in the top curve correspond to the observed data. The dotted, dashed and dashed-dotted lines represent the contributions from gas, the galactic disk and the DM halo, respectively.

errors, consistent with the predictions for a flat universe [1]. The present DM content in the universe is specified by the DM relic density  $\Omega_c h^2$ , for which a value of

$$\Omega_c h^2 = 0.1198 \pm 0.0015$$

was obtained with the Planck data [1]. Here,  $h$  is the Hubble constant and  $\Omega_c = \rho_c / \rho_{\text{crit.}}$ , in which  $\rho_c$  denotes the mass density of cold DM and  $\rho_{\text{crit.}}$  the critical density. This is defined as the total density of the universe for the special case of  $k = 0$  and  $\Lambda = 0$  [2, 20]. For a flat universe, the DM relic density from above corresponds to 26.8% of the total energy. With a relative contribution of 68.3%, most of the energy in the universe consists of Dark Energy [1]. The remaining 4.9% are mostly identified with baryonic matter, while a minor contribution is related to photons and neutrinos. Thus, only a small fraction of the universe can be described by the SM.

However, it is yet unknown what DM consists of. Based on the astrophysical observations described before, candidates for DM must be stable on cosmological time scales and should barely interact with photons. DM can e.g. be made of subatomic particles. Among the particles of the SM, only neutrinos fulfil the requirements above. However, neutrinos are not abundant enough to yield the correct relic density [21]. Therefore, DM must have a different origin. DM candidates are e.g. primordial black holes, axions or sterile neutrinos [2]. Another possibility for DM are *weakly interacting massive particles* (WIMPs), which is also the DM candidate considered in this thesis.

WIMPs are hypothetical particles which have a mass of about 10 GeV to a few TeV and interact only weakly with SM particles. Here, “weakly” means that the particle is not interacting via electromagnetic or strong interactions, but its production is not necessarily tied to the  $W$  or  $Z$ -boson. The mass range is motivated by the so-called WIMP-miracle: The correct DM relic density can be obtained if the DM particles have interactions and a mass at the electroweak scale, i.e.  $\mathcal{O}(100 \text{ GeV})$  [20]. There are three different approaches

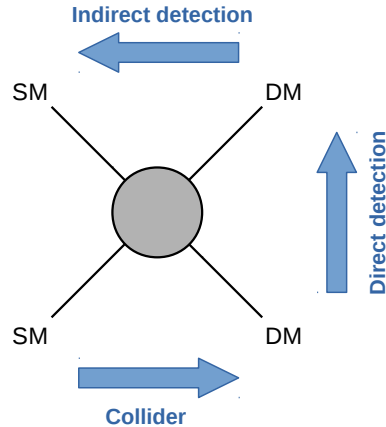


**Figure 2.4:** Illustration of the existing DM search strategies. The arrow indicates the time axis of the diagram for the corresponding search strategy. For example, for collider searches the diagram reads as  $SM + SM \rightarrow DM + DM$ . The blob in the middle stands for a generic SM-DM coupling, i.e. no assumptions on the exact interaction mechanism are made.

to search for WIMPs, as illustrated in Figure 2.4: Direct detection, indirect detection and collider searches. Direct detection experiments, such as CRESST [22] or XENON [23, 24], aim to measure the elastic scattering of an incoming WIMP with a nucleon of the detector (sometimes also recoils against electrons are studied). The associated signature is a nuclear recoil with an energy of about 1 – 100 keV [4]. Indirect detection experiments search for the decay products of WIMP-WIMP annihilation. Due to gravity, WIMPs are expected to accumulate near massive objects like the sun, so that this region of the sky should yield a high annihilation rate. Such signatures can be tested with ground-based neutrino detectors, for example IceCube [25, 26], as well as with satellite experiments like Fermi [27, 28]. In collider experiments, e.g. ATLAS [29] or CMS [30], WIMPs could be produced through the annihilation of SM particles. WIMPs will leave the detector without interaction, so that they cannot be directly observed. However, their presence can be inferred, if they recoil against a SM particle  $X$ , leading to a momentum imbalance that can be measured. This is referred to as  $E_T^{\text{miss}} + X$ , where  $E_T^{\text{miss}}$  denotes the missing transverse momentum variable discussed in Section 4.10, or commonly also mono- $X$  signature. Usually, mono- $X$  signatures arise from initial-state radiation (ISR), i.e. one of the initial two SM particles radiates off a quark, gluon, photon or a gauge boson before it collides. Opposed to that, radiation off the initial state is Yukawa-suppressed in mono-Higgs signatures. Therefore, the production of the Higgs boson is connected to the same production mechanism as of DM. Thus, mono-Higgs signatures represent a way of measuring the effective SM-DM coupling [5], as illustrated in Figure 1.1.

Ideally, one would embed the DM production mechanism into a more complete theory, which can also solve other shortcomings of the SM. The most prominent example for this is Supersymmetry (see e.g. Ref. [31] for more information), for which there are dedicated search programs at the ATLAS and CMS experiments. Such a complex theory, however, has many free parameters, which makes it difficult to test. Therefore, a common approach is to use *simplified models*, in which the studied parameter space is broken down by e.g. imposing

several experimental constraints and considering only certain production mechanisms and decay chains. This allows to focus only on certain signatures as predicted by the model of interest. In many DM searches a reverse approach is used: The starting point is already a simplified model, consisting often only of a single decay chain. However, such very simple models have different shortcomings. For example, they are often not renormalisable, which motivates again the need for a more complex theory. The signal models considered in this thesis represent a step towards this. In these, DM simplified models are used in combination with an extended Higgs sector, which ensures renormalisability. Thus they constitute theoretically consistent processes as they may also appear in a more complicated theory. On the other hand, the models are still simple enough to focus only on certain final state signatures.

## 2.3 Two Higgs doublet models

Although so far the experimental measurements of the Higgs boson are compatible with the SM predictions, these can also be explained by a variety of beyond-the-SM theories with an extended Higgs sector. There are different possibilities to realise an extended Higgs sector, e.g. by adding multiple isospin doublets of complex scalar fields with  $Y = 1$  and  $I = 1/2$ , equivalently to the SM (c.f. Equation 2.20). The simplest possibility for that is a Higgs sector with two such doublets, referred to as *Two Higgs Doublet Model* (2HDM). The theoretical description of the 2HDM is subjected to two major experimental constraints. The first affects the  $\rho$  parameter, which is defined by:

$$\rho = \frac{\sum_{i=1}^n [I_i(I_i + 1) - \frac{1}{4}Y_i^2] v_i}{\sum_{i=1}^n \frac{1}{2}Y_i^2 v_i} = \frac{m_W}{m_Z \cos \theta_W} . \quad (2.33)$$

Here,  $n$  is the number of Higgs multiplets and  $I_i$ ,  $Y_i$  and  $v_i$  are the weak isospin, hypercharge and vacuum expectation value of the  $i$ -th doublet, respectively [32–34]. In general, this relation is valid for any type of scalar multiplets, e.g. also singlets and triplets, which have different values for  $Y$  and  $I$  than the isospin doublets. From electroweak precision measurements of the  $W$  and  $Z$ -boson masses it is known that  $\rho \approx 1$ . This condition is met in the SM and must hold for any number of Higgs multiplets, too. The second constraint is that no flavour-changing neutral currents (FCNC) are observed, i.e. an up-type (down-type) quark cannot transform into another up-type (down-type) quark in a tree-level process. While FCNC are forbidden in the SM, they could in principle occur in the 2HDM. However, there they can be avoided through a suitable choice of the Higgs-fermion couplings. For both Higgs fields of the 2HDM, denoted by  $\phi_1$  and  $\phi_2$ , the coupling to fermions is given by the Yukawa interaction terms as in Equation 2.31. According to the Paschos-Glashow-Weinberg theorem, FCNC are absent if all right-handed fermions of a given charge couple only to a single Higgs doublet [32, 34]. There are different ways to fulfill this condition:

- Type I 2HDM: All right-handed quarks couple to only one Higgs doublet, which is by convention chosen to be  $\phi_2$ .
- Type II 2HDM: Right-handed up-type quarks couple to one Higgs doublet (conventionally  $\phi_2$ ) and down-type quarks to the other one ( $\phi_1$ ).

In both the type I and type II 2HDM it is usually assumed, that the right-handed leptons couple to the same doublet as the right-handed down-type quarks, even though this is not explicitly required by the Paschos-Glashow-Weinberg theorem. Including scenarios, in which the leptons have a different coupling structure, gives two more possibilities:

- Lepton-specific 2HDM: All right-handed quarks couple to  $\phi_2$ , while the right-handed leptons couple to  $\phi_1$ .
- Flipped 2HDM: As in the type II 2HDM, all right-handed up-type and down-type quarks couple to  $\phi_2$  and  $\phi_1$ , respectively, but the right-handed leptons couple to  $\phi_2$ .

Among these four models the type II 2HDM is the most studied one, as this is also the 2HDM present in the minimal supersymmetric model (MSSM). All signal models considered in this thesis are based on a type II 2HDM, in which the charge-parity (CP) symmetry is conserved in the Higgs sector. The most general potential for this kind of 2HDM, which also satisfies the two conditions from above, is given by:

$$\begin{aligned}
 V_H = & \mu_1 \phi_1^\dagger \phi_1 + \mu_2 \phi_2^\dagger \phi_2 + \left( \mu_3 \phi_1^\dagger \phi_2 + \text{h.c.} \right) + \lambda_1 (\phi_1^\dagger \phi_1)^2 + \lambda_2 (\phi_2^\dagger \phi_2)^2 \\
 & + \lambda_3 (\phi_1^\dagger \phi_1) (\phi_2^\dagger \phi_2) + \lambda_4 (\phi_1^\dagger \phi_2) (\phi_2^\dagger \phi_1) + \left( \lambda_5 (\phi_1^\dagger \phi_2)^2 + \text{h.c.} \right),
 \end{aligned}
 \tag{2.34}$$

where all parameters are real [32–34].  $V_H$  contains for both Higgs doublets terms in the form of the SM potential in Equation 2.22. In addition, there are also terms involving a mixing of  $\phi_1$  and  $\phi_2$ . The parameters  $\lambda_1 - \lambda_5$  need to be chosen such as to ensure the stability of the 2HDM potential. A necessary condition for this is that  $V_H$  needs to be bounded from below, i.e. it should have a stable minimum and not diverge to minus infinity. This is given by the following relations [2, 34]:

$$\lambda_1 \geq 0, \quad \lambda_2 \geq 0, \quad \lambda_3 \geq -\sqrt{\lambda_1 \lambda_2}, \quad \lambda_3 + \lambda_4 - |\lambda_5| \geq -\sqrt{\lambda_1 \lambda_2}.
 \tag{2.35}$$

Similar to the SM, the  $W$  and  $Z$ -bosons attain their masses through electroweak symmetry breaking. However, in the 2HDM this leads to five different Higgs bosons. As CP is conserved in  $V_H$ , the mass eigenstates also correspond to CP eigenstates. These are: Two neutral CP-even (*scalar*)  $H$  and  $h$ , of which  $h$  denotes the lighter one, one neutral CP-odd (*pseudoscalar*)  $A$  and two charged scalar Higgs bosons  $H^\pm$  [32–34]. With the chosen  $V_H$ ,  $\phi_1$  and  $\phi_2$  have vacuum expectation values in the form:

$$\langle \phi_1 \rangle = \frac{1}{\sqrt{2}} \begin{pmatrix} 0 \\ v_1 \end{pmatrix}, \quad \langle \phi_2 \rangle = \frac{1}{\sqrt{2}} \begin{pmatrix} 0 \\ v_2 \end{pmatrix}.
 \tag{2.36}$$

An important parameter in the 2HDM is  $\tan \beta$ , which is defined by:

$$\tan \beta = \frac{v_1}{v_2}.
 \tag{2.37}$$

Even though the 2HDM has two different vacuum expectation values, the SM predictions for the gauge boson masses and couplings are still valid. The connection of the 2HDM to the

SM is obtained by setting  $v = \sqrt{v_1^2 + v_2^2}$  in Equation 2.29. Another important parameter in the 2HDM is  $\sin \alpha$ , respectively  $\alpha$ . This is the rotation angle which diagonalises the mass matrix for the two neutral scalar Higgs bosons. The SM Higgs boson  $H^{\text{SM}}$  results from a combination of these:

$$H^{\text{SM}} = h \sin(\alpha - \beta) - H \cos(\beta - \alpha). \quad (2.38)$$

The masses of the newly introduced Higgs bosons, the mixing angles and  $v$  can be obtained from the parameters of  $V_H$ , i.e.  $\mu_1 - \mu_3$  and  $\lambda_1 - \lambda_5$ , through a basis transformation:

$$\left\{ \begin{array}{l} \mu_1, \mu_2, \mu_3, \\ \lambda_1, \lambda_2, \lambda_3, \lambda_4, \lambda_5, \end{array} \right\} \longleftrightarrow \left\{ \begin{array}{l} v, m_h, m_H, m_A, m_{H^\pm}, \\ \cos(\beta - \alpha), \tan \beta, \lambda_3 \end{array} \right\}. \quad (2.39)$$

Usually, 2HDMs are parametrised with the second representation because the Higgs boson masses,  $v$  and the mixing angles are the actual observables of the theory. From the initial parameters of  $V_H$ , only  $\lambda_3$  appears in the second representation. Instead of  $\lambda_3$ , it is in general possible to select another parameter of  $V_H$  in the second representation, e.g.  $\lambda_5$ , like in Ref. [35].

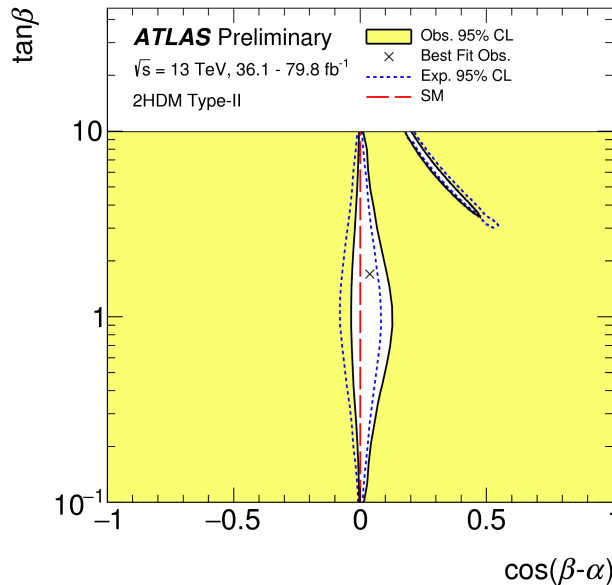


**Figure 2.5:** Excluded phase space (yellow area) for  $\tan \beta$  and  $\cos(\beta - \alpha)$  in the type II 2HDM [36].

The parameters of the 2HDM are subjected to different constraints. First,  $v \approx 246$  GeV must still hold to ensure the correct masses and couplings for the SM gauge bosons. Furthermore, a lower bound on  $\tan \beta$  of about 0.3 is obtained by requiring the Yukawa coupling of the top-quark to be perturbative [32]. In addition, the available phase space for  $\tan \beta$  and  $\cos(\beta - \alpha)$  is restricted by measurements of the Higgs boson couplings. Recent results of the ATLAS experiment are shown in Figure 2.5. From there it follows, that for  $\cos(\beta - \alpha) \approx 0$  arbitrary values of  $\tan \beta$  are allowed, while  $\tan \beta$  is strongly constrained for other choices of

$\cos(\beta - \alpha)$  [36]. The parameter space for which  $\cos(\beta - \alpha) = 0$  is called the *alignment limit*: Here,  $h$  is identical to the SM Higgs boson. Only signal models in the alignment limit are considered in this thesis. Therefore, the mass of  $h$  can be fixed to  $m_h = 125$  GeV.

Moreover, the masses of the charged Higgs bosons  $m_{H^\pm}$  are restricted by loop effects involving  $b$ -quarks [32, 37]. The most stringent constraint comes from  $\bar{B} \rightarrow X_s \gamma$ , where  $\bar{B}$  is a meson consisting of a  $b$ -quark and an anti-down-quark and  $X_s$  denotes a final state with an  $s$ -quark. The underlying  $b \rightarrow s \gamma$  decay proceeds through a loop diagram, as shown in Figure 2.6. If  $H^\pm$  exist, additional diagrams could contribute to that process which have the same form as Figure 2.6, but with the  $W$ -boson replaced by a  $H^\pm$ . As a result, this would affect the decay rate of  $b \rightarrow s \gamma$  [38–42]. The measurement of the decay rate allows to set lower limits on  $m_{H^\pm}$ . Ref. [38] states, that  $m_{H^\pm}$  should be greater than 295 GeV. This particular condition is also considered in the parameter choice of one of the DM models studied in this work, described in Section 2.4.1. More recent publications indicate that  $m_{H^\pm}$  of up to 580 GeV are excluded [41, 42]. However, such loop corrections could be weakened through the existence of other new particles, which are too heavy to be created in the experiment. Therefore, these bounds should only be considered as indicative [37].

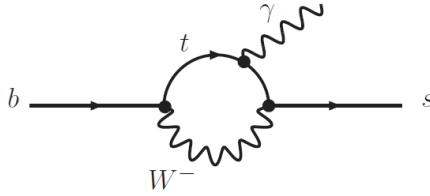


**Figure 2.6:** Feynman diagram for the  $b \rightarrow s \gamma$  decay. Figure taken from Ref. [43].

In addition, precision measurements of  $\rho$  provide constraints on the mass splittings between  $H$ ,  $H^\pm$  and  $A$ . Their existence could lead to additional loop corrections of the  $W$  and  $Z$ -boson, as in Figure 2.2(b). However, the mass corrections vanish for a CP-conserving potential if either  $m_H = m_{H^\pm}$  or  $m_A = m_{H^\pm}$  [44]. In the signal models studied in this work,  $m_A$  is treated as free parameter. Hence, the first condition  $m_H = m_{H^\pm}$  is applied.

## 2.4 Signal models in the mono- $h(b\bar{b})$ analysis

The results of the searches presented in this thesis are interpreted within two different models: The  $Z'$ -2HDM and 2HDM+ $a$ . These are based on a CP-conserving type II 2HDM complemented by a DM mediator sector. In both models the DM particles are assumed to be Dirac fermions, denoted by  $\chi$ . The stability of DM is guaranteed by introducing a new  $\mathbb{Z}_2$  symmetry, under which the DM particles are odd, i.e. they transform like  $\chi \rightarrow -\chi$  [37, 45]. The associated quantum number of the  $\mathbb{Z}_2$  symmetry must be conserved multiplicatively at each interaction vertex. Therefore, DM particles can only be produced in  $\chi\bar{\chi}$  pairs and cannot decay further into other particles [46]. The searches in this work target processes of the  $Z'$ -2HDM and 2HDM+ $a$ , which lead to a SM-like Higgs boson  $h$  in the final state. Only its dominant decay mode, the decay into two  $b$ -quarks, is considered. However, DM searches

are also performed in other Higgs decay channels. For example, the  $Z'$ -2HDM and 2HDM+ $a$  are also studied in the mono- $h(\gamma\gamma)$  analysis [47]. This targets the channel, in which the Higgs boson decays into a pair of photons.

### 2.4.1 $Z'$ -2HDM

In the  $Z'$ -2HDM [48] the DM sector is based on a  $U(1)_{Z'}$  symmetry, which gives rise to a massive spin-1 mediator, the  $Z'$ -boson. The process of interest in this work is shown in Figure 2.7: The  $Z'$ -boson is produced on-shell through quark-anti-quark annihilation and decays further into  $h$  and the pseudoscalar Higgs boson  $A$ . In the parameter space studied here,  $A$  decays exclusively into a pair of DM particles. Furthermore, in the  $Z'$ -2HDM only  $\phi_2$  and right-handed up-type quarks are charged under  $U(1)_{Z'}$ , while  $\phi_1$  and all other fermions are neutral. Therefore, possible constraints from dilepton analyses, which search for resonant decays like  $Z' \rightarrow \ell\ell$ , are evaded.

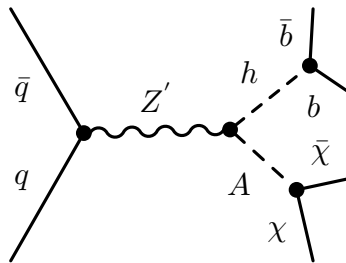


**Figure 2.7:** Feynman diagram for the  $Z'$ -2HDM process studied in the mono- $h(b\bar{b})$  analysis. Figure taken from Ref. [49].

Electroweak symmetry breaking leads to a mixing of the  $Z'$ -boson with the SM  $Z$ -boson. The corresponding masses are given by:

$$\begin{aligned} m_Z^2 &\approx (m_Z^0)^2 - \epsilon^2[(m_{Z'}^0)^2 - (m_Z^0)^2], \\ m_{Z'}^2 &\approx (m_{Z'}^0)^2 + \epsilon^2[(m_{Z'}^0)^2 - (m_Z^0)^2], \end{aligned} \quad (2.40)$$

where  $\epsilon$  denotes the mixing parameter and  $m_Z^0$  and  $m_{Z'}^0$  the masses of the  $Z$  and  $Z'$ -boson in the absence of mixing, respectively. The constraint  $\rho \approx 1$  implies an upper limit on  $g_{Z'}$ , which is the universal coupling strength of the  $Z'$ -boson. The effective coupling constants for the interaction between the  $Z'$ -boson and other particles are obtained through the multiplication of  $g_{Z'}$  with a vertex-specific factor. For example, the coupling in the  $Z' \rightarrow Ah$  decay is proportional to  $g_{Z'} \cos \beta$ .

In this thesis, the properties of the  $Z'$ -2HDM are studied by performing a scan in the  $m_A - m_{Z'}$  phase space, while keeping all other model parameters fixed. The chosen parameter settings follow the recommendations of the ATLAS/CMS Dark Matter forum [50]:

$$\begin{aligned} m_h &= 125 \text{ GeV}, & m_H^\pm &= m_H = 300 \text{ GeV}, & \cos(\beta - \alpha) &= 0, \\ \tan \beta &= 1, & g_{Z'} &= 0.8, & m_\chi &= 100 \text{ GeV}, & g_\chi &= 1, \end{aligned} \quad (2.41)$$

where  $m_\chi$  denotes the mass of the DM particle and  $g_\chi$  the coupling constant for the  $A\chi\bar{\chi}$  vertex. The choice for  $\cos(\beta - \alpha)$  and the Higgs masses follows the motivations presented in

the previous section. The value of 300 GeV for  $m_H$  and  $m_{H^\pm}$  is used to evade constraints from Ref. [38], according to which  $H^\pm$  with masses up to 295 GeV are excluded. For simplicity,  $\tan\beta$  is set to unity, because variations of  $\tan\beta$  do not lead to noticeable kinematic differences [50]. Similarly, changes of  $g_{Z'}$  do not affect the signal kinematics, hence the choice  $g_{Z'} = 0.8$  is rather arbitrary. However, variations of  $\tan\beta$  and  $g_{Z'}$  can still modify the production cross section. Furthermore, it is necessary that  $m_\chi < m_A/2$  to ensure on-shell production of  $A$ . To allow for a flexible choice of  $A$  down to small masses, a relatively low value of  $m_\chi = 100$  GeV is chosen. As long as  $m_\chi < m_A/2$  holds, the kinematic properties are largely independent of  $m_\chi$ . On the other hand, as  $m_\chi > m_h/2$ , the DM mass is still large enough to evade constraints from invisible Higgs decays. In such processes,  $h$  could directly decay into DM. The latest ATLAS results set an upper limit of 11% on the possible  $h \rightarrow$  invisible branching ratio [51]. Lastly, it is assumed that  $A$  decays with a branching ratio of 100% to  $\chi\bar{\chi}$ , thus  $g_\chi = 1$ . From the parameters of the 2HDM (c.f. Equation 2.39), only  $\lambda_3$  is not included in the  $Z'$ -2HDM. Due to the coupling structure in the  $Z'$ -2HDM,  $\lambda_3$  has no impact at all on the production cross section and the kinematics, so that it can be neglected [52].

### $Z'$ -2HDM interpretations in mono- $h(b\bar{b})$ searches

Figure 2.8 shows the exclusion contours for the  $m_A - m_{Z'}$  plane<sup>1</sup> obtained in the mono- $h(b\bar{b})$  search with  $36.1 \text{ fb}^{-1}$  of data [9]. In this,  $m_{Z'}$  is excluded up to 2.6 TeV and  $m_A$  up to 0.6 TeV. For comparison, also the exclusion limits from the  $3.2 \text{ fb}^{-1}$  search [8] are shown. The results of the mono- $h(b\bar{b})$  analyses with  $79.8 \text{ fb}^{-1}$  and  $139 \text{ fb}^{-1}$  of collected data are interpreted using the same parameter settings.

Apart from ATLAS, mono- $h(bb)$  searches are also performed at the CMS experiment [53, 54]. To be able to compare the results between the experiments, the  $139 \text{ fb}^{-1}$  analysis is additionally interpreted using the CMS parameter settings. These are identical to the ones in Equation 2.41, with the only difference that  $m_H^\pm = m_H = m_A$  [54].

### Validity and features of the $Z'$ -2HDM

Although the  $Z'$ -2HDM offers a way of predicting the production of DM in a renormalisable way, its application within the mono- $h(b\bar{b})$  search suffers from different shortcomings.

First, the exclusion contours in Figure 2.8 refer only to the diagram in Figure 2.7. However, a mono- $h(b\bar{b})$  signature could also be produced through the decay  $Z' \rightarrow Zh \rightarrow \nu\bar{\nu}h$ . Like DM, neutrinos can only be indirectly detected by a momentum imbalance, so that the final states  $\nu\bar{\nu}h$  and  $\chi\bar{\chi}h$  are indistinguishable. If  $\tan\beta = 1$ , the production cross sections for  $Z' \rightarrow Ah$  and  $Z' \rightarrow Zh$  have approximately the same order of magnitude [48]. For a more sophisticated study of the  $Z'$ -2HDM, the exclusion limits for the process in Figure 2.8 would need to be rescaled such as to include the contribution of the  $Z' \rightarrow Zh$  process.

Furthermore, most of the phase space, to which the mono- $h(b\bar{b})$  analysis is sensitive, is already excluded by dijet searches [55]. These search for resonant states, such as the  $Z'$ -boson, which decay into a pair of quarks. Constraints from dijet searches were indeed considered in the motivation of the  $Z'$ -2HDM [48]. However, these are based on Tevatron and LHC Run I results. If the latest Run II results are taken into account (c.f. for example Ref. [56–58]),

<sup>1</sup>The statistical methods used to derive these exclusion limits are explained in Section 6.4.1

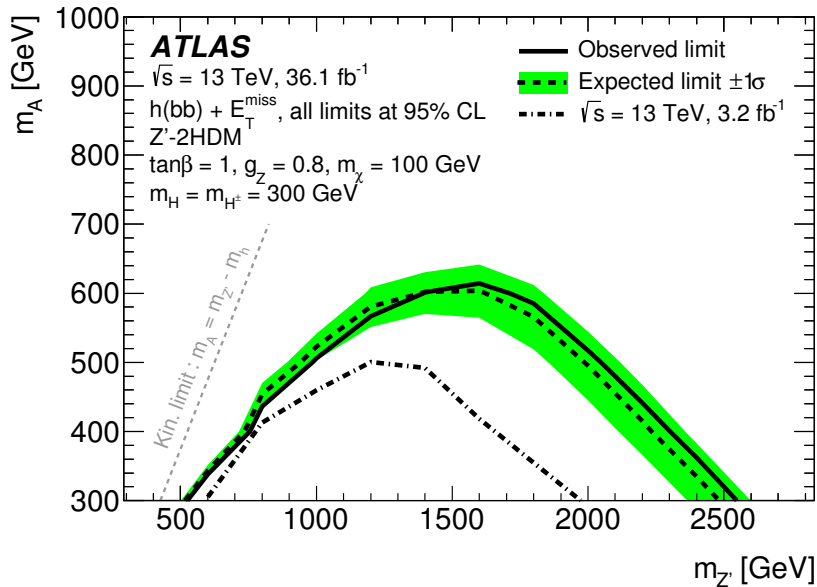


**Figure 2.8:** Exclusion contour in the  $m_{Z'} - m_A$  plane for the  $Z'$ -2HDM process of Figure 2.7 [9]. The solid line shows the observed limit of the mono- $h(bb)$  analysis with  $36.1 \text{ fb}^{-1}$  of collected data, with the region under the contour being the excluded phase space. The dotted line represents the expected limit, i.e. the limit that would be obtained if the data equals the SM background predictions, together with its  $1\sigma$  error (green band). The dotted-dashed line corresponds to the limit of the  $3.2 \text{ fb}^{-1}$  analysis.

the limits obtained are significantly stronger [55]. To evade these constraints, much lower values for  $g_{Z'}$  of 0.2 or smaller would need to be used and the cross sections appropriately rescaled.

Despite these shortcomings, the  $Z'$ -2HDM remains an interesting model to study. It is one of the few currently known models predicting a highly boosted Higgs boson in the final state, which is an experimentally interesting, but not yet sufficiently explored signature. Even if this particular model as such is not realised in nature, it can be used as a benchmark model to study this kinematic region, because another, not yet studied dijet model might lead to this signature and, at the same time, might not be constrained by dijet searches.

### 2.4.2 2HDM+ $a$

The second model studied in this work is the 2HDM+ $a$  [37, 59]. The DM sector is incorporated through a pseudoscalar singlet  $P$ , which couples to  $\chi$ . The interaction is described by the Lagrangian  $\mathcal{L}_\chi$ :

$$\mathcal{L}_\chi = -ig_\chi P \bar{\chi} \gamma_5 \chi, \quad (2.42)$$

where  $g_\chi$  is the dark-sector Yukawa coupling. The most general renormalisable scalar potential for the 2HDM+ $a$  is given by:

$$V = V_H + V_{HP} + V_P. \quad (2.43)$$

Here,  $V_H$  is the 2HDM potential as defined in Equation 2.34 and  $V_{HP}$  denotes the potential, which relates the Higgs doublets  $\phi_1$  and  $\phi_2$  to  $P$ :

$$V_{HP} = P \left( ib_P \phi_1^\dagger \phi_2 + \text{h.c.} \right) + P^2 \left( \lambda_{P1} \phi_1^\dagger \phi_1 + \lambda_{P2} \phi_2^\dagger \phi_2 \right), \quad (2.44)$$

In this,  $b_P$  is the trilinear and  $\lambda_{P1}$  and  $\lambda_{P2}$  the quartic coupling constants of  $V_{HP}$ . Lastly,  $V_P$  is the free potential term of  $P$ :

$$V_P = \frac{1}{2} m_P P^2. \quad (2.45)$$

where  $m_P$  is a parameter with mass dimension. A term with a quartic self-coupling of the form  $\propto P^4$  is not included in  $V_P$ , because it has no relevant effect on the kinematics. The physically observable mediator in the 2HDM+ $a$  is not  $P$  itself, but instead a mixture of  $P$  and the CP-odd field  $A$ . This pseudoscalar mediator is denoted by  $a$ , while  $\theta$  describes the associated mixing angle.

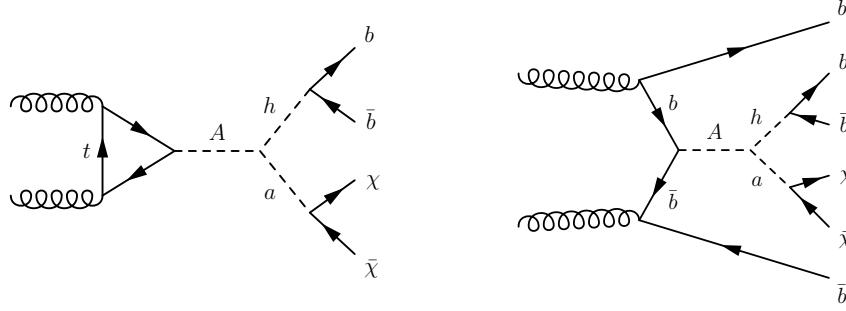


**Figure 2.9:** Representative Feynman diagrams for the 2HDM+ $a$  leading to a mono- $h(b\bar{b})$  signature. The left plot is a gluon-gluon fusion and the right plot a  $b\bar{b}$ -induced process.

The 2HDM+ $a$  can lead to mono- $h(b\bar{b})$  signatures through diagrams like in Figure 2.9. There, a resonantly produced  $A$  decays to  $h$  and  $a$ , which subsequently decays into  $\chi\bar{\chi}$ . Two different production mechanisms can initiate this processes: Gluon-gluon fusion (ggF), which involves a virtual top-quark loop, or  $b\bar{b}$ -annihilation. In the latter, the  $b$ -quarks are initially created through gluon splitting  $g \rightarrow b\bar{b}$ . Thus, this model leads to final states with two additional  $b$ -quarks besides the ones from the  $h \rightarrow b\bar{b}$  decay. The total production cross section of the ggF and  $b\bar{b}$ -induced processes depends on  $\tan\beta$ . In ggF processes, the cross section decreases with increasing  $\tan\beta$ , and vice versa for  $b\bar{b}$ -induced production. The reason for this is, that the couplings of  $H$ ,  $A$  and  $a$  to top quarks are proportional to  $1/\tan\beta$ , while their couplings to bottom quarks are proportional to  $\tan\beta$  [59]. In Ref. [37] it was found, that the ggF and  $b\bar{b}$  cross sections have approximately the same size for  $\tan\beta \approx 5$ . In this work two different values of  $\tan\beta$  are studied, namely  $\tan\beta = 1$  and  $\tan\beta = 10$ , to cover scenarios in which either ggF or  $b\bar{b}$ -induced production is dominating, respectively. Furthermore, different mass configurations for  $A$  and  $a$  are tested, too. For the remaining parameters, the following benchmark values are chosen:

$$\begin{aligned} m_h &= 125 \text{ GeV}, & m_H &= m_A = m_H^\pm, & \sin\theta &= 0.35, \\ m_\chi &= 10 \text{ GeV}, & g_\chi &= 1, & \lambda_3 &= \lambda_{P1} = \lambda_{P2} = 3, \end{aligned} \quad (2.46)$$

which are based on the recommendations of the LHC DM Working Group [37]. These are motivated by the following: First, if  $m_a$  and  $m_\chi$  are sufficiently light,  $h$  could decay to DM via  $h \rightarrow aa^* \rightarrow 2\chi 2\bar{\chi}$ , in which  $a^*$  denotes the complex conjugate of  $a$ . Hence, to evade constraints from invisible Higgs decays [51], only values of  $m_a$  larger than 100 GeV are considered. It is assumed, that  $a$  decays exclusively to  $\chi\bar{\chi}$ , so that the corresponding coupling constant  $g_\chi$  is set to unity. To allow for on-shell production of  $a$ , it must hold that  $m_a > 2m_\chi$ . To keep the possibility of studying  $a$  down to low masses,  $m_\chi = 10$  GeV is chosen.

As mentioned in Section 2.3, modifications of the  $W$  and  $Z$ -boson masses from additional loop diagrams can be avoided by setting  $m_H = m_{H^\pm}$ . The additional requirement  $m_H = m_{H^\pm} = m_A$  ensures a large production rate for the processes in Figure 2.9. The reason for that is the coupling  $g_{Aah}$ , which is i.a. a function of  $m_H$ . For a given  $m_A$ ,  $g_{Aah}$  decreases, if  $m_H$  becomes smaller than  $m_A$ , thereby reducing the production rate for the two processes [59].

The requirement, that the Higgs potential should be bounded from below, must also be ensured in the 2HDM+ $a$ . Due to the additional pseudoscalar sector,  $\lambda_3$  is not only subjected to the constraints of Equation 2.35, but its possible values also depend on the choice of the Higgs boson masses and  $\sin\theta$ . If one wants to allow for  $m_H$ ,  $m_{H^\pm}$  and  $m_A$  up to  $\mathcal{O}(\text{TeV})$ , then this condition is e.g. met with the chosen benchmark  $\lambda_3 = 3$  and  $\sin\theta = 0.35$ . Furthermore, it is assumed that  $\lambda_{P1} = \lambda_{P2} = \lambda_3$ .

### 2HDM+ $a$ interpretations in mono- $h(b\bar{b})$ searches

Interpretations of the ATLAS mono- $h(b\bar{b})$  search within the 2HDM+ $a$  were performed for the first time in Ref. [45]. Figure 2.10 shows the exclusion limits obtained in the  $m_a - m_A$  plane for the benchmark parameters of Equation 2.46 and  $\tan\beta = 1$ . In this, the limits of the mono- $h(b\bar{b})$  search are overlaid with the ones of other DM searches, which are sensitive to the 2HDM+ $a$ . The mono- $h(b\bar{b})$  contour was derived with the results of the the  $36.1 \text{ fb}^{-1}$  analysis. For the chosen parameter settings, the searches with the largest sensitivity are the mono- $h(b\bar{b})$  and mono- $Z(\ell\bar{\ell})$  analyses. The latter targets final states with a  $Z$ -boson decaying to a pair of electrons or muons.

The limits presented in Figure 2.10 were obtained by a reinterpretation of the different DM searches, i.e. the finalised search results were reevaluated with respect to the 2HDM+ $a$  signals. However, the search strategy of the  $36.1 \text{ fb}^{-1}$  mono- $h(b\bar{b})$  analysis was defined by studying the kinematics predicted by the  $Z'$ -2HDM signals. Even though both the  $Z'$ -2HDM and the 2HDM+ $a$  give rise to mono- $h(b\bar{b})$  signatures, the kinematics of the final state particles may be quite different. Therefore, the search strategy is not necessarily optimal for the 2HDM+ $a$  signals. A dedicated optimisation for the 2HDM+ $a$  signals is performed for the first time in the course of the  $139 \text{ fb}^{-1}$  analysis, as discussed in Section 7.3.3.

### Validity and features of the 2HDM+ $a$

A special feature of the 2HDM+ $a$  is its complex phenomenology. Apart from the diagrams in Figure 2.9, mono- $h(b\bar{b})$  signatures can originate from other processes as well. Representative Feynman diagrams are shown in Figure 2.11. For example, the mediator  $a$  can be directly produced through ggF or  $b\bar{b}$ -annihilation and then decay into  $h$  and  $\chi\bar{\chi}$  via an off-shell  $A$ . Another possible production mechanism is *Higgs-Strahlung*. Here, only an  $A$  or  $a$  is produced, which radiates off a  $h$  and subsequently decays to  $\chi\bar{\chi}$ . Lastly, mono- $h(b\bar{b})$  final states can also arise from t-channel diagrams. The interplay of all production mechanisms depends on the

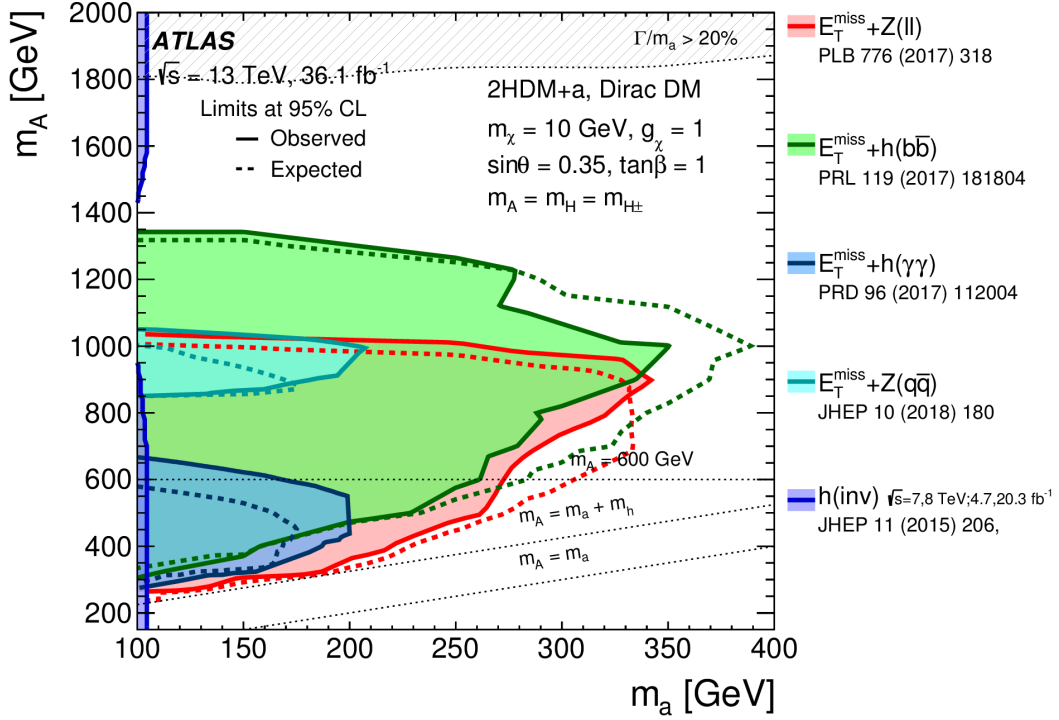


**Figure 2.10:** Exclusion contours in the  $m_A - m_a$  plane for the 2HDM+ $a$  with the parameters of Equation 2.46 and  $\tan\beta = 1$ . [45]. Besides the limits obtained from the  $36.1 \text{ fb}^{-1}$  mono- $h(bb)$  analysis, shown in green, also the exclusion contours from other DM searches are shown. The solid and the dashed lines represent the observed and expected limits, respectively.

model parameters and strongly affects the signal kinematics, as presented in Section 7.3.2.

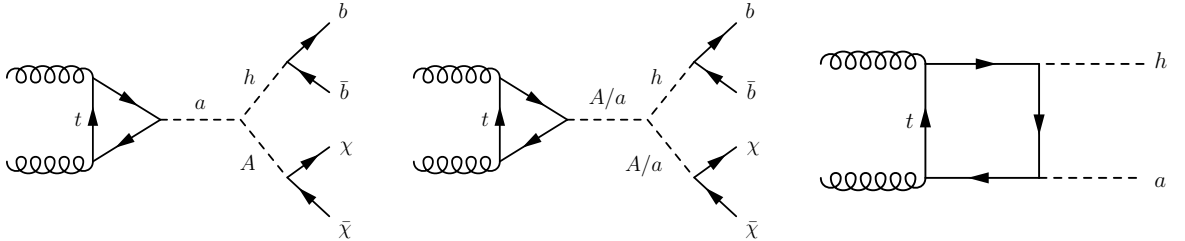


**Figure 2.11:** Feynman diagrams of the 2HDM+ $a$  which lead to mono- $h(bb)$  signatures via an off-shell  $a \rightarrow Ah$  decay (left), Higgs-Strahlung (middle), and a  $t$ -channel diagram. The diagrams are adapted from Ref. [60].

Due to the coupling structure of the pseudoscalars  $A$  and  $a$ , a mono- $h(bb)$  signature in the 2HDM+ $a$  is produced almost exclusively through the interaction with heavy quarks, i.e. either through the top-quark loop in the  $ggF$  processes or through  $b\bar{b}$ -annihilation [59]. For the same reason, dijet or dilepton final states are suppressed in the 2HDM+ $a$ .

Furthermore, the parameter choice of Equation 2.46 is in accordance with constraints from direct and indirect detection experiments. In general, pseudoscalar interactions are

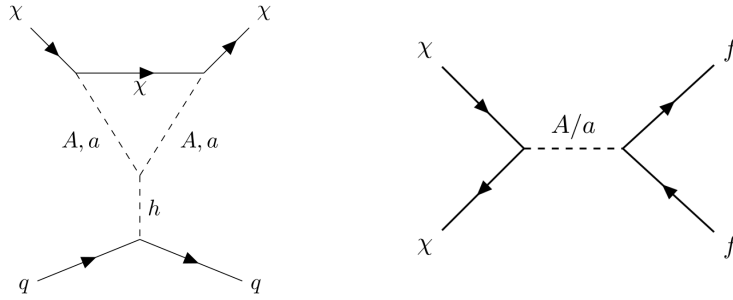


**Figure 2.12:** Representative Feynman diagrams of the 2HDM+ $a$  which lead to signatures relevant for direct detection (left) [61] and indirect detection experiments (right) [37].

suppressed at tree level in direct detection experiments [61], so that they only contribute weakly through loop diagrams, as shown in Figure 2.12. Therefore, collider searches are substantial in the study of the 2HDM+ $a$ . The phase space to which mono- $X$  searches are sensitive to is complementary to the one of direct detection experiments. The former have the highest sensitivity for  $m_a > 2m_\chi$ , while the latter provide the strongest bounds for  $m_a < 2m_\chi$  [37]. Figure 2.12 shows also a representative diagram for indirect detection experiments. Here, a DM pair annihilates through an  $A$  or  $a$  into two SM fermions. However, other final states are possible, too, for example  $hA$ ,  $HZ$  or  $H^\pm W^\pm$ , which subsequently decay into SM fermions. The total DM annihilation cross section in the 2HDM+ $a$  is estimated to be largest for DM masses of approximately 100 GeV – 400 GeV, while it is smallest in the low- $m_\chi$  region [37]. Therefore, with the chosen benchmark of  $m_\chi = 10$  GeV, mono- $X$  searches represent a suitable way of complementing indirect detection measurements.



# Chapter 3

## Experiment

### 3.1 The Large Hadron Collider

The LHC [62] is currently the world's largest particle accelerator and collider. It is located at CERN (from the French *Conseil Européen pour la Recherche Nucléaire*) near Geneva in an underground tunnel of 26.7 km circumference, which was built for the preceding Large Electron Positron Collider (LEP) experiment. In the LHC bunches of hadrons, for which either protons or lead-ions are used, circulate in two counter-rotating beams and are brought to collision at eight interaction points. At four of them, the following experiments are placed: ATLAS (A toroidal LHC apparatus), which is described in detail in the next section, CMS (Compact Muon Solenoid) [30], LHCb (LHC beauty) [63] and ALICE (A Large Ion Collider Experiment) [64]. ATLAS and CMS are general-purpose detectors, which are used for a large variety of research fields, reaching from SM precision measurements to searches for new physics. LHCb and ALICE, on the other hand, are specialised experiments constructed for a particular research goal. LHCb investigates the matter-antimatter asymmetry by analysing decays of hadrons that contain  $b$ -quarks. The ALICE experiment is focused on lead ion-collisions to study the quark-gluon plasma, which is the state of matter that probably existed shortly after the Big Bang.

The LHC was designed to collide protons with a maximum centre-of-mass energy of  $\sqrt{s} = 14$  TeV. From 2010 until 2011, the LHC was operated at  $\sqrt{s} = 7$  TeV, followed by another year of data-taking at  $\sqrt{s} = 8$  TeV. This is referred to as the LHC Run I. The data collected in Run I led to many new insights in the field of particle physics. Among these, one of the greatest achievements was the discovery of the Higgs boson, announced by the ATLAS and CMS collaborations in 2012 [14, 15]. After two years of upgrade and maintenance work, the LHC started its second operational run (Run II) in 2015 with a notably higher centre-of-mass energy of 13 TeV, which lasted until the end of 2018. Since then, the LHC is again shut down for upgrade purposes and will, according to the current schedule, restart operation in 2022 [65]. The searches presented in this thesis are based on the data collected in Run II.

Before the protons are injected into the LHC, they are accelerated through different machines of the CERN accelerator complex, which is shown in Figure 3.1. The start of this accelerator chain is a hydrogen bottle, used as the proton source of the LHC. The hydrogen atoms are ionised and then accelerated by the Linear accelerator 2 (Linac 2) to an energy of 50 MeV [62]. Afterwards, they are fed into the Proton Synchrotron Booster (PSB), followed by the Proton Synchrotron (PS), in which they reach an energy of 1.4 GeV and 25 GeV, respectively. Then, the protons are accelerated to 450 GeV by the Super Proton Synchrotron

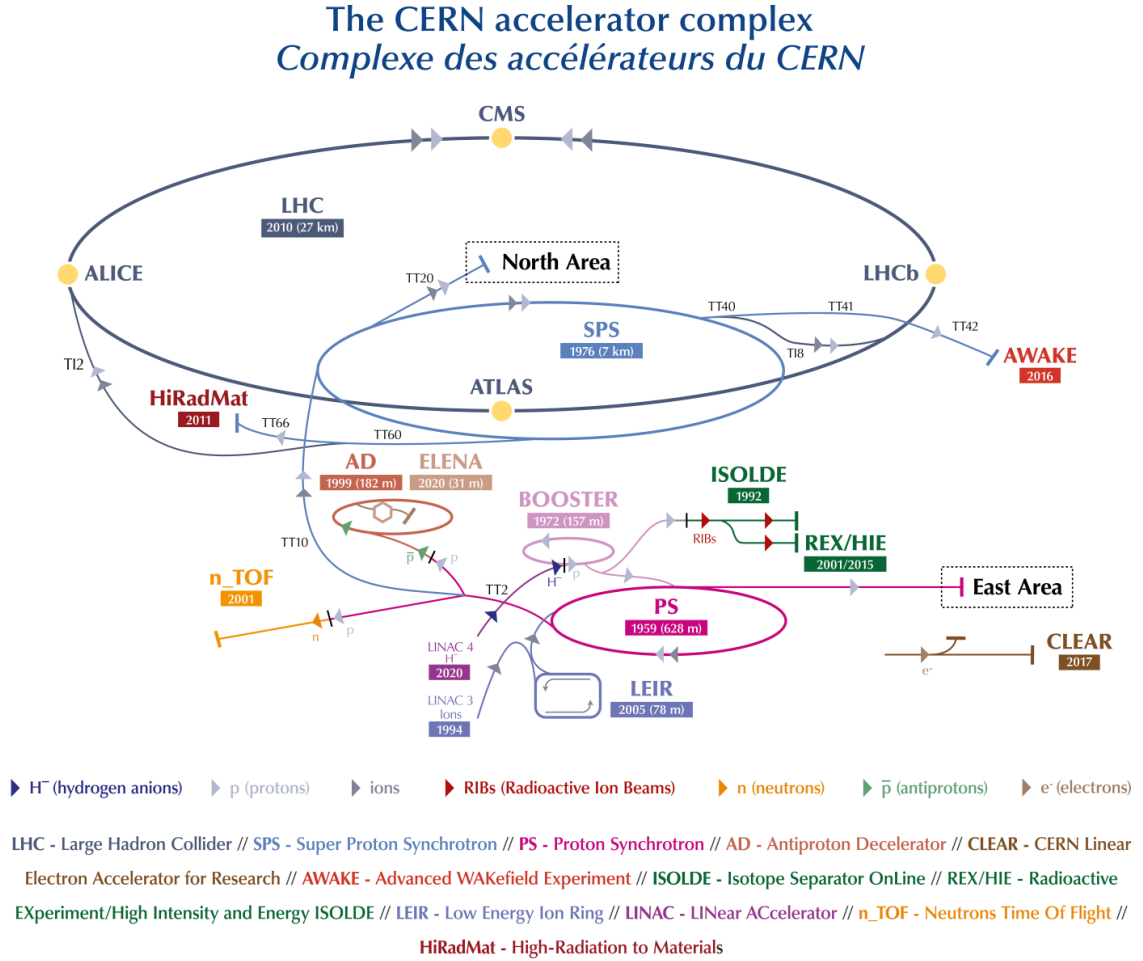


**Figure 3.1:** The CERN accelerator complex [66].

(SPS), before they are injected into the LHC.

The LHC consists of eight arcs and eight straight sections, inherited from the geometrical setup of the LEP experiment. The proton beams are accelerated through radiofrequency cavities and bent to a circular orbit with 1232 superconducting dipole magnets, which are cooled down to 1.9 K with superfluid helium. They provide a maximum magnetic field of 8.33 T. Apart from dipole magnets, the LHC comprises different quadrupole and correction magnets to focus the beams.

The protons travel through the LHC in a vacuum with a nominal bunch spacing of 25 ns. Each beam contains 2808 bunches with about  $1.1 \times 10^{11}$  protons in each bunch. For a certain physics process, the number of events  $N$  generated in the proton-proton ( $pp$ ) collisions is given by:

$$N = \sigma L = \sigma \int \mathcal{L} dt \tag{3.1}$$

where  $\sigma$  is the cross-section of the process of interest and  $L$  the luminosity.  $L$  can be expressed through the time integral of the instantaneous luminosity  $\mathcal{L}$ , which depends on several beam parameters, e.g. the number of bunches in the beam, the revolution frequency and the beam size. The LHC design value for  $\mathcal{L}$  is  $10^{34} \text{ cm}^{-2}\text{s}^{-1}$ . This was exceeded in Run II, in which a maximum value of  $2.1 \times 10^{34} \text{ cm}^{-2}\text{s}^{-1}$  was achieved [67]. Figure 3.2 shows the integrated luminosity  $L$  in Run II as a function of time. The LHC delivered in total  $156 \text{ fb}^{-1}$  of data. Due to inefficiencies in the data acquisition system and data-taking periods, in which the detector was not fully operating, the integrated luminosity recorded by the ATLAS detector amounts to  $147 \text{ fb}^{-1}$ . On this dataset additional quality criteria are imposed, which require that the detector components operated sufficiently well to allow for the reconstruction of physics objects with good quality. This leads to an integrated luminosity of  $139 \text{ fb}^{-1}$  that can be used for physics analyses.

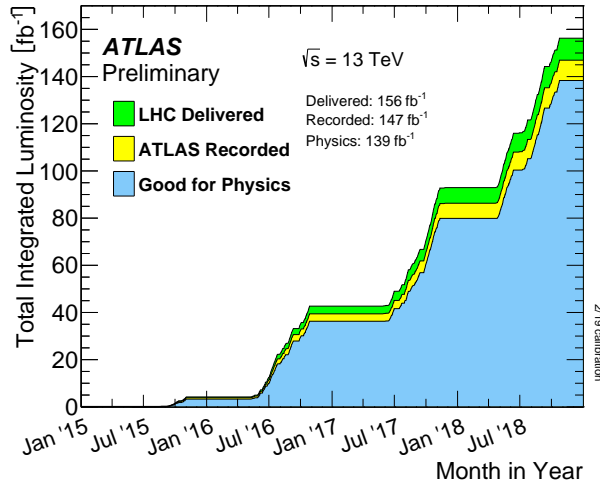


**Figure 3.2:** Integrated luminosity measured in 2015 – 2018 as a function of time [67]. The plot shows the luminosity that was delivered by the LHC (green), recorded by the ATLAS detector (yellow) and the luminosity which passed all data quality criteria to be used for physics analyses (blue).

Apart from the  $pp$  collision of interest, usually multiple other collisions happen in the detector at the same time. These additional collisions are referred to as *pile-up* [68]. Typically, these consist of QCD scattering processes which lead to jets in the forward detector region, i.e. close to the beam line. A good understanding of this background is necessary to discriminate objects of a certain collision from pile-up effects. The primary source of pile-up are collisions that occur within the same bunch crossing. Figure 3.3 shows the mean number of interactions per bunch crossing, denoted by  $\mu$ , in the ATLAS detector. This number depends on the LHC beam conditions and therefore varies between the different data-taking periods. For the entire Run II, the average value of  $\mu$  is approximately 34. Apart from that, a minor contribution to pile-up also comes from collisions of the preceding or subsequent bunch crossing.

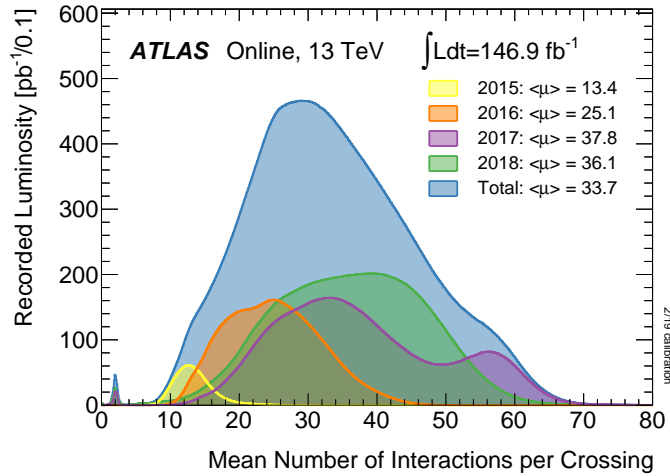


**Figure 3.3:** Luminosity-weighted distribution of the mean number of interactions per bunch crossing [67]. The blue area shows the distribution for the full Run II data. In addition, the distributions for the individual data-taking years in 2015 – 2018 are shown.

## 3.2 The ATLAS detector

The ATLAS detector [29] has a cylindrical layout, with the beam pipe corresponding to its central axis, and a forward-backward symmetry with respect to the nominal interaction point. It has a length of 44 m, a diameter of 25 m and a mass of about 7000 tonnes. The ATLAS detector consists of three subdetector systems arranged in different layers: The detector system closest to the interaction point is the Inner Detector (ID), followed by the calorimeter system and the Muon Spectrometer (MS). One subdetector system is ordered in cylindrical layers around the beam line, which is referred to as *barrel*. To ensure the detection of particles emitted in the very forward or backward direction, the other two sets of subdetector systems, called *end-caps*, are arranged in disks at the ends of the barrel. The layout of the ATLAS detector is shown in Figure 3.4. The information presented in the following sections is generally based on Ref. [29], except when indicated otherwise.

### 3.2.1 The coordinate system

The position of objects created in the  $pp$  collisions are described with a right-handed coordinate system. The origin of this is defined as the nominal interaction point. The  $x$ -axis points towards the centre of the LHC, the  $y$ -axis upwards and the  $z$ -axis along the beam line. The plane spanned by the  $x$  and  $y$ -axis is called the transverse plane. If “invisible” particles, such as neutrinos or DM particles, are produced in  $pp$  collision events, full momentum reconstruction is only possible in the transverse plane (this is explained in detail in Section 4.10). Therefore, many event quantities are measured in it. Due to the geometry of the ATLAS detector, it is useful to express the positions and distances of objects in cylindrical coordinates. The radius is denoted by  $R$ , the azimuthal angle  $\phi$  is the angle around beam line and the polar angle  $\theta$  is the angle from the beam line. The angle  $\theta$  can be expressed through the rapidity

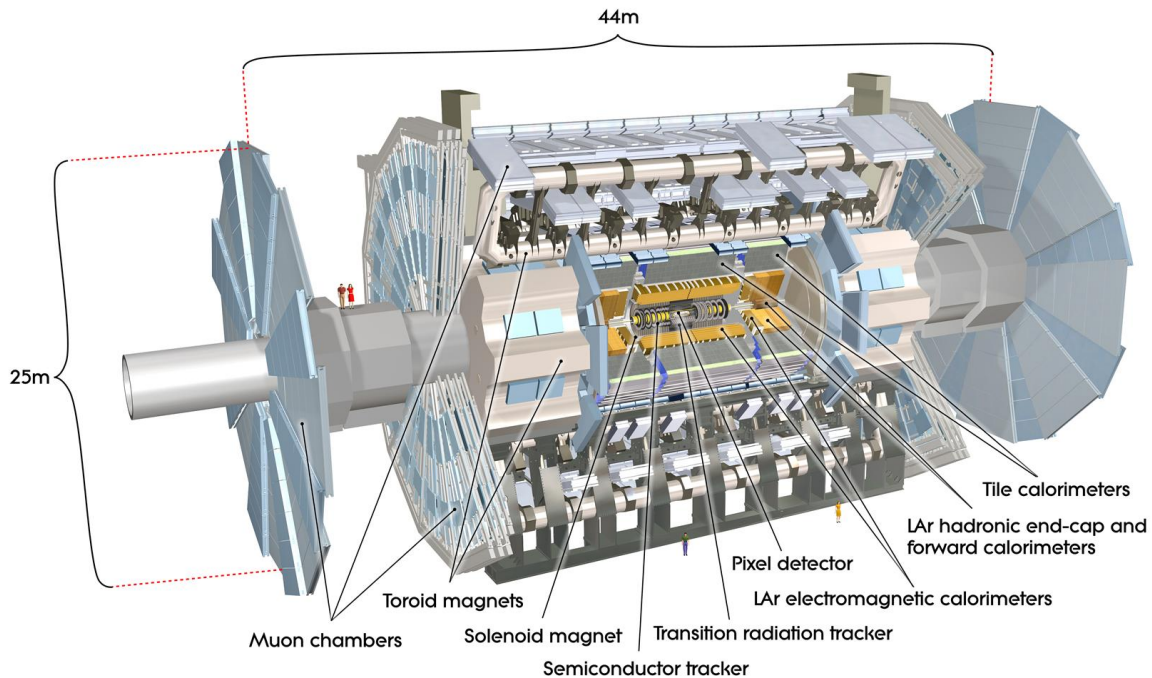


**Figure 3.4:** Overview of the ATLAS detector and its subsystems [69].

$y$ , defined by  $y = -1/2 \ln[(E + p_z)/(E - p_z)]$ , where  $E$  denotes the energy of the object and  $p_z$  its momentum along the beam line. Using  $y$  has the advantage, that the measured difference between two particles is invariant under Lorentz boosts along the  $z$ -axis [2]. Lorentz invariance is an important condition, because the  $pp$  collisions occur at highly relativistic energies. The rapidity  $y$  is mostly used for massive objects, such as jets. Commonly,  $\theta$  is instead expressed by the pseudorapidity  $\eta$ :

$$\eta = -\ln \tan \frac{\theta}{2}. \quad (3.2)$$

This constitutes an approximation for  $y$ , which is valid in the massless limit  $E \approx p$ . An illustration of  $\eta$  for different values of  $\theta$  is shown in Figure 3.5. The angular distance between two objects is denoted by  $\Delta R$ , which is calculated by:

$$\Delta R = \sqrt{\Delta\phi^2 + \Delta\eta^2}. \quad (3.3)$$

### 3.2.2 Magnet system

The ATLAS magnet system consists of one superconducting solenoid surrounding the ID and three superconducting toroids placed outside the calorimeter system. The solenoid immerses the ID into a magnetic field, the toroids the MS. One toroid is located in the barrel region and

<sup>2</sup>Figure created by adapting the LaTeX TikZ code from [70].

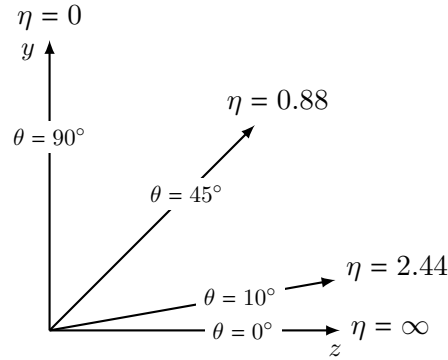


**Figure 3.5:** Illustration of pseudorapidity values  $\eta$  for different polar angles  $\theta$  in the  $y - z$  plane.<sup>2</sup>

the other two in the end-caps. Each of the three toroids is composed of eight racetrack-like coils, which are arranged radially around the beam line.

The magnet system is important to measure the momenta of charged particles. A particle moving in a magnetic field is bent on a curved track due to the Lorentz force. The higher the momentum of the particle, the less it is deflected from its straight trajectory. Therefore, its momentum can be inferred from the strength of the curvature. The direction of the deflection provides information about the electric charge, as positively and negatively charged particles will be bent in opposite directions.

### 3.2.3 Inner Detector

The ID measures the tracks of charged particles and thereby their momenta and charges. It is immersed in a magnetic field of 2 T from the solenoid and it consists of three different detector systems: The pixel tracker, together with the IBL, the silicon microstrip tracker (SCT) and the Transition Radiation Tracker (TRT). The layout of the ID is shown in Figure 3.6. The ID was designed to provide a momentum resolution of  $\sigma_{p_T}/p_T = 0.05\% p_T \oplus 1\%$  [29], where  $p_T$  is the transverse momentum of the particle in GeV. The first term defines the measurement resolution and the latter term accounts for multiple scattering of the particles with the detector material [4]. Furthermore, the ID is used for vertex measurements. This includes the reconstruction of the primary vertex, which is the interaction point of the initial collision, as well as secondary vertices. These are displaced from the primary vertex and originate, if particles with a relatively long lifetime, such as  $b$ -hadrons, decay within the ID. With a lifetime of around a picosecond, the resulting secondary vertices of  $b$ -hadrons are displaced by distances of the order of millimeters [2, 4], so that a high spacial resolution is an essential requirement for the ID.

#### Pixel tracker

The pixel tracker is the innermost part of the ID and it covers the region  $|\eta| < 2.5$ . As the track density is the highest close to the interaction point, the pixel tracker is required to have a sufficiently fine granularity. It consists of the Insertable  $B$ -Layer (IBL) and three consecutive silicon-pixel layers. By combining the signals registered in each pixel sensor, the trajectory of a particle is reconstructed. The IBL is the innermost layer surrounding the

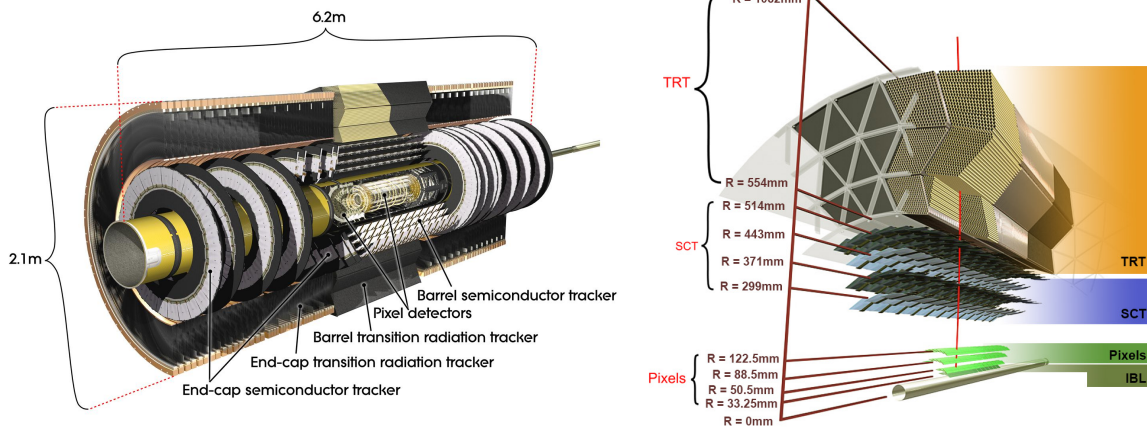


**Figure 3.6:** The overall layout of the ID, including its barrel and end-cap components, are shown on the left [71]. The right plot shows a more detailed view of the ID structure in the barrel [72]. Here, the red line illustrates the potential path of a charged track through the ID.

beam pipe. It has a pixel size of  $50 \mu\text{m}$  in  $R$  and  $250 \mu\text{m}$  in  $z$ -direction and it provides an accuracy of  $8 \mu\text{m}$  in  $R - \phi$  and  $40 \mu\text{m}$  in  $z$  [73, 74]. The other three pixel layers have a minimum pixel size of  $50 \mu\text{m}$  in  $R - \phi$  and  $400 \mu\text{m}$  in  $z$  with an accuracy of  $10 \mu\text{m}$  in  $R - \phi$  and  $115 \mu\text{m}$  in  $z$  ( $R$ ) in the barrel (end-caps) [29].

### Silicon Microstrip Tracker

The SCT consists of eight layers of silicon-microstrip sensors. To measure the particle trajectories in discrete space points, the layers are installed with an alternating arrangement: In the barrel region, four layers are mounted axially to the beam line, while the other four are aligned with a relative angle of  $40 \text{ mrad}$  to the former ones. In the end-caps, one set of layers is placed radially and the other one with a relative angle of  $40 \text{ mrad}$ . The SCT provides tracking information within  $|\eta| < 2.5$  by using  $6.4 \text{ cm}$  long sensors with a strip pitch of  $80 \mu\text{m}$ . It has an accuracy of  $17 \mu\text{m}$  in  $R - \phi$  and  $580 \mu\text{m}$  in  $z$  (barrel) and  $R$  (end-caps) [29].

### Transition Radiation Tracker

The TRT is the outermost part of the ID. It functions as a drift-tube detector and it is composed of straw tubes filled with an Argon and Xenon-based gas mixture [75]. The tube walls are kept at a negative voltage and each tube contains a wire as an anode in its centre. The TRT covers the pseudorapidity range  $|\eta| < 2.0$  and has an accuracy of  $130 \mu\text{m}$  per straw [29]. It has about  $351 \times 10^3$  readout channels in total. Although the TRT provides only  $R - \phi$  information, it is still very important for momentum measurements, because it allows for a much larger number of hits per track than the pixels and the SCT. While the latter have 12 layers in total, in the TRT a particle traverses on average more than 30 drift tubes on its trajectory. The TRT is also used for the discrimination of electrons against pions. For this, the TRT tubes are interleaved with transition radiation material. Transition radiation occurs, when a highly relativistic charged particle passes the boundary between two media with different dielectric constants. The emitted photons are absorbed in the TRT

gas and are thereby detected. The radiation intensity is proportional to the Lorentz factor  $\gamma = E/m$ . With a mass of about 140 MeV, a pion will thus create less transition radiation than an electron of the same energy [76].

### 3.2.4 Calorimeter system

The calorimeter system is used to measure the energy of particles. Two kinds of calorimeters are used in ATLAS: Electromagnetic and hadronic calorimeters. The electromagnetic calorimeter is designed for electrons, positrons and photons, while the hadronic calorimeter measures the energies of strongly interacting particles, e.g. protons and pions, which appear in the detector as jets. The working principle of calorimeters is based on the creation of particle showers. During the passage through the calorimeter, a particle interacts with the detector material, which leads to a cascade of secondary particles. The initial particle is eventually stopped and its energy deposited in the shower. Opposed to the ID, in the calorimeters also particles without an electric charge are detected. All calorimeters in the ATLAS detector are sampling calorimeters, i.e. they use an alternating arrangement of two different materials to create and to measure the shower energy. The layout of the calorimeter system is shown in Figure 3.7.

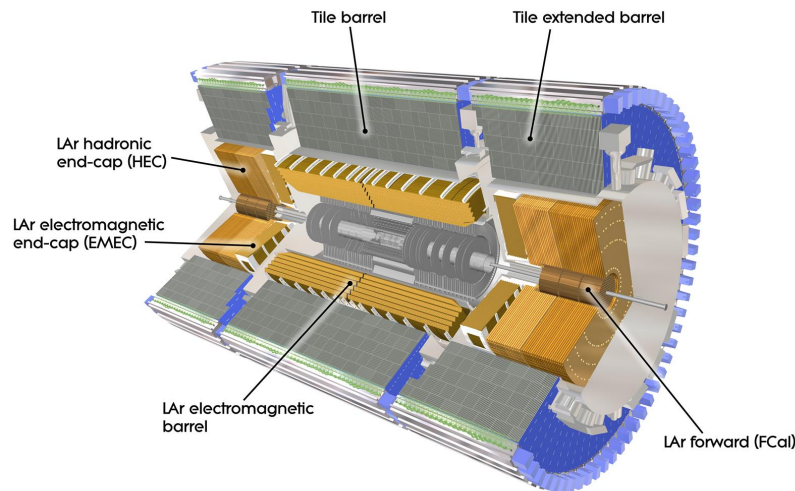


**Figure 3.7:** Layout of the calorimeter system [77].

#### Electromagnetic calorimeter

In the electromagnetic calorimeter the showers are created through two physical processes: Photons split into electron-positron pairs, which themselves can emit photons through Bremsstrahlung. It needs to ensure a good containment of the showers and prevent the punch-through of particles into the HCAL and MS. Therefore, the depth of the calorimeter components is an important design parameter. For electromagnetic calorimeters, the characteristic parameter for this is the radiation length  $X_0$ , which is defined as the mean distance

over which an electron or positron loses all but  $1/e$  of its energy through Bremsstrahlung. It also corresponds to  $7/9$  of the mean free path travelled by a photon until it converts into an electron-positron pair [2]. The electromagnetic calorimeter has a depth of at least  $22 X_0$  and  $24 X_0$  in the barrel and in the end-caps, respectively. The design value for its energy resolution is  $\sigma_E/E = 10\%/\sqrt{E} \oplus 0.7\%$  [29]. Here,  $E$  denotes the energy of a particle in GeV and the term  $10\%/\sqrt{E}$  describes stochastic effects. The  $0.7\%$  uncertainty represents a constant term, which considers residual non-uniformities and resolution variations in time [4].

The barrel provides energy measurements in  $|\eta| < 1.475$  [29]. It is divided into two identical half-barrels separated at  $z = 0$ . The electromagnetic end-cap calorimeter (EMEC) covers the region  $1.375 < |\eta| < 3.2$ . Each end-cap consist of two coaxial wheels, one for the pseudorapidity range  $1.375 < |\eta| < 2.5$  and the other one for  $2.5 < |\eta| < 3.2$ . In both the barrel and the EMEC, liquid Argon (LAr) is used as active medium to measure the energy deposits and lead serves as absorber material to create particle showers. The electrodes and absorber plates are arranged in an accordion-shaped geometry, which allows for a full coverage in  $\phi$  without cracks. In the range  $|\eta| > 2.5$  two active layers are used, while for  $|\eta| < 2.5$  three active layers are installed, because this is the region intended for precision physics. To obtain accurate position measurements, the inner layer is finely segmented in  $\eta$  in this region.

The pseudorapidity coverage of the electromagnetic calorimeter is extended up to  $|\eta| = 4.9$  by the forward calorimeter (FCal), which is described in more detail below. Furthermore, in the range  $|\eta| < 1.8$  a presampler detector is mounted in front of the calorimeter system. This is a LAr layer correcting for the energy which electrons, positrons and photons lose before they reach the calorimeter.

### Hadronic calorimeter

The hadronic calorimeter system consists of the tile calorimeter, the hadronic end-cap calorimeter (HEC) and the FCal. The tile calorimeter and the HEC were designed to give an energy resolution of  $\sigma_E/E = 50\%/\sqrt{E} \oplus 3\%$ , while the design resolution for the FCal is  $\sigma_E/E = 100\%/\sqrt{E} \oplus 10\%$  [29].

The tile calorimeter is placed in the barrel region and it is composed of one central and two extended barrels, which together cover the pseudorapidity range  $|\eta| < 1.7$ . It uses steel as absorber material and scintillating tiles as active medium. The characteristic parameter to describe the depth of a hadronic calorimeter is the interaction length  $\lambda$ , which is a measure for the mean distance traveled by a hadron before it undergoes an inelastic strong interaction. The depth of the tile calorimeter is  $9.7 \lambda$ . Hadronic showers are measured through the detection of ultraviolet scintillation light, which is collected at the tile edges and converted to visible light with wavelength-shifting fibres. The fibres are grouped together, leading to a cell structure with three radial cell layers. These cells define the granularity of the tile calorimeter. In the inner two layers, the cells have a size of  $\Delta\eta \times \Delta\phi = 0.1 \times 0.1$  and  $\Delta\eta \times \Delta\phi = 0.2 \times 0.1$  in the outer layer.

Pseudorapidities of  $1.5 < |\eta| < 3.2$  are covered by the HEC, which consists of two wheels in each end-cap. It uses LAr as active and copper as absorber material. The granularity is determined by a pad structure of the electrodes. These readout cells have a size of  $\Delta\eta \times \Delta\phi = 0.1 \times 0.1$  for  $|\eta| < 2.5$  and  $\Delta\eta \times \Delta\phi = 0.2 \times 0.2$  for larger values of  $|\eta|$ . The HEC has a depth of about  $10 \lambda$ .

The FCal is used for energy measurements within  $3.1 < |\eta| < 4.9$ . It consists of three different modules, of which the first one, FCal1, is devoted to electromagnetic showers. In FCal1, copper is used as absorber and LAr as active medium. FCal2 and FCal3 are designed to detect hadronic showers. These use LAr as active material and as absorber mostly tungsten.

Additional scintillator elements are placed in the gaps between the central barrel, the extended barrels and the FCal. Thereby, the energy loss in the gaps is partially recovered.

### 3.2.5 Muon Spectrometer

Muons are able to penetrate the calorimeters. Hence, they can be measured in a dedicated detector system outside of the other subdetectors. The MS allows to determine the position, charge and momentum of muons in the pseudorapidity range  $|\eta| < 2.7$ . The MS was designed to give a momentum resolution of 10% for muon tracks with a  $p_T$  of 1 TeV [29]. The layout of the MS is shown in Figure 3.8. The muon detection follows the same operation principle as in the ID: A magnetic field bends the muons on a curved trajectory, from which their momenta and charges can be inferred. Inside the MS, the magnetic field generated has a strength of 0.5 T and 1 T in the barrel and the end-caps, respectively. For pseudorapidities of  $|\eta| < 1.4$ , the magnetic field is provided by the barrel toroid and for  $|\eta| > 1.6$  by the end-cap toroids. In the transition region of  $1.4 < |\eta| < 1.6$ , the muons are subjected to a combination of these two magnetic fields.

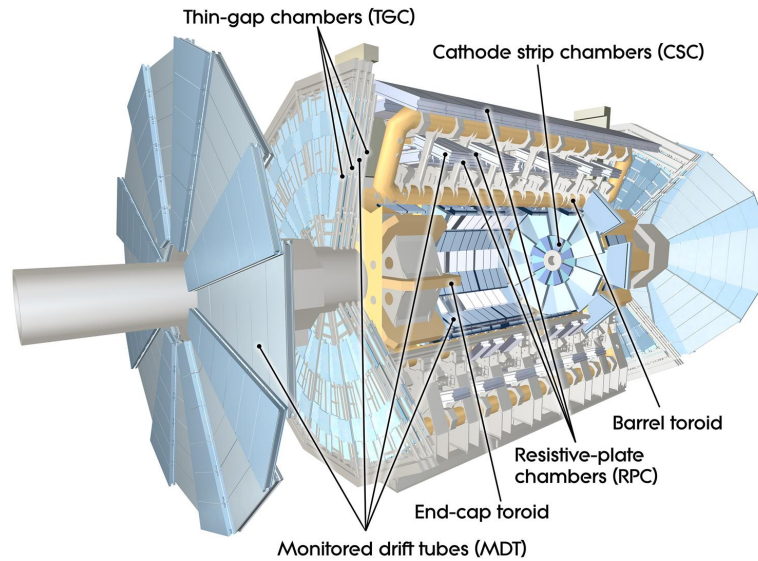


**Figure 3.8:** Layout of the MS [78].

Following the eight-fold geometry of the toroids, the MS is composed of eight octants. In the azimuthal direction, each of the octants is divided into two parts. The muon detectors are arranged in three cylindrical shells in the barrel and in three wheels in the end-caps. The MS consists of four different chamber types: Monitored Drift Tubes (MDTs), Cathode Strip Chambers (CSCs), Resistive Plate Chambers (RPCs) and Thin Gap Chambers (TGCs). The

MDTs and CSCs are high-precision tracking chambers, while the RPCs and TGCs are used i.a. for triggering (cf. Section 3.2.7). These perform triggering on muon tracks in the range  $|\eta| < 2.4$  and therefore need to ensure a fast flow of tracking information.

### Monitored Drift Tubes

The MDT chambers are composed of three to eight layers of drift tubes, which are filled with Ar-CO<sub>2</sub> gas and have a charged wire in the center. In total, they provide up to 20 measurements per track and cover the region  $|\eta| < 2.7$ . The only exception is the innermost end-cap layer, in which they are used only up to  $|\eta| < 2.0$ . The tubes are arranged along  $\phi$  in the barrel as well as in the end-caps. The MDTs provide only spatial information in  $\eta$ -direction, in which they have a resolution of approximately 35  $\mu\text{m}$  per chamber [29]. To determine also the track coordinates in  $\phi$ , the MDT measurements are complemented by information from the RPCs and TGCs.

### Cathode Strip Chambers

The CSCs are located in the innermost end-cap layer, in which they cover the forward region  $2.0 < |\eta| < 2.7$ . There, they are used instead of the the MDTs, as they are high-rate capable and have a better spatial and time resolution. This is necessary because in the forward region the particle flux, and thus also the track density, is much higher than for smaller  $|\eta|$ . CSCs are multiwire proportional chambers filled with Ar-CO<sub>2</sub> gas. Each chamber consists of four consecutive CSC planes and both cathodes of a plane are segmented into strips, one in radial direction and the other one perpendicular to it. This allows to measure the  $\eta$  as well as the  $\phi$  coordinate. The CSCs have a chamber resolution of 40  $\mu\text{m}$  in  $R$  and 5 mm in  $\phi$  [29].

### Resistive Plate Chambers

The RPCs are situated in the barrel and cover pseudorapidities of  $|\eta| < 1.05$ . They are composed of three concentric layers. Each of them consists of two detector layers, thereby allowing for six measurements per tracks in total. The RPCs are gaseous detectors, filled with a C<sub>2</sub>H<sub>2</sub>F<sub>4</sub>-based gas mixture, which have parallel resistive plates as electrodes. Readout strips are placed onto the plates. As for the CSCs, the strips are arranged perpendicularly to each other to determine the  $\eta$  and  $\phi$  coordinates of a track. In both directions, the RPCs have a spatial resolution of 10 mm per chamber [29].

### Thin Gap Chambers

The TGCs are installed in the end-caps. The TGC system in an end-cap consists of nine TGC layers. It is comprised of two concentric rings, an inner ring for the range  $1.05 < |\eta| < 1.92$  and an outer ring for  $1.92 < |\eta| < 2.4$ . As they are used in the forward region, they were designed to have a high-rate capability and a good time resolution. The TGCs are filled with a gas mixture of CO<sub>2</sub> and n-pentane and they have the same operation principle as multiwire proportional chambers. The  $\phi$ -coordinate is measured by the wire groups of the TGCs and the  $\eta$ -coordinate is determined with readout strips, which are azimuthally arranged on the electrodes. The TGCs have a chamber resolution of 2-4 mm in  $R$  and 3-7 mm in  $\phi$  [29].

### 3.2.6 Forward detectors

Apart from the subdetectors described above, a set of four smaller detector systems is installed in the forward region: LUCID-2 [79], ALFA, ZDC and AFP [80]. LUCID-2 is located at a distance of  $\pm 17$  m from the interaction point, while the other three detectors are more than 100 m away from the interaction point. LUCID-2 is the main luminosity monitor for the ATLAS experiment in Run II [81]. It determines the luminosity with *van der Meer scans*. In these scans, the two beams are gradually separated from each other in vertical and horizontal direction. It is measured, how the interaction rate changes as a function of the separation. By calibrating these measurements, the instantaneous luminosity can be inferred. LUCID-2 was integrated into the detector during the long shut-down between Run I and Run II and replaced the preceding LUCID (LUminosity measurement using Cerenkov Integrating Detector) detector. ALFA (Absolute Luminosity For ATLAS) was initially designed for luminosity measurements, but beyond that it is also used to study diffractive processes [82]. The ZDC (Zero-Degree Calorimeter) is mainly used to detect forward neutrons, which is particularly important for analysing heavy-ion collisions. Like LUCID-2, the AFP (ATLAS Forward Proton) project was placed into the ATLAS detector before Run II. It is specialised on diffractive processes in which one or both protons remain intact after the  $pp$  collision.

### 3.2.7 Trigger system

With a spacing time of 25 ns, the proton bunches collide 40 million times per second. As the average event size is approximately 1.3 MB [29], the obtained data rate amounts to several TB/s, which is too large to be fully read out and stored. However, most of these events constitute interactions with only low- $p_T$  hadrons in the final state, whereas the processes studied with the ATLAS detector typically occur at high  $p_T$ . Therefore, a trigger system [83] is used to perform a real-time (*online*) selection of events, that are interesting for physics analyses and that should be recorded.

The ATLAS trigger system consists of a hardware-based first level trigger (Level-1) and a software-based high-level trigger (HLT). The Level-1 trigger reduces the recording rate from 40 MHz down to about 100 kHz. It uses custom electronics to search for high- $p_T$  objects, such as leptons and jets. It is also possible to trigger on the missing transverse momentum, which is the momentum imbalance in the transverse plane arising e.g. from an invisible particle. The Level-1 trigger uses as inputs coarse granularity information from the calorimeters and the MS. Furthermore, it processes information from other detector subsystems, for example LUCID-2. The Level-1 trigger defines so-called *Regions-of-Interest* (RoIs) in the detector, which contain potential high- $p_T$  objects. The RoIs are transferred to the software-based HLT, which applies sophisticated reconstruction algorithms similar to the ones used in physics analyses. For this, it takes full granularity information both from the whole event and from only the RoIs. With the HLT the recording rate is reduced down to about 1 kHz.

### 3.2.8 Data preparation and computing

The raw data recorded in the  $pp$  collisions consists of the sum of the signals measured in the different subdetector systems. However, for physics analyses it is desirable to convert the raw data into a format, which allows to directly access the physics objects and their properties,

for example the coordinates and  $p_T$  of the particles. The object reconstruction is performed using Athena [84]. This is the central ATLAS software framework, which contains also the code used e.g. for triggering, object calibrations and the production of simulations. The reconstructed objects are stored in the xAOD (Analysis Object Data) format [85], which is used for real as well as for simulated data. Usually, physics groups create a reduced format, the Derived xAODs (DxAODs) [86], for their analyses. The DxAODs comprise a subset of the information stored in the xAODs, i.e. objects and events, that are not relevant for particular analyses, are removed. The analysis groups thereby profit from a reduced processing time. The DxAODs serve as inputs to apply analysis specific selections and calibrations. The output files of this process are stored in ROOT [87] format. These are the files used in the analyses presented in this work to perform physics studies.

Most of the processes described above, like the production of DxAODs or running the analysis software, are computationally too intensive to be processed locally. Therefore, these tasks are commonly run at the Worldwide LHC Computing Grid [88]. This is a collaboration with about 170 computing centres across the world, which provides computing resources for the LHC experiments. Physics groups and individual analysers can submit their tasks to the grid, which are then distributed and processed at available computing sites.

### 3.2.9 Simulation

Besides the recording of real data, a substantial aspect in this work is the simulation of  $pp$  collision events. Simulations are used to estimate the SM background processes, to define the analysis strategy as well as to interpret the search results in the context of selected beyond-the-SM signals. Most of the  $pp$  collisions represent only soft QCD interactions. However, physics analyses are typically interested in *hard-scatter processes*, which involve a large momentum transfer or in which heavy particles are produced. Therefore, simulations are generally built for a specific hard processes of interest. Generating these simulations is a complex procedure, which is described in the following. The information presented is based on Ref. [89].

First, one needs to take into account that  $pp$  collisions at the LHC are, in fact, collisions of *partons*, which are the constituents of the protons. Apart from the three valence quarks  $u, u$  and  $d$  defining the proton, it is also possible that gluons or sea quarks, i.e. other quarks within the proton originating from gluon splitting, participate in the collision. The cross section  $\sigma$  to produce a final state  $n$  in  $pp$  collisions is calculated by:

$$\sigma = \sum_{a,b} \int_0^1 dx_a dx_b \int d\Phi_n f_a(x_a, \mu_F) f_b(x_b, \mu_F) \times \frac{1}{2x_a x_b s} |\mathcal{M}_{ab \rightarrow n}|^2(\Phi_n; \mu_F, \mu_R), \quad (3.4)$$

where  $a$  and  $b$  denote the colliding partons,  $\Phi_n$  is the final-state phase space and  $f_a(x_b, \mu_F)$  and  $f_b(x_b, \mu_F)$  are so-called parton distribution functions (PDFs). These describe the probability to find a certain parton  $a$  ( $b$ ) carrying a fraction  $x_a$  ( $x_b$ ) of the proton momentum, if the proton is probed at an energy scale  $\mu_F$ , referred to as factorisation scale. The PDFs cannot be directly calculated, because they depend on non-perturbative effects. Therefore, they are determined from fits to data. There are several sets of publicly available PDFs which can be employed for event simulations. The ones used in this work are based on data collected from

various colliders, including the SLAC, Tevatron, HERA and the LHC [90]. The symbol  $s$  in Equation 3.4 denotes the square of the centre-of-mass energy and  $\mathcal{M}_{ab \rightarrow n}$  represents the matrix element. This describes the dynamics of the hard process. It is calculated from the corresponding Feynman diagrams using a renormalisation scale  $\mu_R$ . The calculation of the matrix element and the phase space is performed using Monte-Carlo (MC) event generators. Hence, simulated events are commonly called MC events. In this work, different generators are used to simulate the various SM and signal processes.

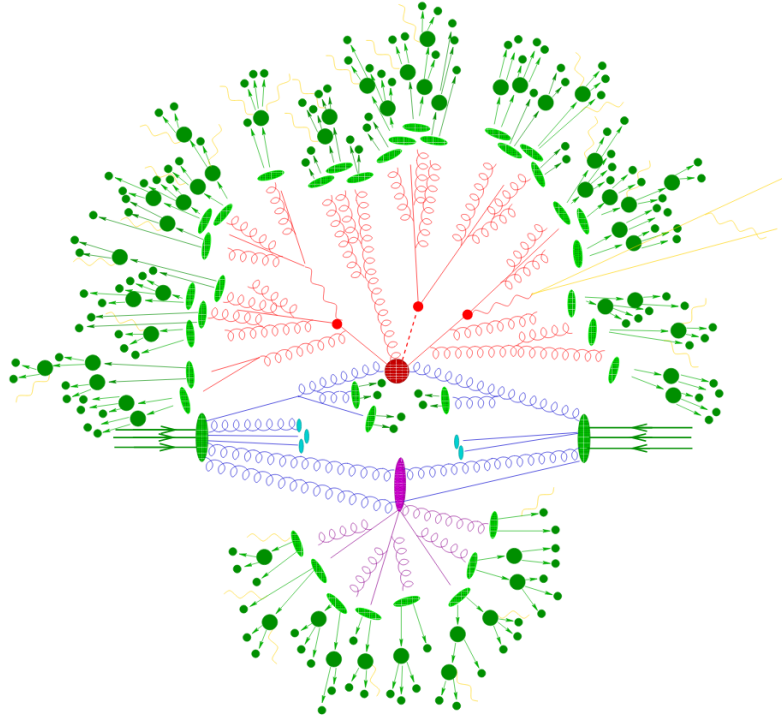


**Figure 3.9:** Illustration of a generated  $t\bar{t}h$  event in a  $pp$  collision. The initial partons in the two protons are depicted by the blue lines. The hard process is indicated by the big red blob and the subsequent decays of the top-quarks and the Higgs boson are shown by the smaller red blobs. The parton shower is illustrated in red, the hadronisation of the quarks and gluons in light green and the hadron decays in dark green. Photon radiation is indicated by the yellow lines. The purple blob and purple lines represent an underlying event. Figure taken from Ref. [91].

Another important aspect in the event simulation is the *parton showering*: The initial partons, but also final-state quarks and gluons, can radiate off gluons, which is referred to as initial and final-state radiation (ISR and FSR, respectively). The gluons, in turn, can split into a pair of quarks, which again can radiate off gluons. This leads to a so-called parton shower. However, at a scale of about 1 GeV [89], the quarks and gluons start hadronising. The simulation of this requires non-perturbative hadronisation models. The different hadrons may be short-lived states, so that also their decays need to be modelled. As electrically charged particles may emit photons, QED radiation effects must be considered in the simulations. Furthermore, it is necessary to simulate *underlying events*. These constitute additional, typically soft parton-parton interactions occurring within the same  $pp$  collision. The different

steps of the event generation are illustrated in Figure 3.9. Apart from them, the simulations used in this work include also effects from pile-up (c.f. Section 3.1). This is modelled by overlaying the hard-process events with other  $pp$  collision events.

To be able to compare the simulated events with recorded data, the simulations are processed with GEANT4 [92], which is a toolkit used to describe the passage of particles through matter. This step takes into account the full ATLAS detector layout and brings the simulated events into a format which is equivalent to the raw data, i.e. consisting of signals and energy deposits within the different detector components. The particle reconstruction and identification is then performed for both data and simulation in the same way, following the methods described in Chapter 4. Apart from this *reco* information, also a *truth record* is stored. The truth record describes the full information present at event-generation level: It contains the history of all particles produced in an event as well as their kinematic properties [93]. This provides detailed insights into the physics of the processes, which is in this form not possible with real data.

For each signal and background process in this work, a certain number of MC events is simulated for a given integrated luminosity. To determine, how many events for this process one would obtain in real data, the MC predictions must be scaled using the cross section of the process and the integrated luminosity of the corresponding dataset.



# Chapter 4

## Object reconstruction and identification

In the following it is explained, how the *physics objects* used in this work are reconstructed from the measured detector signals. Furthermore, it is described which quality criteria the objects must fulfil to be considered in the analysis and which systematic uncertainties are associated to them. A summary of the object definitions used in the mono- $h(b\bar{b})$  searches with  $79.8 \text{ fb}^{-1}$  and  $139 \text{ fb}^{-1}$  of collected data can be found in Section 6.1 and Section 7.2, respectively. These also contain additional information, how the objects are used in the specific search and why certain criteria are applied to them.

### 4.1 Track reconstruction and primary vertex

The trajectories of charged particles can be measured by reconstructing their tracks in the ID. For muons, the trajectories are also measured in the MS, which is described in Section 4.7. The track reconstruction in the ID starts by building clusters in the pixel and SCT sensors, using as inputs the pixels and strips with a signal above a given noise threshold [94]. The clusters from several layers are grouped into three-dimensional measurements, called space points. A combinatorial Kalman filter [95] is used to fit the space points and thereby form track candidates. Different criteria, based on the track and fit properties, are applied to select only tracks of good quality and to resolve ambiguities between overlapping track candidates [94, 96]. The tracks undergo then a separate reconstruction step which also takes into account measurements from the TRT. This inside-out technique represents the baseline track reconstruction method at the ATLAS experiment. However, a reverse approach, in which the track reconstruction is seeded from TRT measurements, is used as well [96, 97]. That allows to detect e.g. secondary particles originating from subsequent decays, which thus may not have enough hits to be reconstructed by the baseline method.

To find the position of the hard-scatter interaction, an iterative vertex-finding and fitting procedure is applied [98, 99]. The tracks considered in this must satisfy a set of quality criteria, e.g. they are required to have  $p_T > 500 \text{ GeV}$  and must have hits in all pixel layers. A candidate vertex is required to have at least two associated tracks passing these requirements. The tracks are used as inputs to a fit which determines the best vertex position. Afterwards tracks, which are not compatible with this vertex, are removed from it. The vertex-finding and fitting is then performed again, using the remaining tracks as inputs, and is repeated until no more vertices can be reconstructed. Generally, the hard-scatter process is expected to produce particles with a relatively high  $p_T$ . Therefore, if a  $pp$ -collision event has multiple such vertices, the one with the largest  $\sum_{\text{tracks}} p_T^2$  value is assumed to correspond to the hard-scatter interaction. This is referred to as the *primary vertex* in the following.

The reconstructed tracks are available within the full ID range of  $|\eta| < 2.5$ . Important properties of a track, which are also used in the definitions of the following physics objects, are the impact parameters  $z_0$  and  $d_0$ . These are defined as the minimum distance in longitudinal, respectively transverse direction of a track relative to the primary vertex, i.e. they describe the distance from the primary vertex to the two points of a track with the closest longitudinal and transverse approach to it.

## 4.2 Small-radius jets

Due to colour confinement, quarks and gluons produced in the  $pp$  collisions will give rise to collimated showers of hadrons, which are referred to as jets. These can be detected by measuring the energy deposits in the calorimeters. In addition to the HCAL, a jet can also lead to energy deposits in the ECAL, because photons and leptons may be produced in it e.g. through semi-leptonic hadron decays or pion decays, such as  $\pi^0 \rightarrow \gamma\gamma$ . The energy deposits in the calorimeters should ideally be grouped such that the reconstructed jet captures all hadronisation products of the initial quark or gluon, as illustrated in Figure 4.1. For this, jet-finding algorithms are used. Two different types of calorimeter jets are considered in this work: Small and large-radius (small-R and large-R) jets, which differ from each other in the jet area size. Small-R jets are described in the following, while an overview of large-R jets is given in Section 4.4.

The small-R jet reconstruction starts with the formation of topological clusters [101]. These are built from ECAL and HCAL cells with a measured energy above a given noise threshold. The clusters are calibrated to the electromagnetic (EM) scale, corresponding to the energy which is deposited by electromagnetically interacting particles [102]. They are then used as seeds for the anti- $k_t$  [103] jet-forming algorithm. This is a sequential recombination algorithm which iteratively combines close-by input objects to a jet. It defines the distance between two objects  $i$  and  $j$  by:

$$d_{ij} = \min(p_{Ti}^{-2}, p_{Tj}^{-2}) \frac{\Delta\phi_{i,j}^2 + \Delta y_{i,j}^2}{R^2}, \quad (4.1)$$

where  $p_{Ti/j}$  are the corresponding transverse momenta,  $\Delta\phi_{i,j}$  their azimuthal separation and  $\Delta y_{i,j}$  their separation in  $y$ , which is the rapidity  $y$  introduced in Section 3.2.1. The radius parameter  $R$  sets a stopping condition on the jet size, for which a value  $R = 0.4$  is used in this work. The exponent “-2” parametrises the relative power of the energy with respect to the distance scales. The anti- $k_t$  algorithm calculates  $d_{ij}$  for all input objects and compares them with the different  $d_{iB} = p_{Ti}^{-2}$ , which represents a distance measure with respect to the beam. If the minimum value is a  $d_{ij}$ , it combines the objects  $i$  and  $j$  and continues with the jet-finding. If a  $d_{iB}$  represents the minimum value, the object  $i$  is considered as a jet and is removed from the input objects. In general, jets formed by the anti- $k_t$  algorithm have a circular, cone-like shape with radius  $R$ .

After that, a calibration procedure is applied to the jet energy scale (JES) [102]. This calibration is performed in different stages: First, the jet direction is changed such as to point to the position of the primary vertex instead of the centre of the detector. Subsequently, the jet is corrected for pile-up effects through a  $p_T$  density subtraction method based on

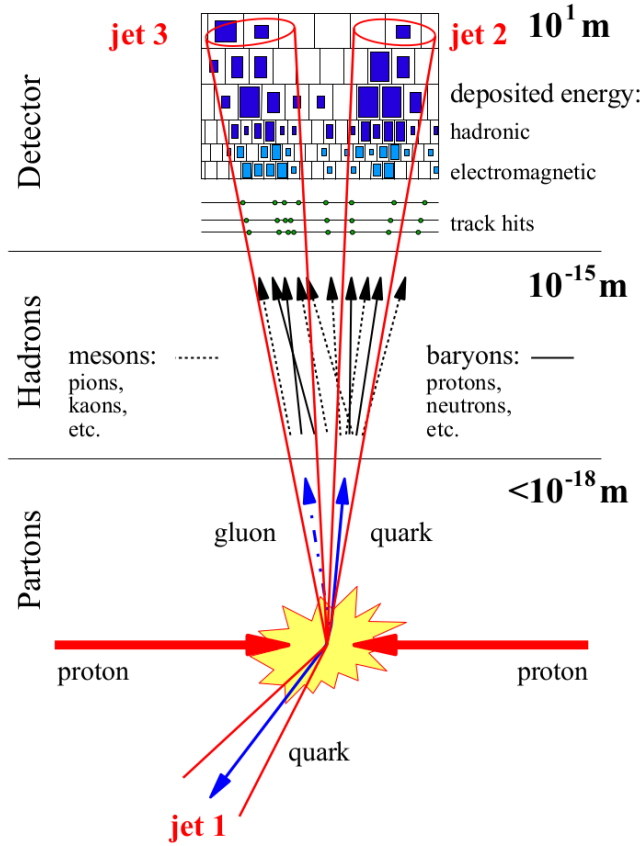


**Figure 4.1:** Illustration of the production of jets in a  $pp$  collision. The figure also indicates the length scale at which an initial quark or gluon hadronises into a particle shower. The energy of the jets is measured in the calorimeters. Furthermore, jets generally have associated tracks in the ID coming from charged hadrons. Figure taken from Ref. [100].

the jet area [104]. A residual pile-up correction is derived using MC simulation. Next, the jet four-momentum is adjusted to the particle level, which is done by comparing them to truth jets in simulated dijet events. These are obtained by clustering truth particles to jets. In a following step, calorimeter, track and muon-segment variables are used to mitigate energy leakage effects and reduce the flavour dependence of the jets. The latter describes the fact that the calorimeter response and jet reconstruction vary depending on which particle initiated the jet. Finally, to correct for JES differences between data and MC, a calibration is applied to jets in data, which is derived using in-situ techniques. The data-MC differences are quantified by studying events, in which the jet recoils against well-measured reference objects, e.g. a  $Z$ -boson decaying into a lepton pair. In-situ techniques are also used to calibrate the jet energy resolution (JER) [105].

To remove jets originating from pile-up processes, the Jet Vertex Tagger [106, 107] (JVT) discriminant is used. This is a multivariate classifier which makes use of tracking information to evaluate, whether a given jet is associated to the primary vertex or to a pile-up interaction. To correct for differences in the JVT efficiency between data and simulation, *scale factors*

are applied to the simulated events in the analysis. These JVT scale factors are derived in  $Z(\rightarrow \mu\mu)+\text{jets}$  events.

Small-R jets with  $|\eta| < 2.5$  and  $2.5 < |\eta| < 4.5$  are called *central* and *forward* jets, respectively. In this work, small-R jets are required to have  $p_T > 20$  GeV, while for forward jets a higher  $p_T$  threshold of 30 GeV is applied to reduce pile-up effects.

Small-R jets reconstructed as explained above, i.e. based only on calorimeter information, are referred to as *EMTopo* jets. This jet type is used in the  $79.8 \text{ fb}^{-1}$  mono- $h(b\bar{b})$  analysis. The  $139 \text{ fb}^{-1}$  analysis uses *PFlow* jets instead. These are reconstructed with the particle flow [108] algorithm, which combines both calorimeter and tracking information. This allows for an improved energy resolution and pile-up stability compared to EMTopo jets. To be used in the particle-flow algorithm, the ID tracks must fulfil different criteria. For example, they must have  $p_T > 500$  MeV and  $|z_0 \sin \theta| < 2$  mm. The latter requirement reduces the number of tracks originating from pile-up interactions, thus ensuring that the tracks are compatible with the primary vertex. The particle flow algorithm matches these tracks to topological clusters and resolves overlaps between the momentum and energy measurements from the ID and the calorimeters, respectively. The resulting track-matched clusters are used as inputs to the anti- $k_t$  algorithm to form  $R = 0.4$  jets. The PFlow JES and JER are calibrated in a similar manner as described above. However, the  $139 \text{ fb}^{-1}$  analysis uses an updated procedure in which the vertex correction is no longer applied to the four-momentum of the jet, but instead directly to the jet constituents during the reconstruction. In this work, the JVT discriminant is only employed for central jets with  $20 \text{ GeV} < p_T < 120 \text{ GeV}$ . In the  $79.8 \text{ fb}^{-1}$  analysis, EMTopo jets must have a discriminant above 0.59 if they have  $|\eta| < 2.4$ , while jets within  $2.4 < |\eta| < 2.5$  are required to have a value above 0.11. In the  $139 \text{ fb}^{-1}$  analysis, PFlow jets must have a discriminant above 0.5.

Systematic uncertainties associated to small-R jets arise from the JES and JER calibrations as well as from the measurement of the JVT efficiency. For the JES, most of them are related to the in-situ measurements. These are affected by uncertainties on e.g. the available MC statistics or from propagated lepton uncertainties. Other major JES uncertainties come from pile-up effects and the flavour dependence. Similarly, the JER measurements have associated systematics from the in-situ measurements. The differences between data and MC are another source of JER uncertainties. An overview of all JES and JER uncertainties affecting the  $79.8 \text{ fb}^{-1}$  and  $139 \text{ fb}^{-1}$  searches can be found in Refs. [102, 105] and Ref. [109], respectively. Uncertainties from the JVT efficiency measurements are attributed e.g. to mis-modelling effects in simulations [106, 107].

### 4.3 Large-radius jets

Large-radius (large-R) jets allow to reconstruct hadronic decays of high-mass particles, e.g.  $Z \rightarrow q\bar{q}$  or  $h \rightarrow b\bar{b}$ , which are produced with large momenta. The separation of the two quarks from the decay can be approximated by [110]:

$$\Delta R \propto \frac{2m}{p_T}, \quad (4.2)$$

where  $m$  and  $p_T$  denote the mass of the initial heavy particle. With increasing  $p_T$ , the quarks are less separated. Eventually, the calorimeter signals from their hadronisation products are

*merged* in a large region of energy deposits. An efficient way to reconstruct these boosted decays is to cluster the calorimeter signals from both quarks using a single large-R jet, for which a radius parameter of  $R = 1.0$  is commonly used in ATLAS physics analyses. This corresponds to the radius that e.g. the decay products from a Higgs boson with a  $p_T$  of 250 GeV would have.

Large-R jets are reconstructed from topological clusters, which are calibrated using the local hadronic cell weighting (LCW) method [101]. This corrects e.g. for signal losses due to inactive detector material. Jets are formed from these clusters using the anti- $k_t$  [103] algorithm with a radius parameter  $R = 1.0$ . The large-R jets undergo a *trimming* [111] procedure to reduce pile-up effects. In this, the jet constituents are reclustered using the  $k_t$  [112, 113] algorithm with a distance parameter  $R_{\text{sub}} = 0.2$ , resulting in a set of subjets located within the original large-R jet. Afterwards, subjets are removed which carry less than a given fraction  $f_{\text{sub}} = 5\%$  of the large-R jet  $p_T$ .

To improve the jet mass resolution, both calorimeter and tracking information are evaluated to derive a combined mass [114]. Only tracks are considered which are ghost-associated [104, 115] to the large-R jet. In this association method, the track four-momenta are used as inputs to the large-R jet clustering, in addition to the calorimeter signals. However, their  $p_T$  is assumed to be infinitely small (thus referred to as *ghosts*), to avoid that the jet axis gets changed. The ghost-association method ensures, that only tracks are selected which are associated to large-R jet constituents passing the trimming. Thereby, effects from pile-up are mitigated.

A calibration is applied which corrects the energy, mass and direction of the large-R jets to the particle scale. The associated scale factors are derived in simulated dijet events. In the  $139 \text{ fb}^{-1}$  search, a subsequent calibration step is applied in which residual data-MC differences in the JES are corrected using in-situ techniques [116]. These are similar to the ones used for small-R jets (c.f. Section 4.2). Only large-R jets with  $p_T > 200 \text{ GeV}$  and  $|\eta| < 2.0$  are considered in the calibration, thus this work also only uses jets satisfying these criteria.

The large-R jets are affected by various sources of uncertainties. These are evaluated in terms of their impact on the JES and JER as well as on the jet mass scale (JMS) and resolution (JMR). In the  $79.8 \text{ fb}^{-1}$  search, both the JES and JMS uncertainties are derived with the so-called  $R_{\text{track}}$  method in which the calorimeter measurements of the jet  $p_T$ , respectively mass, are compared with the ID measurements [114, 117]. The  $R_{\text{track}}$  method includes as systematic uncertainties e.g. variations in the tracking efficiencies and differences in the MC predictions between various generators. In the  $139 \text{ fb}^{-1}$  search, only the JMS uncertainties are estimated using this method, while the JES uncertainties are determined from in-situ measurements [116]. Also the JER uncertainties are derived using in-situ techniques. JMR uncertainties are evaluated by comparing the jet properties from the full-detector simulation with the ones on truth level, which is performed for different physics processes. In this work, only the results obtained for  $h \rightarrow b\bar{b}$  topologies are considered [118].

## 4.4 Variable-radius track jets

Different large-R jet properties, such as the distribution of calorimeter deposits within the jet or the ID activity in front of it, highly depend on which particle initiated the jet. Therefore, to find out whether a large-R jet potentially originates from the decay of a certain heavy particle, jet substructure techniques can be employed. For example, in a boosted  $h \rightarrow b\bar{b}$  decay it is expected, that the hadronisation products of the  $b$ -quarks will lead to two regions in the ID with an accumulation of tracks. Furthermore, in each of them there should occur a  $b$ -quark decay. Therefore, large-R jets coming from  $h \rightarrow b\bar{b}$  decays can be identified by the presence of associated *track jets* and their flavour content can be determined through  $b$ -tagging algorithms (c.f. Section 4.5). Track jets are formed from ID tracks which are clustered with the anti- $k_t$  [103] algorithm. For this, track jets with a fixed radius parameter of  $R = 0.2$  [119] have been used in the preceding mono- $h(b\bar{b})$  searches with  $3.2 \text{ fb}^{-1}$  [8] and  $36.1 \text{ fb}^{-1}$  [9] of collected data.

However, with increasing momentum of the Higgs boson, the two track jets originating from the pair of  $b$ -quarks become more collimated. Eventually, they overlap and cannot be resolved as two distinct track jets any more, as illustrated in Figure 4.2. This leads to a decrease in the identification efficiency of  $h \rightarrow b\bar{b}$  decays. For this reason, variable-radius (VR) track jets [120] have been designed. Equivalently to  $R = 0.2$  track jets, they are reconstructed from ID tracks using the anti- $k_t$  algorithm. However, as the name indicates, a variable radius parameter  $R(p_T)$  is used for them:

$$R(p_T) = \frac{30 \text{ GeV}}{p_T}, \quad (4.3)$$

where  $p_T$  denotes the track jet  $p_T$  and 30 GeV represents a constant factor, which was found to be suitable from performance studies [121]. Two additional parameters  $R_{\min} = 0.02$  and  $R_{\max} = 0.4$  are introduced to set a lower and upper cut, respectively, on  $R(p_T)$ . Compared to the previously fixed value  $R = 0.2$ , VR track jets allow for a significantly smaller radius. Since  $R(p_T)$  shrinks with increasing  $p_T$ , the use of VR track jets allows for an efficient  $h \rightarrow b\bar{b}$  identification even in highly boosted decays. Hence, VR track jets replaced the fixed-radius track jets in the  $79.8 \text{ fb}^{-1}$  analysis. Their impact on the sensitivity to mono- $h(b\bar{b})$  signals is discussed in detail in Section 6.6.

To be considered as  $h \rightarrow b\bar{b}$  decay products, the VR track jets are required to be ghost-associated [104, 115] (c.f. Section 4.4) to a large-R jet. Furthermore, to reduce the impact from pile-up, the tracks entering the VR track jet reconstruction need to satisfy  $z_0 \sin \theta < 3 \text{ mm}$ . Finally, only track jets with  $p_T > 10 \text{ GeV}$  are used in this work. Systematic uncertainties related to VR track jets are fully inherited from  $b$ -tagging uncertainties, which are described below.

## 4.5 $b$ -tagging

A  $b$ -quark produced in a  $pp$  collision will initiate a jet containing a  $b$ -hadron. Due to a lifetime of the order of 1.5 ps [122, 123],  $b$ -hadrons travel a considerable distance before they decay in the ID. For example, a  $b$ -hadron with a  $p_T$  of 50 GeV travels on average 3 mm [122]. This leads to a secondary vertex, as illustrated in Figure 4.2, which can be measured. Tracks emerging

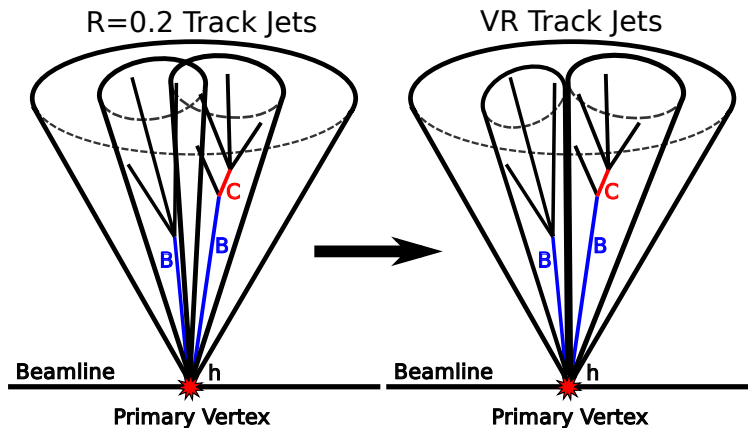


**Figure 4.2:** Illustration of the signature from a boosted  $h \rightarrow b\bar{b}$  decay, reconstructed from a large-radius ( $R = 1.0$ ) calorimeter jet with two associated track jets in the ID. For increasing Higgs boson momenta, the track jets become more collimated. Thus, using VR (right) instead of fixed-radius track jets (left) allows for an efficient  $h \rightarrow b\bar{b}$  identification even in highly boosted topologies. The blue and red lines indicate  $b$  and  $c$ -hadrons, respectively. Their decays lead to secondary vertices in the ID. Figure taken from Ref. [121]

from the secondary vertex do not necessarily point to the primary vertex. Therefore, they generally have quite large longitudinal and transverse impact parameters. This characteristic signature allows to discriminate  $b$ -quark initiated jets from the ones that originate from gluons or quarks of other flavours.

To identify  $b$ -jets, so-called  $b$ -tagging algorithms are used. These use various tracking variables to evaluate, whether the tracks associated to a given jet are compatible with a  $b$ -hadron decay. The performance of these algorithms is studied with respect to their  $b$ -jet identification efficiency as well as their rejection power against other jets. The latter are grouped into  $c$ -quark initiated and light-flavour jets, defined as jets originating from  $u$ ,  $d$  or  $s$ -quarks or gluons. Jets from  $c$ -quarks are studied separately because some  $c$ -hadrons have a sufficiently long lifetime to produce secondary vertices in the ID as well. The algorithms used in this work are based on multivariate techniques and can be applied to both small- $R$  jets and track jets. As tracking information is only available within the ID range of  $|\eta| < 2.5$ , it is not possible to apply  $b$ -tagging algorithms to forward small- $R$  jets. In the  $79.8 \text{ fb}^{-1}$  search,  $b$ -tagging is performed using the MV2c10 [123, 124] discriminant which is defined as the outcome of a Boosted Decision Tree training. In the  $139 \text{ fb}^{-1}$  search, the DL1 algorithm [123] is used instead. This is based on an Artificial Deep Neural Network. For a given  $b$ -jet identification value, the DL1 algorithm allows for a better rejection against  $c$  and light-flavour jets than the MV2c10 algorithm. To be considered as  $b$ -tagged, the (track) jets are required to have a discriminant above a certain value. From the analyser side it is possible to choose between a set of fixed discriminant values, so-called *working points* (WPs). For both searches in this work, a WP is chosen which provides an average  $b$ -jet identification efficiency of 77%, i.e. the probability that a  $b$ -jet within  $|\eta| < 2.5$  is  $b$ -tagged amounts to 77%.

To account for differences in the  $b$ -jet identification efficiency between data and simulation, simulated events in the analysis are corrected using scale factors. These are derived in a

measurement region which is enriched in events with a semi-leptonically decaying top-quark pair [49, 125]. The correction also includes an extrapolation procedure to high- $p_T$  jets. Systematic uncertainties are associated to both the efficiency measurements and the high- $p_T$  extrapolation. These arise e.g. from modelling uncertainties in simulated top-quark pair events. Additionally, uncertainties on the rejection of  $c$  and light-flavour jets are considered.

## 4.6 Electrons and photons

The first step in the reconstruction of electrons and photons is the formation of topological clusters [101] from energy deposits in the ECAL and HCAL. Only the cluster energy measured in the ECAL is used in the subsequent reconstruction steps, except for the transition region, in which also the measurements from the presampler and the gap scintillators are considered [126]. Afterwards, ID tracks are matched to the clusters. The tracks are obtained from the reconstruction and fitting steps described in Section 4.1. They are re-fitted with a dedicated procedure to consider effects from bremsstrahlung. This track matching allows to discriminate electrons from photons: As electrons have an electric charge, they leave a track in the ID, while photons are electrically neutral and are thus invisible in the ID. Therefore, an electron is defined as a cluster with a matched track. For photons, one distinguishes between unconverted and converted photons. The former is a cluster with no matched tracks, while the latter is a cluster which is matched to a conversion vertex. This occurs when a photon converts within the ID into an electron-positron pair. If there are multiple tracks or conversion vertices matched to a certain cluster, additional criteria, based on e.g. the separation of the cluster and the tracks, are applied to resolve the ambiguities. The track-matched topo-clusters are used as seeds to build so-called superclusters. They are constructed using a dynamic algorithm which evaluates, whether a cluster in the vicinity of the seed cluster ( $\Delta\eta \times \Delta\phi = 0.075 \times 0.125$ , for electrons also  $\Delta\eta \times \Delta\phi = 0.125 \times 0.300$ ) is potentially initiated by the same electron or photon. The final supercluster consists of the seed and all its associated satellite clusters. Afterwards, the track-matching is repeated. The superclusters undergo a calibration, which corrects for the energy scale and resolution differences between data and MC. This calibration is performed in  $Z \rightarrow e^+e^-$  events [127].

Before they can be used in physics analyses, the electron and photon candidates need to satisfy additional identification criteria. These are based on different discriminating variables regarding e.g. the shower shapes and the track properties. For electrons, the identification is performed using a likelihood discriminant, which takes these different variables as input and evaluates, if a given supercluster is consistent with an electron signature. As for the  $b$ -tagging of jets, it is possible to choose between different WPs with fixed discriminant values. In this work the LooseAndBLayer [128] WP is used, which requires a hit in the innermost pixel layer in addition to the criteria of the Loose WP [126]. This provides an efficiency of 86% for electrons with  $E_T = 20$  GeV, which gradually increases up to 95% for  $E_T > 100$  GeV.

Physics analyses are typically interested in selecting electrons that are produced in the initial hard process. These are usually well isolated from other objects and are thus called *prompt*. To discriminate them from non-prompt electrons, which originate e.g. from semi-leptonic hadron decays within a jet, isolation criteria are introduced. These are based on the activity measured around the electron in the calorimeters or the ID. The nearby activity

in the calorimeters is quantified with  $E_T^{\text{cone20}}$ . This variable is calculated from the sum of the transverse energy of all topo-clusters, which are located within  $\Delta R < 0.2$  of the electron cluster barycentre. The energy obtained is corrected for the energy contribution from the electron as well as for other effects, e.g. pile-up. In the ID, the surrounding activity is measured with the variable  $p_T^{\text{varcone20}}$ , which is given by the sum of transverse momenta of all tracks with  $p_T > 1$  GeV within a cone of variable size  $\Delta R = \min(10 \text{ GeV}/p_T[\text{GeV}], 0.2)$  around the electron track. The cone size is defined to shrink with increasing  $p_T$  in order to allow for a good selection efficiency of highly boosted particles with collimated decay products. The track-based isolation criteria are more robust against pile-up effects, while the calorimeter-based have the advantage, that they also consider the energy of electrically neutral particles. Like for the identification, different WPs can be chosen for the isolation. In the  $79.8 \text{ fb}^{-1}$  search the LooseTrackOnly WP is used, which takes as input only track-based information. Its requirements on  $p_T^{\text{varcone20}}$  are designed to provide a fixed electron efficiency of 99% [128]. In the  $139 \text{ fb}^{-1}$  search the isolation WP was changed to FCLoose. This WP combines both calorimeter and track information and requires  $E_T^{\text{cone20}}/p_T < 0.20$  and  $p_T^{\text{varcone20}}/p_T < 0.15$ . A dedicated WP, FCHighPtCaloOnly, is used for high- $p_T$  electrons. It requires  $E_T^{\text{cone20}} < \max(0.015 \times p_T, 3.5 \text{ GeV})$  [126]. In the  $79.8 \text{ fb}^{-1}$  and  $139 \text{ fb}^{-1}$  search, the high- $p_T$  WP is applied to electrons with  $p_T > 400 \text{ GeV}$  and  $p_T > 200 \text{ GeV}$ , respectively.

Electrons in this work are required to have  $E_T > 7 \text{ GeV}$ . Moreover, they are restricted to  $|\eta| < 2.47$ , as track reconstruction is only possible in the central detector region. To further suppress pile-up, electrons must satisfy  $|z_0 \sin \theta| < 0.5 \text{ mm}$  and  $d_0/\sigma(d_0) < 5$ .

To correct for differences in the electron selection efficiency between data and MC, scale factors are applied to simulated events in this work. These are derived in a measurement region enriched in  $Z \rightarrow ee$  and  $J/\psi \rightarrow ee$  events and consider efficiency effects from the electron reconstruction, identification and isolation steps [126, 128]. The efficiency measurements are affected by different sources of systematic uncertainties, which are estimated e.g. through variations in the event selection criteria or in the method used to subtract the contribution of background processes. Additional systematic uncertainties associated to electrons come from the calibration of the energy scale and resolution, which are caused e.g. by imperfect knowledge of pile-up effects and the modelling of shower shapes [127].

Also photons need to fulfil various identification criteria. These are defined using cut-based requirements on the different discriminating variables. In this work, photons must pass the quality criteria of the Tight [126] WP and have  $p_T > 25 \text{ GeV}$  and  $|\eta| < 2.37$ . They are only used in the calculation of the missing transverse momentum (c.f. Section 4.10) and in the overlap removal (c.f. Section 4.9), otherwise they are not considered in the analysis.

## 4.7 Muons

Muons leave a track in both the ID and MS. They are first reconstructed separately in these two subsystems. The muon track reconstruction in the ID is performed in the same way as for other charged particles (c.f. Section 4.1). In the MS, this is done by identifying hit patterns in each muon chamber, thereby forming segments. The muon track is obtained by fitting the segment hits from the different layers. Next, the information of the ID and the MS is combined. Four different muon types are considered in this process [129]: The first are called

combined muons, for which a global re-fit is applied to combine the ID and MS hits. The second one are segment-tagged muons. These are defined as ID tracks which, if extrapolated to the MS, are matched to one or more track segments in the MDT or CSC. This type is used for muons which only traverse one layer of the MS chambers. Calorimeter-tagged muons represent a third type. An ID track is considered to be a calorimeter-tagged muon if it is associated to an energy deposit in the calorimeters that is compatible with a minimum-ionising particle. Calorimeter-tagged muons have the largest contamination of *fakes*, i.e. objects originating from other particles than muons or from noise. However, they allow to reconstruct also muons in regions where the MS is not fully instrumented. The last type are so-called extrapolated muons, which are reconstructed solely with MS tracks. They must only satisfy a loose requirement on their compatibility with the primary vertex. Extrapolated muons are mainly used to reconstruct muons in the forward region  $2.5 < |\eta| < 2.7$ , which is outside of the ID coverage. As the reconstruction for the four muon types is performed independently, a muon can belong to multiple of these categories. Therefore, before the muons can be used in physics analyses, it is necessary to resolve these overlaps. If muons from different types share the same ID track, preference is given to combined muons, followed by segment-tagged and lastly calorimeter-tagged muons. Overlaps with extrapolated muons are resolved by evaluating the track properties and the fit quality.

Afterwards, different identification criteria are applied to discard muon tracks with a bad momentum resolution and to discriminate prompt from non-prompt muons. The latter are produced e.g. in pion decays, which typically leads to a “kink” in the associated track. Therefore, many criteria are based on the fit quality of the combined track as well as on the compatibility of the muon  $p_T$ , measured separately in the ID and MS, with the combined  $p_T$ . Another important variable is the  $q/p$  significance, which is defined as  $|q/p|/\sigma(|q/p|)$ . Here,  $q$  and  $p$  denote the charge and momentum of the muon<sup>1</sup>, respectively, obtained from the combination of the ID and MS measurements, and  $\sigma(|q/p|)$  the quadrature sum of the associated uncertainties. This variable is also used in the event cleaning (c.f. Section 5.5), which constitutes a set of criteria used to select only events of good quality. Additionally, requirements on the number of hits in the ID and MS are imposed. Two different WPs, Loose and Medium, are used for the muon identification in this work. The Loose WP considers all four muon types and has a typical efficiency of 97 – 98% in the selection of prompt muons [129]. The Medium WP has an efficiency of about 96% and only uses combined and extrapolated muons, of which the latter are only employed in  $2.5 < |\eta| < 2.7$ . The WPs are defined such that the resulting muon selections are inclusive, i.e. muons identified with the Medium WP constitute a subset of the ones obtained from the Loose WP.

Furthermore, muons in this work are required to be sufficiently isolated from other objects. The isolation requirements are based on the variables  $E_T^{\text{cone20}}$  and  $p_T^{\text{varcone30}}$ , which are defined equivalently to the  $E_T^{\text{cone20}}$  and  $p_T^{\text{varcone20}}$  variables used for the electron isolation (c.f. Section 4.6). The only difference is, that in  $p_T^{\text{varcone30}}$  the isolation cone has a size of  $\Delta R = \min(10 \text{ GeV}/p_T, 0.3)$ . In the  $79.8 \text{ fb}^{-1}$  analysis the LooseTrackOnly WP is used, which is defined such as to give a fixed muon efficiency of 99%, while in the  $139 \text{ fb}^{-1}$  search muons

---

<sup>1</sup>The trajectory of a muon in a magnetic field is described by  $mv^2/r = qvB$ , where the left and the right term denote the centripetal and the Lorentz force, respectively. With a known magnetic field  $B$ , the measurement of the radius  $r$  thus yields the quantity  $q/p$ .

must satisfy the isolation criteria of the FCloose WP. This requires  $p_T^{\text{varcone30}}/p_T < 0.15$  and  $E_T^{\text{cone20}}/p_T < 0.30$  [129].

Muons in this work need to have  $p_T > 7$  GeV. Moreover, to suppress pile-up effects, they must fulfil  $|z_0 \sin \theta| < 0.5$  mm and  $d_0/\sigma(d_0) < 3$ .

Scale factors are applied to simulated events to correct for differences between data and MC in the reconstruction, identification, isolation and track-to-vertex association efficiencies. These are derived in a measurement region that is enriched in  $Z \rightarrow \mu\mu$  and  $J/\psi \rightarrow \mu\mu$  events [130]. The efficiency measurements are affected by different systematic uncertainties arising e.g. from the background estimation technique. Furthermore,  $Z \rightarrow \mu\mu$  and  $J/\psi \rightarrow \mu\mu$  events are used to calibrate the muon momentum scale and resolution and to derive associated systematic uncertainties [129].

## 4.8 $\tau$ -leptons

Due to a lifetime of  $2.9 \times 10^{-13}$  s [2], a  $\tau$ -lepton produced in the hard scattering will usually decay before it can reach the first pixel layer. Therefore, only the  $\tau$ -lepton decay products can be detected. With a branching ratio of about 35%,  $\tau$ -leptons decay leptonically via  $\tau^- \rightarrow \ell^- \bar{\nu}_\ell \bar{\nu}_\tau$ . Here,  $\ell^-$  denotes an electron or muon. This lepton is reconstructed and identified following the techniques described in the previous two sections. The majority of  $\tau$ -leptons decays hadronically, giving rise to final states with jets. Most of them involve the production of one or three charged pions, e.g. via  $\tau^- \rightarrow \pi^- \pi^0 \bar{\nu}_\tau$  or  $\tau^- \rightarrow 2\pi^- \pi^+ \bar{\nu}_\tau$ . The former is called a 1-prong, the latter a 3-prong decay. They lead to one and three tracks in the ID, respectively. This characteristic signature allows to discriminate hadronic  $\tau$ -leptons from conventional jets.

The  $\tau$ -lepton reconstruction uses as input  $R = 0.4$  anti- $k_t$  jets which are calibrated using a local hadronic calibration method [131]. The jets are required to have  $p_T > 10$  GeV and  $|\eta| < 2.5$ . Afterwards, a track matching is performed to identify the pions. Only tracks are used which have  $p_T > 1$  GeV and which fulfil several other criteria regarding the track quality. The tracks are considered as being associated to the  $\tau$ -candidate jet, if they are located within  $\Delta R < 0.2$  around the jet axis.

After the reconstruction, various identification criteria are applied to  $\tau$ -candidates. These are defined using multivariate techniques, which use different variables describing the track properties and shower shapes. Each variable is corrected for pile-up effects. In the 79.8 fb $^{-1}$  analysis, the identification is performed with Boosted Decision Trees (BDT) using the associated Loose WP, which provides an efficiency of 60% and 50% for 1-prong and 3-prong  $\tau$ -leptons, respectively [131]. In the 139 fb $^{-1}$  analysis,  $\tau$ -leptons are identified with a new algorithm based on recurrent neural networks (RNN) which, compared to the BDT approach, allows for a better rejection against fakes, i.e. conventional jets in this case. Also the WP is changed to VeryLoose. This provides a similar fake rejection as the Loose WP of the BDT-based identification, but a significantly higher efficiency, which amounts to 95% for both 1 and 3-prong  $\tau$ -leptons [132].

A calibration is applied to  $\tau$ -leptons, which corrects their energy scale and the response. This considers also effects from pile-up [131]. In this work only  $\tau$ -leptons are used which have  $p_T > 20$  GeV and do not fall in the transition region of  $1.37 < |\eta| < 1.52$ . Systematic

uncertainties are associated to the different reconstruction, identification and calibration steps. However, these have a negligible impact on the mono- $h(bb)$  analyses.

If not stated otherwise, throughout this work the word “ $\tau$ -leptons” only refers to  $\tau$ -leptons from the hadronic decay mode.

## 4.9 Overlap removal

The reconstruction algorithms of the various physics objects are applied independently from each other. Thus, tracks or calorimeter signals may be associated to multiple objects. For example, a jet and an electron could share the same energy deposits in the ECAL. To resolve these ambiguities, a dedicated procedure is applied which removes close-by objects, referred to as *overlap removal*. In this, the distance between objects is measured by  $\Delta R = \sqrt{\Delta\phi^2 + \Delta y^2}$  which, compared to Equation 3.3, uses the rapidity  $y$  instead of  $\eta$ . The overlap removal employs different criteria, which are applied in subsequent order. Only objects passing the full sequence are later used in the analysis. These criteria are described in the following:

- If two electrons have a shared track, the one with the smaller  $p_T$  is rejected.
- A  $\tau$ -lepton is discarded if it overlaps with an electron or muon within  $\Delta R < 0.2$ .
- If an electron and a muon share an ID track and if in addition the muon is calorimeter-tagged, the muon is removed, otherwise the electron is rejected.
- A photon is rejected against an electron or muon, if they overlap within  $\Delta R < 0.4$ .
- If a small-R jet and an electron have  $\Delta R < 0.2$ , then the jet is removed.
- An electron is rejected against a small-R jet, if the two objects have a separation of  $\Delta R < \min(0.4, 0.04 + 10 \text{ GeV}/p_T(e))$ , where  $p_T(e)$  denotes the  $p_T$  of the electron.
- A jet with less than three tracks is removed in favour of a muon, if they are within  $\Delta R < 0.2$  or if the muon is ghost-associated to the jet.
- A muon is rejected against a small-R jet, if the two objects have a separation of  $\Delta R < \min(0.4, 0.04 + 10 \text{ GeV}/p_T(\mu))$ , where  $p_T(\mu)$  denotes the  $p_T$  of the muon.
- If a small-R jet and a  $\tau$ -lepton overlap within  $\Delta R < 0.2$ , the small-R jet is discarded.
- A photon is discarded, if it overlaps within  $\Delta R < 0.4$  with a small-R jet.
- If a large-R jet and an electron have  $\Delta R < 1.0$ , the large-R jet is removed.

## 4.10 Missing transverse momentum

Due to momentum conservation, the vectorial  $p_T$  sum of all particles produced in a  $pp$  collision event must be equal to the total momentum of the two initial partons. This allows to indirectly detect weakly interacting particles, such as neutrinos or possibly DM particles, which escape the detector without a notable signal. While the energy of the protons is known

to be 6.5 TeV, the energy of the colliding partons cannot directly be measured. Therefore, if neutrinos or DM particles are produced in an event, full momentum reconstruction is not possible. This motivates to consider only the transverse momenta: As the protons travel in  $z$ -direction, their momenta in the transverse plane are zero. Hence, a momentum imbalance in the transverse plane may indicate the presence of such “invisible” particles.

The variable used to quantify this momentum imbalance is called *missing transverse momentum*, denoted by  $E_T^{\text{miss}}$ . It is calculated using *hard* and *soft objects* [133]. Hard objects consist of all reconstructed and fully calibrated leptons, photons and small-R jets, as described in the preceding sections. Soft objects constitute tracks, which are associated to the primary vertex, but which are not part of the hard objects. The missing transverse momentum vector  $\mathbf{E}_T^{\text{miss}}$  is defined as the negative  $p_T$  sum of all hard and soft objects:

$$\mathbf{E}_T^{\text{miss}} = - \sum \mathbf{p}_T^e - \sum \mathbf{p}_T^\gamma - \sum \mathbf{p}_T^\mu - \sum \mathbf{p}_T^{\text{small-R jets}} - \sum \mathbf{p}_T^{\text{soft objects}}. \quad (4.4)$$

The variable  $E_T^{\text{miss}}$  is obtained from its magnitude, i.e.  $E_T^{\text{miss}} = |\mathbf{E}_T^{\text{miss}}|$ . In this work,  $\tau$ -leptons are treated as small-R jets in the  $E_T^{\text{miss}}$  calculation. Hence, they are not included in Equation 4.4. Per construction,  $E_T^{\text{miss}}$  is calculated using only small-R, but no large-R jets. To avoid ambiguities from close-by objects, an overlap removal is applied. For this, a dedicated procedure is used which is independent from the one described in Section 4.9. To suppress pile-up, the  $E_T^{\text{miss}}$  reconstruction in this work is performed using the Tight  $E_T^{\text{miss}}$  WP, which excludes the contribution of forward jets with  $|\eta| > 2.4$  and  $20 \text{ GeV} < p_T < 30 \text{ GeV}$  [134].

Systematic uncertainties arise from the  $E_T^{\text{miss}}$  response and resolution [133]. As the  $E_T^{\text{miss}}$  reconstruction uses fully calibrated objects, their corresponding uncertainties are propagated to the  $E_T^{\text{miss}}$  uncertainties. For soft objects, the associated uncertainties are evaluated by comparing  $\mathbf{p}_T^{\text{soft objects}}$  between data and simulation. This is performed in a selection of  $Z \rightarrow \mu\mu$  events.

## 4.11 Object-based $E_T^{\text{miss}}$ significance

Ideally,  $E_T^{\text{miss}}$  in an event would only arise, if neutrinos or other “invisible” particles are produced. This is referred to as *genuine*  $E_T^{\text{miss}}$ . However,  $E_T^{\text{miss}}$  can also originate e.g. from mis-measurements, momentum resolution effects or inefficiencies in the reconstruction and identification of objects. Thus, this is called *fake*  $E_T^{\text{miss}}$ .

To quantify, how genuine the reconstructed  $E_T^{\text{miss}}$  is, the so-called  $E_T^{\text{miss}}$  significance can be used. This has commonly been defined by  $E_T^{\text{miss}}/\sqrt{H_T}$ , where  $H_T$  denotes the scalar  $p_T$  sum of all hard objects. Often, only jets are considered in  $H_T$ . In events with genuine  $E_T^{\text{miss}}$ , the  $E_T^{\text{miss}}$  is expected to be relatively large compared to the  $p_T$  of the jets, photons and leptons. Therefore,  $E_T^{\text{miss}}/\sqrt{H_T}$  has higher values in events with genuine than with fake  $E_T^{\text{miss}}$ . This variable is also used in the  $79.8 \text{ fb}^{-1}$  search (c.f. Section 6.3.2) and is referred to as *event-based*  $E_T^{\text{miss}}$  significance in the following.

A more sophisticated approach is provided by the *object-based*  $E_T^{\text{miss}}$  significance  $\mathcal{S}$ : This novel variable evaluates with a hypothesis test, how consistent the reconstructed  $E_T^{\text{miss}}$  is with the signature of fake or genuine  $E_T^{\text{miss}}$ . The hypothesis test is performed based on a log-likelihood ratio and takes into account the expected resolutions of all objects entering the

$E_T^{\text{miss}}$  calculation and their directional correlations. The  $E_T^{\text{miss}}$  significance  $\mathcal{S}$  can be written in the form:

$$\mathcal{S} = \left( \frac{|\mathbf{E}_T^{\text{miss}}|^2}{\sigma_L^2 (1 - \rho_{LT}^2)} \right)^{\frac{1}{2}}, \quad (4.5)$$

where  $\sigma_L^2$  is the total variance in the longitudinal direction relative to  $\mathbf{E}_T^{\text{miss}}$  and  $\rho_{LT}$  the correlation factor of the longitudinal and transverse measurements [135]. The higher the obtained value for  $\mathcal{S}$  is, the more likely it is that the reconstructed  $E_T^{\text{miss}}$  is genuine. As  $\mathcal{S}$  evaluates only  $E_T^{\text{miss}}$ -related properties, possible variations of  $\mathcal{S}$  are covered by the  $E_T^{\text{miss}}$  uncertainties, so that no additional uncertainties are associated to  $\mathcal{S}$ . In this work, the resolution of pile-up jets and soft objects is not considered in the  $E_T^{\text{miss}}$  variance. This configuration was found to give the best performance for the final state signatures studied in the mono- $h(b\bar{b})$  search, in which it is used for the first time in the course of the  $79.8 \text{ fb}^{-1}$  analysis. A comprehensive discussion on the usage of  $\mathcal{S}$  and its impact on the analysis is given in Chapter 6.

# Chapter 5

## Introduction to the mono- $h(bb)$ analysis

This chapter gives an overview of the general mono- $h(bb)$  analysis strategy as well as of several other aspects, which are common between the searches with  $79.8 \text{ fb}^{-1}$  and  $139 \text{ fb}^{-1}$  of collected data.

### 5.1 Signature and analysis strategy

The mono- $h(bb)$  search targets final states, in which DM is produced in association with a SM-like Higgs boson  $h$ . For the latter, only decays into a pair of  $b$ -quarks are considered. With a branching ratio of about 58%, this constitutes its dominant decay mode. Thus, compared to other decay modes, this channel provides a much larger statistics in DM signal events with mono-Higgs final states. Therefore, the mono- $h(bb)$  search is sensitive to a large variety of DM models. The detector signature of mono- $h(bb)$  final states is illustrated in Figure 5.1. The DM particles leave the detector without interaction and thereby lead to a considerable amount of missing transverse momentum  $E_T^{\text{miss}}$ . For the  $h \rightarrow bb$  decay, one distinguishes between two different signatures depending on the momentum of  $h$ . If  $h$  has a relatively low momentum, the two  $b$ -quarks are sufficiently separated and can be reconstructed as two  $b$ -tagged small-R jets. With increasing momentum, the separation of the  $b$ -quarks gets smaller, so that they eventually cannot be identified as two distinct jets. Instead, such boosted decays are reconstructed as a single large-R jet with two  $b$ -tagged track jets associated to it. These two signatures are referred to as *resolved* and *merged* topologies, which are studied in two disjoint regions. Since the DM particles and  $h$  recoil against each other, the transverse momenta of the DM particles and  $h$  are strongly correlated: The higher the transverse momentum of  $h$ , the higher also  $E_T^{\text{miss}}$ . Therefore,  $E_T^{\text{miss}}$  is a suitable variable to separate the resolved and merged region. For this, a value of  $E_T^{\text{miss}} = 500 \text{ GeV}$  is used.

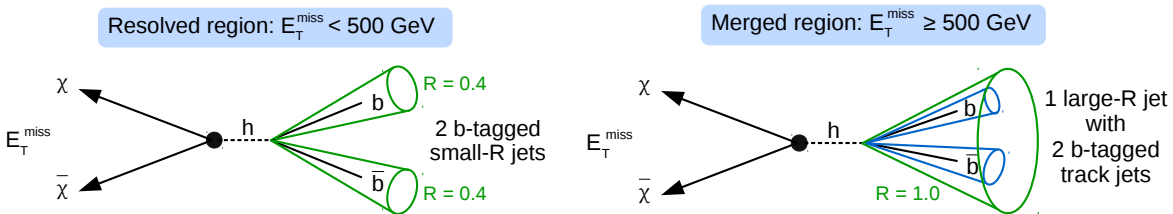


**Figure 5.1:** Illustration of the resolved (left) and merged (right) mono- $h(bb)$  signature. Though not explicitly shown, a signal event can generally contain additional jets from initial or final state radiation.

Compared to all SM processes occurring in the  $pp$  collisions, a possible mono- $h(b\bar{b})$  signal event would only be produced very rarely. Therefore, without any further requirements, the selected dataset consists almost exclusively of events from SM backgrounds. This makes it difficult to notice the signal. To obtain a good signal sensitivity, it is thus necessary to define suitable selection criteria which can enhance the signal-to-background ratio. These criteria, also referred to as *cuts*, are defined based on the multiplicity or kinematic properties of the final state objects. The resulting selection is then enriched in signal events and therefore called *signal region* (SR). For example, signal events typically produce large  $E_T^{\text{miss}}$  due to the escaping DM particles, while most of the SM background processes have a relatively small  $E_T^{\text{miss}}$ . Therefore, the signal-to-background ratio can efficiently be increased by imposing a minimum  $E_T^{\text{miss}}$  threshold, for which a cut of  $E_T^{\text{miss}} > 150$  GeV is used in this work. Since potential mono- $h(b\bar{b})$  signals may largely differ in their kinematic properties, it is common to define multiple SRs, as it is done e.g. for the resolved and merged topology. Another important criterium in the search is the lepton multiplicity. As mono- $h(b\bar{b})$  signals are expected to have only  $E_T^{\text{miss}}$  and jets in the final state, a veto on all leptons is applied in the SRs. However, events with leptons are used to define *control regions* (CRs). These regions are used to estimate the dominant backgrounds in the SRs by normalising the data in the CRs to the MC background predictions. For this purpose, a CR is required to have a high purity in the background process of interest and a negligible signal contamination. Furthermore, it should be kinematically similar, but still disjoint from the SR. The latter condition can be satisfied by selecting leptons instead of vetoing them.

To interpret the observed data with respect to a potential sign of mono- $h(b\bar{b})$  signals, a simultaneous fit is performed in the SRs and CRs. The fit used in the analysis is a so-called *shape fit*. In this, the different regions are split into various bins of certain event variables which show a characteristic shape for signal processes. The main fit variables in the analysis are the invariant mass of the Higgs candidate, denoted by  $m_h$ , and  $E_T^{\text{miss}}$ . In the resolved region,  $m_h$  is calculated as the invariant mass of the leading two  $b$ -jets ( $m_{jj}$ ), i.e. the two  $b$ -jets with the highest transverse momentum. In the merged region,  $m_h$  corresponds to the mass of the leading large- $R$  jet ( $m_J$ ). For signal events,  $m_h$  has a clear peak around the Higgs boson mass at about 125 GeV, as shown in Figure 5.2 for a few representative  $Z'$ -2HDM signals. On the other hand,  $m_h$  typically has a broader distribution for SM background processes. Therefore, by *binning* the SRs in  $m_h$ , i.e. dividing the SRs into multiple  $m_h$  ranges, the shape difference between the processes are revealed. This helps to better separate signal from background. The bin width must be chosen as a compromise between the following two aspects: It should be fine enough to reflect the shape differences, but still provide a sufficiently high data and MC statistics for each bin to ensure a reliable background estimation. For example, with  $E_T^{\text{miss}} > 500$  GeV the data and MC background statistics in the merged region is much lower than in the resolved region. Consequently, a broader  $m_h$  binning needs to be chosen for the merged than for the resolved region.

The average  $E_T^{\text{miss}}$  distribution can differ a lot between the signal models. This is illustrated in Figure 5.2, which shows the  $E_T^{\text{miss}}$  distributions for different  $Z'$ -2HDM signals. With increasing  $Z'$ -masses, the average  $E_T^{\text{miss}}$  moves to higher values: The larger the mass of the  $Z'$ -boson, the more energy is released in its decay, so that the resulting signature mono- $h(b\bar{b})$  signature is more boosted. For a given  $m_{Z'}$ , the average  $E_T^{\text{miss}}$  also becomes larger with an increasing difference between  $m_{Z'}$  and  $m_A$ , because this leads to a more

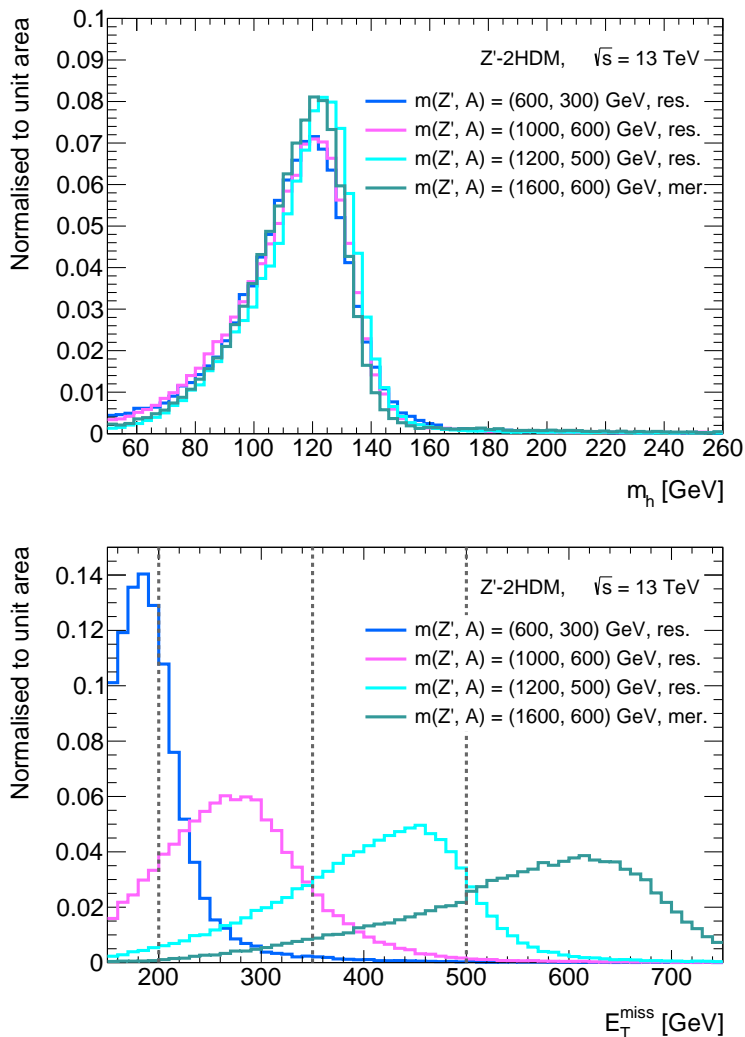


**Figure 5.2:** Normalised distributions of  $m_h$  (top) and of  $E_T^{\text{miss}}$  (bottom) for representative signals of the  $Z'$ -2HDM with  $m_H = m_{H^\pm} = 300$  GeV. The appended strings “res.” and “mer.” indicate, whether the distribution is plotted using the  $m_h$  and  $E_T^{\text{miss}}$  requirements of the resolved region ( $N(b\text{-tagged small-R jets}) \geq 2$ ,  $E_T^{\text{miss}} > 150$  GeV) or the merged region ( $N(\text{large-R jets}) \geq 1$ ,  $N(b\text{-tagged associated track jets}) \geq 2$ ,  $E_T^{\text{miss}} > 500$  GeV). For illustration purposes, no  $E_T^{\text{miss}}$  requirements are applied in the right plot. The vertical lines represent the boundaries of the different  $E_T^{\text{miss}}$  bins.

energetic recoil of  $A$  and  $h$ . For each signal model, the sensitivity can be enhanced by restricting the  $E_T^{\text{miss}}$  range to values, in which the given signal is peaking. Therefore, also an  $E_T^{\text{miss}}$  binning is used in the analysis. The resolved SR is divided into three bins of  $E_T^{\text{miss}} = [150, 200, 350, 500]$  GeV. Due to the lower data and MC background statistics, such a fine  $E_T^{\text{miss}}$  binning is not feasible in the merged SR. Therefore, only a single  $E_T^{\text{miss}}$  bin is used in the  $79.8 \text{ fb}^{-1}$  analysis. In the  $139 \text{ fb}^{-1}$ , the possibility is explored to divide the merged SR into two bins. This is discussed in Section 7.3.4 and Section 7.5.

## 5.2 SM background processes

Apart from potential DM signals, SM processes can lead to a mono- $h(bb)$  signature, too. The dominant backgrounds in the analysis are  $t\bar{t}$ ,  $Z$ +jets and  $W$ +jets processes. These are estimated in two dedicated control regions: A one-muon CR ( $1\mu$ -CR) is used to constrain  $t\bar{t}$  and  $W$ +jets processes, while the  $Z$ +jets background is estimated in a two-lepton CR ( $2\ell$ -CR) with two electrons or muons in the final state. Other backgrounds are single-top and diboson processes, Higgs boson production in association with a  $W$  or  $Z$ -boson ( $Vh$ ) and  $t\bar{t}$  production in association with a  $W/Z$  ( $t\bar{t}V$ ) or Higgs boson ( $t\bar{t}h$ ). These are estimated from MC simulation only. Due their relatively small cross sections, their contribution to the total background is much smaller than for  $t\bar{t}$  and  $W/Z$ +jets processes. A minor contribution comes from the multijet background, which is estimated in a data-driven way. This section gives an overview of the different SM background processes and explains, how they can mimic a mono- $h(bb)$  signal.

### Top-quark pair production

Top-quark pair production ( $t\bar{t}$ ) is the dominant background in the resolved region. This process contributes mostly due to semi-leptonic decays to the SR, as shown in the Feynman diagram of Figure 5.3(a): Each top-quark decays to a  $b$ -quark and a  $W$ -boson. One of the  $W$ -bosons decays into quarks and the other one into a charged lepton and its associated neutrino. Like potential DM particles, neutrinos leave the detector without interaction, so that their presence can only be indirectly inferred from the measurement of  $E_{\text{T}}^{\text{miss}}$ . Therefore, semi-leptonic  $t\bar{t}$  decays can produce a mono- $h(bb)$  signature, if the charged lepton e.g. fails to be identified or falls out of detector acceptance. Such processes are *reducible*, because better reconstruction or analysis techniques would in principle allow to minimise their contamination in the SR.

To estimate the  $t\bar{t}$  background, a one-lepton CR can be used: The purpose is to select the same process as of Figure 5.3(a), but with a successfully reconstructed charged lepton. The one-lepton CR in the analysis is a single-muon region ( $1\mu$ -CR). The reason to use only this lepton type is motivated by certain trigger properties regarding muons, which are explained in Section 5.4.1.

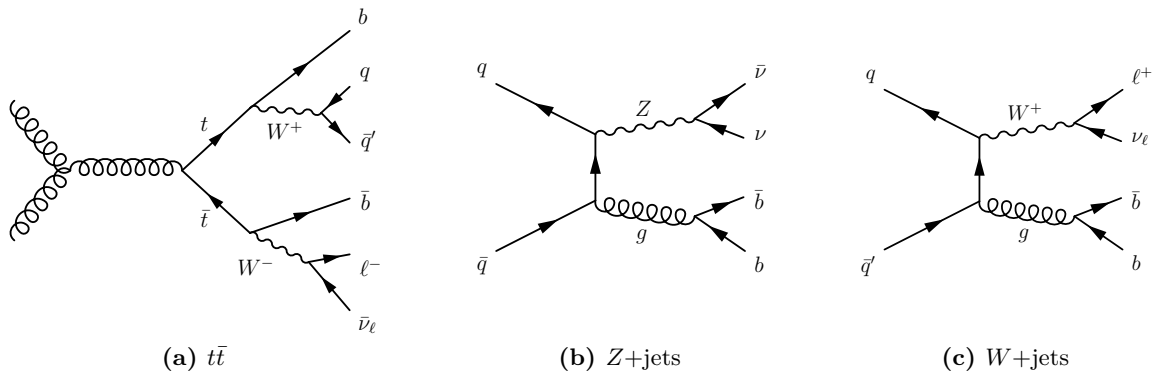


**Figure 5.3:** Representative Feynman diagrams for the dominant SM background processes.

### Z+jets

$Z$ +jets production is the dominant background in the merged SR. An exemplary Feynman diagram for this process is shown in Figure 5.3(b): The  $Z$ -boson decays to a pair of neutrinos, which gives a considerable amount of  $E_T^{\text{miss}}$ , while gluon splitting gives rise to a pair of  $b$ -quarks. Therefore, the resulting final state is indistinguishable from a mono- $h(b\bar{b})$  signal. Such processes are called *irreducible* backgrounds. Contributions from other  $Z$ -boson decay modes, such as its decays to quarks, are negligible because these do not produce sufficiently high  $E_T^{\text{miss}}$  to pass the requirement  $E_T^{\text{miss}} > 150$  GeV.

Apart from the diagram with two  $b$ -quarks, the Higgs boson candidate can also originate from light-flavour or  $c$ -initiated (track) jets, which are falsely  $b$ -tagged. The dominant contributions come from processes involving heavy-flavour quarks. Hence, in this work one additionally distinguishes between  $Z$ +jets processes with heavy and light-flavour production, denoted as  $Z$ +HF and  $Z$ +LF, respectively. These are defined by a labelling procedure, in which the quark flavour of the leading two Higgs candidate (track) jets is determined from truth information (c.f. Section 3.2.9) stored in the MC samples. An event is considered to be a  $Z$ +HF process, if the two Higgs candidate (track) jets are labelled as  $bb$ ,  $bc$ ,  $cc$  and  $bl$ . For example,  $bl$  means that one of the two (track) jets is initiated from a  $b$ , the other one from a light-flavour quark.

The  $Z$ +jets background can be estimated in a two-lepton CR by selecting events, in which the  $Z$ -boson decays into a pair of charged leptons  $\ell^+\ell^-$ . For this, only the decays  $Z \rightarrow e^+e^-$  and  $Z \rightarrow \mu^+\mu^-$  are considered. Since the  $Z$ -boson momentum does not depend on its decay mode,  $Z(\rightarrow \nu\bar{\nu})$ +jets in the SR and  $Z(\rightarrow \ell^+\ell^-)$ +jets events in the  $1\mu$ -CR are kinematically compatible.

### W+jets

The third major background in the mono- $h(b\bar{b})$  analysis is  $W$ +jets production. A representative Feynman diagram for this process is shown in Figure 5.3(c).  $W$ +jets events in the SR come mostly from leptonic  $W$ -boson decays, in which the charged lepton is lost. Therefore, the  $W$ +jets background is estimated together with  $t\bar{t}$  in the  $1\mu$ -CR. Due to the absence of neutrinos, the hadronic decay modes do not produce a large enough  $E_T^{\text{miss}}$  to pass the requirement  $E_T^{\text{miss}} > 150$  GeV. Thus, their contribution negligible. Also for  $W$ +jets events, one distinguishes between heavy-flavour ( $W$ +HF) and light-flavour ( $W$ +LF) processes, which are defined the same way as described above for  $Z$ +jets.

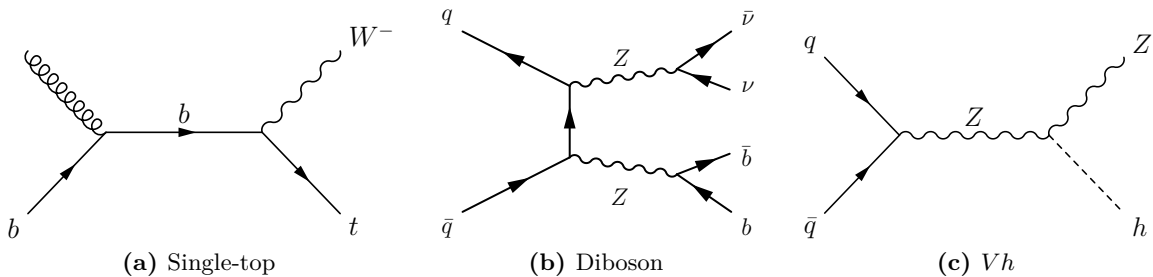


**Figure 5.4:** Representative Feynman diagrams for the subleading SM background processes.

**Single-top**

Single-top events can enter the SRs through three different production modes:  $Wt$ -associated, s-channel and t-channel production. Among them, the dominant process is  $Wt$ -associated production, which is shown in the diagram in Figure 5.4(a). Also this background contributes mainly from decay modes involving one lepton in the final state.

**Diboson**

Diboson processes commonly describe the production of two vector bosons:  $WW$ ,  $WZ$  or  $ZZ$ . These contribute to the SRs e.g. through the diagram shown in Figure 5.4(b). Here, two  $Z$ -bosons are produced, of which one decays into a pair of  $b$ -quarks and the other one into neutrinos.

 **$Vh$** 

The  $Vh$  background describes the production of a vector boson, i.e. a  $W$  or  $Z$ -boson, in association with a Higgs boson. The Feynman diagram for the  $Zh$  process is shown in Figure 5.4(c). If the  $Z$ -boson decays to neutrinos and the Higgs boson to a pair of  $b$ -quarks, the final state signature is identical to a mono- $h(b\bar{b})$  signal.

 **$t\bar{t}V$  and  $t\bar{t}h$** 

In  $t\bar{t}V$  and  $t\bar{t}h$  processes, a top-quark pair is produced together with a  $W$ ,  $Z$  or Higgs boson. Compared to the other backgrounds, their production cross section is very small. Their contribution in final states with two  $b$ -tags, i.e. with no other  $b$ -tagged (track) jets than the Higgs boson candidate, is negligibly small. These backgrounds are not included at all in the  $79.8 \text{ fb}^{-1}$  analysis. However, for events with three or more  $b$ -tags, they have a non-negligible contribution. Since these events are expected to have an important impact on the sensitivity to the  $b\bar{b}$ -induced 2HDM+ $a$  signals (c.f. Figure 2.9), which are analysed within the  $139 \text{ fb}^{-1}$  analysis,  $t\bar{t}V$  and  $t\bar{t}h$  processes are included there as background sources.

**Multijet**

The multijet background originates from processes involving the production of several quarks and gluons, which leads to multiple jets in the final state. In multijet events,  $E_{\text{T}}^{\text{miss}}$  can originate e.g. from fake  $E_{\text{T}}^{\text{miss}}$ , caused by mismeasurements of jet energies, or from neutrinos produced in semi-leptonic hadron decays, e.g. by the underlying process  $b \rightarrow W^- c \rightarrow \ell^- \bar{\nu}_{\ell} c$ . This background typically produces low  $E_{\text{T}}^{\text{miss}}$ , so that its contribution in the analysis is rather small, despite its large production cross section. As a variety of strong interaction processes can give rise to multijet final states, a large MC statistics would be required to model this background properly. However, this is computationally challenging, so that the estimation of multijet processes relies on data-driven methods, as described in Section 6.3.3.

## 5.3 Simulated samples

This section describes, how the different signal and background processes in this work are simulated. A general introduction to the different steps in the simulation of processes  $pp$  collision has been given in Section 3.2.9, so that in the following only the analysis-relevant

settings are discussed. Table 5.1 summarises the MC generators and PDF sets used to model the matrix elements, the parton showering and hadronisation. Furthermore, it indicates if the production cross section of a process is corrected to the theory predictions and to which order in the calculation of the matrix element this correction is applied.

Two different sets of  $Z'$ -2HDM samples are used in the analysis, which are both simulated for several values of  $m_{Z'}$  and  $m_A$ . The first one is generated with the parameters of Equation 2.41, corresponding to the  $Z'$ -2HDM parameter choice also used in previous mono- $h(b\bar{b})$  searches. The other set uses  $m_H = m_{H^\pm} = m_A$  instead of  $m_H = m_{H^\pm} = 300$  GeV. This was introduced to harmonise the parameter settings with the CMS experiment to allow for a comparison of the results in the future. The 2HDM+ $a$  signals are generated in two separate sets as well: One with  $\tan\beta = 1$  and another one with  $\tan\beta = 10$ . In the first one, only diagrams from the ggF production mechanism are included, in the latter one only  $b\bar{b}$ -initiated production, because in either case the contribution from the other production mode is negligible. For each of them, several samples are produced with different values of  $m_A$  and  $m_a$ . The remaining parameters are fixed to the values of Equation 2.46.

$W/Z$ +jets and diboson processes are simulated with SHERPA v2.2 [136] which is also used for the modelling of the parton shower and hadronisation [137]. The parton shower is merged with the matrix elements following the MEPS@NLO prescriptions [138–141]. The  $W/Z$ +jets samples used in this work are so-called *filtered* samples. These are simulated using certain selection criteria (filters) to increase the sample statistics for a given kinematic phase space. In the analysis, the event yield predictions from these samples must be corrected for the associated efficiency of the filters. The  $W/Z$ +jets samples used in the analysis are filtered by  $\max\{p_T(V), H_T\}$ , i.e. the generated processes are filtered and split into different subsamples based on the maximum of the vector boson  $p_T$  and the  $H_T$  in the event, where  $H_T$  defines the scalar sum of the  $p_T$  of the  $W/Z$ -boson and the jets. To improve the modelling in the statistically limited merged region, in the 139 fb $^{-1}$  analysis a set of  $p_T(V)$ -filtered samples is used in addition to the  $\max\{p_T(V), H_T\}$ -filtered ones. In the  $p_T(V)$  samples, the slicing is done according to the  $p_T$  of the  $W/Z$ -boson.

Also for  $t\bar{t}$  processes two separate sets of samples are used in the analysis. One is an inclusive sample, while the other are  $E_T^{\text{miss}}$ -filtered samples. In the analysis of 79.8 fb $^{-1}$  only the inclusive sample was used. The  $E_T^{\text{miss}}$ -filtered samples were introduced in the 139 fb $^{-1}$  analysis to increase the MC statistics in the high- $E_T^{\text{miss}}$  region. Besides the settings listed in Table 5.1, also EVTGEN v1.6.0 [142] is used, with which the decays of  $b$  and  $c$ -hadrons are modelled.

The simulation of  $Vh(b\bar{b})$  processes is performed separately for their productions via quark-anti-quark ( $q\bar{q}$ ) annihilation and gluon-gluon fusion (ggF). As mentioned in the previous section,  $t\bar{t}V$  and  $tth$  processes are only considered in the 139 fb $^{-1}$  analysis. In the  $t\bar{t}V$  samples the decays of  $b$  and  $c$ -hadrons are simulated with EVTGEN v1.2.0 [142].

For all signal and background processes, the detector response is simulated with GEANT4 [92]. The effect of pile-up is modelled by overlaying the hard-scatter process of interest with inelastic  $pp$  events. These are generated with PYTHIA8.186 [143] using the NNPDF 2.3 LO PDF set [144] together with the A3 set of tuned parameters [145]. To correct for differences in the pile-up conditions between data and MC, the simulations used in this work are reweighted such that the mean number of interactions per bunch crossing (c.f. Section 3.1) matches the value observed in data. This is referred to as pile-up reweighting.

Process	Matrix element	PDF (Hard process)	PS + hadron.	Tune	PDF (Parton shower)	Cross section
$Z$ -2HDM	MG5_AMC 2.6.5 [146]	NNPDF3.0 NLO [90]	PyTHIA8.240 [147]	A14 [148]	NNPDF 2.3 LO [149]	Generator LO
2HDM+ $a$	MG5_AMC [146]	NNPDF 3.0 NLO	PyTHIA8.230 [147]	A14	NNPDF 2.3 LO	Generator LO
$W/Z$ +jets	SHERPA v2.2 [136]	NNPDF 3.0 NNLO	SHERPA v2.2 [137]	—	—	NNLO [150]
Diboson	SHERPA v2.2	NNPDF 3.0 NNLO	SHERPA v2.2	—	—	Generator NLO
$h$	PowHEGBox v2 [151–154]	NNPDF 3.0 NLO	PyTHIA8.230	A14	NNPDF 2.3 LO	NNLO [155–161]
single- $t$ ( $Wt$ )	PowHEGBox v2	NNPDF 3.0 NLO	PyTHIA8.230	A14	NNPDF 2.3 LO	NLO [162, 163]
single- $t$ ( $s$ -chan.)	PowHEGBox v2	NNPDF 3.0 NLO	NNPDF 3.0 NLO	A14	NNPDF 2.3 LO	NLO [162, 163]
single- $t$ ( $t$ -chan.)	PowHEGBox v2	NNPDF 3.0 NLO	PyTHIA8.230	A14	NNPDF 2.3 LO	NLO [162, 163]
$Vh(b\bar{b})$ ( $q\bar{q}$ )	PowHEGBox v2	NNPDF 3.0 NLO	PyTHIA8.212 [147]	AZNLO [164]	CTEQ6L1 [165]	NNLO (QCD), NLO (EW) [166–172]
$Vh(b\bar{b})$ (ggF)	PowHEGBox v2	NNPDF 3.0 NLO	PyTHIA8.212	AZNLO	CTEQ6L1	NNLO, NLO [173–175]
$t\bar{t}V$	MG5_AMC v2.3.3 [146]	NNPDF 3.0 NLO	PyTHIA8.210 [147]	A14	NNPDF 2.3 LO	NLO [6]
$t\bar{t}h$	PowHEGBox v2	NNPDF 3.0 NLO	PyTHIA8.230	A14	NNPDF 2.3 LO	NLO [6]

**Table 5.1:** Overview of the generator, PDF and cross section settings for the MC signal and background samples used in this work. Here, MADGRAPH5\_AMC@NLO is abbreviated by MG5\_AMC. Two different PDF sets are typically used for the calculation of the hard process and for the modelling of the parton shower (PS) and the hadronisation. The column “Tune” shows the sets of tuned parameters used in the PS and hadronisation. The last column “Cross section” indicates whether the production cross section of the process is corrected to the theory predictions and up to which order in the calculation of the matrix element this is applied. “LO” corresponds to the leading order, “NLO” to the next-to-leading order and so on. “NNLO” denotes the next-to-next-to-leading logarithmic order. For  $q\bar{q}$ -induced  $Vh(b\bar{b})$  processes, the QCD and electroweak (EW) corrections are applied at different orders. No cross section corrections are applied for signal and diboson processes. For these, the cross section is directly taken from the generator predictions.

## 5.4 Trigger strategy and efficiency calibration

### 5.4.1 Trigger strategy

Different types of triggers are used to select SR and CR events. Since mono- $h(b\bar{b})$  signals predict a considerable amount of  $E_T^{\text{miss}}$ , SR events are selected with unprescaled<sup>1</sup>  $E_T^{\text{miss}}$  triggers. These are used in the  $1\mu$ -CR, too, which is motivated by the following: The  $E_T^{\text{miss}}$  reconstruction in the  $E_T^{\text{miss}}$  trigger algorithm uses calorimeter information only. As muons barely deposit energy in the calorimeters, they are effectively not considered in the reconstruction of the *online*  $E_T^{\text{miss}}$ , i.e. the  $E_T^{\text{miss}}$  as measured by the trigger during the data-taking. On the other hand, *offline* refers to the reconstruction performed on the recorded dataset and on MC samples. The online  $E_T^{\text{miss}}$  spectrum, as seen by the trigger for  $t\bar{t}$  and  $W$ +jets events with a muon, is thus very similar to the corresponding offline distributions measured in zero-lepton events. This does not hold for electrons or  $\tau$ -leptons, because these deposit their energy almost fully in the calorimeters. Therefore, a  $1\mu$ -CR is used to estimate  $t\bar{t}$  and  $W$ +jets processes, making the CR as close as possible to the SR right from the trigger stage.

Furthermore, unprescaled single-electron triggers are used to select  $Z \rightarrow e^+e^-$  events in the  $2\ell$ -CR. These require one electron with an online  $p_T$  above a certain threshold to trigger the event. Apart from that, additional electrons may also be present in the event, allowing to select dileptonic final states with single-lepton triggers. Similarly, unprescaled single-muon triggers are used to select  $Z \rightarrow \mu^+\mu^-$  events in the  $2\ell$ -CR.

Since the beam conditions changed over the time, the trigger menu used at the ATLAS detector was also regularly updated. The trigger menu describes the set of all triggers used to record the data in the different data-taking periods. Triggers of a certain kind can be modified in e.g. the required  $p_T$  or  $E_T^{\text{miss}}$  threshold, the lepton isolation requirements or the  $E_T^{\text{miss}}$  reconstruction algorithms. For example, for  $E_T^{\text{miss}}$  triggers the  $E_T^{\text{miss}}$  threshold was constantly increased, starting from 70 GeV in 2015 and reaching up to 110 GeV in the later periods. This was done to better cope with the increased  $pp$  collision rate (c.f. Section 3.3). Table 5.2 and Table 5.3 give a summary of the  $E_T^{\text{miss}}$ , respectively single-lepton triggers used in this work for the different data-taking periods. The triggers are simulated for all MC samples of the analysis, so that both data and MC are required to pass the listed triggers.

For single-lepton triggers a matching criterium is applied, which requires that an offline lepton is geometrically matched to the lepton object as reconstructed by the trigger algorithm. Additional  $p_T$  requirements are applied onto these offline leptons to avoid selecting leptons, in which the trigger is not yet fully efficient (c.f. Section 5.4.3). For this, among the single-electron (single-muon) triggers fired in the event, the one with the lowest  $E_T$  ( $p_T$ ) threshold is taken as reference trigger. The  $p_T$  of the offline electron must be at least 1 GeV higher than the threshold of the respective trigger. For single-muon triggers, the offline muon must have a  $p_T$  of at least 5% higher than the reference value.

---

<sup>1</sup>An unprescaled trigger accepts every event in which the triggered object passes the required trigger threshold, e.g. a certain  $E_T^{\text{miss}}$  or lepton  $p_T$  value. Opposed to that, prescaled triggers accept only a certain fraction of these events to reduce the recorded event rate.

Period	Int. luminosity	$E_T^{\text{miss}}$ trigger
2015	3.2 fb $^{-1}$	HLT_xe70_mht
2016, B - D3	6.1 fb $^{-1}$	HLT_xe90_mht_L1XE50
2016, D4 - end	26.9 fb $^{-1}$	HLT_xe110_mht_L1XE50
2017, B - D5	12.3 / 12.8 fb $^{-1}$	HLT_xe110_pufit_L1XE55
2017, D6 - end	31.3 / 31.5 fb $^{-1}$	HLT_xe110_pufit_L1XE55
2018	58.5	HLT_xe110_pufit_70_L1XE55

**Table 5.2:** Overview of the  $E_T^{\text{miss}}$  triggers used to select SR and  $1\mu$ -CR events in the different data-taking periods. The capital letters denote the data-taking periods within a given year and appended numbers indicate a subperiod. The integrated luminosity indicates the dataset collected by a given trigger. Two separate luminosity values are given for the  $E_T^{\text{miss}}$  triggers used in 2017. The first number denotes the luminosity used in the 79.8 fb $^{-1}$  search, the second the one in the 139 fb $^{-1}$  search. The reason for the different luminosity values is an update in the Good-Runs-Lists. This led to an increase of 0.7 fb $^{-1}$  in the dataset of 2017 which is labelled as being good for physics.

Period	Single-electron triggers	Single-muon triggers
2015	HLT_e24_lhmedium_L1EM20VH <b>OR</b> HLT_e60_lhmedium <b>OR</b> HLT_e120_lhloose	HLT_mu20_iloose_L1MU15 <b>OR</b> HLT_mu50
2016, A	HLT_e60_lhmedium_nod0 <b>OR</b> HLT_e140_lhloose_nod0	HLT_mu40 <b>OR</b> HLT_mu50
2016, B - D3	HLT_e60_lhmedium_nod0 <b>OR</b> HLT_e140_lhloose_nod0	HLT_mu24_ivarmedium <b>OR</b> HLT_mu50
2016, D4 - end	HLT_e26_lhtight_nod0_ivarloose	HLT_mu26_ivarmedium
2017	<b>OR</b> HLT_e60_lhmedium_nod0	<b>OR</b> HLT_mu50
2018		<b>OR</b> HLT_e140_lhloose_nod0

**Table 5.3:** Overview of the single-lepton triggers used to select  $2\ell$ -CR events in the different data-taking periods. The capital letters denote the data-taking periods within a given year and appended numbers indicate a subperiod. The “**OR**” denotes a logical or, which means that a  $2e$ -CR or  $2\mu$ -CR candidate event must pass at least one of the single-electron and muon triggers that were used in the corresponding period, respectively.

## 5.4.2 Nomenclature and reconstruction algorithms

### $E_T^{\text{miss}}$ triggers

Several properties of an  $E_T^{\text{miss}}$  trigger can be inferred from its naming. As an example, the naming convention is explained with the trigger HLT\_xe110\_mht\_L1XE50: The last expression L1XE50 indicates that a threshold of  $E_T^{\text{miss}} > 50$  GeV is used in the hardware-based level-1 (L1) trigger. The only exception from this convention is the trigger HLT\_xe70\_mht, in which its L1 threshold of 50 GeV is not indicated in the name. An event passing the L1 requirement is subsequently analysed by the software algorithms of the high-level trigger (HLT). The string HLT\_xe110\_mht specifies, that a  $E_T^{\text{miss}}$  threshold of 110 GeV is applied in the HLT and that the mht algorithm is used for the  $E_T^{\text{miss}}$  reconstruction. Apart from mht, there are two

additional algorithms, `cell` and `pufit`, which are used in the  $E_T^{\text{miss}}$  triggers in this work. The  $E_T^{\text{miss}}$  reconstruction in these three algorithms works as follows [176]:

- **Calorimeter cell algorithm (`cell`)**

This represents the simplest HLT algorithm. In this,  $E_T^{\text{miss}}$  is determined from the vectorial sum over the energy deposits in all calorimeter cells.

- **Jet-based algorithm (`mht`)**

In the `mht` algorithm<sup>1</sup>,  $E_T^{\text{miss}}$  is calculated using calibrated jets as inputs which are corrected for pile-up effects. The jets are reconstructed using the anti- $k_T$  algorithm with a radius parameter of  $R = 0.4$ . This procedure also includes the energy deposits of photons, electrons and hadronic  $\tau$ -leptons.

- **Local pile-up suppression algorithm (`pufit`)**

In the `pufit` algorithm,  $E_T^{\text{miss}}$  is reconstructed using topological clusters which are calibrated with the local hadronic cell weighting [101] (LCW) method. The clusters are combined, resulting in objects with a size of approximately  $R = 0.4$ . These are subsequently corrected for pile-up effects through a fit on the energy deposits and their spacial fluctuations. This allows to estimate the transverse energy  $E_T$  of each combined cluster. The pile-up correction is based on the assumption that objects from a hard-scatter process lead to a relatively large  $E_T$ , while pile-up effects typically result in smaller  $E_T$ .

Whether a  $E_T^{\text{miss}}$  trigger uses the `mht` or `pufit` algorithm can be inferred from its name. For the triggers in this work, the `cell` algorithm is only applied in `HLT_xe110_pufit_xe70_L1XE55`, in which it was used in combination with the `pufit` algorithm. Here, the  $E_T^{\text{miss}}$  thresholds of 110 GeV and 70 GeV refer to the `pufit` and `cell` algorithm, respectively.

### Single-electron triggers

At L1, single-electron triggers select events by demanding the presence of at least one cluster in the electromagnetic calorimeter. In the 2015 data-taking periods, the candidate clusters were required to have a minimum  $p_T$  of 20 GeV, while from 2016 to 2018 a requirement of  $p_T > 22$  GeV, supplemented by isolation criteria, was used [177]. However, these thresholds vary by about  $-2$  to  $+3$  GeV depending on the  $\eta$  position of the electron. Most of the single-electron triggers only contain the HLT settings in their names. The naming has the following convention: “`HLT_e`[ $E_T$  threshold in GeV]\_[identification criteria]”. Besides that, the trigger name can have an additional string indicating optional requirements on the isolation. For example, the trigger `HLT_e26_lhtight_nod0_ivarloose` requires an electron candidate with a  $E_T$  of greater 26 GeV. The electron candidate must further satisfy the criteria of the `lhtight` identification working point. The subsequent string `nod0` indicates, that in the identification algorithms no requirements on the transverse impact parameter  $d_0$  are imposed. The last string `ivarloose` denotes a loose isolation criterium which is defined based on the  $E_T$  deposits within a cone of variable size around the electron. A comprehensive

---

<sup>1</sup>The name `mht` originates from the expression “missing- $H_T$ ”, in which  $H_T$  denotes the scalar sum of all jet  $p_T$  in the event.

overview of the single-electron trigger algorithms and their performance is given in Ref. [177].

### Single-muon triggers

The single-muon triggers used in this work are seeded by the L1mu20 trigger, which requires a muon candidate with a  $p_T$  of at least 20 GeV at the L1 stage [178, 179]. The only exception is HLT\_mu20\_i1oose\_L1MU15, in which a  $p_T$  threshold of 15 GeV is applied at L1. For all other muon triggers of Table 5.3, only the settings of the HLT algorithms are specified in the names, following the naming convention “HLT\_mu[ $p_T$  threshold in GeV]”. Some triggers impose additional identification and isolation criteria. This is indicated by an additional string in the name. For example, the trigger HLT\_mu24\_ivarmedium requires a muon candidate with a  $p_T$  of at least 24 GeV. Furthermore, the muon candidate is required to pass a medium isolation selection, which is calculated using information of ID tracks within a cone of variable size around the muon. A detailed description of the muon trigger algorithms and their performance can be found in Ref. [178].

### 5.4.3 Trigger efficiency calibration

An important property of a trigger is its efficiency  $\varepsilon$ . This defines the fraction of events in a reference dataset which fire the trigger of interest:

$$\varepsilon = \frac{\text{Number of events in reference dataset passing the trigger}}{\text{Total number of events in reference dataset}} \quad (5.1)$$

The reference dataset would optimally constitute the set of all  $pp$  collision events. However, as data events can only be recorded, if they pass at least one of the active triggers, the efficiency of a trigger needs to be measured with respect to a set of events selected by another trigger type. In this work, for example,  $E_T^{\text{miss}}$  trigger efficiencies are measured in a reference dataset based on muon triggers, because muons are not considered in the  $E_T^{\text{miss}}$  trigger algorithm. Ideally, the online algorithms of the  $E_T^{\text{miss}}$  and lepton triggers would give identical results to the *offline* reconstruction methods. For example, if events are selected by an  $E_T^{\text{miss}}$  trigger with a threshold of 110 GeV, there should be no events in the analysis with an offline  $E_T^{\text{miss}}$  value of less than 110 GeV. Thus, the efficiency of the trigger, if plotted as a function of the offline  $E_T^{\text{miss}}$ , would in theory describe a step function around the  $E_T^{\text{miss}}$  trigger threshold. However, the online and offline reconstruction methods are not identical and their measurements are also not perfect. Therefore, the “step” is in fact a smooth rising curve, as illustrated in Figure 5.5. This is called the *trigger turn-on*, while the region, in which the trigger is fully efficient, is referred to as *plateau*.

The trigger turn-on is typically not well modelled in MC simulations. Therefore, if physics analyses use events in the turn-on region, the MC predictions need to be appropriately re-scaled to match the trigger efficiency observed in data. For single-electron and muon triggers, the necessary scale factors (SFs) are adopted from the efficiency measurements described in Ref. [177] and Ref. [178], respectively. However, the  $E_T^{\text{miss}}$  trigger efficiency is highly dependent on the kinematics and the background composition of the selected events. Thus,  $E_T^{\text{miss}}$  trigger SFs must be derived within the analysis. The SFs need to be applied in every region selected by  $E_T^{\text{miss}}$  triggers which, in this work, are the SR and  $1\mu$ -CR. A

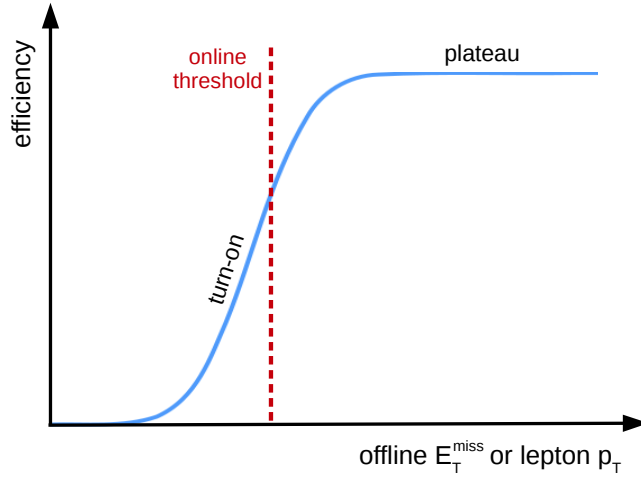


**Figure 5.5:** Illustration of a trigger efficiency curve.

dedicated  $E_T^{\text{miss}}$  trigger efficiency calibration has been developed in the course of the preceding mono- $h(b\bar{b})$  analysis based on the dataset of  $36.1 \text{ fb}^{-1}$  [9]. A comprehensive description of the associated studies can be found in Ref. [180]. This strategy is also used for the trigger calibration in the  $79.8 \text{ fb}^{-1}$  analysis, which is explained in Appendix A.1. In the  $139 \text{ fb}^{-1}$  analysis, several modifications have been introduced regarding the efficiency measurements and the scale factor calculation in order to improve the SF calculations. This new calibration strategy is presented in the following.

### Efficiency measurements

The  $E_T^{\text{miss}}$  trigger efficiency measurements are carried out in a reference region selected by the single-muon triggers of Table 5.3. In addition, the event selection of this measurement region requires the presence of exactly one offline muon with a  $p_T$  greater than 25 GeV and fulfilling the trigger matching criteria described in Section 5.4.1. The efficiency is calculated for each  $E_T^{\text{miss}}$  trigger according to Equation 5.1. This is done separately for data and MC backgrounds. Only the data-taking periods are considered, in which a given trigger also has been used (c.f. Table 5.2). As the trigger efficiencies are highly topology dependent, it is important that the measurement region is as close to the SR and  $1\mu$ -CR as possible. Therefore, most selection criteria of the SR and  $1\mu$ -CR are also applied in the measurement region, with a few modifications to ensure a sufficiently high data and MC statistics in the trigger turn-on. For this, only the event selection of the resolved region needs to be considered, because in the merged region the triggers are already fully efficiency. Since many requirements are applied in both the SR and  $1\mu$ -CR, the efficiency calibration is performed commonly for both regions. The trigger efficiencies are measured as a function of  $E_T^{\text{miss, no } \mu}$  which is defined as the  $E_T^{\text{miss}}$  obtained by excluding the muon contribution from the  $E_T^{\text{miss}}$  calculation of Equation 4.4. This mimics the online  $E_T^{\text{miss}}$  as measured by the trigger. Since the SR contains no leptons,  $E_T^{\text{miss, no } \mu}$  is identical to  $E_T^{\text{miss}}$ . Therefore, the trigger efficiency measured for a given  $E_T^{\text{miss, no } \mu}$  value in the measurement region resembles the efficiency for the corresponding  $E_T^{\text{miss}}$  value in the SR. For the  $1\mu$ -CR, it corresponds to the efficiency at

the same  $E_T^{\text{miss, no } \mu}$  value.

Furthermore, the  $E_T^{\text{miss}}$  trigger efficiencies depend on the background composition. The dominant backgrounds in the single-muon measurement region are  $t\bar{t}$  and  $W$ +jets processes. If two  $b$ -jets are required, the contribution from  $t\bar{t}$  processes is dominant. On the other hand, if a veto on  $b$ -jets is applied, the region consists almost only of  $W$ +jets events. For one  $b$ -jet, there is approximately an equal contribution from  $t\bar{t}$  and  $W$ +jets. As explained in Section 5.2, the dominant backgrounds in the SR are  $t\bar{t}$ ,  $W$  and  $Z$ +jets processes. Although the latter is negligibly small in the measurement region, its trigger efficiency can still be adequately described by the efficiencies obtained in the measurement region: From Figure 5.3(b) and Figure 5.3(c) one can see, that the production mechanisms as well as the final signature of  $W$  and  $Z$ +jets processes are very similar. The biggest difference is the charged lepton, which is present in  $W$ +jets, but not in  $Z$ +jets events. However, in SR events this charged lepton gets “lost” and thereby contributes to  $E_T^{\text{miss}}$ . Hence, the event kinematics of  $W$  and  $Z$ +jets are expected to be very similar and thus also the trigger efficiencies resulting from them. This has been confirmed by comparing the efficiencies measured for  $W$ +jets events with the efficiency for  $Z(\rightarrow \mu^+\mu^-)$ +jets derived in a dedicated dimuon region. More details on this study can be found in Appendix A.2. This also contains additional information on the the exact event selection in the single-muon measurement region. Treating  $W$  and  $Z$ +jets events as a common process, the background composition in the single-muon measurement region with exactly one  $b$ -jet is thus the closest to the SR, i.e. containing approximately equal parts of  $t\bar{t}$  and  $W/Z$ +jets events. Therefore, the trigger efficiencies are measured in events with one  $b$ -jet. However, other  $b$ -jet multiplicities are considered in the calculation of systematic uncertainties, which is described below.

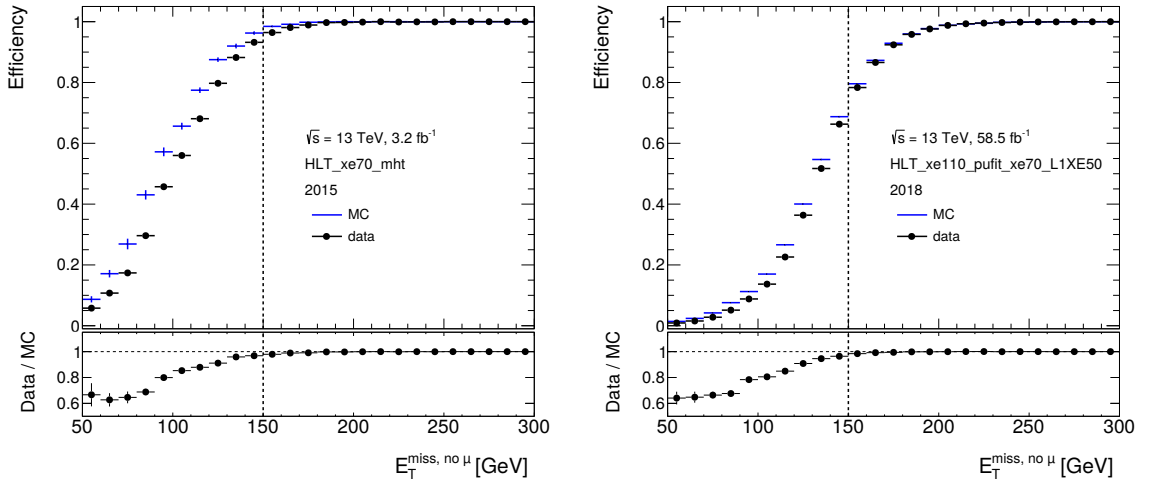


**Figure 5.6:** Trigger efficiencies as a function of the offline  $E_T^{\text{miss, no } \mu}$  measured in data and MC background samples for two representative  $E_T^{\text{miss}}$  triggers. The bottom panels show the ratio of the data and MC efficiencies, i.e. the SF. The efficiencies are derived in a single-muon measurement region. The vertical line at  $E_T^{\text{miss, no } \mu} = 150$  GeV corresponds to the  $E_T^{\text{miss}}$  threshold of the SR, indicating that only the region right from the line is relevant for the analysis.

Figure 5.6 shows the resulting efficiency curves for two representative  $E_T^{\text{miss}}$  triggers. The left plot in Figure 5.6 corresponds to the  $E_T^{\text{miss}}$  trigger used in the 2015 data-taking periods, HLT\_xe70\_mht, the right plot to the trigger used in 2018, HLT\_xe110\_pufit\_L1XE50. Due to the lower HLT threshold, HLT\_xe70\_mht also reaches its efficiency plateau at a lower  $E_T^{\text{miss, no } \mu}$  value than HLT\_xe110\_pufit\_70\_L1XE55.

### Scale factor calculation

As shown in Figure 5.6, the trigger efficiency measured for the SM background processes ( $\varepsilon^{\text{MC}}$ ) does not agree with the efficiency measured in data ( $\varepsilon^{\text{data}}$ ). To correct for this, scale factors (SFs) are used. These are defined by:

$$\text{SF} = \frac{\varepsilon^{\text{data}}}{\varepsilon^{\text{MC}}} . \quad (5.2)$$

The SFs for the two triggers from above are shown in the bottom panels of Figure 5.6. Starting with a minimum value of about 0.6 at  $E_T^{\text{miss, no } \mu} = 50$  GeV, the SFs gradually increase until they eventually reach a maximum at 1. However, at  $E_T^{\text{miss, no } \mu} = 150$  GeV the SFs have not reached yet this plateau. Since the efficiency measured at  $E_T^{\text{miss, no } \mu}$  reflects the efficiency in the SR for  $E_T^{\text{miss}} = 150$  GeV, the MC backgrounds in the low- $E_T^{\text{miss}}$  region of the analysis would be overestimated by a few percent, if no correction is applied. To match the trigger efficiency in data, the background yields in the SR need to be multiplied by the SFs derived in the single-muon region. However, the SFs of Figure 5.6 are evaluated in certain bins, while a physically meaningful SF is expected to have a continuous distribution. Hence, the binned SF measurements need to be fitted with an appropriate fit function. For this, a four-parameter error function is used:

$$f(x) = p_3 \cdot \left[ 1 + \text{erf} \left( \frac{x - p_0}{\sqrt{2}p_1} \right) \right] + p_4 . \quad (5.3)$$

For all  $E_T^{\text{miss}}$  triggers in the analysis, the SFs are measured using  $E_T^{\text{miss, no } \mu}$  bin widths of 10 GeV and are fitted in the range  $E_T^{\text{miss, no } \mu} = [100, 300]$  GeV. The SFs, which need to be applied in the SR and  $1\mu$ -CR, are obtained by evaluating  $f(E_T^{\text{miss, no } \mu})$ . In the case of the SR, this is equivalent to  $f(E_T^{\text{miss}})$ . The results for one representative  $E_T^{\text{miss}}$  trigger are shown in Figure 5.7. The SFs can be successfully described down to about  $E_T^{\text{miss, no } \mu} = 120$  GeV. For lower values the impact of statistical fluctuations becomes more pronounced, so that the SFs for  $100 \text{ GeV} < E_T^{\text{miss, no } \mu} < 120 \text{ GeV}$  are less reliable.

In the SR, the selected signal and background events are kinematically quite similar to each other. Due to that, it can be assumed that the trigger efficiency in signal events is generally the same as for the backgrounds. Hence, the derived SFs are also used to correct the signal predictions.

### Sources of uncertainties

Two different sources of uncertainties are considered in the  $E_T^{\text{miss}}$  trigger calibration. The first one is the statistical uncertainty, which is defined as the  $1\sigma$  uncertainty of the fit. In Figure A.1 this is indicated by the hatched band around the SF curve. The second one is

a systematic uncertainty. It takes into account that the measured SFs may deviate from the *real* SFs in the SR or  $1\mu$ -CR because their background compositions are not completely identical to the one of the measurement region.

To derive the systematic uncertainty, the SFs are calculated for different  $b$ -jet multiplicities. By requiring 0 or  $\geq 2$   $b$ -jets the measurement region is highly enriched in  $W$ +jets and  $t\bar{t}$  events, respectively. The SFs are first measured and fitted for these two selections. Afterwards, the difference to the nominal SF, i.e. the SF measured in events with one  $b$ -jet as described above, is calculated for each of them. For illustration, the three different SF curves for one representative  $E_T^{\text{miss}}$  trigger are shown in Figure 5.8. At each  $E_T^{\text{miss}, \text{no } \mu}$  value, the larger of the two SF differences is taken as the systematic uncertainty, denoted as  $\sigma_{\text{syst}}$ . To be more conservative about the impact of  $\sigma_{\text{syst}}$ , the uncertainty is symmetrised in the analysis, which means that the real SF is assumed to lie within  $\text{SF} \pm 1\sigma_{\text{syst}}$ .

The efficiencies and scale factors measured for the other  $E_T^{\text{miss}}$  triggers in the  $139 \text{ fb}^{-1}$  analysis are shown Section A.3.

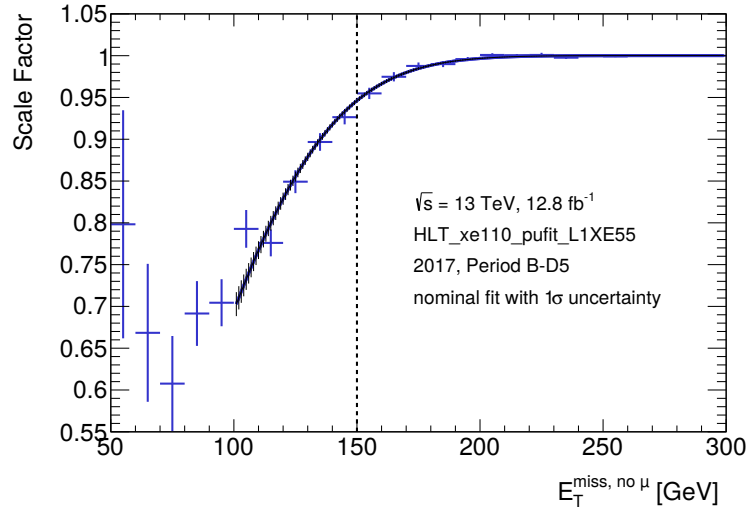


**Figure 5.7:** Measured and fitted trigger SFs for HLT\_xe110\_pufit\_L1XE55. The hatched band indicates the  $1\sigma$  uncertainty of the fit.

## 5.5 Event cleaning

Before  $pp$  collision events can be used for physics analyses, they must fulfil different criteria which ensure, that only events with objects of good quality are selected. This is referred to as *event cleaning*. A first set of criteria is only applied to data:

- The events must be labelled as “being good for physics”. This means that all detector components must have operated sufficiently well to allow the reconstructed physics objects to be of good data quality.

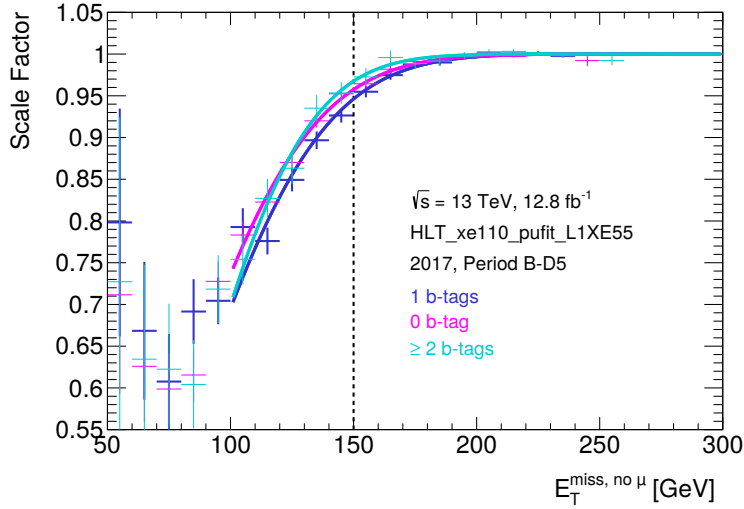


**Figure 5.8:** Measured and fitted trigger SFs for different  $b$ -jet multiplicities. Events with one  $b$ -jet are used to calculate the nominal SFs, while the 0 and  $\geq 2$   $b$ -jet categories are used to derive systematic uncertainties.

- A veto is applied on corrupted events which are caused by problems in the SCT, LAr and tile calorimeter, e.g. from noise bursts. Incomplete events, i.e. events with partially missing detector information, are rejected, too.

The second set of event cleaning requirements is imposed on both data and MC:

- Each event must have a primary vertex as defined in Section 4.1.
- An event is discarded, if it contains one or more muons which are compatible to muons in cosmic rays. A muon is said to have a cosmic ray origin if it has  $|z_0 \sin \theta| > 1$  mm and  $|d_0| > 0.2$  mm.
- Events with a badly measured muon are rejected. This is defined as a muon for which the error on the charge-momentum ( $|q/p|$ ) measurement for the combined muon (c.f. Section 4.7) is larger than 0.4 or, with some tolerance, larger than the values obtained from the ID or MS measurements alone.
- Events containing so-called *bad jets* are vetoed. These can originate from calorimeter noise, cosmic rays or beam induced background. The latter is caused by proton losses upstream the interaction point. Different quality criteria, described in Ref. [181], are applied to remove events with bad jets. They include requirements on the pulse shape in the LAr calorimeters, jet energy ratios and track-based variables. These are only applied on  $R = 0.4$  EMTopo jets (c.f. Section 4.2). No jet cleaning requirements are defined for PFlow and large- $R$  jets.



# Chapter 6

## The $79.8 \text{ fb}^{-1}$ analysis

The variable-radius (VR) track jets and the object based  $E_{\text{T}}^{\text{miss}}$  significance  $\mathcal{S}$ , described in Chapter 4, are novel methods with a great potential to overcome different shortcomings: VR track jets could allow to detect  $h \rightarrow b\bar{b}$  decays even in very boosted regimes, while  $\mathcal{S}$  is a powerful variable to discriminate genuine from fake  $E_{\text{T}}^{\text{miss}}$ . With a final-state signature consisting of a reconstructed  $h \rightarrow b\bar{b}$  decay and  $E_{\text{T}}^{\text{miss}}$ , both the VR track jets and  $\mathcal{S}$  represent promising objects to improve the mono- $h(b\bar{b})$  search. Therefore, they have been implemented and tested within the  $79.8 \text{ fb}^{-1}$  analysis, which is presented in the following.

### 6.1 Object definitions

The analysis uses the physics objects described in Chapter 4. The jet and  $E_{\text{T}}^{\text{miss}}$ -related objects are summarised in Table 6.1. Several selection criteria in the analysis use the so-called *central + forward* jet collection. This sorts the small-R jets by considering first the central and afterwards the forward jets in an event. Within each of the two categories, the jets are ordered by their  $p_{\text{T}}$ . The settings for electrons and muons are summarised in Table 6.2 and Table 6.3, respectively. They are divided into baseline and signal leptons: Looser quality criteria, regarding e.g. the  $p_{\text{T}}$  or the identification WP, are applied to baseline, tighter to signal leptons. Thus, baseline objects provide a larger acceptance, i.e. with them it is more likely to select all leptons produced in the event. On the other hand, signal leptons have a higher purity. This means that the probability for the selected leptons to come from noise or from fakes, for example from a jet misidentified as an electron, is lower for signal than for baseline electrons. Therefore, baseline leptons are generally used for vetoes, like in the SRs, in which a veto on all electrons, muons and  $\tau$ -leptons is applied. For this reason, a loose identification WP is chosen for  $\tau$ -leptons, too. The loose selection allows for a high efficiency of the veto, thereby improving the reduction of backgrounds with real leptons. Also the overlap removal (c.f. Section 4.9) and  $E_{\text{T}}^{\text{miss}}$  calculation is performed using baseline leptons. Signal leptons are typically used when an object is explicitly selected<sup>1</sup>, like in the CRs. Baseline and signal electrons only differ by their  $p_{\text{T}}$  requirements of  $> 7 \text{ GeV}$  and  $> 27 \text{ GeV}$ , respectively, while for muons there are also differences in the identification and isolation criteria. Two definitions for signal muons are used, one for the  $1\mu$ -CR and the other one for the  $2\ell$ -CR. The signal muon requirements are tighter in the  $1\mu$ -CR to suppress processes with non-prompt muons. In these, a muon can originate e.g. from decays of heavy-flavour hadrons inside a jet. Due to the requirement of two same-flavour leptons in the  $2\ell$ -CR, the probability

---

<sup>1</sup>It is important to note, that the term “signal lepton” only refers to a tighter lepton selection. It is not related to the signal regions.

that both originate from fakes or heavy-flavour decays is much smaller than for the single muon in the  $1\mu$ -CR. Hence, a looser object definition may be used than in the  $1\mu$ -CR. This leads to an enhanced acceptance of events in the  $2\ell$ -CR. For the same reason, signal electrons are defined with a rather loose requirement on the identification and isolation.

Object	Kinematic requirements	Identification properties
Small-R jets <i>central</i>	$p_T > 20 \text{ GeV}$ $ \eta  < 2.5$	Type: Anti- $k_t$ $R = 0.4$ EMTopo, JVT $> 0.59$ if $p_T < 120 \text{ GeV}$ and $ \eta  < 2.4$ , JVT $> 0.11$ if $p_T < 120 \text{ GeV}$ and $2.4 <  \eta  < 2.5$ , $b$ -tagging: MV2c10, 77% efficiency, bad-jet cleaning WP: Loose
Small-R jets <i>forward</i>	$p_T > 30 \text{ GeV}$ $2.5 \leq  \eta  < 4.5$	Type: Anti- $k_t$ $R = 0.4$ EMTopo, bad-jet cleaning WP: Loose
Large-R jets	$p_T > 200 \text{ GeV}$ $ \eta  < 2.0$	Type: Anti- $k_t$ $R = 1.0$ LCTopo, trimming: $R_{\text{subjet}} = 0.2$ , $f_{\text{cut}} = 5\%$
VR track jets	$p_T > 10 \text{ GeV}$ $ \eta  < 2.5$	Type: Anti- $k_t$ variable- $R$ track jets, $b$ -tagging: MV2c10, 77% efficiency
$\tau$ -leptons	$p_T > 20 \text{ GeV}$ $ \eta  = [0, 1.37] \text{ or } [1.52, 2.5]$	Type: BDT $\tau$ -leptons identification WP: Loose

**Table 6.1:** Definitions of the jet and  $E_T^{\text{miss}}$ -related objects in the search. Table adapted from Ref. [182].

Electron	$p_T$ [GeV]	$ \eta $	$d_0/\sigma(d_0)$	$ z_0 \sin \theta $ [mm]	Identification	Isolation
baseline	$> 7 \text{ GeV}$	$< 2.47$	$< 5$	$< 0.5$	LooseAndBLayer	LooseTrackOnly /
signal	$> 27 \text{ GeV}$					FCHighPtCaloOnly

**Table 6.2:** Definitions of the baseline and signal electrons in the search. For electrons with  $p_T < 400 \text{ GeV}$  the FCLoose isolation WP is applied, while for higher  $p_T$  the FCHighPtCaloOnly WP is used. Table adapted from Ref. [182].

## 6.2 Event selection

Several event selection criteria are applied to discriminate potential mono- $h(b\bar{b})$  signal events from the SM background. Almost all of them are adopted from the preceding mono- $h(b\bar{b})$  search with  $36.1 \text{ fb}^{-1}$  of collected data [9]. They are initially based on the SM  $Vh(b\bar{b})$  searches of Ref. [183] and Ref. [184]. The motivation behind this is that  $Vh(b\bar{b})$  processes, if  $V$  is a  $Z$ -boson decaying into neutrinos, also leads to a final state with  $E_T^{\text{miss}}$  and a  $h \rightarrow b\bar{b}$  decay. The kinematic properties between  $Vh(b\bar{b})$  processes and mono- $h(b\bar{b})$  signals may otherwise

Muon	$p_T$ [GeV]	$ \eta $	$d_0/\sigma(d_0)$	$ z_0 \sin \theta $ [mm]	Identification	Isolation
baseline	$> 7$ GeV	$< 2.7$	$< 3$	$< 0.5$	Loose	LooseTrackOnly
signal (1 $\mu$ -CR)	$> 25$ GeV	$< 2.5$	$< 3$	$< 0.5$	Medium	FixedCutTightTrackOnly
signal (2 $\ell$ -CR)					Loose	LooseTrackOnly

**Table 6.3:** Definitions of the baseline and signal muons in the search. Table adapted from Ref. [182].

differ, e.g. in the hardness of the  $E_T^{\text{miss}}$  and jet  $p_T$  spectra. Nevertheless, the selection criteria of the SM  $Vh(b\bar{b})$  analysis represent a suitable starting point for the mono- $h(b\bar{b})$  event selection. In the following, the definition and the motivation of the various discriminating variables is described. A summary of the selection criteria is given in Table 6.4.

### 6.2.1 Common selection

As explained in Section 5.1, two different signatures are considered in this work: In the resolved topology the Higgs boson is reconstructed from two  $b$ -tagged small-R jets, while in the merged topology the Higgs boson decay products are collimated in one large-R jet with two  $b$ -tagged track jets associated to it. The resolved and the merged SR share a set of common selection criteria, which are applied after the event cleaning (c.f. Section 5.5). They include following requirements:

- **Lowest unrescaled  $E_T^{\text{miss}}$  trigger**  
SR events are selected with the lowest unrescaled  $E_T^{\text{miss}}$  triggers listed in Table 5.2.
- **Lepton veto**  
The signature in the mono- $h(b\bar{b})$  analysis are final states with  $E_T^{\text{miss}}$  and jets. Therefore, all events with baseline electrons and muons are rejected. Also events containing  $\tau$ -leptons are discarded.
- **Missing transverse momentum**  
Signal events are expected to have a sizeable amount of  $E_T^{\text{miss}}$  from the escaping DM particles. Therefore, the requirement  $E_T^{\text{miss}} > 150$  GeV is imposed.
- **Azimuthal distance between  $E_T^{\text{miss}}$  and jets**  
After the selection criteria above, the resulting dataset comprises a large fraction of multijet events. In these,  $E_T^{\text{miss}}$  can arise from poor jet energy measurements or from semi-leptonic decays inside a jet, so that  $E_T^{\text{miss}}$  is typically close to the corresponding jet. Therefore, to suppress this background,  $E_T^{\text{miss}}$  and the jet are required to have an azimuthal distance  $\Delta\phi(E_T^{\text{miss}}, \mathbf{jet}) > 20^\circ$  (0.345 rad). This cut is applied to the three leading jets of the *central + forward* collection.
- **Azimuthal distance between  $E_T^{\text{miss}}$  and  $p_T^{\text{miss,track}}$**   
Another multijet reduction cut is based on the variable  $p_T^{\text{miss,track}}$  which constitutes a

modified definition of  $E_T^{\text{miss}}$ . Opposed to the  $E_T^{\text{miss}}$  reconstruction (c.f. Section 4.10),  $p_T^{\text{miss,track}}$  does not consider fully calibrated objects. Instead, it is solely calculated from track information. In events with real  $E_T^{\text{miss}}$ , caused e.g. by neutrinos or DM particles,  $E_T^{\text{miss}}$  and  $p_T^{\text{miss,track}}$  should point in the same direction. However, if  $E_T^{\text{miss}}$  is produced due to a mismeasurement of the jet energy in the calorimeter,  $E_T^{\text{miss}}$  will be close to the corresponding jet, while  $p_T^{\text{miss,track}}$  will have no preferred direction. Hence, the requirement  $\Delta\phi(\mathbf{E}_T^{\text{miss}}, \mathbf{p}_T^{\text{miss,track}}) < 90^\circ$  (1.57 rad) is applied.

### 6.2.2 Resolved SR

The resolved SR is restricted to  $E_T^{\text{miss}} < 500$  GeV and requires at least two central  $b$ -tagged small-R jets. Due to the recoil against the DM particles, the jets from the Higgs boson decay are expected to emerge with a relatively high momentum. Additional jets in the event, arising e.g. from initial state radiation, should be rather soft compared to these. Therefore, the Higgs candidate, denoted as  $h_{\text{reco}}$ , is formed by the two  $b$ -jets with the highest  $p_T$ . Apart from that, additional event selection criteria are applied to increase the signal-to-background ratio. The first set of criteria is adopted from the SM  $Vh(b\bar{b})$  search [183, 184]:

- **Leading  $b$ -jet  $p_T$**

In signal events, the  $b$ -jets from the  $h \rightarrow b\bar{b}$  decay are expected to have a fairly high  $p_T$ . Therefore, the leading  $b$ -jet is required to have a  $p_T > 45$  GeV.

- **Scalar  $p_T$  sum of leading jets**

Another requirement is applied on the  $p_T$  of the leading two, respectively three, jets of the *central + forward* jet collection: For events with two jets, the scalar sum of their  $p_T$  must be greater than 120 GeV, while for events with three or more jets, the scalar sum of the leading three jets must be at least 150 GeV. This cut was initially introduced in Run I to remove events, in which the trigger response was mismodelled in simulation.

- **Azimuthal separation between Higgs candidate jets**

The two jets forming  $h_{\text{reco}}$  should be somewhat collimated in signal processes. This is not necessarily the case for the SM backgrounds, like multijet and  $t\bar{t}$  processes. Thus, a cut  $\Delta\phi(\mathbf{j}_1, \mathbf{j}_2) < 140^\circ$  (2.44 rad) is used, where  $\Delta\phi(\mathbf{j}_1, \mathbf{j}_2)$  denotes the azimuthal separation between the two Higgs candidate jets  $j_1$  and  $j_2$ .

- **Azimuthal separation between  $E_T^{\text{miss}}$  and  $h_{\text{reco}}$**

In signal events,  $E_T^{\text{miss}}$  and  $h_{\text{reco}}$  are expected to emerge back-to-back to some extent. Again, this does not necessarily hold for SM backgrounds. Therefore,  $E_T^{\text{miss}}$  and  $h_{\text{reco}}$  are required to have an azimuthal separation  $\Delta\phi(\mathbf{E}_T^{\text{miss}}, \mathbf{h}_{\text{reco}}) > 120^\circ$  (2.09 rad).

After these criteria are applied, the selected events contain a large fraction of  $t\bar{t}$  processes. Therefore, in the course of the 36.1 fb<sup>-1</sup> search additional requirements have been introduced that are particularly designed to reduce this background. A comprehensive description of the underlying optimisation strategy and the motivation for the chosen cut values can be found in Ref. [180]. In the following, a brief summary of these selection criteria is given:

- **Extended  $\tau$ -lepton veto**

The extended  $\tau$ -lepton veto aims to reject events, in which  $\tau$ -leptons failed to be identified. Thereby it helps to reduce the  $t\bar{t}$  as well as other backgrounds with leptons in the final state, e.g.  $W$ +jets or single-top. In these processes, the  $\tau$ -lepton is produced in the decay  $W \rightarrow \tau\nu_\tau$ . Therefore, a veto is applied on events containing one or more  $\tau$ -lepton candidates, which are seeded from small-R jets using the following two conditions: First, the jet must have one to four associated tracks to be similar to the signature from a  $\tau$ -lepton decaying into charged pions (c.f. Section 4.8). Secondly, a jet induced from a  $\tau$ -lepton decay should be close to the corresponding  $\tau$ -neutrino, and thus to  $E_T^{\text{miss}}$ . Hence, a  $\tau$ -lepton candidate  $\tau_{\text{cand.}}$  must fulfil  $\Delta\phi(\tau_{\text{cand.}}, \mathbf{E}_T^{\text{miss}}) < 22.5^\circ$ .

- **$H_T$ -ratio**

In signal events, jets from initial or final state radiation are expected to be rather soft compared to the two jets from the  $h \rightarrow b\bar{b}$  decay. Therefore,  $h_{\text{reco}}$  should be responsible for most of the hadronic activity. A measure for this is  $H_T$ , which is defined as the scalar sum of the  $p_T$  of all small-R jets in the event. On the other hand, in  $t\bar{t}$  decays the top-quark momentum is distributed between the  $b$ -quark and the  $W$ -boson decay products, so that two additional high- $p_T$  jets can originate from the hadronically  $W$ -boson. Therefore, the contribution of  $h_{\text{reco}}$  to  $H_T$  is, on average, smaller for  $t\bar{t}$  than for signal processes. This motivates the  $H_T$ -ratio requirement: The scalar  $p_T$  sum of the leading two jets, which are usually  $h_{\text{reco}}$  in signal events, and of the third leading jet, if present, from the *central + forward* collection should make up the largest fraction of  $H_T$ . For this, a cut value of 0.63 is chosen:

$$\frac{p_T^{j_1} + p_T^{j_2} + p_T^{j_3}}{H_T} > 0.63.$$

- **Angular separation between the Higgs candidate jets**

For signal events, the  $b$ -jets from the Higgs boson decay should be relatively close to each other. However, in  $t\bar{t}$  events the  $b$ -quarks originate from two different particles, the top and the anti-top quark. If the top-quark pair is produced back-to-back, the resulting  $b$ -jets from the two top-quark decays are expected to be on average more separated than the jets from the Higgs boson decay. Therefore, the Higgs candidate jets are required to have an angular distance  $\Delta R(j_1, j_2) < 1.8$ .

- **Veto on additional  $b$ -jets**

Jets from initial or final state radiation are typically induced from gluons or light-flavour quarks. Consequently, signal events should rarely contain a third  $b$ -jet. On the other hand, in  $t\bar{t}$  as well as in single-top processes a third  $b$ -jet occurs more often, because  $W$ -bosons decay with a branching ratio of about 33% into final states with charm-quarks [2]. Similar to  $b$ -hadrons, hadrons from  $c$ -quarks also can lead to secondary vertices. For this reason, a  $c$ -initiated jet is quite often misidentified as a  $b$ -jet. For the 77% WP of the MV2c10 tagger, the probability for a  $c$ -jet to be  $b$ -tagged is about 20% [185]. Therefore, a veto is applied on events that contain three or more  $b$ -jets.

Lastly, the event selection of the resolved SR contains two additional requirements:

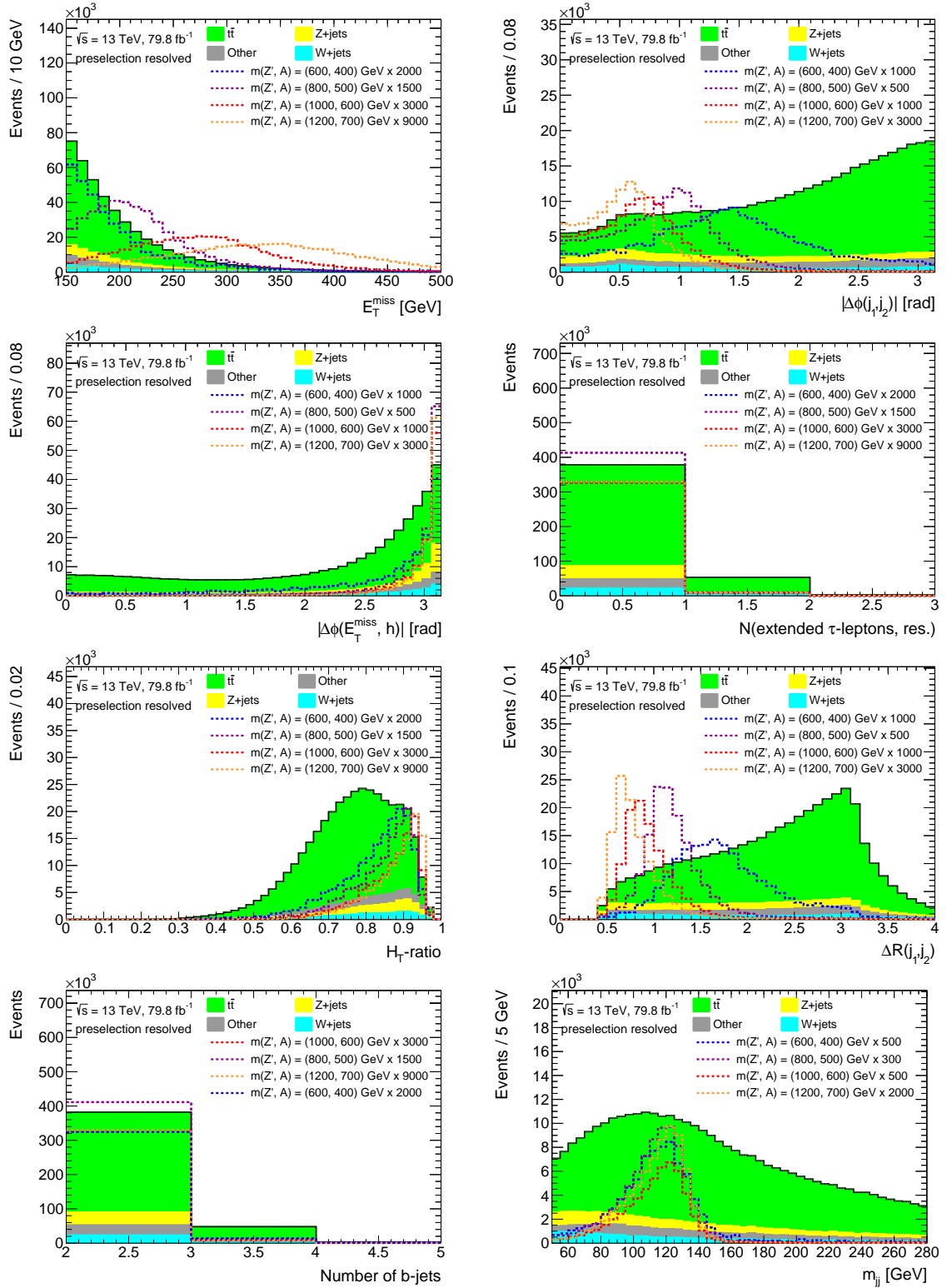


**Figure 6.1:** Preselection distributions of several discriminating variables of the resolved SR, shown for the SM background and four representative  $Z'$ -2HDM signals. For a better visibility, the event yields of the signals are scaled. The associated scale factors are indicated in the plot labels.

- **Higgs candidate mass**

The invariant mass of  $h_{\text{reco}}$  in the resolved region,  $m_{jj}$ , is restricted to values of  $50 \text{ GeV} < m_{jj} < 280 \text{ GeV}$ . While signal events accumulate around  $m_{jj} = 125 \text{ GeV}$ , the Higgs mass sidebands are used to constrain the SM backgrounds in the simultaneous fit, as described in Section 6.4.2. Therefore, a relatively broad  $m_{jj}$  range is chosen.

- **Object-based  $E_{\text{T}}^{\text{miss}}$  significance**

A cut of  $\mathcal{S} > 16$  is introduced to further reduce the multijet background, as explained in Section 6.3.3.

The distribution of the most powerful discriminating variables of the resolved SR are shown in Figure 6.1 for the SM backgrounds as well as for four representative  $Z'$ -2HDM signals of the samples with  $m_H = m_{H^\pm} = 300 \text{ GeV}$ . They are created at a simple preselection level, i.e. with only a few selection criteria applied. That illustrates the initial shape differences between signal and background processes and thus motivates, why cuts on these variables are introduced. Apart from the event cleaning, the  $E_{\text{T}}^{\text{miss}}$  trigger requirement and the lepton veto, the preselection requires the events to have at least two  $b$ -tagged small-R jets,  $E_{\text{T}}^{\text{miss}} > 150 \text{ GeV}$  and  $m_{jj} > 40 \text{ GeV}$ . Two important variables,  $\Delta\phi(\mathbf{E}_{\text{T}}^{\text{miss}}, \mathbf{j}_{1,2,3}^{\text{centr.}+\text{forw.}})$  and  $\mathcal{S}$ , are not included in Figure 6.1. Their impact is discussed in Section 6.3.3.

### 6.2.3 Merged SR

The merged SR targets boosted mono- $h(b\bar{b})$  topologies. Therefore, the event selection requires a sufficiently large  $E_{\text{T}}^{\text{miss}}$  of greater than 500 GeV and the presence of at least one large-R jet, of which the one with the highest  $p_{\text{T}}$  is considered as  $h_{\text{reco}}$ . Furthermore, the leading two associated track jets of  $h_{\text{reco}}$  must be  $b$ -tagged. Three different selection criteria, similar to the ones of the resolved region, are imposed to reduce the remaining  $t\bar{t}$  background:

- **Extended  $\tau$ -lepton veto**

An extended  $\tau$ -lepton veto is applied, in which the  $\tau$ -lepton candidates are reconstructed using the same criteria as in the resolved region. A veto is applied on all events with a  $\tau$ -lepton candidate that lies outside of  $h_{\text{reco}}$ , i.e.  $\Delta R(\tau_{\text{cand.}}, h_{\text{reco}}) > 1.0$ .

- **$H_{\text{T}}$ -ratio**

In the merged region,  $H_{\text{T}}$  is calculated as the scalar  $p_{\text{T}}$  sum of  $h_{\text{reco}}$  and of all small-R jets with  $\Delta R(\text{jet}, h_{\text{reco}}) > 1.0$ . The condition  $\Delta R(\text{jet}, h_{\text{reco}}) > 1.0$  is necessary to avoid a double-counting of objects because, no overlap removal is performed between small-R and large-R jets (c.f. Section 4.9). In signal events, a significant fraction of  $H_{\text{T}}$  should be carried by  $h_{\text{reco}}$ , for which a cut value of 0.43 has been found to be suitable:

$$\frac{p_{\text{T}}^{h_{\text{reco}}}}{H_{\text{T}}} > 0.43 .$$

- **Veto on non-associated  $b$ -tagged track jets**

In  $t\bar{t}$  processes in the merged region,  $h_{\text{reco}}$  usually originates only from one top-quark, involving the production of a  $c$ -quark from the  $W$ -boson decay. The  $b$ -quark from

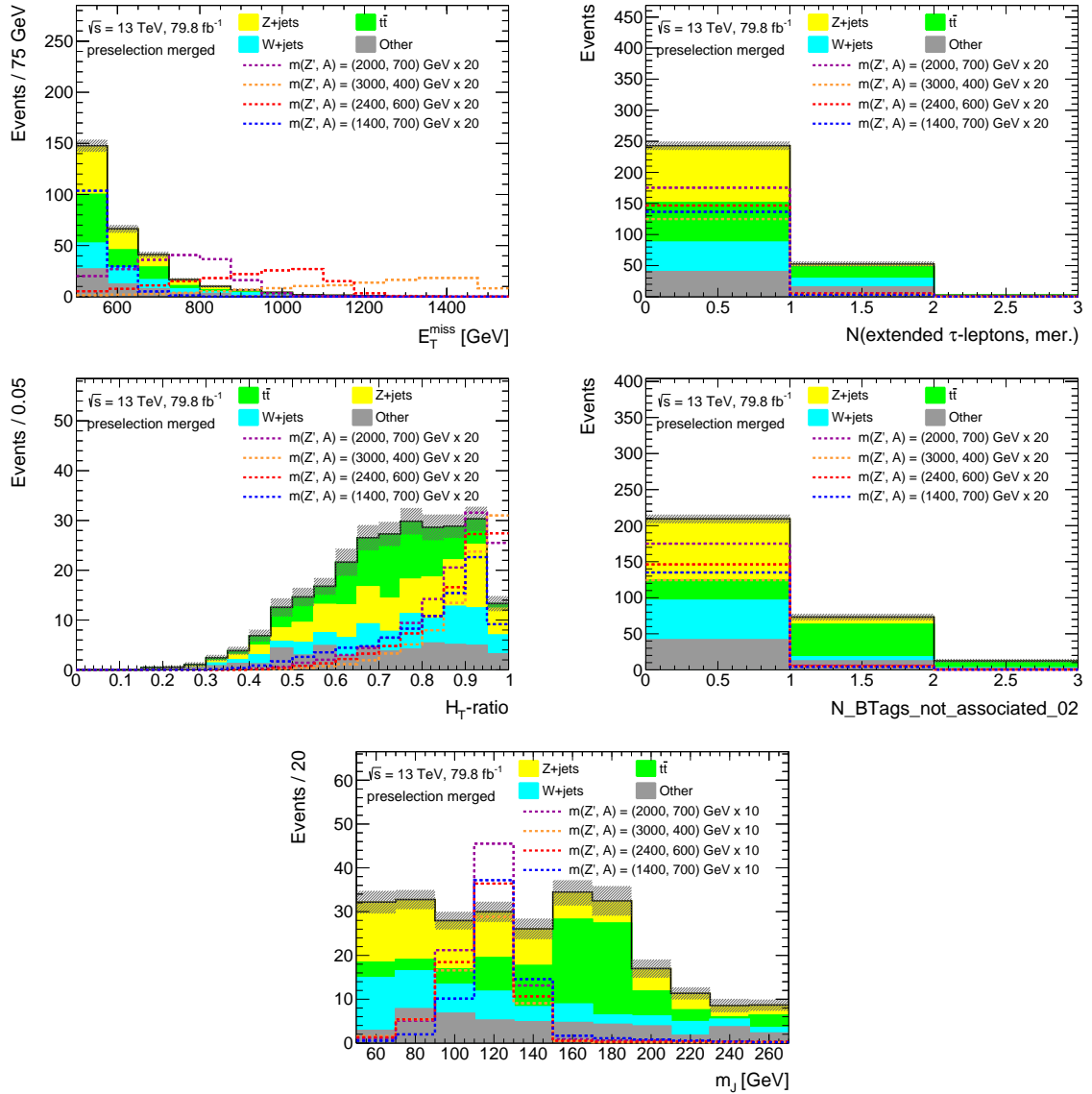


**Figure 6.2:** Preselection distributions of several discriminating variables of the merged SR, shown for the SM background and four representative  $Z'$ -2HDM signals. For a better visibility, the event yields of the signals are scaled. The associated scale factors are indicated in the plot labels.

the other top-quark decay can give rise to a third  $b$ -tagged track jet, which is located outside the Higgs candidate jet, i.e.  $\Delta R(\mathbf{b}, \mathbf{h}_{\text{reco}}) > 1.0$ . Therefore, a veto is applied on all events containing one or more non-associated  $b$ -tagged track jets.

Apart from these, two additional criteria are applied in the merged SR:

- **VR track jet overlap removal**

To avoid ambiguities in the  $b$ -tagging, it is necessary to ensure that the leading two associated track jets,  $\text{VR}_1$  and  $\text{VR}_2$ , are not concentric. Therefore, they are required to be separated by at least  $\Delta R(\mathbf{VR}_1, \mathbf{VR}_2) > R_{\text{min}}$  from each other, in which  $R_{\text{min}}$  denotes the smaller of the two track jet radii.

- **Higgs candidate mass**

The invariant mass of  $h_{\text{reco}}$ ,  $m_J$ , is restricted to values of  $50 \text{ GeV} < m_J < 270 \text{ GeV}$ . This defines the range of the  $m_J$  histogram used in the simultaneous fit. As for the resolved SR, a relatively broad  $m_J$  range is chosen to constrain the SM backgrounds through the Higgs mass sidebands in the simultaneous fit. For  $t\bar{t}$  events, this has a pronounced peak around the top-quark mass at 173 GeV.

Figure 6.2 shows the main discriminating variables of the merged SR for the SM backgrounds as well as four representative  $Z'$ -2HDM signals of the samples with  $m_H = m_{H^\pm} = 300 \text{ GeV}$ . They are shown at a preselection level, which includes the event cleaning criteria, the  $E_{\text{T}}^{\text{miss}}$  trigger requirement and the lepton veto. In addition, the requirements  $E_{\text{T}}^{\text{miss}} > 500 \text{ GeV}$  and  $m_J > 40 \text{ GeV}$  are applied. Furthermore, the two leading associated track jets of  $h_{\text{reco}}$  must be  $b$ -tagged.

## 6.3 Background estimation

The background composition in the resolved and merged SR before the simultaneous fit is shown in Figure 6.3. The three largest backgrounds are  $t\bar{t}$  and  $W/Z$ +jets production, with  $t\bar{t}$  being the dominant background in the resolved and  $Z$ +jets in the merged region. The  $W/Z$ +jets backgrounds are dominated by heavy-flavour processes ( $W/Z$ +HF), while the light-flavour ( $W/Z$ +LF) components have only a minor contribution. Smaller backgrounds in the SR come from single-top, diboson and  $Vh(b\bar{b})$  production. The subleading processes are estimated solely from MC, while the MC predictions for  $t\bar{t}$  and  $W/Z$ +HF are constrained through a simultaneous fit to data (c.f. Section 6.4). To allow for a precise background normalisation, two dedicated CRs,  $1\mu$ -CR and  $2\ell$ -CR, are used. Like in the SR, they are split into a merged and a resolved region. The event selection in the two CRs is adopted from the  $36.1 \text{ fb}^{-1}$  search [9] and is initially based on the CR definitions of the SM  $Vh(b\bar{b})$  search [183, 184]: Since also many SR criteria are taken from there, the background composition in this and the SM  $Vh(b\bar{b})$  search are generally very similar to each other. Therefore, also the background estimation can be performed in a similar way. Figure 6.3 considers all backgrounds except multijet processes because these must be estimated in a fully data-driven way.

In the following, the event selection of the  $1\mu$ -CR and  $2\ell$ -CR is described and the estimation of the multijet background is explained.

Resolved	Merged
lowest unprescaled $E_T^{\text{miss}}$ trigger	
veto on baseline light leptons and $\tau$ -leptons	
$E_T^{\text{miss}} > 150$ GeV	
$\Delta\phi(\mathbf{E}_T^{\text{miss}}, \mathbf{j}_{1,2,3}^{\text{centr.,+forw.}}) > 20^\circ$	
$\Delta\phi(\mathbf{E}_T^{\text{miss}}, \mathbf{p}_T^{\text{miss,track}}) < 90^\circ$	
$E_T^{\text{miss}} < 500$ GeV	$E_T^{\text{miss}} \geq 500$ GeV
$N(b\text{-jets}) \geq 2$	$N(\text{large-R jets}) \geq 1$
$p_T(j_1) > 45$ GeV	VR <sub>1</sub> and VR <sub>2</sub> $b$ -tagged
$\sum_{i=1}^{2(3)} p_T(j_i^{\text{centr.,+forw.}}) > 120$ (150) GeV	—
$\Delta\phi(\mathbf{j}_1, \mathbf{j}_2) < 140^\circ$	—
$\Delta\phi(\mathbf{p}_T, \mathbf{h}_{\text{reco}}) > 120^\circ$	—
$\mathcal{S} > 16$	—
extended $\tau$ -veto, resolved	extended $\tau$ -veto, merged
$N(b\text{-jets}) = 2$	$N(\text{non-associated } b\text{-tagged track jets}) = 0$
$H_T$ -ratio, resolved	$H_T$ -ratio, merged
$\Delta R(\mathbf{j}_1, \mathbf{j}_2) < 1.8$	$\Delta R(\mathbf{VR}_1, \mathbf{VR}_2) > R_{\text{min}}$
$50 \text{ GeV} < m_{jj} < 280$ GeV	$50 \text{ GeV} < m_J < 270$ GeV

**Table 6.4:** Summary of the event selection in the resolved and merged SR. Table adapted from Ref. [180].

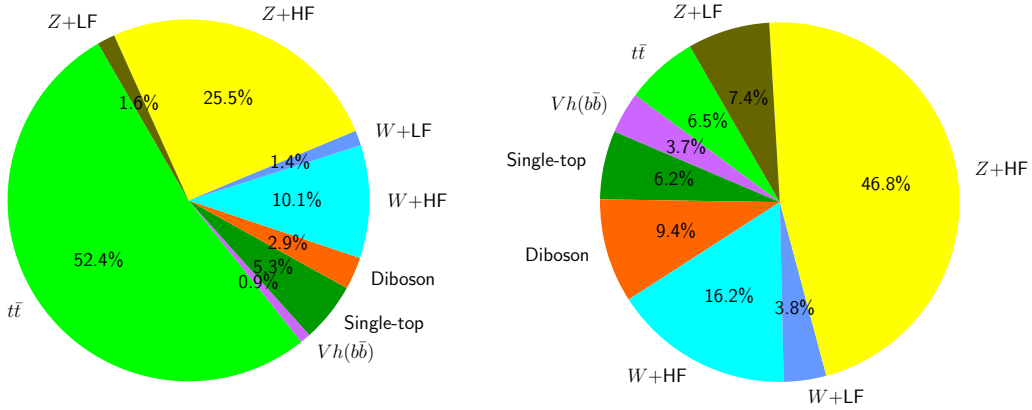


**Figure 6.3:** Background composition in the resolved (left) and merged SR (right) before the simultaneous fit.

### 6.3.1 $1\mu$ -CR

The  $1\mu$ -CR is designed to estimate the  $t\bar{t}$  and  $W$ +jets background. A single-lepton selection is used, because these two processes contribute to the SR mainly through decay modes involving the production of a charged lepton which, however, fails to be identified or falls out of acceptance.

Events in the  $1\mu$ -CR are selected with the same set of  $E_T^{\text{miss}}$  triggers as in the SR. They are required to contain exactly one signal muon and no additional baseline muons. Furthermore, a veto is applied on any baseline electrons and  $\tau$ -leptons. To allow for an event selection which is kinematically as close as possible to the SR, all  $E_T^{\text{miss}}$  and jet-related selections of Table 6.4, except for  $\mathcal{S}$ , are applied in the  $1\mu$ -CR, too. This also includes the extended  $\tau$ -lepton veto. However, for the  $E_T^{\text{miss}}$  and all other  $E_T^{\text{miss}}$ -based cuts, not the standard  $E_T^{\text{miss}}$  is used, but instead  $E_T^{\text{miss, no } \mu}$ . This is the  $E_T^{\text{miss}}$  obtained by removing the muon contributions in the  $E_T^{\text{miss}}$  calculation of Equation 4.4. For example, the SR cut  $E_T^{\text{miss}} > 150$  GeV is replaced by  $E_T^{\text{miss, no } \mu} > 150$  GeV in the  $1\mu$ -CR. Using  $E_T^{\text{miss, no } \mu}$  instead of  $E_T^{\text{miss}}$  allows to better mimic the  $t\bar{t}$  and  $W$ +jets kinematics of SR events in which the charged lepton gets lost and thereby effectively contributes to  $E_T^{\text{miss}}$ .

Figure 6.4 shows the background composition in the  $1\mu$ -CR before the simultaneous fit which demonstrates, that the resulting selection is very pure in  $t\bar{t}$  and  $W$ +jets events.

As practically no leptons are expected from mono- $h(b\bar{b})$  signals, the  $1\mu$ -CR also satisfies the criterium of having a negligible signal contamination. The only possibility for a  $h \rightarrow b\bar{b}$  decay to produce leptons in the final state comes from semileptonic hadron decays. However, since these occur within or in the vicinity of a jet, such leptons typically do not pass the isolation criteria. Other decay modes, such as  $h \rightarrow W^+W^-$ , may also lead to a lepton in the final state, but they generally do not contain two  $b$ -tagged small-R jets, respectively one large-R jet with two associated  $b$ -tagged track jets, with an invariant mass around 125 GeV.

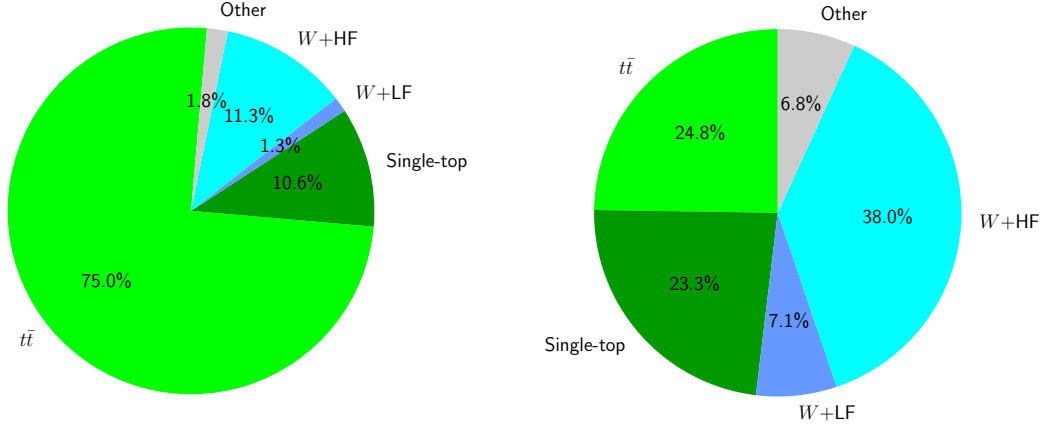


**Figure 6.4:** Background composition in the resolved (left) and merged 1μ-CR (right) before the simultaneous fit.

### 6.3.2 2ℓ-CR

The 2ℓ-CR is used to constrain the  $Z$ +jets background. As the  $Z$ -boson momentum does not depend on its decay modes, one can use  $Z(\rightarrow e^+e^-/\mu^+\mu^-)$ +jets events to estimate the kinematics of  $Z \rightarrow \nu\bar{\nu}$ +jets. In signal events, leptons may only be produced in semi-leptonic hadron decays. Therefore, the requirement of two isolated leptons ensures that the 2ℓ-CR is signal-free. In the 2ℓ-CR, events are initially selected with the single-lepton triggers of Table 5.3. They are required to have exactly two electrons or muons, of which at least one must satisfy the signal-lepton criteria of Table 6.2 or Table 6.3, respectively. To increase the acceptance of  $Z(\rightarrow \ell^+\ell^-)$ +jets events, the second lepton may also only be of baseline quality. Furthermore, the leading signal lepton must pass the trigger-matching criteria described in Section 5.4.1. Due to different reconstruction, identification and trigger requirements, the  $Z(\rightarrow \ell^+\ell^-)$ +jets selection efficiencies in the 2ℓ-CR are not identical to the efficiencies for  $Z \rightarrow \nu\bar{\nu}$ +jets in the SR. However, these differences are in general relatively small, i.e. the associated uncertainties from this are typically smaller than other sources of systematic uncertainties. Thus, no correction for these differences is applied.

After that, a large fraction of the selected events consists of dileptonic  $t\bar{t}$  processes, in which both top-quarks decay as  $t \rightarrow Wb \rightarrow \ell\nu b$ . Therefore, additional selection criteria need to be applied to enhance the  $Z$ +jets purity in the 2ℓ-CR. In  $Z$ +jets events the invariant mass of the lepton pair,  $m_{\ell\ell}$ , is expected to be close to the  $Z$ -boson mass of 91 GeV, which is not necessarily the case for  $t\bar{t}$  events. Hence, the dielectron and dimuon invariant mass is restricted to the range  $83 \text{ GeV} < m_{ee} < 99 \text{ GeV}$  and  $71 \text{ GeV} < m_{\mu\mu} < 106 \text{ GeV}$ , respectively. For dimuon events, a wider mass window is chosen due to momentum resolution effects, which cause a relatively broad  $m_{\mu\mu}$  distribution in the merged region. Additionally, a cut on the event-based  $E_T^{\text{miss}}$  significance, defined as  $E_T^{\text{miss}}/\sqrt{H_T}$  and introduced in Section 4.11, is used in the resolved region to further reduce the  $t\bar{t}$  background. Here,  $H_T$  is defined as the scalar sum of all jet and lepton  $p_T$  in the event. This variable quantifies, how large  $E_T^{\text{miss}}$  is with respect to the total hadronic activity in the event and thus can discriminate genuine from fake  $E_T^{\text{miss}}$ . The former corresponds to the  $E_T^{\text{miss}}$  from e.g. neutrinos or DM particles, while

the latter is caused by e.g. resolution effects and jet mismeasurements. In  $Z(\rightarrow \ell^+\ell^-)+\text{jets}$  events, the resulting  $E_T^{\text{miss}}$  is expected to be mostly fake, while dileptonic  $t\bar{t}$  events contain a considerable amount of genuine  $E_T^{\text{miss}}$  from the two escaping neutrinos. Therefore, the former process lies predominantly at low values of  $E_T^{\text{miss}}/\sqrt{H_T}$ , the latter at higher ones, so that the requirement  $E_T^{\text{miss}}/\sqrt{H_T} < 3.5 \sqrt{\text{GeV}}$  is imposed in the resolved  $2\ell$ -CR. The use of  $E_T^{\text{miss}}/\sqrt{H_T}$  is adopted from the  $2\ell$ -CR criteria of the preceding  $36.1 \text{ fb}^{-1}$  analysis. However, it would also be possible to use  $\mathcal{S}$  instead of this.

Except for the multijet reduction cuts, i.e.  $\mathcal{S}$  and the different requirements on the azimuthal separation of the different objects, all  $E_T^{\text{miss}}$  and jet-related requirements of Table 6.4 are also applied in the  $2\ell$ -CR. In these,  $E_T^{\text{miss}}$  is replaced by  $p_T^{\ell\ell}$  which is defined as the vectorial sum of the two lepton  $p_T$ . This is done to imitate the kinematics of  $Z(\nu\bar{\nu})+\text{jets}$  events in the SR, in which  $E_T^{\text{miss}}$  comes mostly from the two neutrinos.

Using this selection, the  $2\ell$ -CR is very pure in  $Z+\text{jets}$  processes, as shown in Figure 6.5.

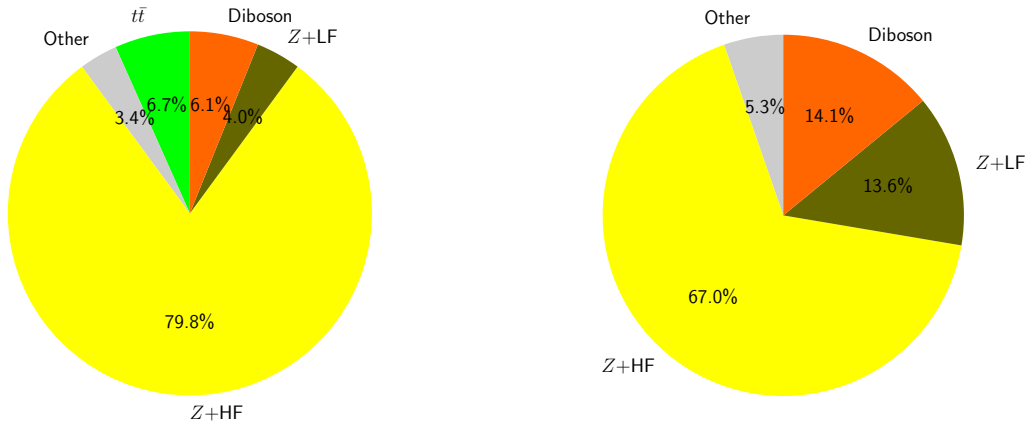


**Figure 6.5:** Background composition in the resolved (left) and merged  $2\ell$ -CR (right) before the simultaneous fit.

### 6.3.3 Multijet background and $E_T^{\text{miss}}$ significance

Multijet processes can mimic a mono- $h(b\bar{b})$  signature if e.g. the jet energies are mismeasured or if neutrinos are produced from semi-leptonic hadron decays. This can lead to a sufficiently large  $E_T^{\text{miss}}$  to pass the trigger and  $E_T^{\text{miss}}$  requirements of the SR. The Higgs boson candidate can originate e.g. from gluon splitting ( $g \rightarrow b\bar{b}$ ). As described in Section 6.2, various selection criteria are applied to suppress the multijet background. Despite that, a small fraction of multijet events may still enter the SR, which makes it necessary to include an estimate for them in the search. However, the higher the applied  $E_T^{\text{miss}}$  cut, the less likely it is that a jet energy mismeasurement or a semi-leptonic hadron decay can produce such a large amount of  $E_T^{\text{miss}}$ . Therefore, the multijet contribution decreases with increasing  $E_T^{\text{miss}}$ . In the mono- $h(b\bar{b})$  search of  $36.1 \text{ fb}^{-1}$ , the multijet background was only estimated for the resolved SR and found to be completely negligible in the merged SR. This is also the case for the  $1\mu$ -CR and  $2\ell$ -CR, in which a lower multijet contamination than in the SR is expected due to the requirement of an isolated lepton. In the following, the multijet estimate is therefore

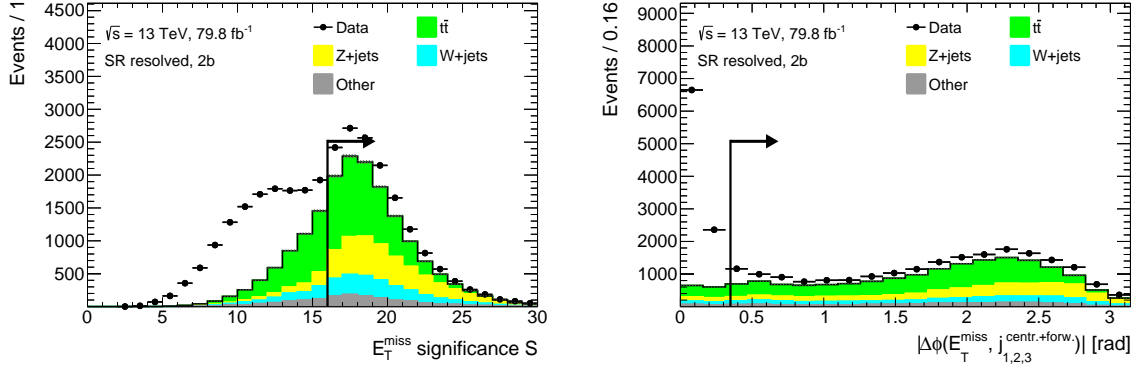


**Figure 6.6:** Distribution of  $\mathcal{S}$  and  $\Delta\phi(\mathbf{E}_T^{\text{miss}}, \mathbf{j}_{1,2,3}^{\text{centr.}+\text{forw.}})$  for data and MC backgrounds after applying the full event selection of the resolved SR, but excluding the cuts on these two variables and blinding the region  $70 \text{ GeV} < m_{jj} < 140 \text{ GeV}$ . The arrow indicates the cut value which otherwise is applied. The strong data-MC offset in the region left from the arrow is caused by the multijet background. Right from the arrow, there is still a small data-MC offset which comes from a mismodelling issue in SHERPA v2.2 affecting the production of  $Z$ +jets with  $b$  and  $c$ -hadrons.

only performed for the resolved SR.

To further reduce the multijet background in the resolved SR, a cut on the object-based  $E_T^{\text{miss}}$  significance  $\mathcal{S}$  is introduced. As explained in Section 4.11, this novel variable is designed to discriminate genuine from fake  $E_T^{\text{miss}}$ . High values of  $\mathcal{S}$  indicate genuine, low values fake  $E_T^{\text{miss}}$ . Therefore, the multijet background predominantly resides at low values of this variable, in contrast to other SM backgrounds with real  $E_T^{\text{miss}}$ , e.g.  $Z(\rightarrow \nu\bar{\nu})$ +jets. This is illustrated in the left plot of Figure 6.6, which shows the distribution of  $\mathcal{S}$  before the simultaneous fit. It is obtained by applying the selection criteria of the resolved SR (c.f. Table 6.4), but excluding the cuts on  $\mathcal{S}$  and  $\Delta\phi(\mathbf{E}_T^{\text{miss}}, \mathbf{j}_{1,2,3}^{\text{centr.}+\text{forw.}})$ , which are the two most powerful multijet reduction variables of the analysis. Furthermore, to avoid effects from a potential mono- $h(b\bar{b})$  signal in data, the region around the Higgs mass window is *blinded*, i.e. events with  $70 \text{ GeV} < m_{jj} < 140 \text{ GeV}$  are not considered. The right plot in Figure 6.6 shows the distribution of  $\Delta\phi(\mathbf{E}_T^{\text{miss}}, \mathbf{j}_{1,2,3}^{\text{centr.}+\text{forw.}})$  for the same selection. In both plots, there is a clear data-MC offset in the left-hand side caused by the multijet background. This demonstrates that with the chosen cut values for  $\mathcal{S}$  and  $\Delta\phi(\mathbf{E}_T^{\text{miss}}, \mathbf{j}_{1,2,3}^{\text{centr.}+\text{forw.}})$  the multijet background can efficiently be suppressed.

However, it is still necessary to investigate, whether there is a remaining multijet contribution in the SR. As mentioned in Section 5.2, it is difficult to properly model multijet processes in MC, hence they need to be estimated in a data-driven way. A commonly used technique is the so-called ABCD method. In this, the multijet contamination is determined via an extrapolation strategy based on four different regions. These differ between each other in their multijet requirements and are labelled as A, B, C and D. Region D represents the SR, while region A constitutes a multijet-enriched CR. The ABCD method developed for the mono- $h(b\bar{b})$  search is illustrated in Figure 6.7. Region A is defined by inverting the two most powerful multijet reduction criteria, namely the cuts on  $\Delta\phi(\mathbf{E}_T^{\text{miss}}, \mathbf{j}_{1,2,3}^{\text{centr.}+\text{forw.}})$  and  $\mathcal{S}$ . With this, region B and C are obtained by inverting only the cut on  $\Delta\phi(\mathbf{E}_T^{\text{miss}}, \mathbf{j}_{1,2,3}^{\text{centr.}+\text{forw.}})$  and  $\mathcal{S}$ ,

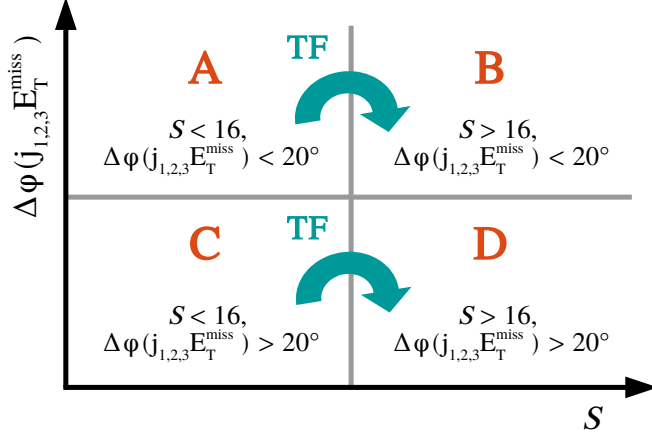


**Figure 6.7:** Illustration of the ABCD method used in the mono- $h(b\bar{b})$  search.

respectively. The ABCD method works as follows: First, the multijet contamination in A, B and C are estimated by taking the difference of data and the MC backgrounds. This is done separately for each of the three different  $E_T^{\text{miss}}$  bins  $E_T^{\text{miss}} = [150, 200, 350, 500]$  GeV of the resolved region, as introduced in Section 5.1. The resulting multijet yields for the  $i$ -th  $E_T^{\text{miss}}$  bin are denoted by  $N_A^i$ ,  $N_B^i$  and  $N_C^i$ , with  $i = 1, 2, 3$ . Afterwards, a transfer factor is calculated which accounts for the efficiency of the  $\Delta\phi(\mathbf{E}_T^{\text{miss}}, \mathbf{j}_{1,2,3}^{\text{centr.}+\text{forw.}})$  cut:

$$\text{TF}^i = \frac{N_B^i}{N_A^i}. \quad (6.1)$$

Finally, the estimated multijet yields of region C are scaled with their associated  $\text{TF}^i$  to obtain the number of multijet events in  $i$ -th  $E_T^{\text{miss}}$  bin:

$$N_A^i = \text{TF}^i \times N_C^i. \quad (6.2)$$

To avoid a distortion of the results from a potential mono- $h(b\bar{b})$  signal, events in the Higgs mass window ( $70 \text{ GeV} < m_{jj} < 140 \text{ GeV}$ ) are not included in the multijet estimate.

With this method, the estimated yields for the multijet background in the three different  $E_T^{\text{miss}}$  bins were found to be substantially smaller than the statistical uncertainty of the data [49, 182] (calculated as the square root of the number of the data events). As an additional check, the estimated multijet background was implemented in the simultaneous fit using a 100% uncertainty. Also after the fit, the contribution was much smaller than the data statistical uncertainty [182]. Therefore, the multijet background can safely be neglected in the further course of the analysis.

## 6.4 Statistical analysis

This section describes the statistical evaluation of the mono- $h(b\bar{b})$  analysis, which is performed with a binned likelihood binned. First, an introduction to the mathematical concepts is given, which follows closely Ref. [186]. After that, the fit setup of the analysis is explained.

### 6.4.1 Mathematical concepts

For the interpretation of the search results, a simultaneous fit of the data and MC predictions is performed in all SRs and CRs. The underlying methods of the fit are based on frequentist statistics. In this, the probability to observe a certain outcome of an experiment is defined as its relative frequency in the limit  $N \rightarrow \infty$ , where  $N$  denotes the number of experiments. These must be repeatable and carried out under identical conditions [187].

#### The likelihood

The level of agreement, or also disagreement, of the observed data with respect to a given model is quantified using hypothesis tests. These are performed by evaluating a likelihood which describes the statistical model of the analysis, i.e. the signal and background predictions in the different SRs and CRs as well as the corresponding uncertainties. To ensure a correct statistical evaluation of the analysis, a necessary condition is that the events of the several regions are disjoint, which means that a certain event can only be contained in one of the two regions. For example, an event of the resolved SR must not be in the merged SR or in a CR. In this work, the HISTFACTORY [188] package is used to build the likelihood and its associated probability density function (p.d.f.). The parameters of the p.d.f. are adjusted during the fit. The p.d.f. contains *normalisation factors* which are used to scale the background processes. Thereby potential mismodelling effects in simulations can be corrected. Both the signal and background predictions are affected by so-called *nuisance parameters*. These describe the impact of systematic uncertainties. A single nuisance parameter can affect the overall normalisation of an observable, i.e. change the event yield by a constant scale factor, distort the shape of the kinematic variables, or also both at the same time. The nuisance parameters are included as priors in the fit and are initially determined from auxiliary measurements. For example, the uncertainties associated to the  $E_T^{\text{miss}}$  trigger efficiency calibration are already determined before the fit.

As explained in Section 5.1, the fit used in this work is a so-called *shape fit*. In this, the SRs and CRs are divided (*binned*) in ranges of some variables which show a characteristic shape for certain signal or background processes, thereby helping to discriminate them from other processes. For example,  $m_h$  has a clear peak around 125 GeV for signal events, while for the SM background it is generally broader. The variable used for the shape fit is measured in a histogram of  $N$  bins. The content of each bin is assumed to follow a Poisson probability distribution:

$$P(n_j | \mu s_j + b_j) = \frac{(\mu s_j + b_j)^{n_j}}{n_j!} e^{-(\mu s_j + b_j)}, \quad (6.3)$$

which describes the probability to observe  $n_j$  events in bin  $j$  given a Poisson probability function with an expectation value  $\nu_j = \mu s_j + b_j$ . Here,  $s_j$  and  $b_j$  are the expected number of signal and background events in bin  $j$ , which are a function of their associated normalisation factors and nuisance parameters. The parameter  $\mu$  denotes the signal strength. This is the *parameter of interest* in the analysis which is tested in the hypothesis test. A value of  $\mu = 0$  corresponds to the background-only hypothesis, which postulates the absence of a signal, while a value of 1 represents the nominal signal expectation of the signal+background hypothesis.

The nuisance parameters are modelled with Gaussian distributions:

$$G(\alpha) = \frac{1}{\sqrt{2\pi}} e^{-\left(\frac{\alpha-\alpha^0}{2}\right)^2}, \quad (6.4)$$

where  $\alpha$  denotes a nuisance parameter in the search. In the fit,  $\alpha$  can be varied around  $\alpha^0$ , which is the central value of the corresponding auxiliary measurement. To construct the p.d.f. for any combination of nuisance parameter values, HISTFACTORY uses various interpolation and extrapolation algorithms, which are further described in Ref. [188].

With the two equations from above, the likelihood is obtained by:

$$L(\mu, \boldsymbol{\eta}, \boldsymbol{\alpha}) = \prod_{j=1}^N P(n_j | \nu_j(\mu, \boldsymbol{\eta}, \boldsymbol{\alpha})) \prod_{k=1}^M G(\alpha_k). \quad (6.5)$$

Here, the first product runs over all  $N$  bins of the analysis, including all bins of the SRs as well as the CRs, and the second product over all  $M$  nuisance parameters. The parameters  $\boldsymbol{\eta}$  and  $\boldsymbol{\alpha}$  describe the sets of normalisation factors and nuisance parameters used in the analysis, with  $\boldsymbol{\alpha} = (\alpha_1, \dots, \alpha_M)$ . The final likelihood built by HISTFACTORY also considers the statistical uncertainty of the MC samples as well as the luminosity uncertainty. In the following, the statistical uncertainties, the luminosity uncertainty,  $\boldsymbol{\eta}$  and  $\boldsymbol{\alpha}$  are collectively denoted by  $\boldsymbol{\theta}$ . The p.d.f. built by HISTFACTORY is equivalent to  $L(\mu, \boldsymbol{\theta})$ , if the observed data is assumed to be fixed.

### Hypothesis testing

A certain value of  $\mu$  is tested using a profile likelihood ratio  $\lambda(\mu)$  as test statistic [186], which is defined by:

$$\lambda(\mu) = \frac{L(\mu, \hat{\boldsymbol{\theta}})}{L(\hat{\mu}, \hat{\boldsymbol{\theta}})}. \quad (6.6)$$

In the numerator,  $\hat{\boldsymbol{\theta}}$  is the value of  $\boldsymbol{\theta}$  which maximises  $L(\mu, \boldsymbol{\theta})$  for the given value of  $\mu$ . In the denominator,  $\hat{\mu}$  and  $\hat{\boldsymbol{\theta}}$  are the estimators of  $\mu$  and  $\boldsymbol{\theta}$  for which  $L(\mu, \boldsymbol{\theta})$  is maximal. By definition,  $\lambda(\mu)$  can only range from 0 to 1. Values close to 1 indicate a good agreement of the observed data with the hypothesised  $\mu$ . Usually, this is expressed by  $-2 \ln \lambda(\mu)$ , where higher values imply a worse compatibility between the data and  $\mu$ . Due to  $\boldsymbol{\theta}$ , the distribution of  $\lambda(\mu)$  as a function of  $\mu$  is broader than if all parameters were fixed. This demonstrates how the systematic uncertainties lead to a loss of information about  $\mu$ . Hence, it is desirable to keep the uncertainties in the analysis as small as possible.

The exact form of the test statistic depends on the use case. For example, if the observed data shows an excess over the SM background expectations, one would want to quantify, how significant this excess is. For that, a hypothesis test performed in which the background-only predictions constitute the null hypothesis. This is tested against the alternative hypothesis, which postulates the signal+background model. To claim the discovery of a positive signal, it is necessary to reject the background-only hypothesis. The associated test statistic of this

test is given by:

$$q_0 = \begin{cases} -2 \ln \lambda(0) & \hat{\mu} \geq 0. \\ 0 & \hat{\mu} < 0. \end{cases} \quad (6.7)$$

Here, two separate definitions of the test statistic  $q_0$  are used depending on whether  $\hat{\mu}$  is greater or smaller than zero. The reason for this is the following: The studied signal processes in the mono- $h(bb)$  search may lead, if they exist, only to an increase in the SR event yields compared to the background-only expectations, but their presence cannot reduce the total yield<sup>1</sup>. Therefore, an under-fluctuation of the data should not be used to reject the background-only hypothesis, so that  $q_0$  is fixed to 0 for  $\hat{\mu} < 0$ .

On the other hand, if the observed data is in good agreement with the SM background predictions, certain signal models can be excluded and *upper limits* can be set on the signal strength  $\mu$ . In this kind of test the null and alternative hypothesis need to be swapped, i.e. the signal+background hypothesis must be rejected in favour of the background-only hypothesis. Similarly to  $q_0$ , observing more events as predicted by the signal+background model should not be regarded as an indication against this hypothesis. Therefore, the corresponding test statistic is defined by:

$$q_\mu = \begin{cases} -2 \ln \lambda(\mu) & \hat{\mu} \leq \mu. \\ 0 & \hat{\mu} > \mu. \end{cases} \quad (6.8)$$

After the calculation of the test statistic,  $p$ -values are used to quantify the discovery or exclusion sensitivity of the performed hypothesis test. The  $p$ -value gives the probability of obtaining a result that has an equal or greater incompatibility with the tested hypothesis than the observed data. A given hypothesis is considered to be excluded, if the  $p$ -value lies below a specified threshold. For the two test statistics from above, the  $p$ -value is computed by:

$$p_0 = \int_{q_{0,\text{obs}}}^{\infty} f(q_0|0) dq_0, \quad p_\mu = \int_{q_{\mu,\text{obs}}}^{\infty} f(q_\mu|\mu) dq_\mu, \quad (6.9)$$

where  $f(q_0|0)$  and  $f(q_\mu|\mu)$  denote the p.d.f of the associated test statistic under the assumption of the background-only or signal+background hypothesis, respectively, and  $q_{0,\text{obs}}$  and  $q_{\mu,\text{obs}}$  are the observed values of  $q_0$  and  $q_\mu$ . The  $p$ -value is usually expressed through the significance  $Z$  in units of Gaussian standard deviations  $\sigma$ . It is obtained from the  $p$ -value by:

$$Z = \Phi^{-1}(1 - p), \quad (6.10)$$

where  $\Phi^{-1}$  denotes the quantile of the standard Gaussian. In the particle physics community, the *observation* of a positive signal is regarded as a discovery if  $Z \geq 5\sigma$ , corresponding to  $p_0 \leq 2.9 \times 10^{-7}$ . With  $3\sigma$  it is commonly considered as *evidence*. For the *exclusion* of a signal model it is common to use a threshold of  $p_\mu = 0.05$  ( $Z = 1.64 \sigma$ ), which is thus called the 95% confidence level (CL). As the exclusion test is based on the evaluation of

<sup>1</sup>A reduction of the total event yields with respect to the background-only expectations may be possible e.g. in experiments involving oscillation and interference effects.

the signal+background hypothesis, this is also referred to as the  $CL_{s+b}$  method and the associated  $p_\mu$  is denoted by  $p_{s+b}$ .

One distinguishes between observed and expected limits. The observed limit corresponds to the test results using the actually observed data, while the expected limit is defined as the limit which would be obtained from the statistical test, if the observed data is equal to the SM background expectations.

### The $CL_s$ method

Using the  $CL_{s+b}$  method can be problematic, if the expected signal yield is very small. If  $s+b \approx b$ , the signal+background and background-only models are practically indistinguishable. In principle, the analysis should not be sensitive to such signal models. However, an under-fluctuation of the data could lead to a small enough value for  $p_{s+b}$ , so that the signal gets falsely excluded. To prevent the exclusion of models which the analysis is not sensitive to, the  $CL_s$  [189, 190] method was established. This method takes into account both  $p_{s+b}$  and  $p_b$ . The latter denotes the  $p$ -value for the alternative, i.e. background-only hypothesis of the exclusion test:

$$p_b = \int_{-\infty}^{q_{\mu, \text{obs.}}} f(q_\mu | \mu) dq_\mu. \quad (6.11)$$

With  $p_{s+b}$  and  $p_b$ , the  $CL_s$  value is calculated by:

$$CL_s = \frac{p_{s+b}}{1 - p_b}. \quad (6.12)$$

As for  $CL_{s+b}$ , a signal is considered as excluded if  $CL_s \leq 0.05$ . With the above definition, the  $CL_s$  method represents a more conservative approach for the significance calculation than the  $CL_{s+b}$  value: If  $p_{s+b}$  is small, then  $p_b$  will have a large value. The denominator in Equation 6.12 will, in turn, be small, leading to a  $CL_s$  value of close to 1. Therefore, this will prevent the false exclusion of a signal in the case of a small  $p_{s+b}$ . On the other hand, if  $p_{s+b}$  is large,  $p_b$  will be small. Hence,  $CL_s \approx p_{s+b}$ , so that in this case the  $CL_s$  and  $CL_{s+b}$  methods lead to consistent results. Therefore, instead of  $CL_{s+b}$ , the  $CL_s$  method is used for the interpretation of the mono- $h(b\bar{b})$  search results.

### 6.4.2 Fit setup of the analysis

The fit setup of this analysis is based on the fit of the preceding  $36.1 \text{ fb}^{-1}$  analysis, from which e.g. the choice of the normalisation factors as well as the different fit variables and their binning is adopted. This is presented in the following.

Besides the signal strength  $\mu$ , the statistical model contains three additional floating parameters to constrain the normalisation of the  $t\bar{t}$ ,  $W$ +HF and  $Z$ +HF backgrounds.

As described in Section 5.1, an  $E_T^{\text{miss}}$  binning is applied in the SRs because the mono- $h(b\bar{b})$  signals can be differently boosted. The resolved region is split into three  $E_T^{\text{miss}}$  bins in the ranges  $E_T^{\text{miss}} = [150, 200, 350, 500]$  GeV, while for the merged region a single bin with  $E_T^{\text{miss}} > 500$  GeV is used. The same binning is also applied to the CRs, but instead of  $E_T^{\text{miss}}$ , the corresponding  $E_T^{\text{miss}}$  proxy is used, which is  $E_T^{\text{miss, no } \mu}$  in the  $1\mu$ -CR and  $p_T^{\ell\ell}$  in the  $2\ell$ -CR.

The fit variable in the SR is the Higgs candidate mass  $m_h$ , i.e.  $m_{jj}$  and  $m_J$ , which is fitted in the range 50 – 280 GeV in the resolved and 50 – 270 GeV in the merged region. Signal events accumulate near the Higgs boson mass in the range of approximately 70 GeV <  $m_h$  < 140 GeV. On the other hand,  $W/Z$ +HF and  $t\bar{t}$  processes have a much broader  $m_h$  distribution. Therefore, choosing this relatively wide fit range helps to further constrain the dominant SM backgrounds. This means that the Higgs mass sidebands of  $m_h < 70$  GeV and  $m_h > 140$  GeV effectively act as additional control regions.

A bin width of 5 GeV is used for the  $m_h$  histograms in the two lowest  $E_T^{\text{miss}}$  bins. As the data and MC background statistics decrease with increasing  $E_T^{\text{miss}}$ , a broader bin width needs to be chosen in the high- $E_T^{\text{miss}}$  regions to avoid large statistical fluctuations. This, in turn, allows for a more reliable and stable background estimation. Therefore, in the  $E_T^{\text{miss}}$  bin of 350 – 500 GeV and in the merged SR, a  $m_h$  bin width of 10 GeV and 20 GeV is used, respectively. In the 1 $\mu$ -CR, the muon charge is used as fit variable. As the  $t\bar{t}$  and  $W$ +jets backgrounds are simultaneously estimated in this region, a fit in the muon charge helps to distinguish between these two processes: In  $t\bar{t}$  events the muons will on average be equally positively and negatively charged, because the top and the anti-top quark have the same probability of decaying into leptons or hadrons. On the other hand, in  $W$ +jets events the muon will predominantly be positively charged since the LHC is a  $pp$  collider, so that it is more likely that a given reaction will produce a positively than a negatively charged final state. In the 2 $\ell$ -CR no particular fit variable is used. Instead, only the event yields in the different  $E_T^{\text{miss}}$  ranges are fitted.

The  $E_T^{\text{miss}}$  bins and fit variables in the different regions are summarised in Table 6.8.

	<b>0 lepton</b>	<b>1 muon</b>	<b>2 leptons</b>
Region	SR	$t\bar{t}$ and $W$ +jets CR	$Z$ +jets CR
$E_T^{\text{miss}}$ or $E_T^{\text{miss}}$ proxy	$E_T^{\text{miss}}$	$E_T^{\text{miss, no } \mu}$	$p_T^{\ell\ell}$
	Resolved: [150,200), [200,350) and [350,500) GeV Merged: Larger than 500 GeV		
Fit variable in each $E_T^{\text{miss}}$ bin	$m_h$	muon charge	Event yield

**Figure 6.8:** Summary of the fit variables and  $E_T^{\text{miss}}$ -proxy ranges used in the analysis. Table taken from Ref. [49].

### Pruning and smoothing of nuisance parameters

To improve the fit stability, the histograms of most of the nuisance parameters in the search are subjected to a smoothing procedure. The applied smoothing algorithm performs an iterative modification of the bin contents in the histograms until they become monotonic in the fitted variable. Moreover, to save computation time and to further stabilise the fit, nuisance parameters with a negligibly small impact on the sensitivity are removed from the fit setup. For this, a pruning threshold of 0.5% is chosen, which means that a nuisance parameter is discarded, if the yield difference of the systematic and the nominal histograms of a given fit variable is less than 0.5% in every bin.

The systematic uncertainties, which are considered as nuisance parameters in the fit, are described in the following section.

## 6.5 Uncertainties

The analysis is affected by various sources of uncertainties coming from the normalisation factors, the MC statistics of the simulated samples and from systematic uncertainties. The latter are categorized into experimental and theory uncertainties. Experimental uncertainties originate from detector effects and the reconstruction, identification and calibration of the various physics objects described in Chapter 4. Theory uncertainties are related to the MC predictions for the signal and background samples used in the analysis.

### 6.5.1 Experimental uncertainties

The dominant experimental uncertainties come from the calibration of the  $b$ -tagging efficiency, the jets and the luminosity measurements. As explained in Section 3.2.6, the integrated luminosity is determined through van-der-Meer scans. These are calibrated with the techniques described in Ref. [81], resulting in a luminosity uncertainty of 2% for the years 2015-2017. The  $b$ -tagging uncertainties arise mostly from the calibration of the  $b$ -jet tagging efficiency, while the uncertainties on the  $c$ -jet tagging and the mis-tag rate only have a minor impact. For VR track jets, a significant uncertainty comes from the high- $p_T$  extrapolation described in Section 4.5. The dominant uncertainties associated to small-R and large-R jets come from the jet energy scale and resolution (JES and JER). For these, a strongly reduced set of systematic uncertainties is used, in which several uncertainty sources are combined into only three JES and a single JER nuisance parameters [191]. This is computationally less expensive and reduces the complexity of the statistical model. However, the disadvantage of this representation is, that correlation effects between the different uncertainty sources are worse modelled than if considering them independently.

Other important experimental uncertainties come from the  $E_T^{\text{miss}}$  soft-term resolution and scale as well as from the  $E_T^{\text{miss}}$  trigger efficiency calibration presented in Section 5.4.3. Sources of uncertainties, which have a minor impact on the analysis, come from the lepton identification, energy and momentum scales, the single-electron and muon trigger efficiencies and from pile-up reweighting. The impact of this is evaluated by varying the corresponding pile-up reweighting factors by 4%.

### 6.5.2 Theory uncertainties

Possible sources of theory uncertainties are e.g. missing higher-order terms in the calculation of the matrix element, the choice of the generator, PDF and the parametrisation of the parton shower and hadronisation. The theory uncertainties can affect the overall normalisation of a MC sample or its shape. Shape uncertainties need to be evaluated for the fit variables of the search to account for possible bin-to-bin migrations: This means that a systematic variation may change the event kinematics such that an event, which is in a certain bin in the nominal histogram, falls into another bin in the systematic histogram. The applied background uncertainties as well as their treatment in the fit are mostly adopted from the SM  $Vh(b\bar{b})$  search of  $36.1 \text{ fb}^{-1}$  [184]. In the following, a brief summary of their implementation in this analysis is given.

As the normalisation of  $t\bar{t}$  and  $W/Z+\text{HF}$  processes is constrained during the fit, no

uncertainties on their overall normalisation are included. However, uncertainties on the relative normalisation of  $W/Z$ +HF are applied which allow the  $bb$ ,  $bc$ ,  $bl$  and  $cc$  fractions of the total  $W/Z$ +HF backgrounds to float by up to 20%. For  $Z$ +HF, this uncertainty is applied separately for the SR and the  $2\ell$ -CR. An additional uncertainty of 20% is included which accounts for differences between the  $Z$ +HF normalisation in the SR and  $2\ell$ -CR. Moreover, uncertainties of 30% and 10% are used for the  $cl$  and  $ll$  components of  $W/Z$ +jets, respectively. These numbers were derived from data-MC comparisons in events with zero  $b$ -tagged jets [192]. For single-top processes, an uncertainty of 4.6% is applied to  $s$ -channel, 4.4% to  $t$ -channel and 6.2% to  $Wt$ -associated production [184]. The diboson normalisation uncertainties amount to 25%, 26% and 20% for  $WW$ ,  $WZ$  and  $ZZ$  production, respectively. For  $Vh(bb)$  processes, a normalisation uncertainty of 30% is used. This value is chosen based on the measurement uncertainties of the latest results of the  $Vh(bb)$  search, in which the dataset of 79.8 fb<sup>-1</sup> was analysed [193]. Shape uncertainties are included for all SM background processes, except for  $Vh(bb)$  production. These consider differences in the  $m_h$ ,  $E_T^{\text{miss}}$  and  $E_T^{\text{miss}}$  proxy distributions in the SR and CRs and are derived following the strategy of the  $Vh(bb)$  search [184].

Instead of uncertainties on the shape or overall normalisation, relative acceptance uncertainties on the  $E_T^{\text{miss}}$  distributions are calculated for the  $Z'$ -2HDM signals. They describe the fact that  $E_T^{\text{miss}}$  shape differences can alter the normalisation across the different bins. The values applied are adopted from the preceding 36.1 fb<sup>-1</sup> mono- $h(bb)$  search [9, 180].

### 6.5.3 Breakdown of dominant uncertainties

The dominant uncertainties in the search are summarised in Table 6.9. Their impact on the sensitivity is quantified for three selected signal points:  $(m_{Z'}, m_A) = (0.6 \text{ TeV}, 0.3 \text{ TeV})$ ,  $(m_{Z'}, m_A) = (1.4 \text{ TeV}, 0.6 \text{ TeV})$  and  $(m_{Z'}, m_A) = (2.6 \text{ TeV}, 0.3 \text{ TeV})$ . As shown in Figure 5.2, the  $E_T^{\text{miss}}$  distribution of the  $Z'$ -2HDM signals move to higher values for increasing  $m_{Z'}$ . Hence, the chosen signal points represent different kinematic regimes, reaching from the resolved low- $E_T^{\text{miss}}$  region up to highly boosted topologies of the merged region. Table 6.9 shows the relative uncertainties on the expected exclusion limits for these three signals. The uncertainties are split into a statistical and a systematic component. The statistical uncertainty is obtained by fixing all nuisance parameters to their best fit value. Thereby the effect of systematic uncertainties is practically ruled out, so that the remaining uncertainty represents an estimate for the uncertainties due to the statistical model chosen. For all three signal points, the  $b$ -tagging and the background theory uncertainties belong to the dominant systematic uncertainties. For the two more boosted signals, the MC statistics has a major impact, too. However, for these two signals the main uncertainty source comes from the statistics, which has an impact that is even larger than the total systematic uncertainty. For the low- $E_T^{\text{miss}}$  signal, the systematic uncertainty dominates over statistical uncertainty.

## 6.6 Results

The post-fit distributions of the muon charge in the  $1\mu$ -CR and the event yields in the  $2\ell$ -CR are shown in Figure 6.10 and Figure 6.11, respectively. Additionally, the distributions of the total MC background before the fit are indicated by the blue dotted line. In the SR, no excess of data with respect to the SM background expectations is found. The yields of

Source of uncert.	Impact [%]		
	(a)	(b)	(c)
<i>b</i> -tagging	4.0	8.0	10
<i>V</i> +jets modeling	3.5	6.0	5.0
Top modeling	3.7	4.8	4.5
MC statistics	1.8	5.4	4.9
SM $Vh(b\bar{b})$	0.8	3.2	2.1
Diboson modeling	0.8	1.5	1.1
Signal modeling	3.0	2.5	1.5
Luminosity	2.0	2.5	2.5
Small- <i>R</i> jets	1.4	3.0	2.0
Large- <i>R</i> jets	0.2	1.0	2.0
$E_T^{\text{miss}}$	1.2	1.7	1.1
Leptons	0.2	0.8	0.7
Total syst. uncert.	6.5	13	13
Statistical uncert.	2.3	20	22
Total uncertainty	7	24	25

**Figure 6.9:** Breakdown of the uncertainties in the search, shown for three representative  $Z'$ -2HDM signal points: (a)  $(m_{Z'}, m_A) = (0.6 \text{ TeV}, 0.3 \text{ TeV})$ , (b)  $(m_{Z'}, m_A) = (1.4 \text{ TeV}, 0.6 \text{ TeV})$  and (c)  $(m_{Z'}, m_A) = (2.6 \text{ TeV}, 0.3 \text{ TeV})$  [49]. The impact is expressed as relative uncertainty on the signal strength. Although the luminosity uncertainty has a fixed pre-fit value of 2%, its impact varies between the different signals. The reason is that this uncertainty is only applied to the non-floating backgrounds and the signal. As the background composition in the different bins of the search changes due to the freely floating backgrounds, the luminosity uncertainty can have a different value at post-fit level. The bottom of the table shows the total systematic, the statistical and the total uncertainty. The total uncertainty is defined as the quadrature sum of the total systematic and the statistical uncertainties. Due to anti-correlations between the nuisance parameters, the total systematic uncertainties can be smaller than the quadrature sum over the individual sources.

the data and MC backgrounds in the SR after the fit are summarised in Table 6.12. For the three  $E_T^{\text{miss}}$  bins of the resolved region, the data and the SM background expectations agree well within the uncertainties. However, in the merged region, the observed data lies slightly below the background predictions. The  $m_h$  distributions in the four  $E_T^{\text{miss}}$  bins are shown in Figure 6.13. Again, the background distributions before the fit are indicated by a dotted lined. The presented yields and data-MC plots correspond to the results obtained after a background-only fit, i.e. the fit is performed assuming no signal is present. The signal+background hypothesis was tested as well. However, for no signal point studied in this analysis a significant deviation compared to the background-only expectations was obtained. Before the fit, a data offset of about 10-20% with respect to the SM background is seen in all  $E_T^{\text{miss}}$  bins of the SR and  $2\ell$ -CR, which comes from modelling issues in the simulated samples. These are corrected by the normalisation factors and by the nuisance parameters with a normalisation effect. The resulting normalisation factors for  $t\bar{t}$ ,  $W$ +HF and  $Z$ +HF are  $1.10 \pm 0.08$ ,  $1.51 \pm 0.22$  and  $1.42 \pm 0.10$ , respectively. Nuisance parameters contributing to the normalisation come e.g. from the jet energy scale and resolution, which are shifted up to  $1\sigma$  from their nominal predictions.

As no excess of data over the SM background predictions is observed around the Higgs-

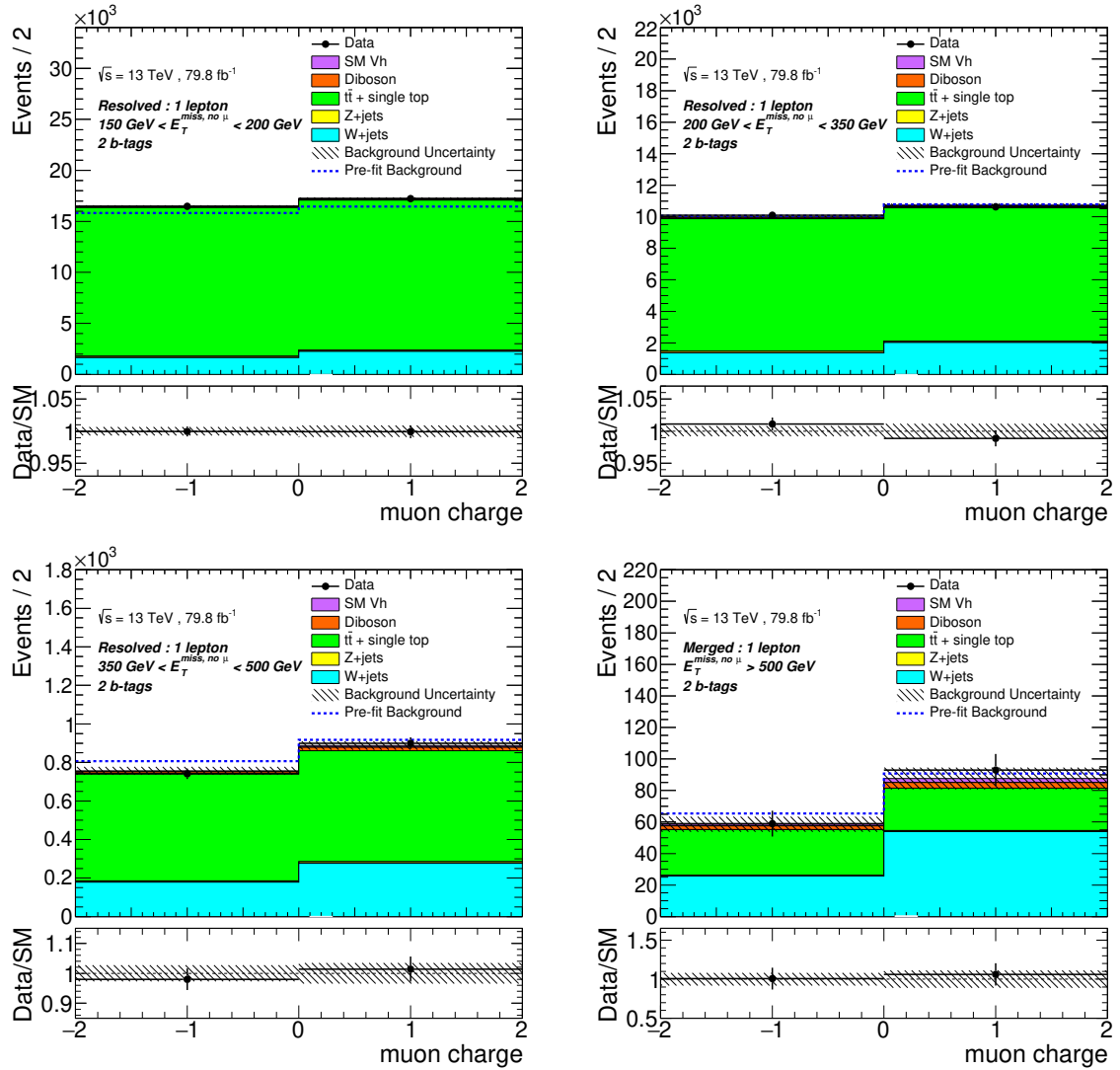


**Figure 6.10:** Distribution of the muon-charge in the four different  $E_T^{\text{miss}}$  bins of the  $1\mu$ -CR after the background-only fit. The MC pre-fit yields are indicated by the blue dotted line.

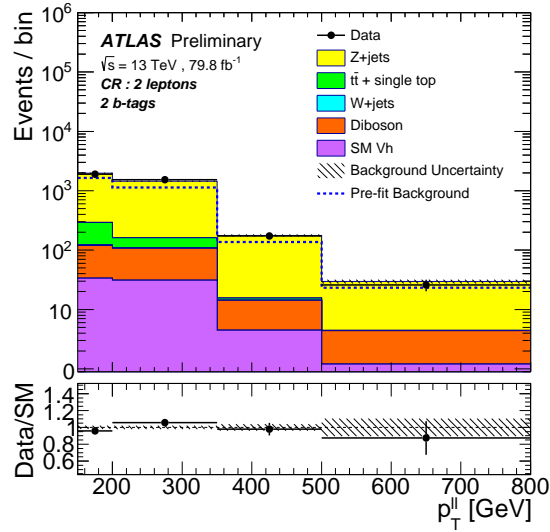


**Figure 6.11:**  $2\ell$ -CR event yields in the four different  $E_T^{\text{miss}}$  bins after the background-only fit [49]. The background yields before the fit are indicated by the blue dotted line.

Category	Range in $E_T^{\text{miss}}$ [GeV]			
	[150, 200)	[200, 350)	[350, 500)	[500, $\infty$ )
W+jets	3020 $\pm$ 530	2240 $\pm$ 360	184 $\pm$ 32	26.4 $\pm$ 5.7
Z+jets	6330 $\pm$ 450	5180 $\pm$ 340	565 $\pm$ 37	80.5 $\pm$ 6.3
$t\bar{t}$ + single top quark	11 800 $\pm$ 350	6450 $\pm$ 200	308 $\pm$ 25	10.8 $\pm$ 2.5
Diboson	438 $\pm$ 67	400 $\pm$ 59	49.0 $\pm$ 11	9.37 $\pm$ 1.7
Vh	136 $\pm$ 39	129 $\pm$ 37	17.3 $\pm$ 5.0	3.86 $\pm$ 1.1
Bkg	21 700 $\pm$ 140	14 400 $\pm$ 110	1120 $\pm$ 25	131 $\pm$ 7.2
Data	21 818	14 350	1128	119

**Figure 6.12:** Observed yields in the four  $E_T^{\text{miss}}$  bins of the SR after the background-only fit for the different background processes, the sum of all backgrounds as well as the observed data [49]. Due to anti-correlations between the nuisance parameters of the search, the total background uncertainties may be smaller than those of the individual processes.

mass window in the SR, exclusion limits are set in the  $m_{Z'} - m_A$  plane of the  $Z'$ -2HDM for the samples with  $m_H = m_{H^\pm} = 300$  GeV. The resulting exclusion contour is shown in Figure 6.14. The limits reach up to about  $m_A = 670$  GeV and  $m_{Z'} = 2.8$  TeV. For  $m_{Z'} < 1.4$  TeV, the expected and observed exclusion limits agree well, while for  $m_{Z'} > 1.4$  TeV the observed limit is slightly stronger than the expected one because the data yields in the merged SR are a bit lower than the SM background predictions. However, the observed and expected limits are still consistent within the  $1\sigma$  uncertainty of the background-only hypothesis. The new search results exceed the limits of the preceding  $36.1 \text{ fb}^{-1}$  analysis, shown as the blue dashed-dotted line, especially for high  $m_{Z'}$  values.

However, compared to the previous search, the available dataset increased by about  $44 \text{ fb}^{-1}$ . To determine, how much of the observed improvement originates from changes in the analysis strategy and how much from the luminosity increase, the expected limit of the

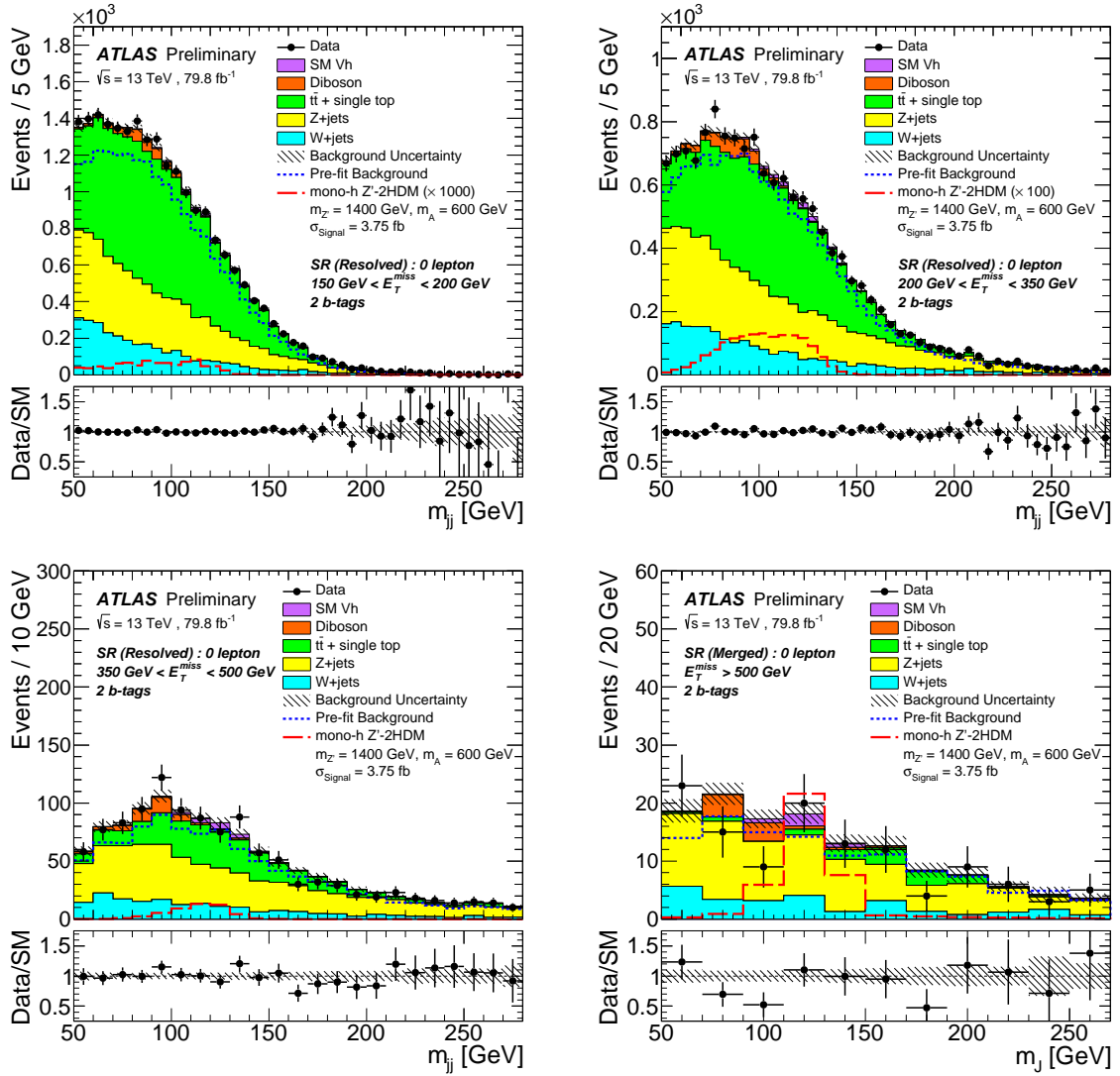


**Figure 6.13:** Distribution of  $m_h$  in the four different  $E_T^{\text{miss}}$  bins of the SR after the background-only fit [49]. The background yields before the fit are indicated by the blue dotted line. The red dashed line shows the distribution of a representative  $Z'$ -2HDM signal.

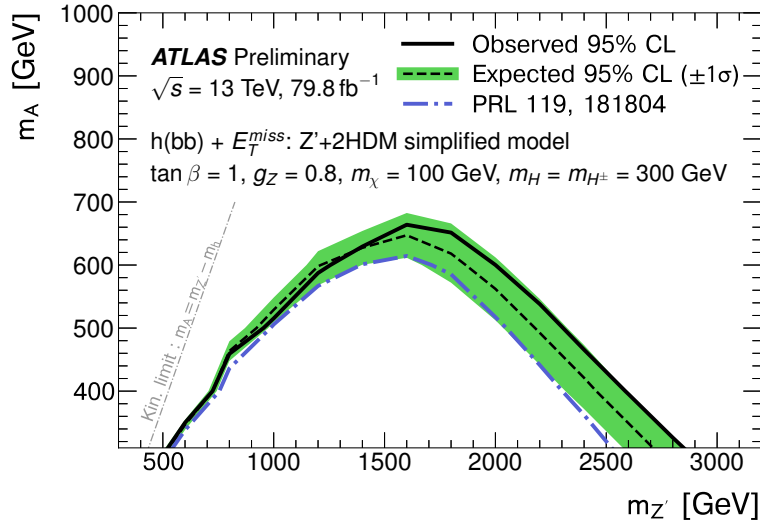


**Figure 6.14:** Observed (solid line) and expected exclusion contour (dashed line) along with its  $1\sigma$  uncertainties (green band) for the  $Z'$ -2HDM [49]. The blue dashed-dotted line represents the observed limit of the  $36.1 \text{ fb}^{-1}$  search. The limits are shown at 95% confidence level.

$36.1 \text{ fb}^{-1}$  search is re-evaluated for a luminosity of  $79.8 \text{ fb}^{-1}$  and compared to the expected limits of the current search. The previous search, however, also included regions with 1  $b$ -tag in the fit setup<sup>1</sup>. Hence, to also remove effects from this difference, only the 2  $b$ -tagged region is included in the luminosity scaling. The results of this are shown in Figure 6.15: Up to about  $m_{Z'} = 1.6 \text{ TeV}$ , the two contours are identical. For larger  $m_{Z'}$  they start to diverge, with the contour of the current search being the one that covers higher  $m_{Z'}$  and  $m_A$  values. For  $m_A = 300 \text{ GeV}$ , the expected limit reaches up to  $m_{Z'} = 2.7 \text{ TeV}$  and thereby exceeds the expected limit of the rescaled  $36.1 \text{ fb}^{-1}$  search by about 200 GeV. To better quantify this improvement, a direct comparison of the expected upper limit values of the two searches is performed. Figure 6.16 shows the expected limits on  $\mu$  as a function of  $m_{Z'}$  for  $m_A = 500 \text{ GeV}$ . The bottom panel shows the ratio of the two limit curves. Up to about  $m_{Z'} = 1.8 \text{ TeV}$ , the ratio is approximately one and then continuously increases, with a value of three at  $m_{Z'} = 3 \text{ TeV}$ . Thus, with the current search a sensitivity improvement of up to 200% was achieved.

As the difference in the limits is only visible for relatively large  $m_{Z'}$ , the sensitivity improvements mostly come from analysis changes in the merged region with respect to the  $36.1 \text{ fb}^{-1}$  search. These include a reduced uncertainty on the MC statistics (due to the introduction of additional MC samples simulating the 2017 data-taking periods) and a  $b$ -tagging efficiency WP. This was changed from a previously used value of 70% to 77%. However, these only have a minor impact on the signal sensitivity. The main improvement in

<sup>1</sup>In the resolved 1  $b$ -tag region,  $h_{\text{reco}}$  is reconstructed with the  $b$ -tagged jet and the central, not  $b$ -tagged jet with the largest  $p_T$ . In the merged region still the leading two associated track jets are used, of which only one is  $b$ -tagged. The 1  $b$ -tag category allows to detect signal events, in which one of the two Higgs boson jets fails to be  $b$ -tagged. However, including this category leads only to a limited sensitivity improvement. Therefore, for the scope of this search it was decided to only use the 2  $b$ -tag bins to simplify the fit setup.

the merged region is the use of VR instead of fixed-radius track jets. This result proves that VR track jets significantly enhance the sensitivity of the search to highly-boosted signatures and thus fulfil their design purpose.

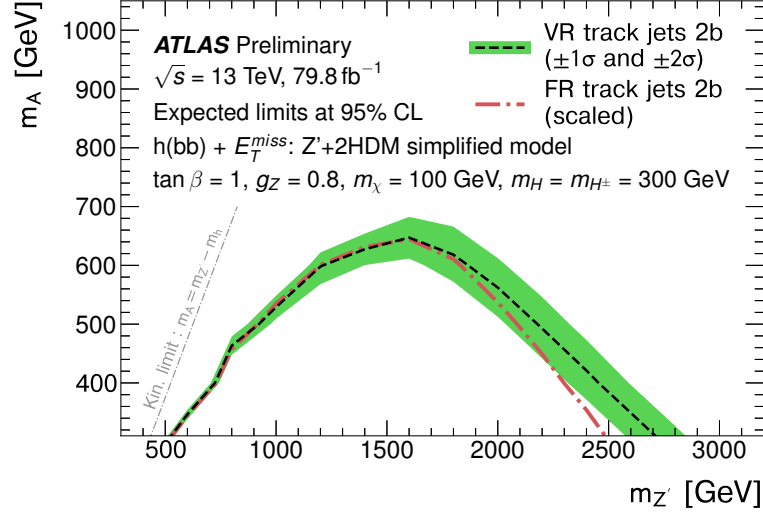


**Figure 6.15:** Comparison of the expected exclusion contours of the  $Z'$ -2HDM for this search (black dashed line) with the expected limit of the preceding  $36.1 \text{ fb}^{-1}$  search (red dotted-dashed line), which is based on fixed-radius (FR) track jets. To allow for a fair comparison, the latter is scaled up to a luminosity of  $79.8 \text{ fb}^{-1}$  [49]. The limits are shown at 95% confidence level.

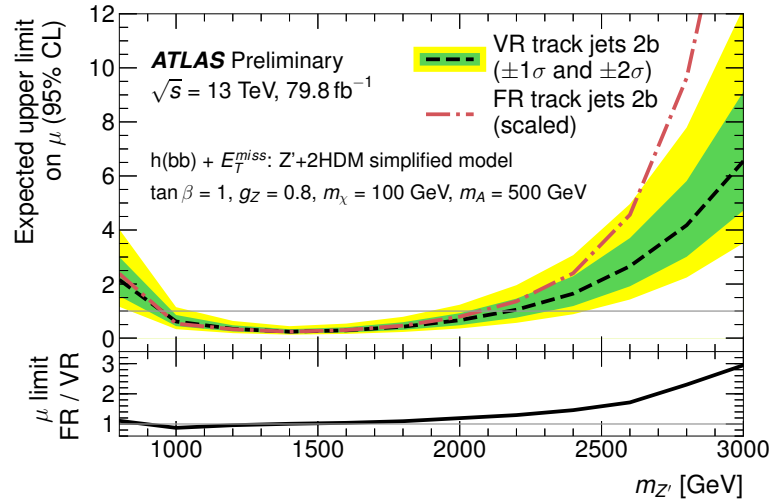


**Figure 6.16:** Comparison of the expected exclusion limits on  $\mu$  (black dashed line) of the  $Z'$ -2HDM for this search with the expected limit of the  $36.1 \text{ fb}^{-1}$  search (red dotted-dashed line), which is based on fixed-radius (FR) track jets. To allow for a fair comparison, the latter is scaled up to a luminosity of  $79.8 \text{ fb}^{-1}$ . The expected limits are shown as a function of  $m_{Z'}$  for  $m_A = 500 \text{ GeV}$  [49]. The limits are shown at 95% confidence level.

# Chapter 7

## The 139 fb<sup>-1</sup> analysis

### 7.1 Motivation and improvements

This chapter presents the mono- $h(b\bar{b})$  analysis based on the complete dataset of  $pp$  collisions recorded in Run II, which corresponds to an integrated luminosity of 139 fb<sup>-1</sup>. In this analysis, a comprehensive optimisation of the search strategy is performed. This includes improvements in various aspects of the analysis:

- **Improved object definitions**

Various changes in the reconstruction and identification of physics objects have been introduced, which allow for a better fake rejection and pile-up resistance. A discussion on the new object definitions is given in Section 7.2.

- **Muon-in-jet correction**

If a  $b$ -hadron inside a jet decays into a muonic final state, e.g. through the process  $b \rightarrow Wc \rightarrow \mu\bar{\nu}_\mu c$ , then the contributions of the muon and the neutrino are not considered in the jet energy and  $p_T$  reconstruction. This can distort the measured value of the Higgs boson candidate mass  $m_h$ . Therefore, the  $m_h$  resolution can be improved by correcting the jet four-momenta for the energy loss of the muons, referred to as muon-in-jet correction. With the standard object reconstruction methods, such muons would typically fail the selection criteria of the search, especially the isolation requirements. Consequently, for this correction a much looser collection of muons is necessary: The muons need to pass the quality criteria of the Loose identification WP [129], lie within  $|\eta| < 2.7$  and have a minimum  $p_T$  of only 5 GeV. Furthermore, they are not considered in the overlap removal procedure of Section 4.9 and no isolation criteria are imposed onto them. In the resolved region the muon-in-jet correction is applied to the two  $b$ -tagged small-R jets forming the Higgs boson candidate  $h_{\text{reco}}$ . If a muon has an angular distance of  $\Delta R < 0.4$  with respect to the jet axis, its four-momentum is added to the four-momentum of the corresponding jet. In case that there is more than one muon within  $\Delta R < 0.4$ , only the closest one is used for the correction. In the merged region the correction is applied to the leading large-R jet, for which the two muons closest to the jet axis are used. A comparison of the  $m_h$  distribution with and without the muon-in-jet correction is shown in Figure 7.1 for representative signal models of the resolved and merged topology. The improved  $m_h$  resolution also increases the sensitivity of the search, particularly in the merged SR. There, the expected exclusion limits are found to become up to 7% stronger by that [60]. The muon-in-jet correction has already been used within the 36.1 fb<sup>-1</sup> mono- $h(b\bar{b})$  search, however, with the small difference

that in the merged region the two muons were matched to the leading two associated track jets instead of the large-R jet axis [9, 180].

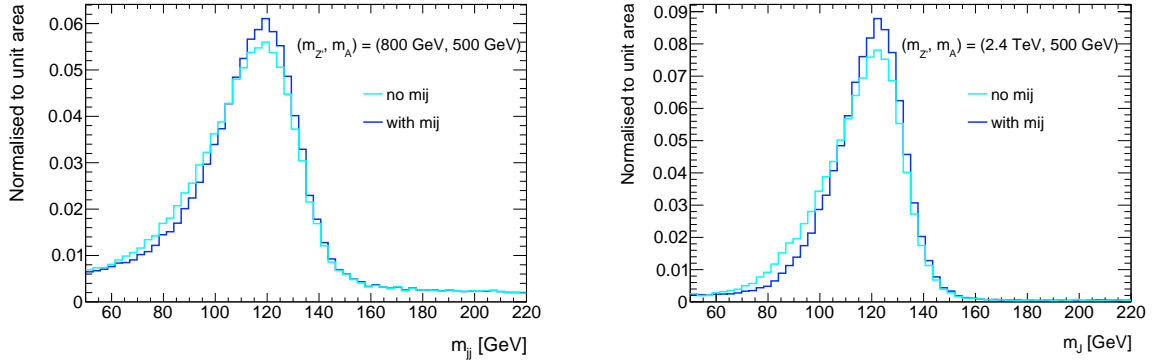


**Figure 7.1:** Distributions of  $m_h$  with and without the muon-in-jet correction (mij) in the resolved (left) and merged topology (right) for two representative signals of the  $Z'$ -2HDM with  $m_H = m_{H^\pm} = 300 \text{ GeV}$ . The  $m_{Z'}$  and  $m_A$  values of the chosen signals are indicated in the plot labels. The distributions are normalised to unit area and are obtained by applying the preselection criteria of Section 7.3.1.

- **Signal models**

In addition to the previously used  $Z'$ -2HDM signals with  $m_H = m_{H^\pm} = 300 \text{ GeV}$ , the ggF and  $b\bar{b}$ -induced 2HDM+ $a$  signals are considered as additional benchmark models. Furthermore, for the  $Z'$ -2HDM an interpretation with  $m_H = m_{H^\pm} = m_A$  is performed to allow for a future comparison of the results with the CMS experiment (c.f. Section 2.4.1).

- **Event selection**

It should be studied whether a modification of the cut values in Table 6.4 or the introduction of new discriminating variables can improve the sensitivity of the search.

- **Fit categories**

As discussed in Section 5.1, a shape fit exploits the shape differences between the different signal and background processes and thus represents a powerful way to enhance the sensitivity of the search to many different signal models. Hence, it will be studied whether the analysis can profit from having further fit categories apart from the  $m_h$  and  $E_T^{\text{miss}}$  bins used in the  $79.8 \text{ fb}^{-1}$  analysis.

## 7.2 Object definitions

The object definitions of this analysis are mostly adopted from the  $79.8 \text{ fb}^{-1}$  search (c.f. Section 6.1) and the reconstruction of the various objects is described in detail in Chapter 4. Therefore, in the following only the differences with respect to the previous search will be briefly discussed.

An overview of the jet-related objects of the search is given in Table 7.1. Compared to the  $79.8 \text{ fb}^{-1}$  analysis, this includes improvements in the small-R jet reconstruction, the

$\tau$ -lepton identification as well as in the  $b$ -tagging performance. These changes allow for a better fake rejection and stability against pile-up effects. The electron and muon settings are summarised in Table 7.2 and Table 7.3, respectively. For both lepton types, the isolation requirements have been improved. Baseline muons are now restricted to  $|\eta| < 2.5$  instead of  $|\eta| < 2.7$ : Muons in the range  $2.5 < |\eta| < 2.7$  are only reconstructed from MS information, as they are outside of the ID coverage (c.f. Section 4.7). Therefore, they suffer from a larger fake contamination. To simplify the analysis, a common signal muon definition is used in the  $1\mu$ -CR and  $2\ell$ -CR. The signal muon in the  $1\mu$ -CR and the leading muon in the  $2\ell$ -CR are required to have  $p_T > 25$  GeV. The subleading muon in the  $2\ell$ -CR needs to have a minimum  $p_T$  of only 7 GeV, but otherwise is required to pass all signal muon criteria.

With respect to the  $79.8 \text{ fb}^{-1}$  analysis, there are also changes concerning the object-based  $E_T^{\text{miss}}$  significance  $\mathcal{S}$ , for which a cut of  $\mathcal{S} > 16$  was used previously. Due to updates in the jet calibrations, the distribution of this variable was shifted to lower values. Approximately the same level of multijet rejection is now already achieved with a requirement of  $\mathcal{S} > 12$ , if otherwise the same selection as of Table 6.4 is applied.

Object	Kinematic requirements	Identification properties
Small-R jets <i>central</i>	$p_T > 20 \text{ GeV}$ $ \eta  < 2.5$	Type: Anti- $k_t$ $R=0.4$ PFlow, JVT $> 0.50$ if $p_T < 120 \text{ GeV}$ and $ \eta  < 2.5$ , $b$ -tagging: DL1, 77% efficiency,
Small-R jets <i>forward</i>	$p_T > 30 \text{ GeV}$ $2.5 \leq  \eta  < 4.5$	Type: Anti- $k_t$ $R = 0.4$ PFlow,
Large-R jets	$p_T > 200 \text{ GeV}$ $ \eta  < 2.0$	Type: Anti- $k_t$ $R = 1.0$ LCTopo, trimming: $R_{\text{subject}} = 0.2$ , $f_{\text{cut}} = 5\%$
VR track jets	$p_T > 10 \text{ GeV}$ $ \eta  < 2.5$	Type: Anti- $k_t$ variable- $R$ track jets, $b$ -tagging: DL1, 77% efficiency
$\tau$ -leptons	$p_T > 20 \text{ GeV}$ $ \eta  = [0, 1.37] \text{ or } [1.52, 2.5]$	Type: RNN $\tau$ -leptons, identification WP: VeryLoose

**Table 7.1:** Definitions of the jet-related objects.

Electron	$p_T$ [GeV]	$ \eta $	$d_0/\sigma(d_0)$	$ z_0 \sin \theta $ [mm]	Identification	Isolation
baseline	$> 7 \text{ GeV}$	$< 2.47$	$< 5$	$< 0.5$	LooseAndBLayer	FCLoose /
signal	$> 27 \text{ GeV}$					FCHighPtCaloOnly

**Table 7.2:** Definitions of the baseline and signal electrons. For electrons with  $p_T < 200$  GeV the FCLoose isolation WP is applied, while for higher  $p_T$  the FCHighPtCaloOnly WP is used.

Muon	$p_T$ [GeV]	$ \eta $	$d_0/\sigma(d_0)$	$ z_0 \sin \theta $ [mm]	Identification	Isolation
baseline	$> 7$ GeV	$< 2.5$	$< 3$	$< 0.5$	Loose	FCLoose
signal (leading)	$> 25$ GeV	$< 2.5$	$< 3$	$< 0.5$	Medium	FixedCutTightTrackOnly
signal (subleading)	$> 7$ GeV					

**Table 7.3:** Definitions of the baseline and signal muons.

### 7.3 Signal region optimisation

As mentioned in Section 7.1, one focus of this analysis is to study, whether the event selection can be optimised to enhance the sensitivity of the search. This is motivated by various reasons: First, several of the selection criteria presented in Section 6.2 are just adopted from former iterations of the SM  $Vh(b\bar{b})$  search [183, 184]. If  $V$  is a  $Z$ -boson which decays into neutrinos, the final state is characterised by  $E_T^{\text{miss}}$  and a  $h \rightarrow b\bar{b}$  decay. However, apart from that, the kinematic properties of  $Vh(b\bar{b})$  can largely differ from mono- $h(b\bar{b})$  DM signals, e.g. in the shape of the  $E_T^{\text{miss}}$  and jet  $p_T$  distributions. Therefore, the selection criteria of the SM  $Vh(b\bar{b})$  analysis are not necessarily optimal for this analysis. Furthermore, the previously used selection criteria were optimised for a smaller integrated luminosity. The increased dataset of 139 fb<sup>-1</sup> may allow to tighten some of the event selection criteria without to be statistically limited in the SRs. Lastly, thus far all aspects of the analysis strategy were optimised based on the kinematics of the  $Z'$ -2HDM signals. With the introduction of the 2HDM+ $a$  signals, it is necessary to make sure that the event selection is also appropriate for these. Therefore, the optimisation of the event selection is performed by studying the kinematic distributions for various signals of the  $Z'$ -2HDM as well as of the 2HDM+ $a$ . The final cuts should be chosen such as to ensure an adequate sensitivity for all signal models. Thereby, a possible over-optimisation to a particular model is avoided, which makes the search generically sensitive to a wide range of potential beyond-the-SM signals with a mono- $h(b\bar{b})$  topology.

#### 7.3.1 Event preselection

The event selection optimisation requires to study the shapes of different discriminating variables for both signal and SM background processes. This is performed at a basic preselection level, for which a limited set of selection criteria is defined. These are expected to have a marginal impact on the signal acceptance, but already reduce a considerable fraction of SM background events. Apart from the standard event cleaning described in Section 5.5, this requires events to pass an  $E_T^{\text{miss}}$  trigger according to Table 5.2. Furthermore, a veto is applied on baseline electrons and muons as well as on  $\tau$ -leptons. Instead of  $E_T^{\text{miss}} > 150$  GeV, a more conservative  $E_T^{\text{miss}}$  cut of  $> 120$  GeV is imposed. After these common requirements, different topology-dependent selection criteria are applied. For the resolved topology these are the following:

- $E_{\text{T}}^{\text{miss}} < 500 \text{ GeV}$
- Extended  $\tau$ -lepton veto of the resolved region
- $N(\text{central small-R jets}) \geq 2$
- $N(b\text{-jets}) \geq 1$
- $m_{jj} > 40 \text{ GeV}$ . In the case of only one  $b$ -jet in the event,  $m_{jj}$  is calculated using the one  $b$ -jet and the non- $b$ -tagged central jet with the highest  $p_{\text{T}}$ .

For the merged topology the preselection criteria are:

- $E_{\text{T}}^{\text{miss}} \geq 500 \text{ GeV}$
- Extended  $\tau$ -lepton veto of the merged region
- $N(\text{large-R jets}) \geq 1$
- At least one of the two leading associated track jets of  $h_{\text{reco}}$  must be  $b$ -tagged.

In both topologies the minimum requirement on the  $b$ -tagging multiplicity is lowered to one. Thereby also such events are considered, in which one of the two Higgs candidate (track) jets fails to be  $b$ -tagged. To be used in the optimisation studies, an event must pass either the resolved or the merged preselection.

### 7.3.2 Kinematic properties of the 2HDM+ $a$ signals

The kinematics of the 2HDM+ $a$  signals are highly different compared to the  $Z'$ -2HDM. There, the  $p_{\text{T}}$  of  $h_{\text{reco}}$  and  $E_{\text{T}}^{\text{miss}}$  move to higher values with increasing  $m_{Z'}$  and with an increasing mass difference  $\Delta(m_{Z'}, m_A)$ , as discussed in Section 5.1. However, such a simple correlation is not observed in the 2HDM+ $a$ . The normalised  $E_{\text{T}}^{\text{miss}}$  distributions for a few representative signals of the ggF-induced 2HDM+ $a$  are shown in Figure 7.2. These correspond to the distributions obtained after applying the preselection criteria described above, but removing the  $E_{\text{T}}^{\text{miss}} < 500 \text{ GeV}$  and  $E_{\text{T}}^{\text{miss}} \geq 500 \text{ GeV}$  for the resolved and merged regimes, respectively. This is done to avoid a sharp change of the event kinematics at  $E_{\text{T}}^{\text{miss}} = 500 \text{ GeV}$  and thereby ensure a smooth  $E_{\text{T}}^{\text{miss}}$  distribution. For the signal point  $(m_A, m_a) = (300 \text{ GeV}, 150 \text{ GeV})$  the average  $E_{\text{T}}^{\text{miss}}$  is relatively low. With increasing  $m_A$  and  $\Delta(m_A, m_a)$ , the  $E_{\text{T}}^{\text{miss}}$  spectrum moves to higher values. In Figure 7.2, the signal point with the largest average  $E_{\text{T}}^{\text{miss}}$  is  $(m_A, m_a) = (1.3 \text{ TeV}, 500 \text{ GeV})$ . However, for higher  $m_A$ , the  $E_{\text{T}}^{\text{miss}}$  distribution gradually moves again to lower values. The signal point  $(m_A, m_a) = (1.8 \text{ TeV}, 100 \text{ GeV})$ , which is the signal with the largest  $m_A$  as well as with the largest mass splitting  $\Delta(m_A, m_a)$ , even has an average  $E_{\text{T}}^{\text{miss}}$  lower than  $(m_A, m_a) = (300 \text{ GeV}, 150 \text{ GeV})$ . Hence, for most of the signal points in the 2HDM+ $a$  the events predominantly lie in the resolved region of  $E_{\text{T}}^{\text{miss}} < 500 \text{ GeV}$ . The same behaviour as for  $E_{\text{T}}^{\text{miss}}$  is observed for the jet  $p_{\text{T}}$  distributions of  $h_{\text{reco}}$  as well.

The reason for this is, that for large  $m_A$  the contribution from non-resonant production mechanisms dominates [37]. This can be illustrated by analysing the truth information stored in the MC signal samples, which allows to access the types and kinematic properties

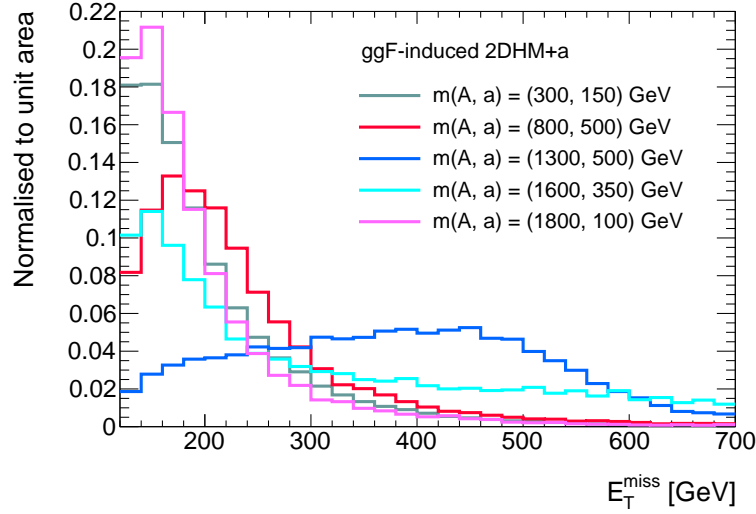


**Figure 7.2:**  $E_T^{\text{miss}}$  distribution for representative signals of the ggF-induced 2HDM+ $a$ . These are obtained after applying the preselection criteria of Section 7.3.1, but excluding the the  $E_T^{\text{miss}}$  cut of  $< 500$  GeV and  $\geq 500$  GeV for the resolved and merged region, respectively.

of all generator-level particles. Furthermore, for each particle it is possible to see, up to the initial hard scatter, from which particle it originates and if it subsequently decays into or radiates off other particles. Thereby, the decay chains in the process of interest can be reconstructed. To understand the full event kinematics of the signals, the studies are performed with dedicated truth samples with no preselection criteria applied at all. Figure 7.3 shows the production modes obtained for the the signal models of Figure 7.2, except for  $(m_A, m_a) = (1.8 \text{ TeV}, 100 \text{ GeV})$ . For this, the signal  $(m_A, m_a) = (1.8 \text{ TeV}, 150 \text{ GeV})$  is shown instead. In addition, also the invariant mass of the DM pair and the Higgs boson, denoted as  $m_{\chi\bar{\chi}h}$ , is calculated and shown in Figure 7.3.

For  $(m_A, m_a) = (300 \text{ GeV}, 150 \text{ GeV})$ , almost all events originate from resonant  $A \rightarrow ah$  production, corresponding to the Feynman diagram in Figure 2.9. This leads to the distinct peak at  $m_{\chi\bar{\chi}h} = 300 \text{ GeV}$ . Resonant production dominates also for  $(m_A, m_a) = (800 \text{ GeV}, 500 \text{ GeV})$ , but this model has also smaller contributions coming from the off-shell  $a \rightarrow Ah$  decay and  $t$ -channel production of the pseudoscalar  $a$  (c.f. Figure 2.11). The former is responsible for the second peak at  $m_{\chi\bar{\chi}h} = 500 \text{ GeV}$ , while the latter has no characteristic  $m_{\chi\bar{\chi}h}$  value. For  $(m_A, m_a) = (1.3 \text{ TeV}, 500 \text{ GeV})$ , i.e. the signal with the highest  $E_T^{\text{miss}}$  spectrum, nearly all events come from the resonant  $A \rightarrow ah$  production mode, thus the  $m_{\chi\bar{\chi}h}$  distribution has a single peak around 1.3 TeV. However, for  $(m_A, m_a) = (1.6 \text{ TeV}, 350 \text{ GeV})$  there are no events at all originating from resonant production. Instead, most events come from the off-shell  $a \rightarrow Ah$  decay and  $t$ -channel production. Therefore, the  $m_{\chi\bar{\chi}h}$  distribution has two pronounced regions: The peak at 350 GeV from the  $a \rightarrow Ah$  process and a smeared distribution around 500 GeV caused by the  $t$ -channel diagrams. Lastly, for  $(m_A, m_a) = (1.8 \text{ TeV}, 150 \text{ GeV})$ , i.e. the signal with the largest largest  $m_A$  and  $\Delta(m_A, m_a)$ , all events originate from  $t$ -channel production, causing thus a rather low  $E_T^{\text{miss}}$  spectrum. Similar results are also seen for the  $b\bar{b}$ -induced 2HDM+ $a$  signals. However, they generally

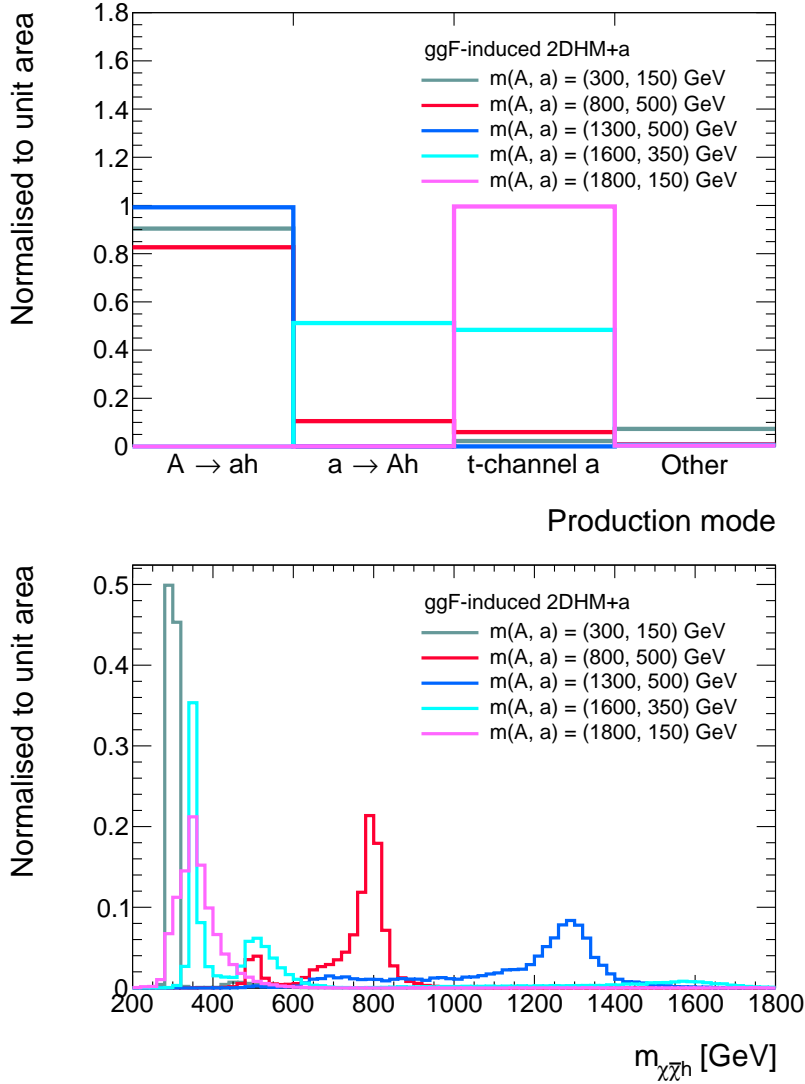


**Figure 7.3:** The top plot shows the fractional contribution of the different production modes for five representative signals of the ggF-induced 2DHM+ $a$ . The bottom plot shows the associated  $m_{\chi\bar{\chi}h}$  distributions, normalised to unit area.

have lower  $E_T^{\text{miss}}$  values and a larger contribution from non-resonant production modes, as discussed in Appendix B.

### 7.3.3 Optimisation of the resolved SR

In Section 6.6 it has been shown, that the analysis strategy of the  $79.8 \text{ fb}^{-1}$  search significantly enhanced the sensitivity to  $Z'$ -2HDM signals with large  $m_{Z'}$  with respect to the  $36.1 \text{ fb}^{-1}$  search. These represent highly boosted mono- $h(b\bar{b})$  signatures. However, for small  $m_{Z'}$  values, only a small sensitivity improvement was observed compared to the  $36.1 \text{ fb}^{-1}$  analysis, as shown in Figure 6.14. If the two analyses are compared for the same luminosity (c.f.

Figures 6.15—6.16), the sensitivities of the two searches are nearly identical. Consequently, the small sensitivity improvement was caused only by the luminosity. Events from these signals mostly lie in the resolved SR. This motivates to perform a thorough optimisation of the event selection in the resolved SR to enhance the sensitivity of the search also in this kinematic phase space. Moreover, the newly introduced 2HDM+ $a$  signals typically produce rather low  $E_T^{\text{miss}}$ . Thus, to allow for a good sensitivity to these models, it is crucial to have suitable event selection in the resolved SR. As discussed in Section 6.3, the dominant background in the resolved SR are  $t\bar{t}$  processes. This is particularly large in the lowest  $E_T^{\text{miss}}$  bin, in which it constitutes more than 60% of the total background. Hence, a key point of the optimisation is to find a way to reduce the large  $t\bar{t}$  contamination.

The studies presented in the following have initially been performed based on the object definitions of the 79.8 fb<sup>-1</sup> search. Furthermore, also the muon-in-jet correction was not considered. However, all plots in this section are updated to these changes to demonstrate, that the optimisation strategy and its conclusions remain valid. For simplicity, in the optimisation the  $t\bar{t} + V/h$  processes are not considered, because their contribution to the SM background in the resolved region is considerably below 1%, which is less than the statistical uncertainty of the total background. However, in the final evaluation of the search results they are included again.

## Discriminating variables

The first step in the SR optimisation is to find suitable discriminating variables which show a distinct shape difference between signal processes and SM backgrounds. With a cut on such a variable, the signal-to-background ratio can be increased which, in turn, helps to improve the sensitivity of the search. The studies are performed at preselection level, i.e. after applying the requirement of Section 7.3.1. The following variables are studied:

- **Missing transverse momentum**

Even though a sizeable amount of  $E_T^{\text{miss}}$  is expected to be produced by the escaping DM particles, the cut  $E_T^{\text{miss}} > 150$  GeV may be too large for certain signal models, e.g. the  $Z'$ -2HDM signals with small  $m_{Z'}$ . Therefore, it is studied whether the acceptance, and thus the sensitivity, for such models can be increased by lowering the  $E_T^{\text{miss}}$  threshold down to 120 GeV. This is the lowest value which could reasonably be used in the analysis without suffering from issues in the  $E_T^{\text{miss}}$  trigger calibration (c.f. Section 5.4.3).

- **Object-based  $E_T^{\text{miss}}$  significance**

This variable has been initially introduced to suppress the multijet background, because it efficiently discriminates fake from genuine  $E_T^{\text{miss}}$ . As mono- $h(b\bar{b})$  signals are expected to have considerable amount of genuine  $E_T^{\text{miss}}$ , it is studied whether a tighter cut may also increase the sensitivity to mono- $h(b\bar{b})$  signals.

- **Number of  $b$ -jets**

With a  $b$ -tagging efficiency WP of 77%, there is only a 59% probability of correctly identifying the two jets from the  $h \rightarrow b\bar{b}$  decay as  $b$ -jets. In 35% of the cases only one of the two will be  $b$ -tagged. To enhance the signal acceptance, one could e.g. choose a higher  $b$ -tagging efficiency WP or loosen the  $b$ -jet requirement to  $\geq 1b$  jet.

However, both would also increase the SM background contamination, which can lead to a reduction in the sensitivity. In the  $36.1 \text{ fb}^{-1}$  analysis, 1  $b$ -jet events were instead used as additional fit category, i.e. the number of bins as presented in Section 6.4.2 is doubled by an additional categorisation of events with exactly one and two  $b$ -jets, in the following denoted as  $1b$  and  $2b$ , respectively. Using disjoint regions allows to profit from the additional  $1b$  events without to reduce the sensitivity contribution from  $2b$  events. The impact of the  $1b$  category on the sensitivity of the  $79.8 \text{ fb}^{-1}$  search was found to be marginal and therefore it has been omitted. However, with a modified event selection and the new 2HDM+ $a$  signals, it may be useful to re-introduce the  $1b$  category again. In  $1b$  events,  $h_{\text{reco}}$  is formed using the one  $b$ -jet and the non- $b$ -tagged central small-R jet with the highest  $p_{\text{T}}$ .

Furthermore, from Figure 2.9 it is expected that the  $b\bar{b}$ -induced 2HDM+ $a$  signals have a considerable fraction of events with three or more  $b$ -jets, in the following abbreviated as  $3b+$  events. Here, the additional  $b$ -jets come from the two spectator  $b$ -quarks, which are produced in the initial gluon splitting. On the other hand, the SM background is very low for large  $b$ -jet multiplicities. Therefore, including the  $3b+$  events into the analysis could significantly enhance the sensitivity to the  $b\bar{b}$ -induced 2HDM+ $a$  signals, especially if being used as an additional fit category. In  $3b+$  events, the two leading  $b$ -jets are used to reconstruct  $h_{\text{reco}}$ .

- **$p_{\text{T}}$  of the Higgs candidate jets**

In signal events,  $E_{\text{T}}^{\text{miss}}$  is highly correlated to the Higgs boson momentum, so that the two jets from the Higgs boson decay are expected to emerge with a relatively high  $p_{\text{T}}$ . Therefore, the  $p_{\text{T}}$  of the leading  $b$ -jet as well as the vectorial  $p_{\text{T}}$  sum<sup>1</sup> of the two jets forming  $h_{\text{reco}}$ , denoted as  $p_{\text{T}}(\mathbf{j}_1, \mathbf{j}_2)$ , are used for the optimisation. The latter represents the  $p_{\text{T}}$  of  $h_{\text{reco}}$ . As for  $m_{jj}$ , also for  $p_{\text{T}}(\mathbf{j}_1, \mathbf{j}_2)$  the muon-in-jet correction is applied.

- **$H_{\text{T}}$ -ratio of the leading two and three ( $b$ )-jets**

These two variables, denoted by  $H_{\text{T}}^{2b}$ -ratio and  $H_{\text{T}}^{3b}$ -ratio, are similar to the  $H_{\text{T}}$ -ratio described in Section 6.2.2. However, instead of using the leading jets of the *central+forward* jet collection, here the  $b$ -jets are prioritised, because in signal events the two  $b$ -jets from the  $h \rightarrow b\bar{b}$  decay are generally expected to carry a significant fraction of the total  $H_{\text{T}}$ . On the other hand, in SM background processes the  $b$ -jets are not necessarily among the highest- $p_{\text{T}}$  jets. The  $H_{\text{T}}^{2b}$  and  $H_{\text{T}}^{3b}$ -ratio are thus calculated by:

$$H_{\text{T}}^{2b}\text{-ratio} = \frac{p_{\text{T}}(j_1) + p_{\text{T}}(j_2)}{H_{\text{T}}}, \quad (7.1)$$

$$H_{\text{T}}^{3b}\text{-ratio} = \frac{p_{\text{T}}(j_1) + p_{\text{T}}(j_2) + p_{\text{T}}(j_3)}{H_{\text{T}}}, \quad (7.2)$$

---

<sup>1</sup>Instead of the vectorial, initially the scalar  $p_{\text{T}}$  sum of the two jets forming  $h_{\text{reco}}$  was considered in this study. The two distributions are generally very similar. The scalar sum just lies on average at slightly higher values. However, it was decided to replace the scalar by the vectorial sum because the latter is regarded as being more physical in the sense that it directly corresponds to the  $p_{\text{T}}$  of  $h_{\text{reco}}$ , while the scalar sum is only a proxy for that.

where  $j_1$  and  $j_2$  are the two  $h_{\text{reco}}$  jets (in  $1b$  events,  $j_2$  is the leading non- $b$ -tagged central jet) and  $j_3$  is, if present, the third-leading  $b$ -jet. Otherwise  $j_3$  is the leading non- $b$ -tagged central small-R jet in the event.

- **Angular separation between the Higgs boson candidate jets  $\Delta R(j_1, j_2)$**

The variable  $\Delta R(j_1, j_2)$  constituted the most powerful  $t\bar{t}$  reduction variable in the preceding two mono- $h(b\bar{b})$  searches and is described in Section 6.2.2. It should be studied whether a modified value of this variable can further enhance the sensitivity.

- **Number of central small-R jets**

A cut on the number of central small-R jet may help to further reduce the  $t\bar{t}$  background: While signal events contain at least two jets from the  $h \rightarrow b\bar{b}$  decay, semi-leptonic  $t\bar{t}$  decays (c.f. Figure 5.3(a)) are expected to produce at least four jets, with two jets originating from the  $b$ -quarks and the other two from the hadronic decay of one  $W$ -boson. Thus, a sensitivity gain may be achieved by vetoing events with large jet multiplicities.

- **Transverse mass variables  $m_{\text{T}}^{b,\text{min}}$  and  $m_{\text{T}}^{b,\text{max}}$**

The variables  $m_{\text{T}}^{b,\text{min}}$  and  $m_{\text{T}}^{b,\text{max}}$  describe the *transverse mass* of  $E_{\text{T}}^{\text{miss}}$  and the  $b$ -jet which has the minimum ( $b_{\text{min}}$ ) or maximum ( $b_{\text{max}}$ ) azimuthal distance relative to  $\mathbf{E}_{\text{T}}^{\text{miss}}$ , respectively. They are defined by:

$$m_{\text{T}}^{b,\text{min}/\text{max}} = \sqrt{2p_{\text{T}}^{b,\text{min}/\text{max}} E_{\text{T}}^{\text{miss}} (1 - \cos \Delta\phi(\mathbf{b}_{\text{min}/\text{max}}, \mathbf{E}_{\text{T}}^{\text{miss}}))} \quad (7.3)$$

These two variables have already been used in different ATLAS searches with zero-lepton final states, e.g. in Ref. [194], and are designed to suppress semi-leptonic  $t\bar{t}$  processes. In these, the lepton fails to be identified or falls out of acceptance. The lepton  $p_{\text{T}}$  thus contributes to  $E_{\text{T}}^{\text{miss}}$ , so that  $m_{\text{T}}^{b,\text{min}}$  and  $m_{\text{T}}^{b,\text{max}}$  are effectively a proxy for the top-quark mass<sup>1</sup>. Hence, for  $t\bar{t}$  events the  $m_{\text{T}}^{b,\text{min}}$  and  $m_{\text{T}}^{b,\text{max}}$  distributions show a steep drop-off at about 170 GeV. On the other hand, mono- $h(bb)$  signal processes have on average larger values for  $m_{\text{T}}^{b,\text{min}}$  and  $m_{\text{T}}^{b,\text{max}}$ , which makes them promising discriminating variables. In  $1b$  events, the closest  $b$ -jet is at the same time the furthest one, so that  $m_{\text{T}}^{b,\text{min}}$  and  $m_{\text{T}}^{b,\text{max}}$  are identical in this case.

Figures 7.4 – 7.5 show the distributions of the different discriminating variables for the SM background and for four representative signal models:  $(m_{Z'}, m_A) = (1 \text{ TeV}, 600 \text{ GeV})$  from the  $Z'$ -2HDM with  $m_H = m_{H^\pm} = 300 \text{ GeV}$ ,  $(m_A, m_a) = (1.3 \text{ TeV}, 500 \text{ GeV})$  and  $(m_A, m_a) = (600 \text{ GeV}, 350 \text{ GeV})$  from the ggF-induced 2HDM+ $a$  and  $(m_A, m_a) = (800 \text{ GeV}, 150 \text{ GeV})$  from the  $b\bar{b}$ -induced 2HDM+ $a$  signal grid. The chosen  $Z'$ -2HDM signal is a model which is just not covered by the exclusion contour of the 79.8 fb<sup>-1</sup> search (c.f. Figure 6.14). The other 2HDM+ $a$  signals are models in a similar sensitivity range, i.e. with an expected exclusion limit close to the 95% confidence level. With their different mediator masses and production

<sup>1</sup>The variables  $m_{\text{T}}^{b,\text{min}}$  and  $m_{\text{T}}^{b,\text{max}}$  are a special case of the originally defined transverse mass variable  $m_{\text{T}}$ . This was introduced to suppress  $W$ +jets processes with a leptonically decaying  $W$ -boson. It is calculated according to 7.3, but with the  $b$ -jet replaced by the lepton.

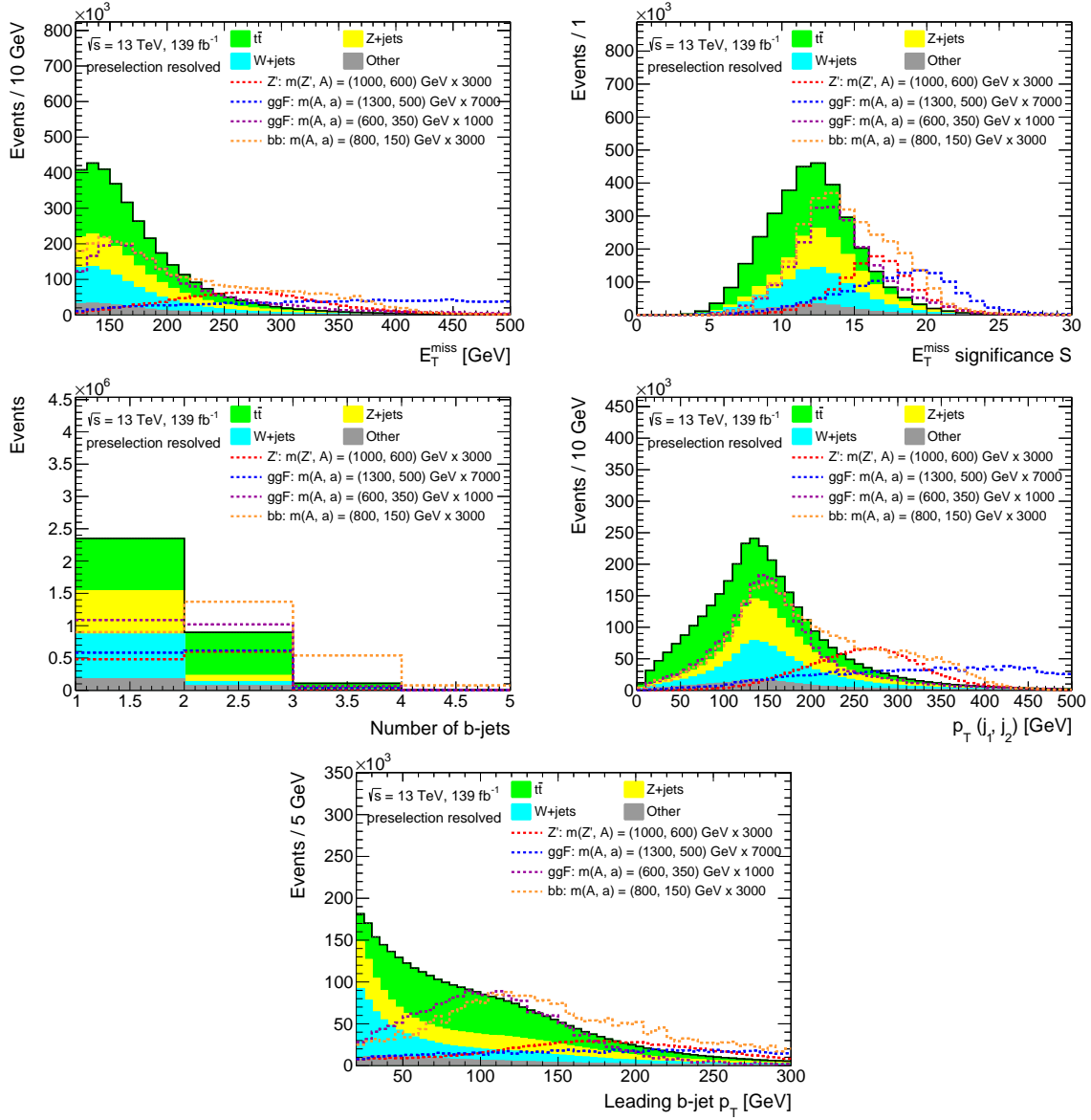


**Figure 7.4:** Preselection distributions for several discriminating variables studied in the optimisation, shown for the SM background and four representative signal models. For a better visibility, the signal yields are scaled with the factors indicated in the plot labels.

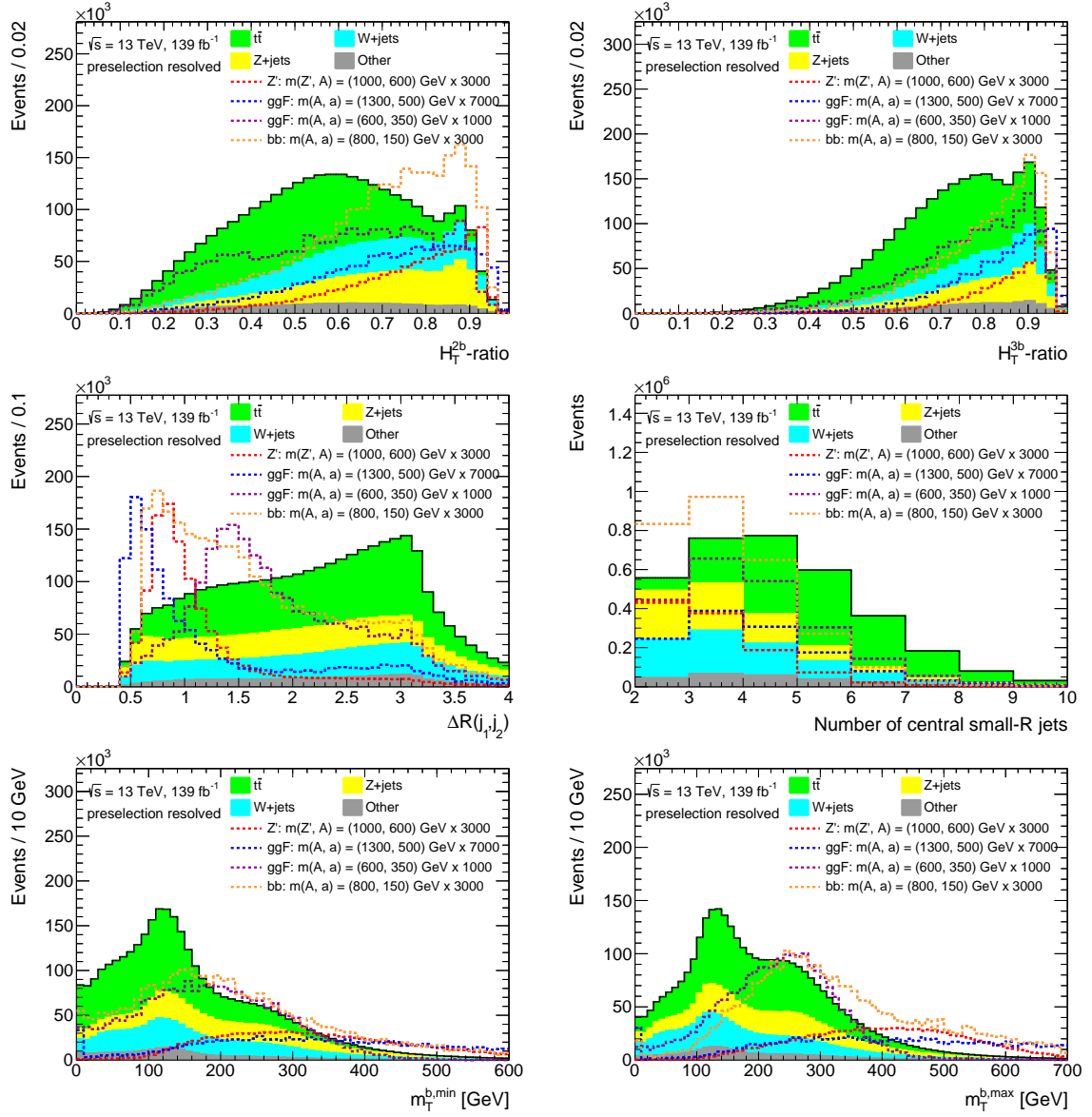


**Figure 7.5:** Preselection distributions for the  $t\bar{t}$  reduction variables studied in the optimisation, shown for the SM background and four representative signal models. For a better visibility, the signal yields are scaled with the factors indicated in the plot labels.

mechanisms, these four signals represent the large kinematic variety that potential mono- $h(b\bar{b})$  signals may have. Though not included in the plots above, also various other signals of these three grids were investigated during the optimisation. For the  $Z'$ -2HDM only signals with  $m_{Z'} < 1.5$  TeV were studied because signals with larger  $m_{Z'}$  predominantly lie in the merged region. No signal models of the new  $Z'$ -2HDM with  $m_H = m_{H^\pm} = m_A$  are considered in the optimisation. This grid is only included in the final interpretation of the search results.

## Optimisation strategies

After promising discriminating variables have been found, one needs to determine which cut values would give the best possible sensitivity. The variables described in the previous section are, at least to some extent, correlated with each other. Therefore, it is necessary to understand, how the choice of different cut combinations affects the signal sensitivity.

### Scan of cut combinations with *ahoi*

The *ahoi* software package [195] represents a suitable method to study the effect of different cut combinations. It takes as input the MC samples of the SM backgrounds and the signals of interests, which are defined in a configuration file. Also the discriminating variables and their cut values, which one intends to test, are specified in this file. The *ahoi* package performs a scan over all possible combinations and evaluates for each of them the signal efficiency and background rejection, measured with respect to the signal and background yields obtained at a given preselection level.

Apart from the criteria described above, two additional requirements are added to the preselection criteria in this study: First, all events need to satisfy  $\Delta\phi(\mathbf{E}_T^{\text{miss}}, \mathbf{j}_{1,2,3}^{\text{centr.}+\text{forw.}}) > 20^\circ$ . Besides  $\mathcal{S}$ , this constituted the most powerful multijet-reduction cut of the  $79.8 \text{ fb}^{-1}$  search. Hence, it is used in this analysis as well. Furthermore, in terms of the sensitivity of the search, only events with  $m_{jj}$  around the Higgs boson mass are interesting. Therefore, the cut scan is restricted to the region  $70 \text{ GeV} < m_{jj} < 140 \text{ GeV}$  which, as can be seen from Figure 7.1, captures most signal events. The sidebands of this Higgs mass window are used to constrain the dominant SM backgrounds in the simultaneous fit and thus should not be considered here. Based on this preselection, a scan over different values for the various discriminating variables is performed. The cuts tested are summarised in Table 7.4. Altogether, they correspond to 1.97 million different cut combinations. For most variables also the possibility is included to not apply a cut at all, e.g. for the transverse mass and  $H_T$ -ratio variables.

The outcome of such a cut scan is demonstrated in Figure 7.6 for a representative signal. The left plot shows the number of cut combinations as a function of the signal efficiency and background rejection. In terms of the signal-to-background ratio, the best cut combination for a given signal efficiency is the one which rejects as much background as possible. By connecting these points for all signal efficiency values, the Receiver Operating Characteristic (ROC) curve is obtained. With the *ahoi* tool it is possible to access the signal efficiency, background rejection and cut values of every combination that is on the ROC curve. These combinations are generally expected to give the best sensitivity.

In a next step, *ahoi* takes the cut combinations on the ROC curve and calculates the

Variable	Cut value
$E_{\text{T}}^{\text{miss}}$	$> \{120, 150, 200, 300, 400\}$ GeV
$S$	$> \{10, 14, 18\}$
$p_{\text{T}}(j_1)$	$> \{0, 70, 100, 130\}$ GeV
$p_{\text{T}}(\mathbf{j}_1, \mathbf{j}_2)$	$> \{0, 120, 170, 220\}$ GeV
$H_{\text{T}}^{2b}$ -ratio	$> \{0, 0.6, 0.75, 0.9\}$
$H_{\text{T}}^{3b}$ -ratio	$> \{0, 0.6, 0.75, 0.9\}$
$\Delta R(\mathbf{j}_1, \mathbf{j}_2)$	$< \{1.0, 1.7, 2.4, 5.0\}$
$m_{\text{T}}^{b,\text{min}}$	$> \{0, 140, 180, 220\}$ GeV
$m_{\text{T}}^{b,\text{max}}$	$> \{0, 140, 180, 220\}$ GeV
$N(\text{central small-R jets})$	$\leq \{3, 4, 5, 100\}$
$N(b\text{-jets})$	$\geq \{1, 2\}$

**Table 7.4:** Discriminating variables and their cut values tested with *ahoi*. Even though the different  $E_{\text{T}}^{\text{miss}}$  cuts are effectively already included in the search through the  $E_{\text{T}}^{\text{miss}}$  binning in the fit setup, different cut values are scanned to find out, in which kinematic phase space the studied signals lie. For the number of  $b$ -jets only the inclusive selections with  $\geq 1$  and  $\geq 2$   $b$ -jets are included. Later in the section also the effect of having  $1b$ ,  $2b$  and  $3b+$  events as separate fit categories is discussed.

significance for each of them. The formula used for this represents an approximation for the discovery significance  $Z$ , described in Section 6.4.1, and is referred to as *asimov significance*. It is defined by [196]:

$$Z = \left( 2(s+b) \ln \left[ \frac{(s+b)(b+\sigma_b^2)}{b^2 + (s+b)\sigma_b^2} \right] - 2 \frac{b^2}{\sigma_b^2} \ln \left[ 1 + \frac{\sigma_b^2 s}{b(b+\sigma_b^2)} \right] \right)^{1/2}, \quad (7.4)$$

where  $s$  and  $b$  are the number of expected signal and background events, respectively, and  $\sigma_b$  the uncertainty on the background. As shown in Table 6.12, the post-fit background uncertainties in the resolved SR were found to be very small in the 79.8 fb<sup>-1</sup> search ( $\mathcal{O}(1\%)$ ). Therefore, only the statistical uncertainty of the background is considered in  $\sigma_b$  for this test, while any effects from systematic uncertainties are neglected. The right plot in Figure 7.6 shows the resulting significance as a function of the signal efficiency. For this particular model, the significance is maximal for signal efficiencies in the range of about 0.4 to 0.5, so that the corresponding cut combinations are good candidates for a possible SR definition. As can be seen from the ROC curve, these reject more than 99% of the background events present at preselection level. However, an event selection which leads to a good sensitivity for one model, is not necessarily also suitable for another one. To find out which kinematic phase space is preferred by which model, the study is repeated for various signal points.

In these studies, the signal and background events are randomly divided into two statistically independent sets of samples and the cut scans are performed separately for each of them. This is a common approach in machine learning techniques. In analogy to that, the two sets are denoted as *train* and *test* samples. If the ROC and significance curves for the two sets show large discrepancies, this may be an indication that the optimisation results are not trustworthy. For example, the cuts may be too tight for the available MC statistics, so that the resulting significances suffer from large statistical fluctuations.

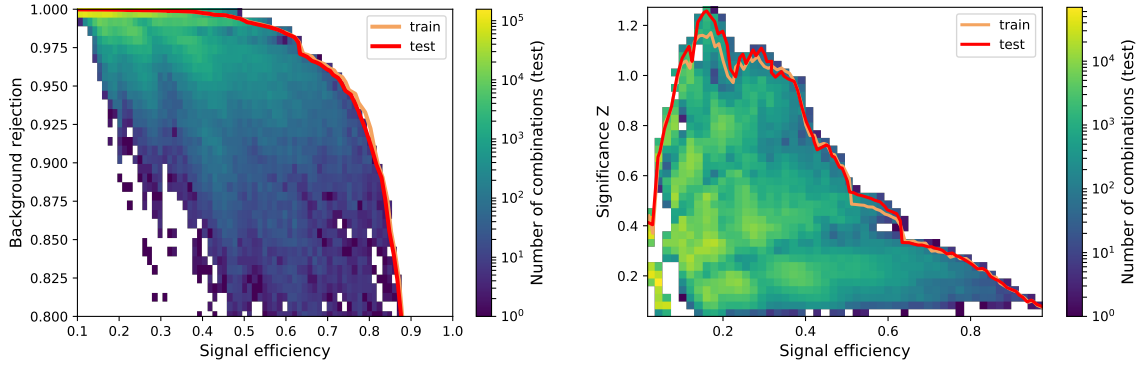


**Figure 7.6:** ROC curve (left) and significance curve as a function of the signal efficiency (right) for the ggF-induced 2HDM+ $a$  signal  $(m_A, m_a) = (1.3 \text{ TeV}, 500 \text{ GeV})$  resulting from the *ahoi* cut scan. The scan is performed independently for a train and test sample. The resulting ROC and significance curves for the two test samples are generally close to each other, which assures that the cut combinations are not affected by statistical fluctuations or other error sources.

### $N - 1$ plots

Another approach to investigate the effect of different cut combinations on the sensitivity is to study the corresponding  $N - 1$  plots: An  $N - 1$  plot shows the distribution of a variable after all selections of a cut combination are applied, except for the cut on the variable which is plotted. The bottom panel of such a plot indicates, which significance one would obtain for different signals, if the cut on the variable plotted is applied at a certain value. As for the *ahoi* studies, the significance is calculated using the asimov formula of Equation 7.4. Figure 7.7 shows the distribution of the  $N - 1$  plots for the SR definition, which is eventually used in this search. The motivation behind the choice of these particular variables and associated cut values is discussed below. The positions of the arrows indicate the cut values applied and their direction specifies, whether this cut restricts the variable from above or below. That also determines the reading direction of the significance distribution: For a variable which is restricted from below (cuts with “ $>$ ” or “ $\geq$ ”), e.g.  $E_{\text{T}}^{\text{miss}}$ , the bottom panel shows how the significance changes, if the cut value is continuously increased. Hence, the significance distribution should be read from left to right. This means that the values for  $s$  and  $b$ , that enter Equation 7.4, are the ones obtained by integrating all signal, respectively background events, in which the variable has a value greater than a given threshold. Vice versa, for a cut which restricts a variable from above (cuts with “ $<$ ” or “ $\leq$ ”), e.g. the number of central small-R jets, the significance panel should be read from right to left.

In this optimisation,  $N - 1$  plots are used complementary to the *ahoi* cut scans: After a few promising cut combinations are identified with *ahoi*, the associated  $N - 1$  plots are created. Based on these, the cut values are adjusted by comparing the significance distributions between the different signals. For example, with the *ahoi* scan a cut may be found to be suitable for one certain signal, but the  $N - 1$  plots could show, that it is too tight for all other signals. The cut is then adjusted to give an adequate sensitivity for all signals. This can modify the distributions of the other variables, which then also may need to be adjusted. Therefore, this step was performed several times before deciding on the final selection.

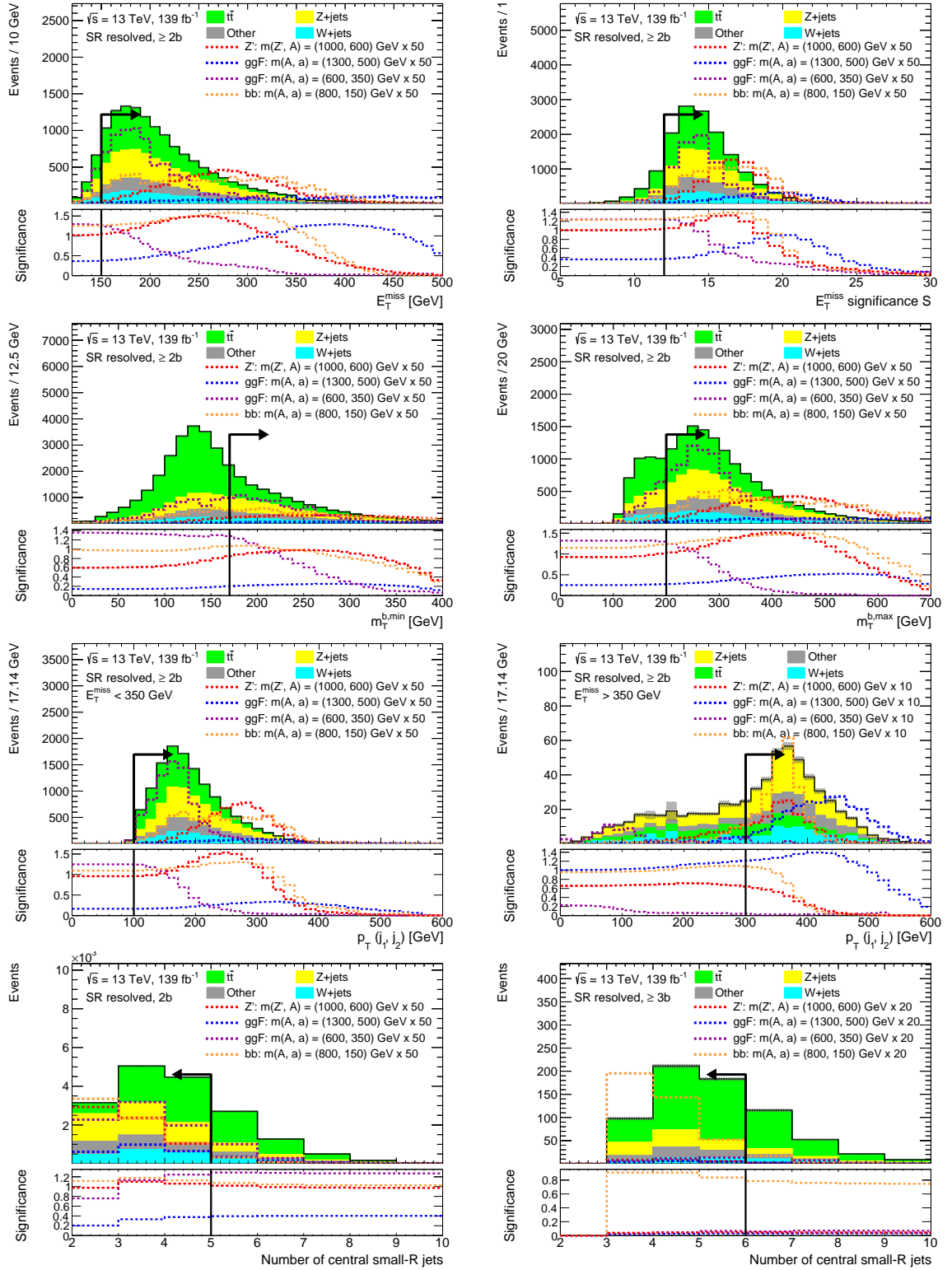


**Figure 7.7:** N-1 plots for selected discriminating variables in the resolved SR, using the definitions of Table 7.5. The signal yields are scaled with the factors indicated in the plot labels. As two different cut values are applied for them,  $p_T(j_1, j_2)$  and  $N(\text{central small-R jets})$  are shown separately for the corresponding  $E_T^{\text{miss}}$  region or  $b$ -jet multiplicity, respectively.

## Results

The optimisation studies have lead to many insights in the kinematic properties of the signal models. For some variables, striking differences between the  $Z'$ -2HDM and 2HDM+ $a$  signals are observed, but eventually a SR definition could be found, which is suitable for most signals. The results of the studies are summarised in the following:

- No significance gain is obtained by loosening the  $b$ -jet requirement to  $\geq 1$   $b$ -jet.
- Allowing for  $E_T^{\text{miss}}$  values down to 120 GeV can increase the significance for signals which have a rather low  $E_T^{\text{miss}}$  spectrum by a few percent. However, with lower  $E_T^{\text{miss}}$ , the contribution from multijet processes becomes larger, so that it may not be possible to neglect this background any more. Thus, to avoid a complication of the analysis it has been decided not to lower the  $E_T^{\text{miss}}$  threshold.
- Due to its large correlation with  $E_T^{\text{miss}}$ , the distribution of  $\mathcal{S}$  is automatically shifted to higher values, when the  $E_T^{\text{miss}}$  threshold is increased. Therefore, the  $E_T^{\text{miss}}$  binning of the search makes a cut on higher  $\mathcal{S}$  redundant. Instead, only a moderate requirement of  $\mathcal{S} > 12$  is applied to suppress the remaining multijet background in the SR.
- The  $t\bar{t}$  background is very efficiently suppressed by the variables  $m_T^{b,\text{min}}$  and  $m_T^{b,\text{max}}$ , for which a cut of 170 GeV and 200 GeV was found to be suitable, respectively.
- In signal events,  $E_T^{\text{miss}}$  and  $p_T(\mathbf{j}_1, \mathbf{j}_2)$  are highly correlated, as illustrated in Figure 7.8 for two representative signals of the  $Z'$ -2HDM and 2HDM+ $a$ . However, this is not necessarily the case for the SM background, so that the sensitivity of the search can be increased if an  $E_T^{\text{miss}}$ -dependent cut on  $p_T(\mathbf{j}_1, \mathbf{j}_2)$  is introduced: For  $E_T^{\text{miss}} < 350$  GeV,  $p_T(\mathbf{j}_1, \mathbf{j}_2)$  is required to be at least 100 GeV, while for  $350$  GeV  $< E_T^{\text{miss}} < 500$  GeV a cut of  $p_T(\mathbf{j}_1, \mathbf{j}_2) > 300$  GeV is applied. An additional cut on the leading  $b$ -jet  $p_T$  does not lead to a notable significance increase and is therefore deprecated.
- The number of central small-R jets depends highly on the signal model: The  $Z'$ -2HDM predicts on average the smallest jet multiplicities, followed by the  $b\bar{b}$  and lastly the ggF-induced 2HDM+ $a$  signals. For most  $Z'$ -2HDM signals, restricting the number of central small-R jets to about three would be optimal, while for the ggF-induced 2HDM+ $a$  samples it would be best not to apply a cut at all. As a compromise, a cut of  $N(\text{central small-R jets}) \leq 4$  and  $\leq 5$  is chosen for  $2b$  and  $3b+$  events, respectively. A looser cut is applied for  $3b+$  events to ensure a sufficiently large data and MC statistics.
- Additional requirements on the  $H_T^{2b}$  and  $H_T^{3b}$ -ratio as well as on  $\Delta R(\mathbf{j}_1, \mathbf{j}_2)$  are useful for the  $Z'$ -2HDM signals, but have no notable effect on the 2HDM+ $a$  signals. For ggF-induced signals in the low- $E_T^{\text{miss}}$  region, i.e. very small or very large  $m_A$ , they even lead to a decrease in sensitivity. Therefore, they are not included in the event selection.

It can be concluded, that the  $Z'$ -2HDM represents signals with an “ideal” mono- $h(b\bar{b})$  signature: The jet multiplicity is relatively low, the two jets from the  $h \rightarrow b\bar{b}$  decay are quite collimated and are responsible for most of the hadronic activity. These models would in

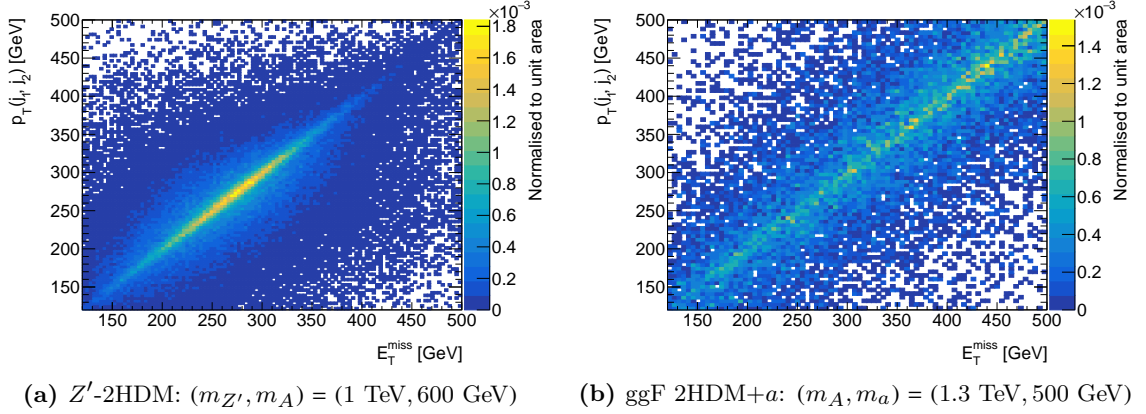


**Figure 7.8:** Number of events as a function of  $p_T(\mathbf{j}_1, \mathbf{j}_2)$  and  $E_T^{\text{miss}}$  for two representative signals, normalised to unit area.

general profit from a tighter selection, including e.g. also cuts on the  $H_T^{2b}$  or  $H_T^{3b}$ -ratio and on  $\Delta R(\mathbf{j}_1, \mathbf{j}_2)$ . A more comprehensive description of the  $Z'$ -2HDM signal kinematics can be found in Ref. [197], which shows a dedicated optimisation for these signals and discusses possible SR definitions. The results of these studies also served as basis for the optimisation presented in this work. However, the 2HDM+ $a$  signals are kinematically more similar to the SM background, especially the ggF-induced models in the low- $E_T^{\text{miss}}$  region. Therefore, a more conservative event selection is chosen for this search. Ideally, one would define separate SRs for these models. Since the  $Z'$ -2HDM and 2HDM+ $a$  signal models differ in the jet multiplicity, it has been considered to use the number of jets could as additional fit category. However, this leads to a relatively low statistics in some regions of the analysis, e.g. in the  $E_T^{\text{miss}}$  range of 350 GeV – 500 GeV, and also to a complication of the fit setup. Therefore, it was decided not to use the jet multiplicity as fit category and instead define the SR as a compromise, which allows for an adequate sensitivity for all signal models. The SR definition is summarised in Table 7.5 and the  $N - 1$  plots for the most important discriminating variables are shown in Figure 7.7.

Compared to the event selection of the  $79.8 \text{ fb}^{-1}$  analysis (c.f. Table 6.4), several multijet reduction cuts are missing in the new SR definition. The impact of the different multijet reduction variables were carefully investigated and a multijet estimate was repeated for the new event selection, following the ABCD method presented in Section 6.3.3. These studies showed, that with the cuts on  $\mathcal{S}$  and  $\Delta\phi(\mathbf{E}_T^{\text{miss}}, \mathbf{j}_{1,2,3}^{\text{centr.}+\text{forw.}})$  the multijet background is already negligibly small, so that no additional requirements on  $\Delta\phi(\mathbf{E}_T^{\text{miss}}, \mathbf{p}_T^{\text{miss,track}})$ ,  $\Delta\phi(\mathbf{j}_1, \mathbf{j}_2)$  and  $\Delta\phi(\mathbf{p}_T, \mathbf{h}_{\text{reco}})$  are needed.

The left-hand plots in Figure 7.9 show the significance obtained with the newly defined resolved SR for all signal models studied, shown as a function of their  $m_{Z'}/m_a$  and  $m_A$  values. Also the effect of the shape fit is partially indicated: Events are selected separately in the three  $E_T^{\text{miss}}$  bins of 150 – 200 GeV, 200 – 350 GeV and 350 – 500 GeV. These are further categorised into  $2b$  and  $3b+$  events, thus resulting in six different bins in total. For simplicity, the  $m_{jj}$  binning is neglected in this study. Instead, only the requirement  $70 \text{ GeV} < m_{jj} < 140 \text{ GeV}$  is

imposed. For each of these six bins, the significance is calculated using Equation 7.4. Finally, the total significance  $Z$  for the resolved SR is estimated by:

$$Z = \sqrt{\sum_i Z_i^2}, \quad (7.5)$$

where  $Z_i$  is the significance obtained for the  $i$ -th of the six bins. Equation 7.5 represents an approximation for the total significance of a search, which is generally valid as long as the impact of statistical and systematic uncertainties in the individual bins is small enough. For the  $Z'$ -2HDM and the ggF-induced 2HDM+ $a$  grid, several signal models have a significance above the evidence threshold of  $3\sigma$ , while for the  $b\bar{b}$ -induced 2HDM+ $a$  grid this is only the case for two signals. By comparing the ggF and  $b\bar{b}$ -induced signal points with the same  $m_A$  and  $m_a$  values one can see, that the significance for the  $b\bar{b}$ -induced 2HDM+ $a$  signals is all over the grid much lower than for the ones from ggF production. The reason for this is that the  $b\bar{b}$ -induced signals have a larger contribution from non-resonant production modes, so that they usually have a lower  $E_T^{\text{miss}}$  spectrum than the ggF-induced signals. Consequently, the  $b\bar{b}$ -induced signals also have a larger fraction of events which do not pass the  $E_T^{\text{miss}}$  cut of  $> 150$  GeV. This leads to a smaller acceptance of signal events and thus also to a lower sensitivity. More details on this can be found in Appendix B.

To quantify the improvement with respect to the previous search, the significance is also evaluated for the resolved SR of the  $79.8 \text{ fb}^{-1}$  search, but using an integrated luminosity of  $139 \text{ fb}^{-1}$  to allow for a fair comparison. A few modifications are added to the event selection the  $79.8 \text{ fb}^{-1}$  search: The cut  $\mathcal{S} > 16$  is reduced to a value of  $> 12$  to account for the changes in  $\mathcal{S}$  due to the updated jet calibrations. Furthermore, also the requirement on  $\Delta\phi(\mathbf{E}_T^{\text{miss}}, \mathbf{p}_T^{\text{miss,track}})$  is omitted<sup>1</sup>. With this selection, the significance in the region  $70 \text{ GeV} < m_{jj} < 140 \text{ GeV}$  is determined separately for the three different  $E_T^{\text{miss}}$  bins, using only the  $2b$  category as in the  $79.8 \text{ fb}^{-1}$  search. Again, the total significance of the resolved SR is calculated from Equation 7.5. The right-hand plots in Figure 7.9 show the ratio of the significances obtained with the optimised and the old resolved SR. For all points of the three signal grids, the ratio is always greater than one, which means that the new event selection leads to a significance improvement for all signal points studied. The significance increase in the three different signal grids ranges from about 10 – 50% for the  $Z'$ -2HDM and 5 – 30% for the ggF-induced 2HDM+ $a$  signals (neglecting some statistically limited outlier points, e.g.  $(m_A, m_a) = (400 \text{ GeV}, 150 \text{ GeV})$  with a significance which is highly different compared to the neighbouring points). The largest ratios are seen for the  $b\bar{b}$ -induced 2HDM+ $a$  signals, for which an improvement of approximately 50 – 100% is achieved. This sensitivity increase is mostly attributed to the newly introduced  $3b+$  category. Without it, the significance ratios are comparable to the ones obtained for the ggF-induced 2HDM+ $a$  signals.

It was also studied, whether the analysis may profit from  $1b$  events, if they are added as separate fit categories. For this, the significance comparison is repeated by introducing three additional  $E_T^{\text{miss}}$  bins with  $1b$  events. This did not lead to a notable improvement compared to the setup with the  $2b$  and  $3b+$  categories only, and therefore it is not used here.

<sup>1</sup>The cut on  $\Delta\phi(\mathbf{E}_T^{\text{miss}}, \mathbf{p}_T^{\text{miss,track}})$  has initially been introduced to remove effects from non-collisional background which was found to be negligible with the object definitions of this analysis and after imposing  $b$ -tag requirements.

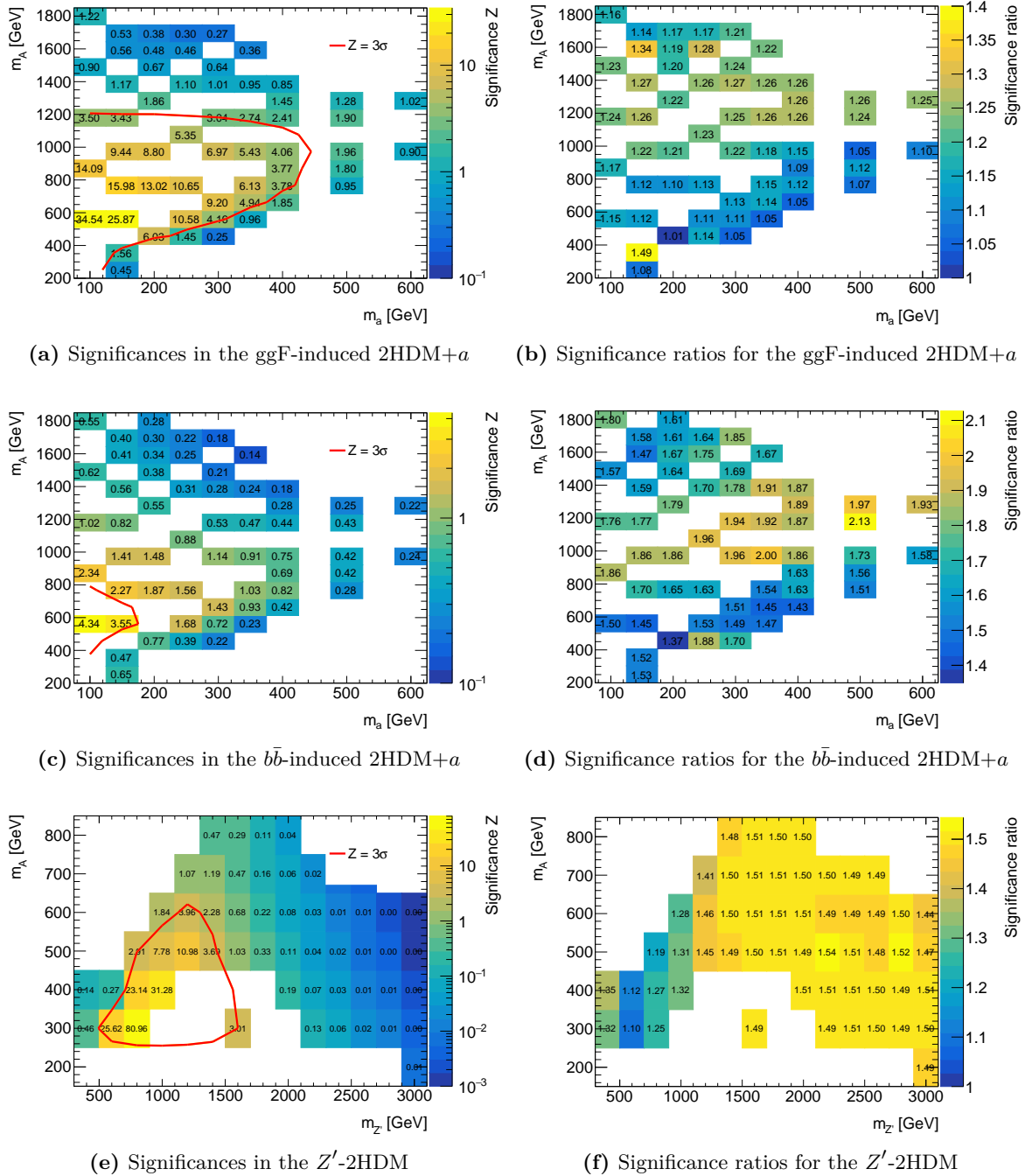


**Figure 7.9:** Significances in the resolved region for the different signal points used in the search (left) and the significance ratios with respect to the old event selection (right). The  $Z'$ -2HDM grid corresponds to the one with  $m_H = m_{H^\pm} = 300 \text{ GeV}$ . The red line indicates the  $3\sigma$  contour for the discovery significance.

Resolved	Merged
lowest unrescaled $E_T^{\text{miss}}$ trigger	
veto on baseline light leptons and $\tau$ -leptons	
$E_T^{\text{miss}} > 150$ GeV	
$\Delta\phi(\mathbf{E}_T^{\text{miss}}, \mathbf{j}_{1,2,3}^{\text{centr.}+\text{forw.}}) > 20^\circ$	
$E_T^{\text{miss}} < 500$ GeV	$E_T^{\text{miss}} > 500$ GeV
extended $\tau$ -veto, resolved	extended $\tau$ -veto, merged
$N(\text{central small-R jets}) \geq 2$	$N(\text{central large-R jets}) \geq 1$
$N(b\text{-jets}) \geq 2$	VR <sub>1</sub> and VR <sub>2</sub> $b$ -tagged
$S > 12$	$\Delta R(\mathbf{VR}_{1,2}, \mathbf{VR}_i) > R_{\min}$
$p_T(\mathbf{j}_1, \mathbf{j}_2) > 100$ GeV if $E_T^{\text{miss}} < 350$ GeV, $p_T(\mathbf{j}_1, \mathbf{j}_2) > 300$ GeV if $E_T^{\text{miss}} \geq 350$ GeV	—
$m_T^{b,\min} > 170$ GeV	—
$m_T^{b,\max} > 200$ GeV	—
$N(\text{central small-R jets}) \leq 4$ if $N(b\text{-jets}) = 2$ , $N(\text{central small-R jets}) \leq 5$ if $N(b\text{-jets}) \geq 3$	—
$50 \text{ GeV} < m_{jj} < 280 \text{ GeV}$	$50 \text{ GeV} < m_J < 270 \text{ GeV}$

**Table 7.5:** Event selection in the resolved and merged SR. Table adapted from Ref. [60].

### 7.3.4 Event selection in the merged SR

After the optimisation of the resolved SR, also the event selection of the merged SR has been re-evaluated following the same optimisation strategy as presented before. Events are studied after the preselection of the merged region, as described in Section 7.3.1. In addition to these, also the requirements  $\Delta\phi(\mathbf{E}_T^{\text{miss}}, \mathbf{j}_{1,2,3}^{\text{centr.}+\text{forw.}}) > 20^\circ$  and  $70 \text{ GeV} < m_J < 140 \text{ GeV}$  are applied. The discriminating variables considered in this optimisation are  $E_T^{\text{miss}}$ , the  $H_T$ -ratio variable as used in the preceding searches (c.f. Section 6.2.3), the leading large-R jet  $p_T$  and the number of large-R jets. The latter two constitute the equivalents of  $p_T(\mathbf{j}_1, \mathbf{j}_2)$  and the number of central small-R jets in the resolved region. For the  $Z'$ -2HDM several signals with  $m_{Z'} > 1.5 \text{ TeV}$  are chosen for this study. As mentioned before, signals of the 2HDM+ $a$  mostly lie in the resolved SR. However, some signal models, such as  $(m_A, m_a) = (1.3 \text{ TeV}, 500 \text{ GeV})$  of the ggF-induced samples, also have a considerable fraction of events with  $E_T^{\text{miss}} > 500 \text{ GeV}$ , as shown in Figure 7.2. Therefore, they are included in the optimisation, too. Generally, the significance to the  $Z'$ -2HDM signals can be increased by including cuts on all of the variables described above. Similar to the resolved SR,  $E_T^{\text{miss}}$  and the leading large-R jet  $p_T$  are highly correlated and the optimal cut values for them depend on how strongly boosted

a given signal is. For  $E_T^{\text{miss}}$ , this is illustrated by the  $N - 1$  plot in Figure 7.10. However, as discussed in Section 7.3.2, in the 2HDM+ $a$  the signals typically have smaller  $E_T^{\text{miss}}$  than in the  $Z'$ -2HDM and only few signal models have a considerable fraction of events with  $E_T^{\text{miss}} > 500$  GeV. For most of the 2HDM+ $a$  points, increasing the  $E_T^{\text{miss}}$  threshold leads to a decrease in the sensitivity. Furthermore, including cuts on the  $H_T$ -ratio, the leading large-R jet  $p_T$  and the number of large-R jets results in a reduction of the significance, too. Consequently, the significance is predominantly driven by the signal acceptance. Therefore, no new discriminating variables are added to the event selection of the merged SR and also the previously used  $H_T$ -ratio requirement is removed.

With the chosen event selection the 2HDM+ $a$  signal kinematics are favoured over the  $Z'$ -2HDM. However, a possibility to increase the sensitivity to the highly-boosted  $Z'$ -2HDM signals, while at the same time preserving the sensitivity to the less boosted signals, is to split the merged region into two, or even more,  $E_T^{\text{miss}}$  bins. As this is a statistically limited region, it needs to be studied with all systematic uncertainties included, which binning choice is realisable. A discussion on this is given in Section 7.5.

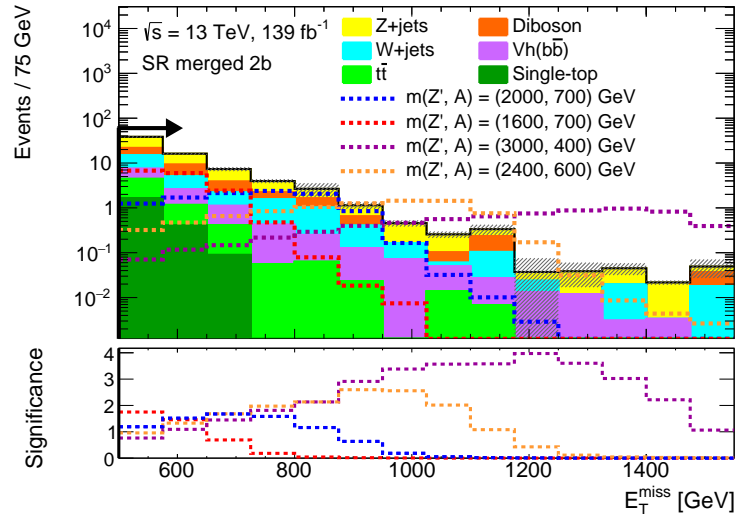


**Figure 7.10:**  $N-1$  plot for the  $E_T^{\text{miss}}$  distribution in the merged  $2b$  SR, shown for representative signals of the  $Z'$ -2HDM with  $m_H = m_{H^\pm} = 300$  GeV. The shaded area shows the statistical uncertainty of the SM background. One can see that with increasing  $m_{Z'}$ , the maximum of the significance curve moves to higher values, indicating that these signals would prefer a higher  $E_T^{\text{miss}}$  threshold than 500 GeV. This motivates to also divide the merged SR into multiple  $E_T^{\text{miss}}$  bins.

The impact of including the  $1b$  and  $3b+$  categories in the analysis has also been studied for the merged SR. Events are considered to be in the  $1b$  region, if only one of the leading two track jets associated to  $h_{\text{reco}}$  is  $b$ -tagged and if there are no additional  $b$ -tagged track jets outside of  $h_{\text{reco}}$ . In the  $3b+$  region, the two leading track jets associated to  $h_{\text{reco}}$  are required to be  $b$ -tagged and, additionally, there needs to be at least one non-associated  $b$ -tagged track jet in the event. This is motivated by the production diagrams of the  $b\bar{b}$ -induced 2HDM+ $a$  signals (c.f. Figure 2.9): The two  $b$ -quarks, which do not originate from the  $h \rightarrow b\bar{b}$  decay, are expected to be emitted in relatively forward direction, so that they should be well separated

from  $h_{\text{reco}}$ . As for the resolved region, the  $1b$  fit category has a marginal impact on the significance for all signal models, while the  $3b+$  region helps to improve the significance for the  $bb$ -induced 2HDM+ $a$  signals. Therefore, only the  $3b+$  category is included in the analysis.

With respect to the  $79.8 \text{ fb}^{-1}$  search, the event selection in the merged region contains another modification regarding the overlap removal of VR track jets. Previously, it was only required that the leading two associated track jets of  $h_{\text{reco}}$  are not concentric (c.f. Section 6.2.3). However, this still leaves the possibility that they are concentric with other track jets. Therefore, the requirement of the  $78.8 \text{ fb}^{-1}$  analysis,  $\Delta R(\mathbf{VR}_1, \mathbf{VR}_2) > R_{\min}$ , is extended to  $\Delta R(\mathbf{VR}_{1,2}, \mathbf{VR}_i) > R_{\min,i}$ . Here,  $\mathbf{VR}_i$  denotes any of the other track jets associated to  $h_{\text{reco}}$  and  $R_{\min,i}$  the corresponding minimum radius of  $\mathbf{VR}_i$  and  $\mathbf{VR}_1$ , respectively  $\mathbf{VR}_2$ .

The event selection criteria of the merged SR in this search are summarised in Table 7.5.

## 7.4 Background estimation

Because of the optimised selection and the new  $3b+$  fit category,s it is also necessary to reevaluate the background estimation strategy. Figure 7.11 shows the background compositions before the simultaneous fit in the resolved and merged SR for the  $2b$  and  $3b+$  channels, respectively. Compared to the  $79.8 \text{ fb}^{-1}$  search (c.f. Figure 6.3), the  $t\bar{t}$  contamination in the resolved  $2b$  SR decreased from 52% to 34%. In this analysis, the dominant background comes no longer from  $t\bar{t}$ , but from  $Z$ +jets processes which constitute an irreducible background. This improvement is attributed to the newly introduced cuts on  $m_{\text{T}}^{b,\min}$ ,  $m_{\text{T}}^{b,\max}$  and the number of central small-R jets, which effectively reduce the  $t\bar{t}$  background. In the  $3b+$  channels,  $t\bar{t}$  processes are still the largest background in both the resolved and merged SR. In general,  $t\bar{t}$ ,  $Z$ +jets and  $W$ +jets remain the three dominant backgrounds in the various SR channels. For  $W/Z$ +jets, the dominant contribution comes from heavy-flavour (HF) processes. Therefore, the background estimation strategy can generally be adopted from the previous search: A  $1\mu$ -CR is used to estimate  $t\bar{t}$  and  $W$ +HF processes, a  $2\ell$ -CR for  $Z$ +HF. However, the CR definitions need to be readjusted to the new event selection of the SR. In this context, also other CR-specific assumptions and selections, which were used in previous analysis iterations, should be revised. Similar to the SR, the CRs are largely based on the definitions used in earlier iterations of the SM  $Vh(b\bar{b})$  search and were not explicitly tested for the mono- $h(b\bar{b})$  analysis. This motivates to perform a thorough optimisation of the CRs, too. In the following, the corresponding studies are presented. As explained in Section 7.3.3, with the new event selection it is not necessary to include a multijet estimation into the analysis. Hence, this will not be further discussed.

### 7.4.1 $1\mu$ -CR

In previous mono- $h(b\bar{b})$  searches, a  $1\mu$ -CR was used to estimate the  $t\bar{t}$  and  $W$ +HF background, which originates mostly from decay modes with a charged lepton in the final state. The motivation for this is that muons are not included in the reconstruction algorithms of the  $E_{\text{T}}^{\text{miss}}$  trigger. Therefore, the  $E_{\text{T}}^{\text{miss}}$  distribution for  $t\bar{t}$  and  $W$ +jets in  $1\mu$ -CR events, as seen by the trigger, is very similar to the  $E_{\text{T}}^{\text{miss}}$  distribution of  $t\bar{t}$  and  $W$ +jets events in the SR. This makes the event selection of the  $1\mu$ -CR kinematically as close as possible to the SR right

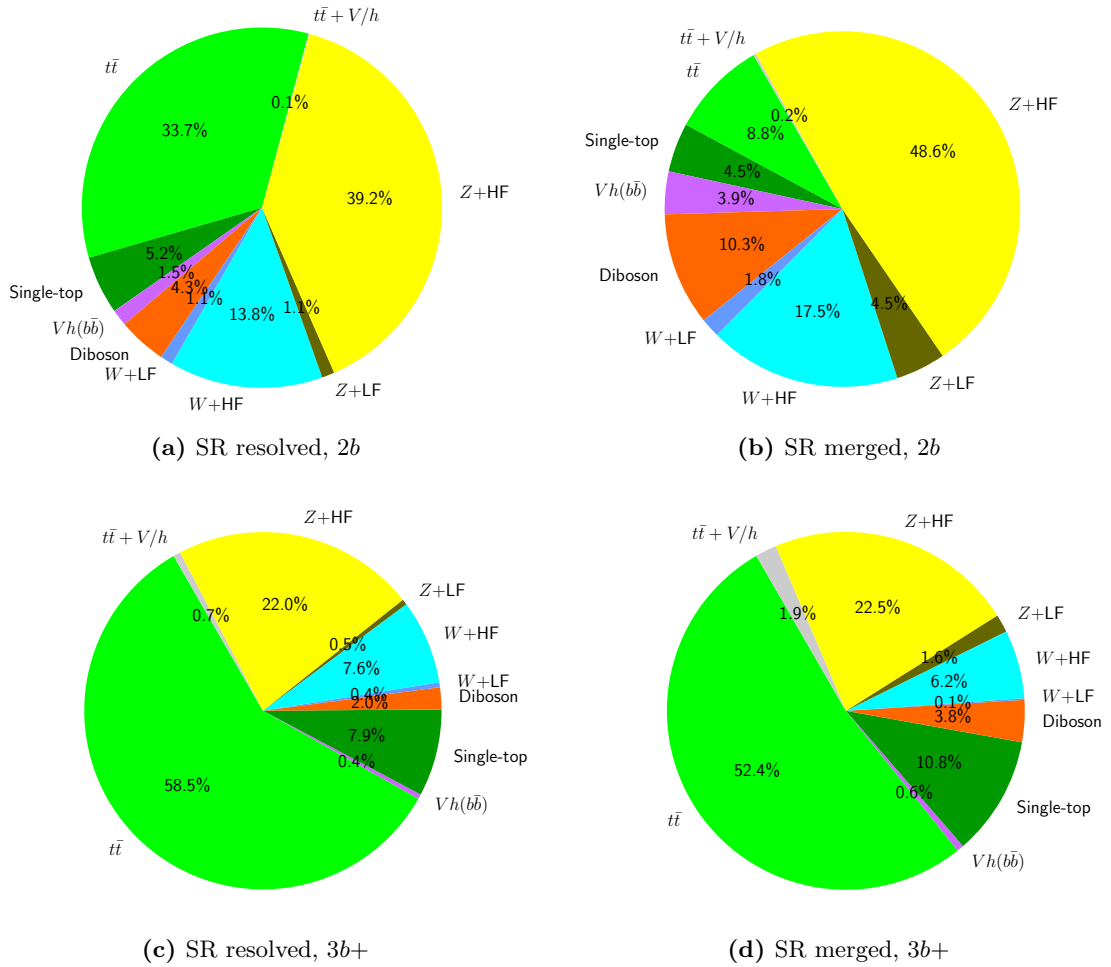


**Figure 7.11:** Background composition in the SR before the simultaneous fit.

from the trigger stage. However, apart from decays with muons,  $t\bar{t}$  and  $W$ +jets events in the SR can also originate from decay modes involving electrons and  $\tau$ -leptons. A dedicated study on this was performed within the  $36.1 \text{ fb}^{-1}$  search, in which it was found that most of the  $t\bar{t}$  and  $W$ +jets events originate from decay modes involving  $\tau$ -leptons. The  $\nu_\tau$  (and the  $\nu_e$  or  $\nu_\mu$  in case of a leptonic  $\tau$ -decay) produced in its decay represents an additional source of  $E_T^{\text{miss}}$ , so that the kinematics of events with a  $\tau$ -lepton may differ from the decay modes with only an electron or a muon [180]. That raises the question, whether a  $1\mu$ -CR alone is sufficient to estimate the kinematic behaviour of  $t\bar{t}$  and  $W$ +jets events from decays with  $\tau$ -leptons.

First, it is studied which decay modes are the most relevant ones with the new SR definitions. For this, the full SR event selection is applied to the  $t\bar{t}$  and  $W$ +jets samples of the search. The events are then classified according their underlying decay modes which, as explained in Section 7.3.2, can be done by using the truth information stored in the MC samples. Figure 7.12 shows the results for  $t\bar{t}$  processes in the resolved and merged SR. As expected, most events come from semi-leptonic decays and the largest fraction of them

involves the production of a  $\tau$ -lepton. On the other hand, dileptonic or full-hadronic processes only play a minor role.

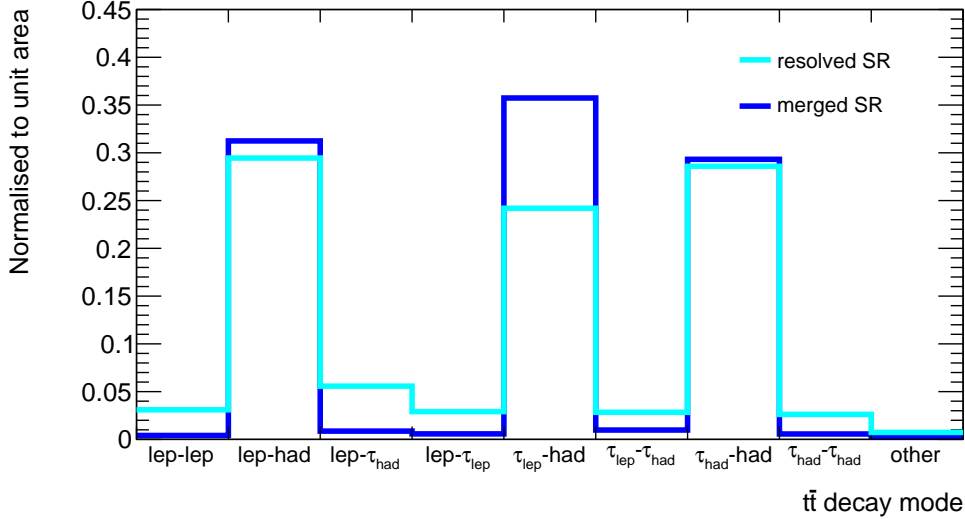


**Figure 7.12:** Fractional contribution of the  $t\bar{t}$  decay modes in the resolved and merged SR. These are inclusive in  $2b$  and  $3b+$  events. The two parts in the labels indicate the decay modes of the top quarks: “lep” denotes a decay in which a light lepton is produced in the subsequent  $W$ -boson decay,  $\tau_{\text{lep}}$  and  $\tau_{\text{had}}$  describe the decays via a leptonically and hadronically decaying  $\tau$ -lepton, respectively, and in the category “had” the  $W$ -boson decays into quarks. Dileptonic decay modes are negligibly small for the merged topology because a Higgs candidate in  $t\bar{t}$  events can typically only be obtained, if a top-quark decays hadronically and if the decay involves a  $c$ -quark. This results in the required large- $R$  jet with two associated track jets, which are initiated by the  $b$  and  $c$ -quark.

Due to the large contribution from decay modes with  $\tau$ -leptons, it is necessary to compare their kinematic properties with the ones involving only light leptons. For this, the shapes of various discriminating variables are plotted separately for the different decay modes. Figure 7.13 shows as an example the distributions of  $m_h$  and  $E_T^{\text{miss}}$  for  $t\bar{t}$  processes in the resolved and merged SR, normalised to unit area. The error bands represent the statistical uncertainty of the MC sample. In general, the distributions agree well with each other. A small disagreement is seen in the  $E_T^{\text{miss}}$  distribution of the resolved SR for events with a leptonically decaying  $\tau$ -lepton. However, if all systematic uncertainties are considered, the distribution still agrees with the other two decay modes within the uncertainties. Therefore, it can be concluded, that a  $1\mu$ -CR is sufficient to appropriately estimate the kinematics of  $t\bar{t}$  and  $W$ +jets events from decay modes involving  $\tau$ -leptons. In the following, the event selection of the  $1\mu$ -CR is summarised.

As in the  $1\mu$ -CR of the  $79.8 \text{ fb}^{-1}$  search, events are selected with  $E_T^{\text{miss}}$  triggers. They are required to have exactly one signal muon with  $p_T > 25 \text{ GeV}$  and no additional baseline muons otherwise. A veto is applied on events containing baseline electrons and  $\tau$ -leptons. To be kinematically as close to the SR as possible, all  $E_T^{\text{miss}}$  and jet-related selections of Table 7.5 are applied in the  $1\mu$ -CR, too. In these,  $E_T^{\text{miss}}$  is again replaced by  $E_T^{\text{miss, no } \mu}$ . Opposed to the previous search, the  $1\mu$ -CR selection of this analysis also contains the requirement

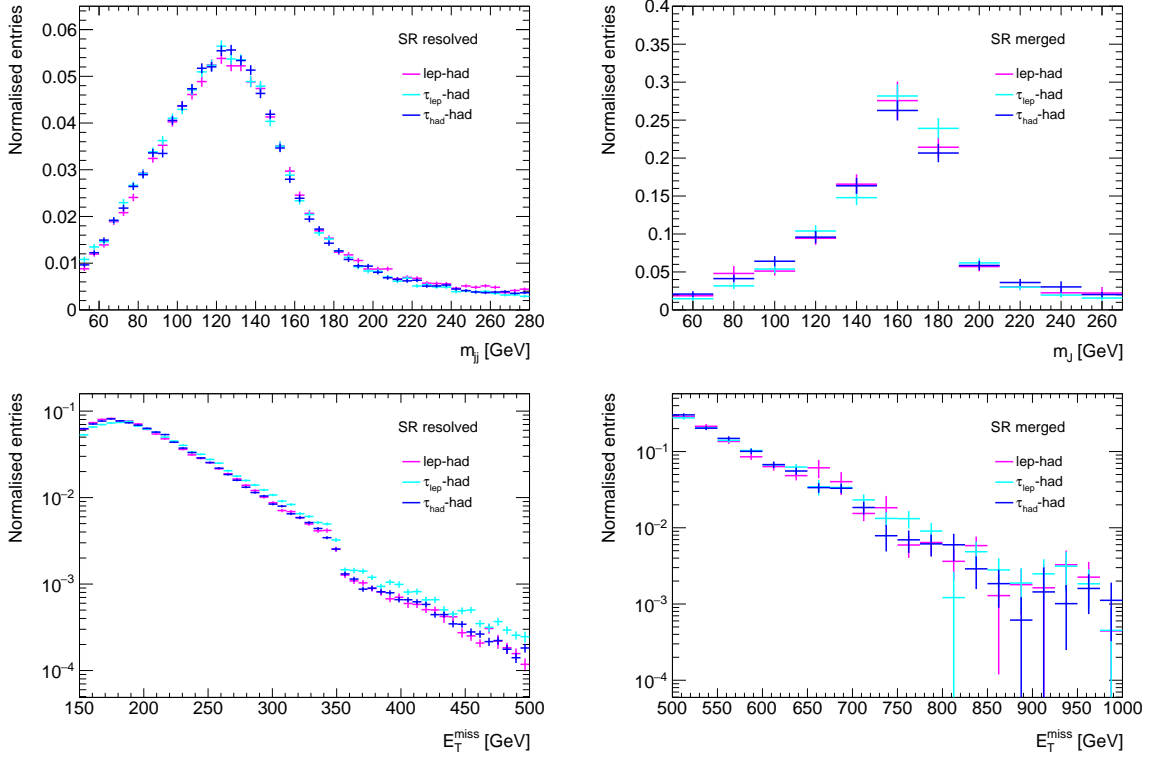


**Figure 7.13:** Distributions of  $m_h$  and  $E_T^{\text{miss}}$  for  $t\bar{t}$  events in the resolved and merged SR, shown separately for semi-leptonic processes with a light lepton, a leptonically or a hadronically decaying  $\tau$ -lepton. The distributions are inclusive in  $2b$  and  $3b+$  events. The error bands show only the uncertainty related to the MC statistics. For the  $E_T^{\text{miss}}$  distribution in the resolved SR, the dip at  $E_T^{\text{miss}} = 350$  GeV is caused by the requirement on  $p_T(\mathbf{j}_1, \mathbf{j}_2)$ , which at this values is increased from  $> 100$  GeV to  $> 350$  GeV (c.f. Table 7.5).

$\mathcal{S} > 12$ , which is calculated using  $E_T^{\text{miss, no } \mu}$  as input for  $E_T^{\text{miss}}$ .

Figure 7.14 shows the background compositions before the simultaneous fit in the resolved and merged  $1\mu$ -CR for the  $2b$  and  $3b+$  channels. All four regions have a high purity in  $t\bar{t}$  and  $W$ +jets events. However, in the  $3b+$  region  $W$ +jets processes constitute only a minor background compared to  $t\bar{t}$ . The signal contamination in the  $1\mu$ -CR is negligible: In a  $h \rightarrow b\bar{b}$  decay, a lepton may only arise from a semi-leptonichadron decays. However, this usually does not pass the isolation criteria.

#### 7.4.2 $2\ell$ -CR

After the  $1\mu$ -CR, also for the  $2\ell$ -CR the motivations behind several event selection criteria are scrutinized. The corresponding studies are performed after a basic preselection: Events of the  $2\ell$ -CR must pass at least one of the single-lepton triggers according to Table 5.3 and the leading lepton needs to satisfy the trigger matching requirements of Section 5.4.1. Furthermore, the events need to have exactly two signal electrons or muons with the quality criteria described in Section 7.2. A veto is applied on additional baseline light leptons and

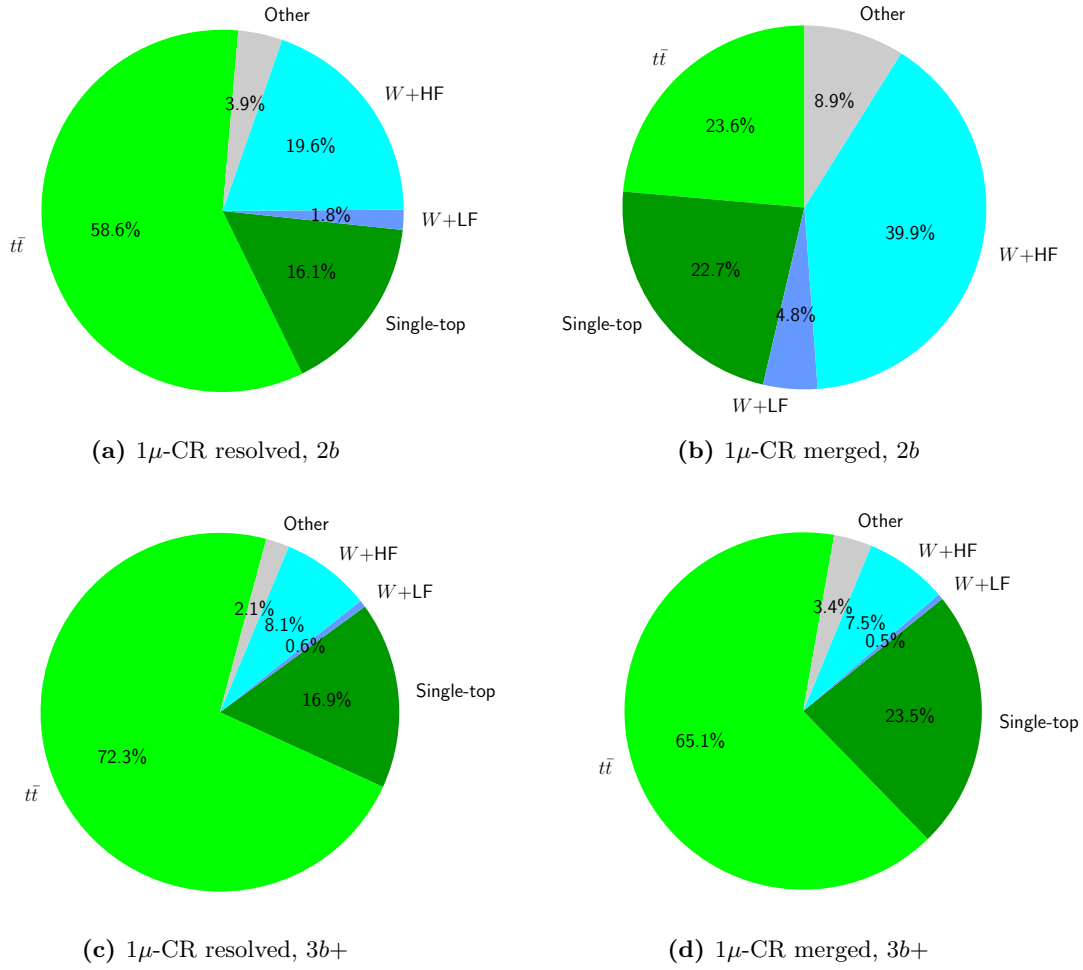


**Figure 7.14:** Background composition in the  $1\mu$ -CR before the simultaneous fit.

$\tau$ -leptons. Moreover, the events must have  $m_h > 40$  GeV and  $\geq 2$   $b$ -tags, i.e.  $\geq 2b$ -jets in the resolved region or a  $h_{\text{reco}}$  with two associated  $b$ -tagged track jets in the merged region.

The first criterion studied is the  $Z$ -boson mass window for  $m_{\ell\ell}$ . In the  $79.8 \text{ fb}^{-1}$  analysis different  $m_{\ell\ell}$  ranges were used for the electron and muon channel (c.f. Section 6.3.1). In this search, the requirement is simplified to  $|m_{\ell\ell} - m_Z| < 10$  GeV. For both channels, this was found to be sufficient enough to reduce the  $t\bar{t}$  background and still keep most of the  $Z$ +jets events. Furthermore, the opposite-sign requirement on the lepton charges is imposed in both the electron and muon channel, because no noticeable acceptance gain in  $Z(\rightarrow l^+l^-)$ +jets events is observed by allowing for same-sign charges.

Another point is the choice of the  $E_T^{\text{miss}}$  proxy. Previously,  $p_T^{\ell\ell}$  was used, as most of the  $E_T^{\text{miss}}$  in  $Z(\rightarrow \nu\bar{\nu})$ +jets events in the SR is expected to come from the two neutrinos. However, there may be a non-negligible amount of  $E_T^{\text{miss}}$  originating e.g. from energy mis-measurements, which is then not taken into account. Following the approach of using  $E_T^{\text{miss, no } \mu}$  in  $1\mu$ -CR, it is studied whether  $p_T^{\ell\ell}$  can be replaced by  $E_T^{\text{miss, no } \ell\ell}$ , which is the  $E_T^{\text{miss}}$  obtained by excluding

the two leptons in the  $E_T^{\text{miss}}$  calculation. Thus, the  $2\ell$ -CR would become kinematically closer to the SR. Figure 7.15 shows the distributions of  $p_T^{\ell\ell}$  and  $E_T^{\text{miss, no } \ell\ell}$  in the resolved region after applying the  $2\ell$ -preselection cuts,  $|m_{\ell\ell} - m_Z| < 10$  GeV and the opposite-sign requirement. The  $Z$ +jets purity is much higher, if  $p_T^{\ell\ell}$  is used as  $E_T^{\text{miss}}$  proxy, while for  $E_T^{\text{miss, no } \ell\ell}$  there is a significant contribution from  $t\bar{t}$  processes. However, after a cut on the  $E_T^{\text{miss}}$  significance, approximately the same  $Z$ +jets purity can be obtained for both  $E_T^{\text{miss}}$  proxy choices. Hence, it was decided to use  $E_T^{\text{miss, no } \ell\ell}$  as new  $E_T^{\text{miss}}$  proxy in the  $2\ell$ -CR.

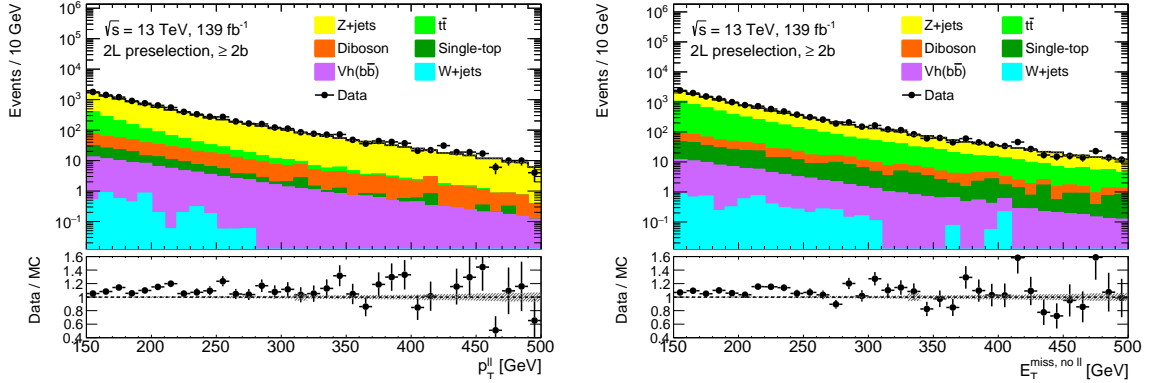


**Figure 7.15:** Distribution of  $p_T^{\ell\ell}$  (left) and  $E_T^{\text{miss, no } \ell\ell}$  (right) after applying the  $2\ell$ -preselection cuts of the resolved topology (i.e. including  $N(b\text{-jets} \geq 2)$  and  $m_{jj} > 40$  GeV),  $|m_{\ell\ell} - m_Z| < 10$  GeV and the opposite-sign requirement.

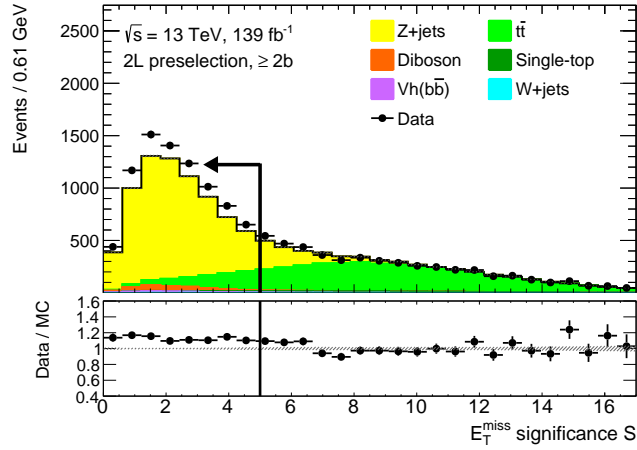


**Figure 7.16:** Distribution of  $\mathcal{S}$  after applying the  $2\ell$ -preselection cuts of the resolved topology (i.e. including  $N(b\text{-jets} \geq 2)$  and  $m_{jj} > 40$  GeV),  $|m_{\ell\ell} - m_Z| < 10$  GeV, the opposite-sign requirement and  $E_T^{\text{miss, no } \ell\ell} > 150$  GeV. A cut value of  $\mathcal{S} < 5$ , as indicated by the arrow, is used to suppress the remaining background in the resolved  $2\ell$ -CR. The reason for the data-MC discrepancy in the left-hand side of the plot comes from a MC mismodelling issue in SHERPA v2.2 affecting the production of  $Z$ +jets with  $b$  and  $c$ -hadrons. .

In this search, the variable  $E_T^{\text{miss}}/\sqrt{H_T}$  is replaced by the object-based  $E_T^{\text{miss}}$  significance  $\mathcal{S}$ . As explained in Section 5.4.1, dileptonic  $t\bar{t}$  processes usually contain a considerable amount of genuine  $E_T^{\text{miss}}$  from the two escaping neutrinos, while the  $E_T^{\text{miss}}$  in  $Z(\rightarrow \ell^+\ell^-)+\text{jets}$  events mostly originates from resolution effects and mis-measurements. Therefore,  $t\bar{t}$  events typically lie at higher values of  $\mathcal{S}$  than  $Z(\rightarrow \ell^+\ell^-)+\text{jets}$ , as shown in Figure 7.16. A cut of  $\mathcal{S} < 5$  has been found to be suitable to suppress most of the remaining  $t\bar{t}$  background. In the merged region with  $E_T^{\text{miss, no } \ell\ell} > 500$  GeV, the  $t\bar{t}$  contamination is negligibly small, as the  $t\bar{t}$  background in the  $2\ell$ -CR originates from dileptonic decays. However, to obtain a Higgs candidate in  $t\bar{t}$  events, one top-quark would need to decay hadronically, thus leading to a large-R jet, and involve a  $c$ -quark in the subsequent  $W$ -boson decay. The  $b$  and the  $c$ -quark can give rise to two  $b$ -tagged associated track jets.

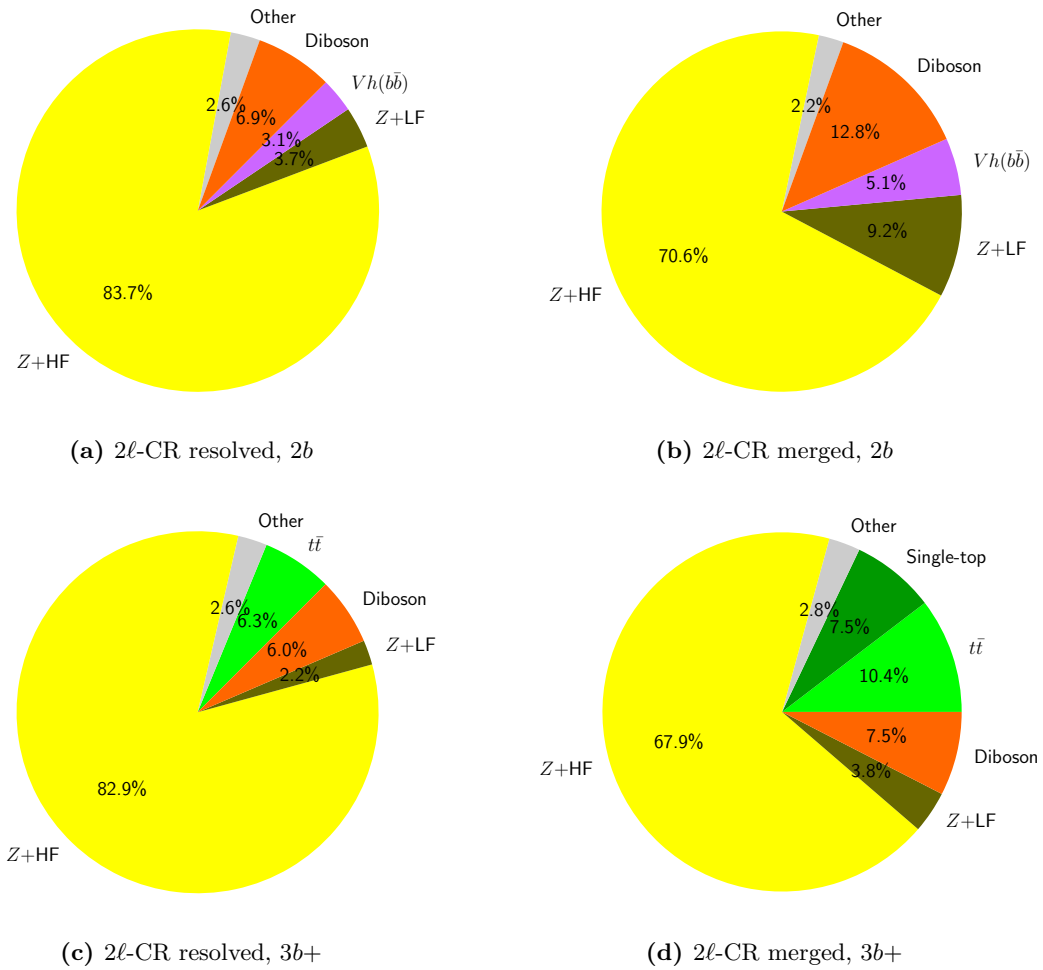


**Figure 7.17:** Background composition in the  $2\ell$ -CR before the simultaneous fit.

The remaining event selection criteria of the  $2\ell$ -CR are used to mimic the SR kinematics. Like in the  $1\mu$ -CR, all  $E_T^{\text{miss}}$  and jet-related cuts of Table 7.5 are applied. That includes also the multijet-reduction cuts, which were not considered in the  $2\ell$ -CR selection of previous

analyses. In all these requirements,  $E_T^{\text{miss}}$  is replaced by  $E_T^{\text{miss, no } \ell\ell}$ . This holds also for  $\mathcal{S} > 12$ , in which  $\mathcal{S}$  is calculated using  $E_T^{\text{miss, no } \ell\ell}$ . Therefore, it is denoted by  $\mathcal{S}^{\text{no } \ell\ell}$ . Consequently, two different versions of the object-based  $E_T^{\text{miss}}$  significance are used in the resolved 2 $\ell$ -CR: The requirement on the standard  $\mathcal{S}$  helps to reduce the  $t\bar{t}$  background, while the one on  $\mathcal{S}^{\text{no } \ell\ell}$  imitates the multijet-reduction cut of the SR.

Figure 7.17 shows the background composition before the simultaneous fit in the resolved and merged 2 $\ell$ -CR for the 2 $b$  and 3 $b$ + channels. All four regions are very pure in  $Z$ +jets events. However, in the 3 $b$ + channels there is a larger contribution from  $t\bar{t}$  events than in the 2 $b$  channels. As in the previous analysis, the 2 $\ell$ -CR is completely signal free.

## 7.5 Statistical analysis

The statistical evaluation of the search results is performed using a binned likelihood fit. The fit setup, e.g. the fit variables in the different regions and their binning, is based on the setup of the 79.8 fb<sup>-1</sup> analysis, which is described in Section 6.4. Therefore, the focus of this section is the description of the newly introduced concepts, which are mainly related to the implementation of the 3 $b$ + category and the high- $E_T^{\text{miss}}$  bin. As explained in Section 7.3, the 2 $b$  and 3 $b$ + categories in the resolved region represent events with exactly two and  $\geq 3$   $b$ -tagged small-R jets, respectively. In the merged region, 2 $b$  (3 $b$ +) means, that the leading two track jets associated to  $h_{\text{reco}}$  are both  $b$ -tagged and that there are no (at least one) additional  $b$ -tagged track jet(s) outside of  $h_{\text{reco}}$ .

Four normalisation factors are applied to scale the  $t\bar{t}$ ,  $W$ +HF and  $Z$ +HF backgrounds. Two of them are used for  $Z$ +HF processes: One for 2 $b$ , the other one for 3 $b$ + events. For  $W$ +HF only a single normalisation factor is used, because the  $W$ +HF contribution is very small in the 3 $b$ + regions. Also for  $t\bar{t}$  a single normalisation factor is applied, as the  $t\bar{t}$  production mechanisms in 2 $b$  and 3 $b$ + events are the same: In most 3 $b$ + events the third  $b$ -tag arises from a falsely  $b$ -tagged  $c$ -initiated (track) jet from the  $W$ -boson decay rather, than from quarks of e.g. initial state radiation processes.

An overview of the different event categories in the fit setup is given in Table 7.6. As in the previous analysis, the fit variable used in the SR is  $m_h$  and in the 2 $\ell$ -CR only the event yield is fitted. In the 1 $\mu$ -CR the muon charge is used again to discriminate  $W$ +jets from  $t\bar{t}$  processes, but only for 2 $b$  events. Due to the low  $W$ +jets contamination in the 3 $b$ + channels of the 1 $\mu$ -CR, only the event yield is fitted there. The  $E_T^{\text{miss}}$  proxy in the SR, 1 $\mu$ -CR and 2 $\ell$ -CR is  $E_T^{\text{miss}}$ ,  $E_T^{\text{miss, no } \mu}$  and  $E_T^{\text{miss, no } \ell\ell}$ , respectively. The resolved SR and CRs are again divided into three  $E_T^{\text{miss}}$ -proxy ranges of [150, 200, 350, 500] GeV. This binning is used for both the 2 $b$  and 3 $b$ + categories. In previous iterations of the analysis only a single  $E_T^{\text{miss}}$  bin of  $> 500$  GeV was used in the merged SR due to the generally low statistics in this region. The increased dataset of 139 fb<sup>-1</sup> allows to split the merged SR without to be statistically limited. For this, different  $E_T^{\text{miss}}$  ranges were studied with respect to their sensitivity and the statistics in the different bins. The best performance was obtained with  $E_T^{\text{miss}}$  ranges of 500 – 750 GeV and  $> 750$  GeV. That results in a significant sensitivity increase of more than 100% for the  $Z'$ -2HDM signals with large  $m_{Z'}$  (estimated from comparing the expected upper limits) [60]. However, splitting the merged region is statistically only feasible for 2 $b$  events in the SR. Thus, a single  $E_T^{\text{miss}}$ -proxy bin of  $> 500$  GeV is used for the 3 $b$ + SR and the CRs.

	<b>0-lepton</b>	<b>1-muon</b>	<b>2-leptons</b>
Fitted observable	$m_h$ distribution	Muon charge ( $2b$ ), yield ( $3b+$ )	yield
Aim	SR	$t\bar{t}$ and $W$ +jets CR	$Z$ +jets CR
$b$ -tag multiplicities	$2b, 3b+$		
$E_T^{\text{miss}}$ proxy	$E_T^{\text{miss}}$	$E_T^{\text{miss, no } \mu}$	$E_T^{\text{miss, no } \ell\ell}$
Binning	Resolved: [150,200], [200,350] and [350,500] GeV $2b$ SR merged: [500,750] and [750, $\infty$ ) GeV Other merged: [500, $\infty$ ) GeV		

**Table 7.6:** Summary of the fit variables and  $E_T^{\text{miss}}$ -proxy ranges used in the analysis. Table adapted from Ref. [198].

The  $m_h$  binning used in this analysis is summarised in Table 7.7. The binning choice for the resolved  $2b$  SR as well as for  $E_T^{\text{miss}} = [500, 750]$  GeV in the merged  $2b$  SR is adopted from the  $79.8 \text{ fb}^{-1}$  analysis. Compared to these, for the  $3b+$  category broader bin widths must be chosen due to the lower data and MC statistics. For  $3b+$  events in the  $E_T^{\text{miss}}$  ranges [150, 200, 350] GeV, a  $m_h$  bin width of 10 GeV is used, while for the range  $E_T^{\text{miss}} = [350, 500]$  GeV and the merged channel a three-bin scheme is applied, i.e.  $m_h$  is divided into three bins, of which the central one covers most of the Higgs boson peak. The bin widths are chosen such as to ensure a sufficient statistics in all three bins. This three-bin approach is also used in the  $2b$  SR for events with  $E_T^{\text{miss}} > 750$  GeV.

$b$ -tags	$E_T^{\text{miss}}$ [GeV]				
	150-200	200-350	350-500	500-750	750- $\infty$
$2b$	5 GeV	5 GeV	10 GeV	20 GeV	3 bins: [50,90,150,270] GeV
$3b+$	10 GeV	10 GeV	3 bins: [50,110,150,280] GeV	3 bins: [50,90,150,270] GeV	

**Table 7.7:**  $m_h$  binning used in the different  $E_T^{\text{miss}}$  and  $b$ -tag bins in the SR. Table adapted from Ref. [198]

To improve the fit stability, the fit variable histograms associated to the nuisance parameters are smoothed and pruned following the procedures described in Section 7.3. In this analysis, one-sided nuisance parameters are additionally symmetrised. Furthermore, if a nuisance parameter has asymmetric up and down variations with respect to the nominal histogram, the averaged values are applied as variations in the fit.

## 7.6 Uncertainties

Different sources of uncertainties are considered as nuisance parameters in the fit. These include uncertainties due to the limited MC statistics and the normalisation factors as well as systematic uncertainties. They are grouped into experimental, i.e. detector-related, and theory uncertainties. The latter describe uncertainties associated to the simulation of the signal and background samples.

### 7.6.1 Experimental uncertainties

Experimental uncertainties arise from the methods used to reconstruct, identify and calibrate the various objects of the search. A comprehensive description on these is given in Chapter 4. Uncertainties related to the energy scale and resolution of the small-R jets (JES and JER, respectively) are implemented using the CategoryReduction [109] scheme. Compared to the strongly reduced set of JES and JER uncertainties used in the 79.8 fb<sup>-1</sup> analysis (c.f. Section 6.5.1), the CategoryReduction preserves more correlational effects between the different uncertainty sources. This represents a more precise treatment of these uncertainty sources, which is not only important for the analysis itself, but especially also for future combination efforts with other DM searches. The uncertainty on the integrated luminosity for the 2015-2018 data-taking periods amounts to 1.7% [81]. Due to inter-year correlations between the luminosity measurements, this value is smaller than the 2% uncertainty used in the 79.8 fb<sup>-1</sup> analysis for the 2015-2017 periods. Uncertainties related to the pile-up reweighting are also in this analysis evaluated by varying the corresponding reweighting factors by 4%. Additional uncertainties are associated to the efficiency calibration of  $E_T^{\text{miss}}$  triggers (c.f. Section 5.4.3) and single-lepton triggers [177, 178].

### 7.6.2 Theory uncertainties

Different sources of theory uncertainties are included in this analysis which are evaluated in the following way:

- **Missing higher orders in the matrix element**

Uncertainties associated to missing higher orders in the calculation of the matrix element are estimated by varying the renormalisation and factorisation scales ( $\mu_R$  and  $\mu_F$ ) independently by a factor of two.

- **PDF and  $\alpha_s$**

The choice of the PDF and the strong coupling constant  $\alpha_s$  constitutes other sources of uncertainties. They are determined following the PDF4LHC prescription [199].

- **Merging scale and resummation**

For samples generated with SHERPA v2.2, i.e.  $W/Z$ +jets and diboson processes, uncertainties are associated to the merging of the matrix element with the parton shower. They are estimated by varying the merging scale by a factor of two. Furthermore, uncertainties related to the resummation procedure used in the parton shower modelling are considered [200].

- **Matching of the matrix element with the parton shower**

For all samples which are generated at NLO ( $t\bar{t}$ , single-top and  $W/Z$ +jets), uncertainties associated to the matching of the matrix element with the parton shower are included. These are derived based on a comparison of the nominal  $t\bar{t}$ , single-top and  $W/Z$ +jets samples with alternative samples, which are generated with MADGRAPH5\_AMC@NLO [146].

- **Parton shower and hadronisation**

Uncertainties related to the modelling of the parton shower and the hadronisation are evaluated by performing a comparison of samples simulated with alternative showering and hadronisation generators. For this, HERWIG7 [201, 202] and MADGRAPH5\_AMC@NLO are used.

- **Eigentune parameters**

Uncertainties are associated to the choice of the set of tuned parameters, which are applied in the hadronisation and showering. Their derivation is described in Ref. [148].

The uncertainties from above are evaluated with respect to their impact on the overall normalisation of the different signal and background processes as well as on the shapes of the fit variables  $m_h$ , the muon charge and the  $E_T^{\text{miss}}$  proxy. No normalisation uncertainties are included for the signal samples, because their normalisation is varied by testing the signal strength  $\mu$ . Also, no normalisation uncertainties are applied to the floating backgrounds, i.e.  $W/Z$ +HF and  $t\bar{t}$ . These instead have uncertainties associated to the normalisation factors obtained from the fit. Furthermore, no theory systematics are assigned to  $t\bar{t}V/h$  processes, because their contribution to the total background in the different SR and CR bins is only  $\mathcal{O}(1\%)$  or less.

### 7.6.3 Impact of uncertainties

Table 7.8 shows the relative impact of the different uncertainties on the signal strength uncertainty for three  $Z'$ -2HDM signals with  $m_H = m_{H^\pm} = m_A$ . These are chosen such as to represent signals from different kinematic regimes: For the signal  $(m_{Z'}, m_A) = (800 \text{ GeV}, 500 \text{ GeV})$  events have an  $E_T^{\text{miss}}$  spectrum that mostly lies within the resolved SR, for  $(m_{Z'}, m_A) = (1.4 \text{ TeV}, 1 \text{ TeV})$  at the boundary of the resolved and merged SR and for  $(m_{Z'}, m_A) = (2.8 \text{ TeV}, 300 \text{ GeV})$  almost exclusively in the merged SR. The first line in Table 7.8 represents the relative impact obtained by fixing all nuisance parameters to their best fit value, so that the effect of systematic uncertainties is ruled out. Therefore, this represents an estimate for uncertainties due to the statistical model chosen. Signals with events predominantly in the merged SR are dominated by the statistical uncertainty, while for signals in the resolved region the largest impact comes from the jet-related uncertainties, the  $t\bar{t}$  normalisation factor as well as from the theory uncertainties.

Source of uncertainty	Impact ( $\Delta\mu/\mu$ ) [%]		
	$(m_{Z'}, m_A)$ [GeV]		
	(800,500)	(1400,1000)	(2800,300)
Total uncertainty	51	52	58
All parameters fixed to best fit value ("statistical uncertainty")	28	42	54
Floating normalization	23	10	2
All normalizations	25	12	4
All but normalizations	39	28	21
Jets	18	11	4
$b$ -tagging	5	8	13
$E_T^{\text{miss}}$ soft term and pile-up	3	3	1
Other detector-related uncertainties	5	4	2
$Z$ +HF normalization	11	7	2
$W$ +HF normalization	8	7	< 1
$t\bar{t}$ normalization	20	5	1
$Z$ theoretical uncertainties	6	10	< 1
$W$ theoretical uncertainties	3	5	< 1
$t\bar{t}$ theoretical uncertainties	10	4	3
Other theoretical uncertainties	20	11	4
Signal uncertainties	< 1	< 1	< 1
MC sample statistics	13	12	14

**Table 7.8:** Breakdown of the uncertainties in the search for representative signal models of the  $Z'$ -2HDM with  $m_H = m_{H^\pm} = m_A$ , expressed as relative uncertainty on the signal strength limit [198]. Due to anti-correlations between the nuisance parameters, the total systematic uncertainties can be smaller than the quadrature sum over the individual sources.

## 7.7 Results

The event yields obtained in the different CR bins after the simultaneous fit are shown in Figure 7.18. The event yields observed in the different  $E_T^{\text{miss}}$  bins for the  $2b$  and  $3b+$  SRs are summarised in Table 7.9 and Table 7.10, respectively. The corresponding  $m_h$  distributions are shown in Figure 7.19 and Figure 7.20, respectively. A good data-MC agreement is seen for all bins. The only exception is the  $E_T^{\text{miss}}$  bin of 350 GeV – 500 GeV of the  $3b+$  category, for which a slight deficit of data compared to the SM predictions is observed around the Higgs boson peak. The data-MC plots and tables correspond to the results obtained with a background-only fit, i.e. the simultaneous fit performed assuming that no signal is present. The discovery significance for the signal+background hypothesis was tested for all signal models studied in this work, too. However, no significant deviation from the background-only predictions was found. The background distributions before this fit are indicated in Figure 7.19 and Figure 7.20 by the blue dashed line.

In most bins of the SR and  $2\ell$ -CR, a small deficit of SM background predictions is seen compared to data. This is corrected in the fit by the normalisation factors and by the nuisance

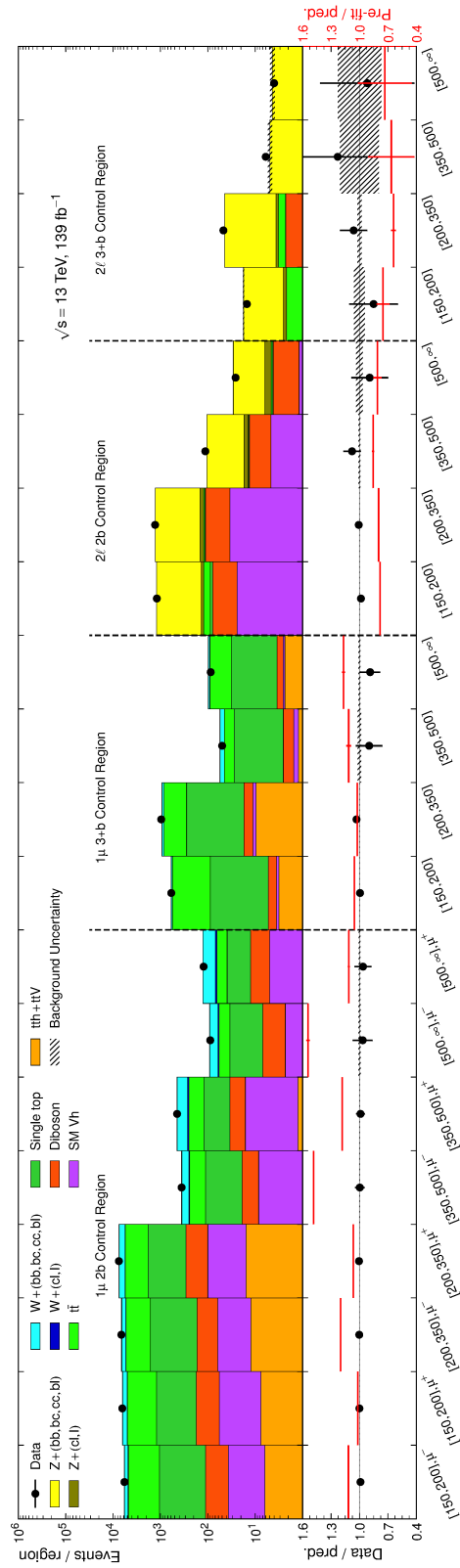


**Figure 7.18:** Data and MC background yields in the different  $1\mu$ -CR and  $2\ell$ -CR bins of the analysis after the background-only fit [198]. The level of agreement between data and MC backgrounds before the fit is indicated by the red lines in the ratio panel.

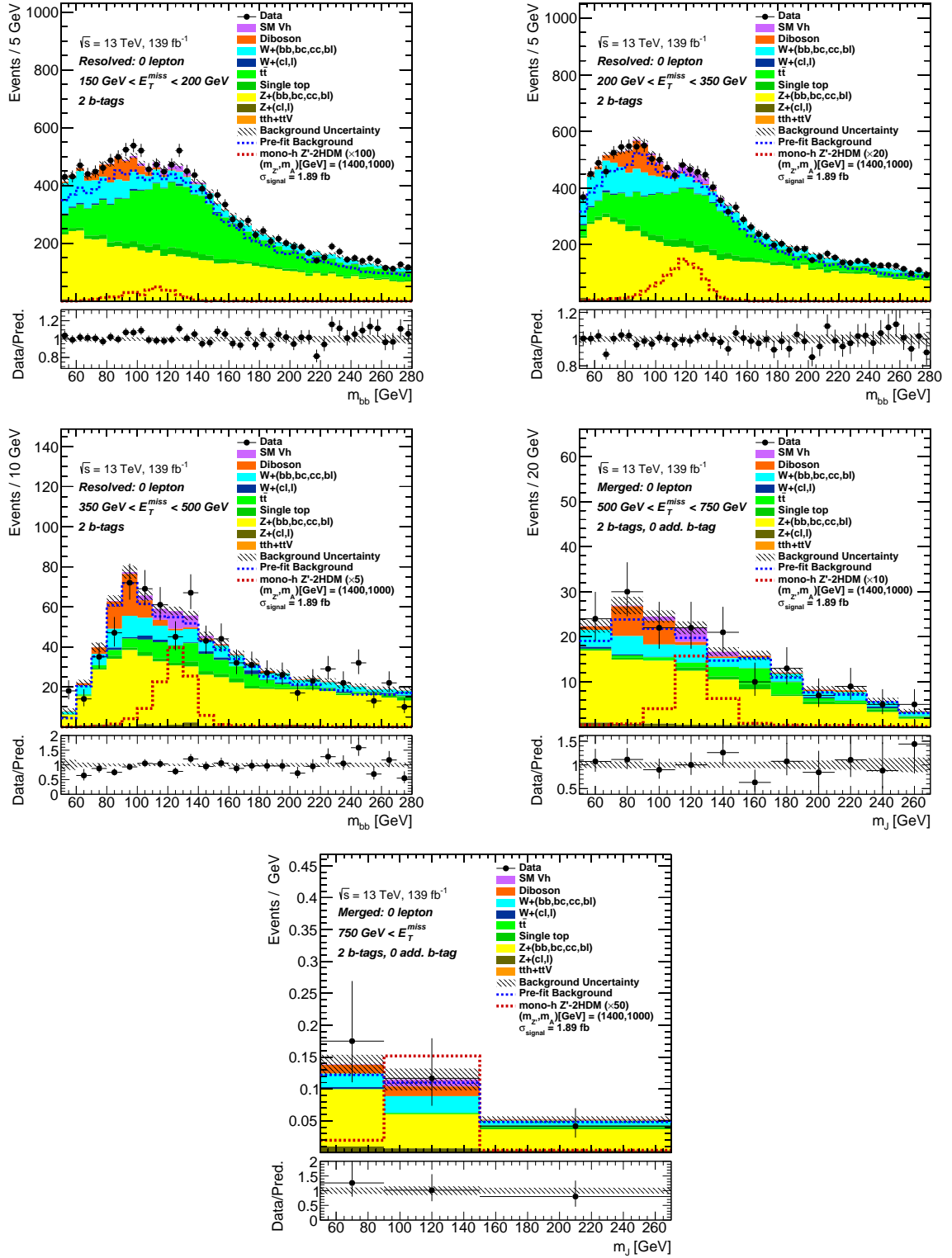


**Figure 7.19:** Distribution of  $m_h$  for data and MC backgrounds in the  $2b$  SR after the background-only fit [198]. The MC background yields before the fit are indicated by the blue dashed line. The distribution of a representative signal from the  $Z'$ -2HDM with  $m_H = m_{H^\pm} = m_A$  is shown by the red line. For visibility, its yields are scaled by a constant factor as indicated in the labels.

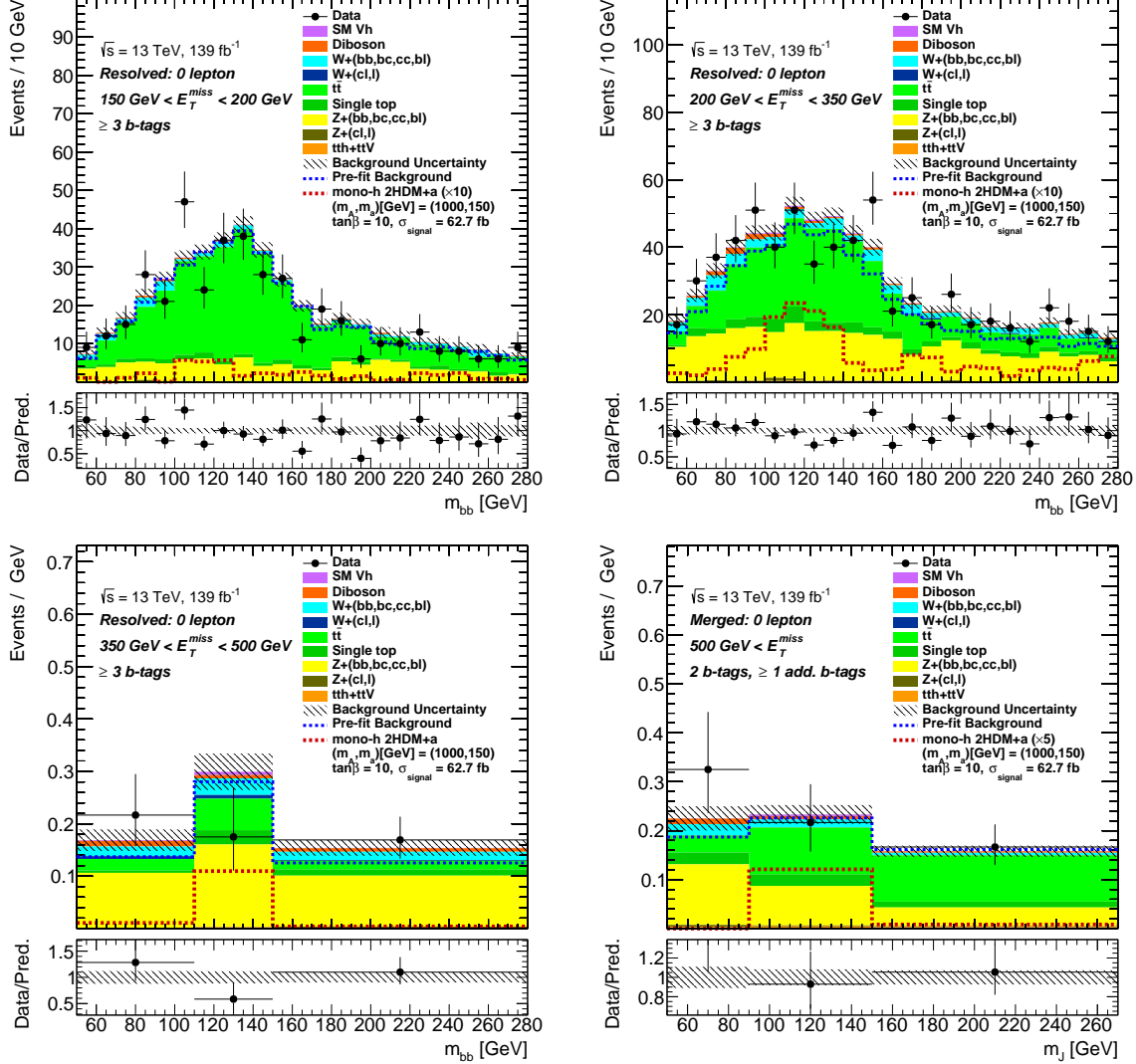


**Figure 7.20:** Distribution of  $m_h$  for data and MC backgrounds in the  $3b+$  SR after the background-only fit [198]. The MC background yields before the fit are indicated by the blue dashed line. The distribution of a representative signal from the  $b\bar{b}$ -induced 2HDM+ $a$  is shown by the red line. For visibility, its yields are scaled by a constant factor as indicated in the labels. The  $m_h$  distribution for signals of the  $b\bar{b}$ -induced 2HDM is broader than for the other models considered in this work, e.g. the  $Z'$ -2HDM signal shown in Figure 7.19. The two spectator  $b$ -quarks in the production mechanism of the  $b\bar{b}$ -induced model lead to ambiguities in the assignment of the  $b$ -jets to  $h_{\text{reco}}$ . The signal entries in the high and low- $m_h$  region thus come from events, in which the leading two  $b$ -jets do not correspond to the Higgs boson decay products.

	2 <i>b</i> , 150-200	2 <i>b</i> , 200-350	2 <i>b</i> , 350-500	2 <i>b</i> , 500-750	2 <i>b</i> , > 750
<i>Z</i> +HF	6410 ± 350	7160 ± 350	508 ± 27	96 ± 7	9.8 ± 1.7
<i>Z</i> +light jets	69 ± 14	130 ± 27	18 ± 4	4.6 ± 1.1	1.21 ± 0.34
<i>W</i> +HF	1540 ± 270	1680 ± 270	101 ± 17	24 ± 4	2.7 ± 0.8
<i>W</i> +light jets	83 ± 32	92 ± 32	14 ± 5	1.7 ± 0.6	0.20 ± 0.08
Single-top	580 ± 130	580 ± 130	21 ± 7	3.2 ± 1.6	0.45 ± 0.28
<i>t</i> $\bar{t}$	4780 ± 260	3400 ± 200	81 ± 7	12.4 ± 1.4	0.44 ± 0.07
Diboson	450 ± 50	600 ± 70	55 ± 8	15.2 ± 1.9	1.59 ± 0.31
<i>Vh</i> ( <i>b</i> $\bar{b}$ )	151 ± 11	202 ± 14	26.5 ± 2.0	5.7 ± 0.6	0.72 ± 0.12
<i>t</i> $\bar{t}$ + <i>V</i> / <i>h</i>	7.7 ± 0.4	11.8 ± 0.5	0.45 ± 0.05	0.287 ± 0.029	0.036 ± 0.006
Total background	14070 ± 110	13860 ± 100	825 ± 19	163 ± 7	17.2 ± 1.9
Data	14259	13724	799	168	19

**Table 7.9:** Observed yields for data and SM backgrounds in the different  $E_T^{\text{miss}}$  bins of the 2*b* SR after the background-only fit [198]. Due to anti-correlations between the nuisance parameters of the search, the total background uncertainties may be smaller than those of the individual processes.

	3 <i>b</i> +, 150-200	3 <i>b</i> +, 200-350	3 <i>b</i> +, 350-500	3 <i>b</i> +, >500
<i>Z</i> +HF	98 ± 14	272 ± 27	26.0 ± 3.3	15.5 ± 1.9
<i>Z</i> +light jets	0.6 ± 0.4	2.8 ± 0.7	0.33 ± 0.11	0.44 ± 0.11
<i>W</i> +HF	20 ± 5	45 ± 10	4.0 ± 1.0	2.2 ± 0.4
<i>W</i> +light jets	0.01 ± 0.04	1.7 ± 0.8	0.7 ± 0.4	0.027 ± 0.024
<i>t</i> $\bar{t}$	281 ± 18	261 ± 20	5.4 ± 0.6	18.5 ± 1.6
Single-top	24 ± 7	56 ± 15	2.7 ± 1.0	3.6 ± 1.0
Diboson	4.7 ± 1.4	12.9 ± 2.3	1.8 ± 0.4	1.24 ± 0.30
<i>Vh</i> ( <i>b</i> $\bar{b}$ )	0.64 ± 0.28	2.9 ± 0.6	0.40 ± 0.08	0.229 ± 0.026
<i>t</i> $\bar{t}$ + <i>V</i> / <i>h</i>	1.77 ± 0.17	3.93 ± 0.26	0.372 ± 0.035	0.79 ± 0.08
Total background	431 ± 15	657 ± 21	42 ± 4	42.6 ± 2.9
Data	408	658	42	46

**Table 7.10:** Observed yields for data and SM backgrounds in the different  $E_T^{\text{miss}}$  bins of the 3*b*+ SR after the background-only fit [198]. Due to anti-correlations between the nuisance parameters of the search, the total background uncertainties may be smaller than those of the individual processes.

parameters with a normalisation effect. The following normalisation factors are obtained:  $0.93 \pm 0.08$  for *t* $\bar{t}$ ,  $0.95 \pm 0.14$  for *W*+HF,  $1.41 \pm 0.09$  for *Z*+HF in 2*b* events and  $1.85 \pm 0.24$  for *Z*+HF in 3*b*+ events. Furthermore, several nuisance parameters have been shifted from their nominal predictions within  $\pm 1\sigma$ , for example some JER uncertainties.

As no excess of data over SM background predictions is seen, exclusion limits are set on the different signal models. The expected and observed exclusion limits for the ggF-induced 2HDM+*a* signals are shown in Figure 7.21. The limits reach up to about 1.6 TeV in  $m_A$  and 520 GeV in  $m_a$ . For comparison, also the exclusion contour from the 36.1 fb<sup>-1</sup> mono-*h*(*b* $\bar{b}$ ) analysis is displayed, which corresponds to the same contour as shown in Figure 2.10. Compared to that, the limits are pushed by approximately 200 GeV in  $m_A$  as well as in  $m_a$ . The results for the *b* $\bar{b}$ -induced 2HDM+*a* signals are shown in Figure 7.22. The observed limits reach up to 1 TeV in  $m_A$  and 300 GeV in  $m_a$ , which deviates up to  $2\sigma$  from the

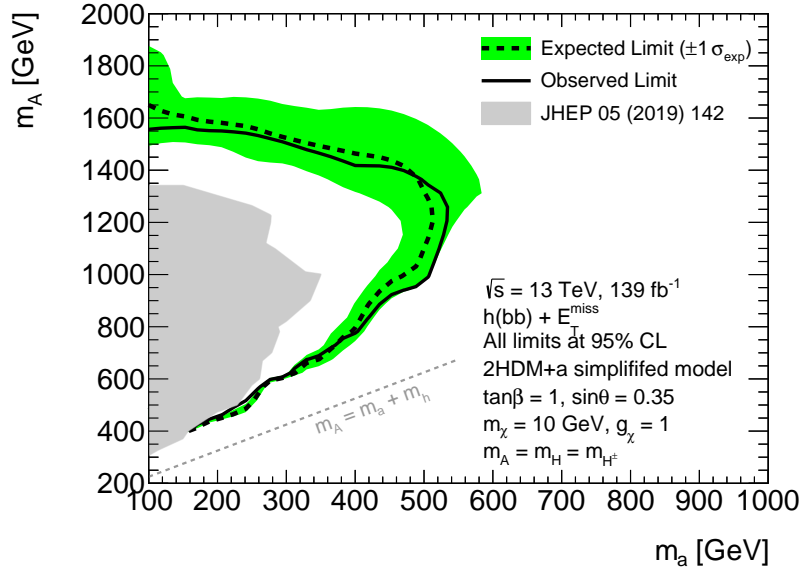


**Figure 7.21:** Observed (solid line) and expected exclusion contour (dashed line) at 95% confidence level along with its  $1\sigma$  uncertainties (green band) for the  $ggF$ -induced 2HDM+ $a$  signals [198]. For comparison, also the observed limit obtained by the  $36.1 \text{ fb}^{-1}$  analysis is shown (grey area), which is taken from Ref. [45]. This corresponds to the mono- $h(bb)$  exclusion contour displayed Figure 2.10.

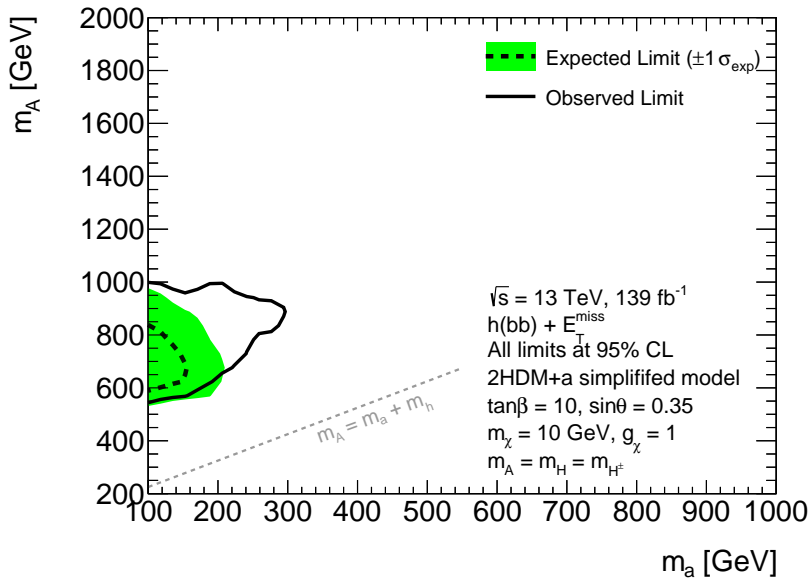


**Figure 7.22:** Observed (solid line) and expected exclusion contour (dashed line) at 95% confidence level along with its  $1\sigma$  uncertainties (green and yellow band, respectively) for the  $bb$ -induced 2HDM+ $a$  signals [198].

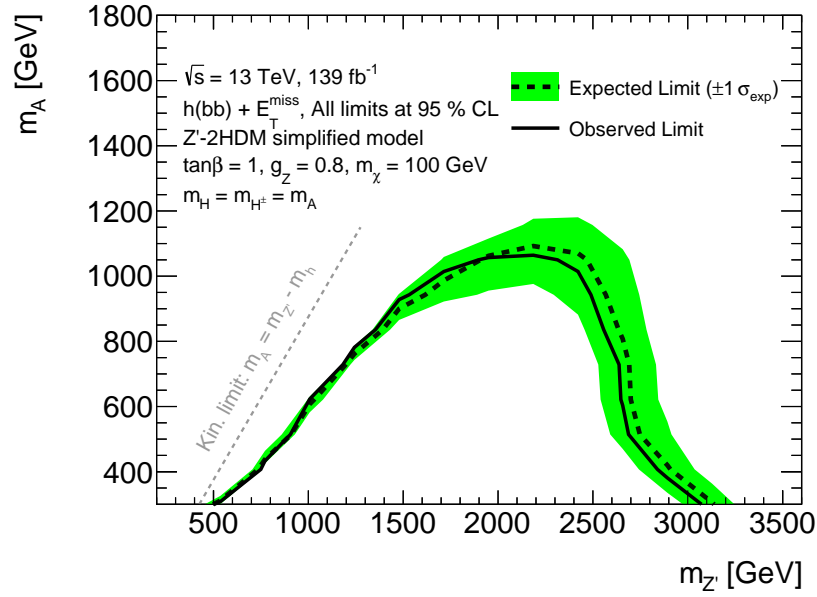


**Figure 7.23:** Observed (solid line) and expected exclusion contour (dashed line) at 95% confidence level along with its  $1\sigma$  uncertainties (green band) for the  $Z'$ -2HDM signals with  $m_H = m_{H^\pm} = m_A$ . [198].

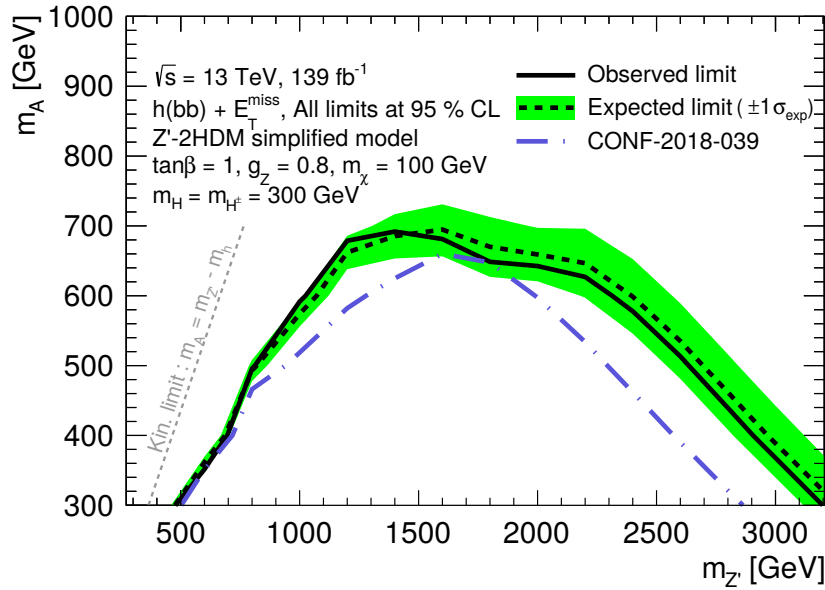


**Figure 7.24:** Observed (solid line) and expected exclusion contour (dashed line) at 95% confidence level along with its  $1\sigma$  uncertainties (green band) for the  $Z'$ -2HDM signals with  $m_H = m_{H^\pm} = 300$  GeV. For comparison, also the observed exclusion contour (purple-blue line) of the 79.8 fb<sup>-1</sup> analysis is shown.

corresponding expected limits. This difference is caused by the data deficit around the Higgs peak for  $E_T^{\text{miss}} = [350, 500]$  GeV in the  $3b+$  SR. The expected and observed exclusion limits for the other signal grids do not show such large differences, because from the models studied in this work only the  $b\bar{b}$ -induced 2HDM+ $a$  signals have a significant contribution of events in the  $3b+$  region. In comparison to the ggF-induced 2HDM+ $a$ , the exclusion contour for the  $b\bar{b}$ -induced models covers a much smaller phase space. As explained in Section 7.3.3, the reason for this is that the acceptance to the  $b\bar{b}$ -induced models is lower, because they have a larger contribution from non-resonant production modes. This leads to a lower  $E_T^{\text{miss}}$  spectrum, so that the signal events do not pass the  $E_T^{\text{miss}}$  trigger requirement and the cut  $E_T^{\text{miss}} > 150$  GeV. Nevertheless, the result in Figure 7.22 demonstrates, that for the first time the mono- $h(b\bar{b})$  search is sensitive to the  $b\bar{b}$ -induced 2HDM+ $a$  signals. This improvement is mostly attributed to the newly introduced  $3b+$  fit category. Without it, none of the signals in the  $m_A - m_a$  plane of Figure 7.22 would lie within the exclusion reach.

The expected and observed exclusion contours for the  $Z'$ -2HDM signal grid with  $m_H = m_{H^\pm} = m_A$  are shown in Figure 7.23. The limits reach up to about 3.1 TeV in  $m_{Z'}$  and 1.1 TeV in  $m_A$ . This is the first time that the mono- $h(b\bar{b})$  analysis is interpreted with this parameter choice. These parameter settings are harmonised with the CMS experiment, which will allow to compare the ATLAS and CMS results in the future. The exclusion contours for the  $Z'$ -2HDM signals with  $m_H = m_{H^\pm} = 300$  GeV are shown in Figure 7.24. The limits in  $m_A$  reach up to 700 GeV. With respect to the  $79.8 \text{ fb}^{-1}$  analysis, the limits could be pushed to higher  $m_A$  values, particularly in the region of about  $800 \text{ GeV} < m_{Z'} < 1.5 \text{ TeV}$  and  $m_{Z'} > 2 \text{ TeV}$ . The limits on  $m_{Z'}$  are pushed to 3.2 TeV, compared to a previous maximum value of 2.7 TeV.

To quantify, how much of this sensitivity improvement comes from the luminosity increase and how much is caused by the new analysis strategy, the expected limit of the  $79.8 \text{ fb}^{-1}$  analysis is scaled up to a luminosity of  $139 \text{ fb}^{-1}$  and compared with the expected limit of this analysis. The results are shown in Figure 7.25: Also with the same luminosity, the expected limit of this analysis exceeds the previous one. In terms of the sensitivity to the  $Z'$ -2HDM signals, the two most important changes in the analysis strategy are the optimised event selection in the resolved region and the additional SR bin of  $E_T^{\text{miss}} > 750$  GeV in the fit setup. Smaller improvements in the sensitivity come e.g. from the updated  $b$ -tagging algorithm and the muon-in-jet correction. The high- $E_T^{\text{miss}}$  bin considerably improves the sensitivity for highly boosted mono- $h(b\bar{b})$  signals models and is thus the main reason for the huge sensitivity increase in the region  $m_{Z'} > 2 \text{ TeV}$ . In the second region with a notable sensitivity increase, i.e. around  $800 \text{ GeV} < m_{Z'} < 1.5 \text{ TeV}$ , the signals predominantly lie in the resolved SR, so that this improvement mostly arises from the optimised event selection presented in Section 7.3.3. Between these two regions with a clear sensitivity improvement, i.e. around  $m_{Z'} = 1.7 \text{ TeV}$ , the two contours are very close to each other. The corresponding signals have a  $E_T^{\text{miss}}$  spectrum that peaks in the lower merged  $E_T^{\text{miss}}$  bin of  $500 - 750$  GeV. Hence, they do not profit much from the additional  $E_T^{\text{miss}}$  bin in the fit setup and the new resolved event selection. As no major changes in the event selection of the merged SR were introduced since the  $79.8 \text{ fb}^{-1}$  analysis, there is thus also no big difference in the sensitivity of the two analyses in this region. Moreover, for  $m_{Z'} < 800 \text{ GeV}$  the two exclusion contours are close to each other as well. These are signals with relatively small  $m_{Z'}$  and small mass differences  $\Delta(m_{Z'}, m_A)$ . Therefore, they generally have a very low  $E_T^{\text{miss}}$  spectrum, which

limits the acceptance and thus also the sensitivity to these models.

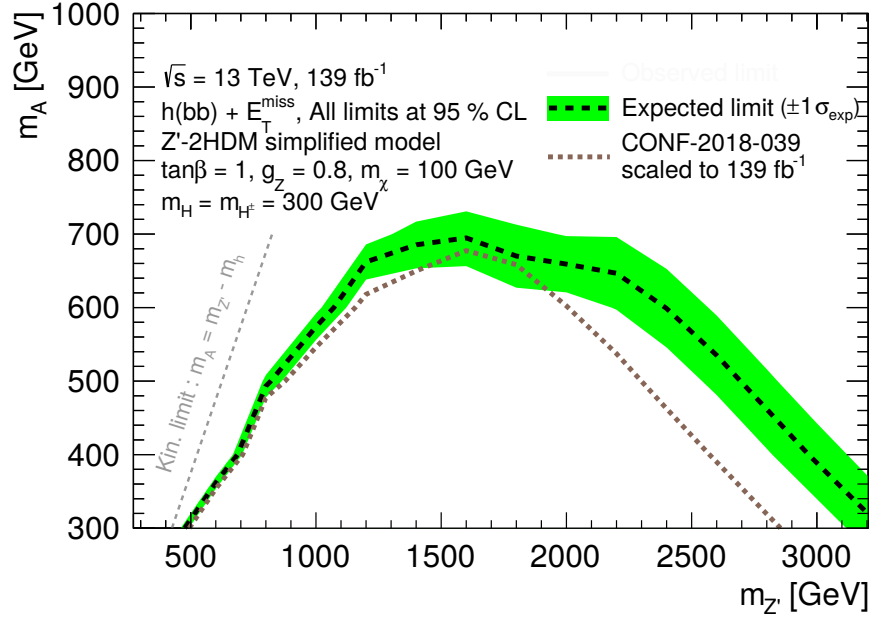


**Figure 7.25:** Expected exclusion limits at 95% confidence level for the  $Z'$ -2HDM with  $m_H = m_{H^\pm} = 300 \text{ GeV}$ . The black dashed line and the green band represent the expected limit of this analysis with its  $1\sigma$  uncertainties. The brown dotted line shows the expected limit of the preceding  $79.8 \text{ fb}^{-1}$  analysis, scaled up to a luminosity of  $139 \text{ fb}^{-1}$ .

# Chapter 8

## Future prospects

In this chapter, future prospects for the mono- $h(b\bar{b})$  analysis are presented. These discuss how the analysis strategy can be further improved, which other DM models can be probed with the analysis and how the sensitivity to certain models can be enhanced by a combination with other DM searches.

### 8.1 Analysis strategy

Several changes in the analysis strategy may lead to an additional sensitivity improvement of the search. For example, signal models with a rather low  $E_T^{\text{miss}}$  spectrum, e.g. the  $Z'$ -2HDM signals with small  $m_{Z'}$  as well as a major part of the  $bb$ -induced 2HDM+ $a$  signals, would profit from a  $E_T^{\text{miss}}$  threshold lower than 150 GeV. With the  $E_T^{\text{miss}}$  trigger calibration strategy presented in Section 5.4.3 it would be possible to extend the  $E_T^{\text{miss}}$  range of the analysis down to at least 120 GeV. With lower  $E_T^{\text{miss}}$  the contribution from multijet processes becomes larger. Therefore, this would also require to reevaluate the multijet-estimation technique.

Moreover, it could be studied whether additional discriminating variables may be found to increase the sensitivity to the different signal models. Particularly, the  $bb$ -induced 2HDM+ $a$  should be carefully investigated because for these signals the sensitivity reach of the analysis is still very limited. A possibility to increase the signal-to-background ratio for these models might be to introduce requirements on forward jets: From Figure 2.9 it is expected, that the two spectator  $b$ -quarks will be emitted opposed to each other in forward direction. Therefore, one could e.g. demand the presence of two forward jets with a large separation in  $\eta$ .

Thus far, the resolved and the merged SR were separated with a sharp cut at  $E_T^{\text{miss}} = 500$  GeV. However, the transition from the resolved to the merged topology actually proceeds continuously with increasing  $E_T^{\text{miss}}$ . This limits the acceptance to signals with a  $E_T^{\text{miss}}$  spectrum around this boundary, e.g. the  $Z'$ -2HDM signals with  $m_{Z'}$  values around 1.5 TeV for the grid with  $m_H = m_{H^\pm} = 300$  GeV. Events from these signals may have  $E_T^{\text{miss}} > 500$  GeV, but could be compatible with the resolved topology, and vice versa for  $E_T^{\text{miss}} < 500$  GeV and the merged topology. Therefore, such signals may profit from additional SR definitions around this  $E_T^{\text{miss}}$  boundary. For example, for the  $E_T^{\text{miss}}$  bins of 350 GeV – 500 GeV and 500 GeV – 750 GeV one could also consider events from the merged and resolved topology, respectively.

Future optimisation studies should also revise the binning choices in the fit setup. In this work it was shown, that the sensitivity to certain signal models can be highly increased by splitting the merged SR into two  $E_T^{\text{miss}}$  ranges. This motivates to study, whether e.g. a finer  $E_T^{\text{miss}}$  binning could be used in the resolved SR.

As shown in Table 7.8, one of the dominant uncertainties in the  $139 \text{ fb}^{-1}$  analysis arises from the  $t\bar{t}$  normalisation. A redefinition of the CRs may help to reduce this uncertainty and thus enhance the sensitivity of the search. Instead of estimating the  $t\bar{t}$  and  $W$ +jets backgrounds together in a  $1\mu$ -CR, one could try to define two separate CRs by following e.g. the approach of the SM  $Vh(b\bar{b})$  analysis [16, 184]. In this, the  $t\bar{t}$  background is estimated using a dilepton CR with an electron-muon pair. By requiring the two leptons to be of opposite flavour the contribution of  $Z$ +jets processes is largely suppressed, so that the resulting selection is very pure in dileptonic  $t\bar{t}$  events. The  $W$ +jets background in the SM  $Vh(b\bar{b})$  analysis is estimated in a single-lepton ( $e$  or  $\mu$ ) region. To enrich the CR in  $W$ +jets events the transverse mass  $m_{\text{T}}^W$  is used. This variable is defined by:

$$m_{\text{T}}^W = \sqrt{2p_{\text{T}}^{\ell} E_{\text{T}}^{\text{miss}} (1 - \cos \Delta\phi(\ell, \mathbf{E}_{\text{T}}^{\text{miss}}))}, \quad (8.1)$$

which is equivalent to the definition of the top-quark mass proxy in Equation 7.3, just that the  $b$ -jet is replaced by the lepton. In single-lepton events  $m_{\text{T}}^W$  thus represents a proxy for the  $W$ -boson mass. Therefore, requiring  $m_{\text{T}}^W \lesssim m_W$  keeps a high fraction of  $W$ +jets events, while effectively reducing other backgrounds such as  $t\bar{t}$ .

## 8.2 Axion-like particles

The  $Z'$ -2HDM and 2HDM+ $a$  signals studied in this work are based on the assumption of WIMP-like DM. However, DM may also be realised in other forms, for example as axions or axion-like particles. These are so-called Nambu-Goldstone bosons which arise from a spontaneous symmetry breaking of a global  $U(1)$  symmetry [2, 203]. This generally predicts massless Nambu-Goldstone bosons. However, they can still acquire masses e.g. due to quantum effects. In this case, they are referred to as pseudo-Nambu-Goldstone bosons. The axion was initially introduced within the Peccei-Quinn mechanism to solve the *strong CP problem*, i.e. to explain why there is apparently no CP violation in QCD interactions. Axion-like particles (ALPs) represent a generalisation of the axion in the sense that they are (pseudo-)Nambu-Goldstone bosons which are not tied to the strong CP problem. With axions and ALPs it is possible to have DM candidates with masses much below the electroweak scale of  $\mathcal{O}(100 \text{ GeV})$ .

In  $pp$  collisions, ALPs may originate through various production mechanisms. A discussion on possible ALP interactions and corresponding collider signatures is given in Ref. [203]. Some of these have recently been explored by the mono-photon and the  $E_{\text{T}}^{\text{miss}}$  +jets analyses [204, 205]. Apart from these, ALP-production can also be probed in mono- $h$  final states. Figure 8.1 shows the corresponding Feynman diagram for this process: An initial quark pair annihilates to a virtual  $Z$ -boson or photon, which subsequently decays into a Higgs boson and an ALP, denoted by  $a$ . The coupling  $Z/\gamma \rightarrow ah$ , and thus also the kinematics and cross sections of the process, depend on different parameters as indicated in Figure 8.1. A detailed description of these different parameters can be found in Ref. [203]. Another important parameter of the theory is  $f_a$  which is the energy scale characterising the symmetry breaking. For the mono- $h$  signature the dominant parameters are  $f_a$ , the two coupling constant  $\tilde{a}_{2D}$  and  $\tilde{a}_3$  and the mass of the ALP ( $m_a$ ).

The sensitivity of the  $139 \text{ fb}^{-1}$  mono- $h(b\bar{b})$  analysis to such ALP signatures has been

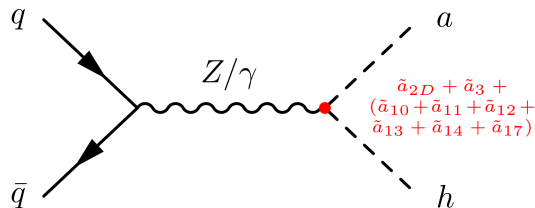


**Figure 8.1:** Production mechanism for ALPs in a mono- $h$  signature. The red term indicates the different coupling constants relevant for the  $Zah$  and  $\gamma ah$  vertex. The dominant contribution comes from  $\tilde{a}_{2D}$  and  $\tilde{a}_3$ . Figure taken from Ref. [203].

investigated within Ref. [206]. For this, ALP signals were generated for different choices of  $\tilde{a}_{2D}$  and  $\tilde{a}_3$  using  $f_a = 1$  TeV and  $m_a = 1$  MeV. The discovery significance was calculated according to Equation 7.4 and Equation 7.5 for the resolved event selection and the  $E_T^{\text{miss}}$  binning of the  $139 \text{ fb}^{-1}$  analysis. This showed, that several signals already have a discovery significance above the evidence threshold of  $3\sigma$ , while for other signals the significance is vastly smaller. To find out, whether the sensitivity to these models can be further enhanced, the kinematic variables for these signals were studied and compared with the  $Z'$ -2HDM. The most striking differences were observed for  $E_T^{\text{miss}}$  and the  $p_T$  of the Higgs boson candidate. It was found, that the distributions from the ALP signals are generally broader and, most importantly, have a maximum at relatively low  $E_T^{\text{miss}}$  values. Therefore, the sensitivity to these models may also be increased by extending the analysis to lower  $E_T^{\text{miss}}$  values in the future, as described in the previous section.

### 8.3 Combinations

To enhance the sensitivity to certain signal models, the mono- $h(b\bar{b})$  search results can be statistically combined with other analyses which are sensitive to the same models, but in different final states. Here, the 2HDM+ $a$  is particularly interesting, because this represents a theoretically well motivated model in which the sensitivity from collider signatures is complementary to direct and indirect detection (c.f. Section 2.4.2). For the parameter space probed in this work (c.f. Equation 2.46) it is particularly important to perform a statistical combination with the mono- $Z(\ell^+\ell^-)$  [207] and  $tW + E_T^{\text{miss}}$  analyses. The exclusion contour of the  $36.1 \text{ fb}^{-1}$  mono- $Z(\ell^+\ell^-)$  analysis is shown in Figure 2.10 together with the limits from other DM searches, e.g. the  $36.1 \text{ fb}^{-1}$  mono- $h(b\bar{b})$  analysis. In this, the searches with the widest sensitivity reach are the mono- $h(b\bar{b})$  and mono- $Z(\ell^+\ell^-)$  analyses. The former is more sensitive to high  $A$  masses, the latter to low  $A$  masses. The  $tW + E_T^{\text{miss}}$  analysis targets final states with  $E_T^{\text{miss}}$  produced in association with a top-quark and a  $W$ -boson. There are no published results for this analysis yet, but from the studies in Refs. [37, 208] it is expected, that this analysis will lead to a considerable contribution to the sensitivity.

In general, the sensitivity to signals with a relatively low  $E_T^{\text{miss}}$  can be enhanced by studying mono-Higgs processes, in which the Higgs boson decays into two photons, as presented in Refs. [47, 209]. Since the  $E_T^{\text{miss}}$  trigger efficiency rapidly decreases for  $E_T^{\text{miss}} \lesssim 100$  GeV and ( $b$ -)jet triggers are only available for relatively high jet- $p_T$  thresholds, there are no suitable physics objects available for triggering soft mono- $h(b\bar{b})$  final states. On the other hand, the

$h \rightarrow \gamma\gamma$  decay gives a very clean detector signature that can be well discriminated from the remaining QCD interactions within the  $pp$  collision. A diphoton final state thus allows to trigger down to relatively low  $p_T$  values, thereby allowing for a high acceptance to models with low  $E_T^{\text{miss}}$ . Hence, the mono- $h(\gamma\gamma)$  provides a better sensitivity to 2HDM+ $a$  signals with small  $m_A$  and  $m_a$ , as shown in Figure 2.10, or to  $Z'$ -2HDM signals with small  $m_{Z'}$ , which is shown in Figure 8.2. For the  $Z'$ -2HDM with  $m_H = m_{H^\pm} = 300$  GeV a statistical combination was performed in Ref. [45] using the mono- $h(b\bar{b})$  and mono- $h(\gamma\gamma)$  analyses with  $36.1 \text{ fb}^{-1}$  of collected data.

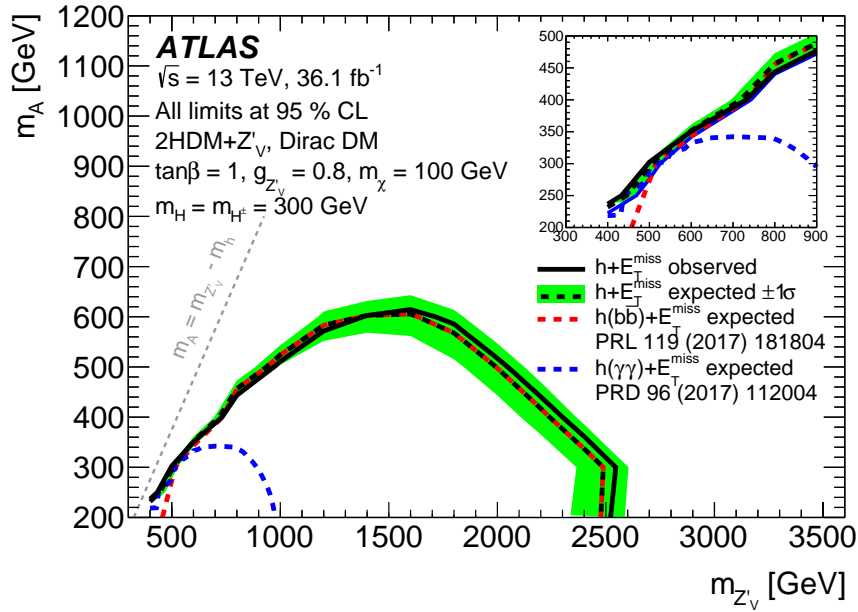


**Figure 8.2:** Expected exclusion contours for the  $Z'$ -2HDM with  $m_H = m_{H^\pm} = m_A$ , obtained with the mono- $h(b\bar{b})$  (red curve) and mono- $h(\gamma\gamma)$  (blue curve) analyses with  $36.1 \text{ fb}^{-1}$  of collected data. The sensitivity of the mono- $h(b\bar{b})$  search reaches to considerably higher  $A$  and  $Z'$  masses. The mono- $h(\gamma\gamma)$  analysis is more sensitive to low  $Z'$  masses. To better illustrate this, a zoomed-in version of the exclusion contour for low  $Z'$  masses is shown in the top right of the plot. The expected and observed exclusion contours resulting from a statistical combination of the two searches is indicated by the solid and dashed black line, respectively. Since this region is close to the kinematic limit  $m_A = m_{Z'} - m_h$ , up to which resonant  $Z'$  production is possible, the statistical combination results only in a slightly stronger exclusion contour than the individual processes. However, for other not kinematically limited signal models the effect may be much larger. The kink in the exclusion contour at around  $m_{Z'} = 2.5 \text{ TeV}$  is caused by the competing decay channel  $A \rightarrow t\bar{t}$ , which starts to contribute for  $m_A > 2m_t$ . Figure taken from Ref. [45].

# Chapter 9

## Conclusion

In this thesis two searches for Dark Matter with the ATLAS detector were presented, which are based on the data collected in proton-proton collision with a centre-of-mass energy of 13 TeV at the Large Hadron Collider (LHC). The searches target so-called mono- $h(b\bar{b})$  final states, in which Dark Matter particles are produced in association with a Standard Model Higgs boson decaying into a pair of  $b$ -quarks. As the Dark Matter particles are not visible in the detector, they give rise to missing transverse momentum ( $E_T^{\text{miss}}$ ), while for the Higgs boson decay one distinguishes between two signatures. For a low momentum of the Higgs boson, the decay leads to a resolved topology consisting of two  $b$ -tagged small-radius jets. For a high momentum, the decay products are collimated in a single large-radius jet with two  $b$ -tagged track jets in the Inner Detector associated to it. This is referred to as merged topology. Mono- $h(b\bar{b})$  final states consist of  $E_T^{\text{miss}}$  and jets. Therefore, to search for possible Dark Matter signals, signal regions with no leptons are defined. Events with leptons are used in dedicated control regions to estimate the dominant Standard Model backgrounds, which are  $t\bar{t}$ ,  $W$ +jets and  $Z$ +jets processes.

The statistical evaluation of the search results is performed with a simultaneous fit, which takes into account information from the different signal and control regions. The main fit variable in the signals regions is the mass of the Higgs boson candidate, denoted by  $m_h$ . In the resolved region  $m_h$  corresponds to the invariant mass of the leading two  $b$ -jets. In the merged region  $m_h$  is the mass of the leading large-radius jet. For Dark Matter signals with a mono- $h(b\bar{b})$  signature,  $m_h$  shows a distinct peak around the Higgs boson mass at 125 GeV, while for the Standard Model backgrounds  $m_h$  is generally broader. Apart from the Higgs peak, also its sidebands are used in the statistical evaluation, because this helps to further constrain the backgrounds. As the Higgs boson and the Dark Matter particles recoil against each other, their momenta are highly correlated and they depend on how strong this recoil is. To ensure a good sensitivity to signals of different kinematic regimes,  $m_h$  is fitted in multiple ranges of  $E_T^{\text{miss}}$ .

At the ATLAS experiment, mono- $h(b\bar{b})$  searches have already been performed before. However, for many potential Dark Matter models, these searches were not yet sufficiently sensitive. Therefore, in the two searches presented in this thesis, various improvements in the analysis strategy are introduced to increase the sensitivity. The first analysis uses the dataset recorded by the ATLAS detector from 2015 to 2017, corresponding to an integrated luminosity of  $79.8 \text{ fb}^{-1}$ . The main features of this analysis are the newly introduced object-based  $E_T^{\text{miss}}$  significance  $\mathcal{S}$  and variable-radius track jets. The variable  $\mathcal{S}$  is designed to discriminate genuine  $E_T^{\text{miss}}$ , coming e.g. from neutrinos or Dark Matter particles, from fake  $E_T^{\text{miss}}$  caused e.g. by energy mismeasurements. With a requirement on  $\mathcal{S}$ , the multijet background is

reduced so much that it can be completely neglected in the analysis. Variable-radius track jets represent a novel approach to reconstruct track jets: Instead of using a fixed jet radius as in previous searches, a variable radius is employed, which decreases with increasing track jet  $p_T$ . Thereby an overlap of the two track jets from the  $h \rightarrow b\bar{b}$  decay can be avoided, allowing for an efficient Higgs boson identification even for large momenta. The search is evaluated for a certain parameter subset of the  $Z'$ -2HDM simplified model, which is a Two-Higgs-Doublet-Model with a heavy  $Z'$ -boson as Dark Matter mediator. The use of variable-radius track jets results in a significant sensitivity improvement for  $Z'$ -2HDM signals with highly boosted  $h \rightarrow b\bar{b}$  decays.

The second search analyses the full Run II dataset of proton-proton collisions which was recorded from 2015 to 2018, corresponding to an integrated luminosity of  $139 \text{ fb}^{-1}$ . In this, the 2HDM+ $a$  is introduced as an additional benchmark model, where  $a$  denotes a pseudoscalar Dark Matter mediator. This model has two production mechanisms: Gluon-gluon fusion and  $b\bar{b}$ -induced production. The latter gives rise to two  $b$ -quarks besides the ones from the  $h \rightarrow b\bar{b}$  decay. To increase the sensitivity to these signals, a new fit category is defined which considers final states with three or more  $b$ -tags. For events with two  $b$ -tags an additional  $E_T^{\text{miss}}$  fit categorisation is introduced, which splits the merged signal region into two  $E_T^{\text{miss}}$  ranges of  $500 - 750 \text{ GeV}$  and greater than  $750 \text{ GeV}$ . This enhances the sensitivity to all signal models with a highly boosted mono- $h(b\bar{b})$  topology. Especially for the  $Z'$ -2HDM signals, a significant sensitivity increase is obtained. Furthermore, a thorough optimisation of the event selection in the resolved signal region is performed, which represents the main focus of this thesis. The aim is to define an event selection which, in addition to the  $Z'$ -2HDM, is also suitable for the 2HDM+ $a$  signals, because for these no dedicated optimisation was performed before in a mono- $h(b\bar{b})$  search. A central aspect is to suppress the contribution from  $t\bar{t}$  processes, which constitute the dominant background. In this optimisation, the shapes of several kinematic variables are investigated with respect to their potential to separate signal from background processes. Moreover, it is studied how combinations of different requirements on the variables affect the sensitivity. The optimised event selection contains e.g. requirements on the newly introduced variables  $m_T^{b,\text{min}}$  and  $m_T^{b,\text{max}}$  which represent proxies for the top-quark mass. With this selection, the  $t\bar{t}$  background can be significantly reduced and a considerable increase in the sensitivity is obtained for all signal models.

Moreover, an  $E_T^{\text{miss}}$  trigger calibration strategy is presented. This needs to be applied because the trigger efficiency is not well modelled in simulation. Therefore, scale factors are calculated to correct the simulations to the efficiencies measured in data. With this strategy a successful calibration is possible down to  $E_T^{\text{miss}} = 120 \text{ GeV}$ , which would allow to extend the analysis in the future to  $E_T^{\text{miss}}$  values below the current threshold of  $E_T^{\text{miss}} > 150 \text{ GeV}$ .

No excess of data over Standard Model background expectations is observed. Therefore, exclusion limits are derived for the  $Z'$ -2HDM and 2HDM+ $a$  signals. In the  $Z'$ -2HDM, limits are set on the mass of the  $Z'$ -boson and the pseudoscalar Higgs boson  $A$ . With the full Run II dataset,  $Z'$  masses up to  $3.2 \text{ TeV}$  and  $A$  masses up to  $700 \text{ GeV}$  are excluded. Variations in the mass of  $A$  are also considered for deriving limits in the 2HDM+ $a$ . This is interpreted for two different parameter choices, in which either gluon-gluon fusion or  $b\bar{b}$ -induced production dominates. For the former, the limits on the mass of  $A$  reach up to  $1.6 \text{ TeV}$  and up to  $520 \text{ GeV}$  for the mass of  $a$ . For signals from  $b\bar{b}$ -induced production, the mass limits on  $A$  and  $a$  reach up to  $1 \text{ TeV}$  and  $300 \text{ GeV}$ , respectively.

---

Although no excess is seen, a large phase space remains in which the mono- $h(b\bar{b})$  search is not yet sensitive, but where physics beyond the Standard Model may hide. Therefore, possible improvements to the analysis strategy could help to increase the sensitivity in the future. In the highly boosted regime the search is mainly limited by the low data statistics. Here, a considerable sensitivity improvement may already be achieved by an increase in data. A third data-taking period for proton-proton collisions at the LHC is currently in preparation, which will presumably start in 2022 and deliver about  $350 \text{ fb}^{-1}$  of data [65, 210]. Afterwards, the LHC will undergo a high-luminosity upgrade. During the fourth data-taking period,  $3000 \text{ fb}^{-1}$  of data are expected to be delivered [210, 211]. The increased data statistics together with improved analysis techniques will allow to extend the reach of search for Dark Matter considerably, hopefully revealing a Dark Matter signal at collisions in near future.



# Appendix



# Appendix A

## Additional information on $E_T^{\text{miss}}$ trigger efficiency calibration

This chapter contains supplementary information to Section 5.4.3, in which the trigger efficiency calibration of the  $139 \text{ fb}^{-1}$  analysis was described.

### A.1 Strategy in the $79.8 \text{ fb}^{-1}$ analysis

In the following, the calibration strategy of the  $79.8 \text{ fb}^{-1}$  analysis is explained. It uses the same strategy established in the course of the  $36.1 \text{ fb}^{-1}$  search, which is documented in detail in Ref. [180].

#### Event selection

Events in the measurement region are selected with the single-muon trigger of Table 5.3. In addition, events must contain exactly one signal muon with  $p_T > 25 \text{ GeV}$  which needs to pass the trigger matching criteria of Section 5.4.1. To make the measurement region kinematically as close as possible to the SR and  $1\mu$ -CR, all other jet and  $E_T^{\text{miss}}$ -related cuts (except the cut  $E_T^{\text{miss}} > 150 \text{ GeV}$ ) of Table 6.4 are applied in the measurement region, using  $E_T^{\text{miss, no } \mu}$  as  $E_T^{\text{miss}}$  proxy. However, after this selection the resulting statistics in the measurement region is relatively low, which makes it difficult to perform a reliable fit on the scale factors (SFs). Therefore, to increase the statistics, the requirement  $N(b\text{-jets}) = 2$  is dropped, so that the SFs are measured inclusively in all  $b$ -jet multiplicities.

Except for the muon-specific requirements, the only difference in the SR and  $1\mu$ -CR event selection is the cut on  $\mathcal{S}$ . It has been found that this cut alone does not have a notable impact on the SF behaviour. Therefore, the SF derived for the SR are used for the  $1\mu$ -CR as well.

#### Scale factor calculation

The SFs are measured as a function of  $E_T^{\text{miss, no } \mu}$ , for which a bin width of  $2 \text{ GeV}$  is used. They are fitted in the range from  $120 - 300 \text{ GeV}$  using a fit function  $f(x)$ , which is based on an error function with two free parameters,  $p_0$  and  $p_1$ . It is given by:

$$f(x) = 0.5 \cdot \left[ 1 + \operatorname{erf} \left( \frac{x - p_0}{\sqrt{2}p_1} \right) \right]. \quad (\text{A.1})$$

Figure A.1 shows as an example the SF curve for one of the  $E_T^{\text{miss}}$  triggers used in 2016, HLT\_xe110\_mht\_L1XE50. In the region relevant to the analysis, i.e.  $E_T^{\text{miss, no } \mu} > 150 \text{ GeV}$ ,

the fit curve describes the measured points sufficiently well. However, for the lower turn-on the fit function is clearly not well suited. Therefore, to ensure a better SF description, the calibration strategy was optimised in the  $139 \text{ fb}^{-1}$ , in which the SFs can be successfully described down to at least  $E_T^{\text{miss}} = 120 \text{ GeV}$ . This improvement is mainly attributed to the change in the fit function, for which a four-parameter error function is used in the  $139 \text{ fb}^{-1}$  analysis (c.f. Equation A.1).

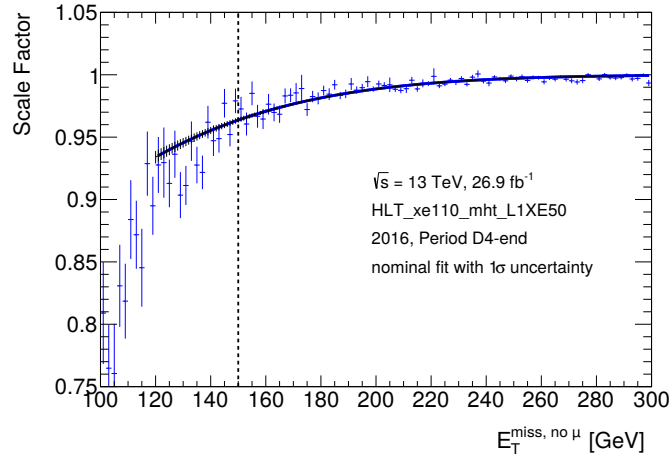


**Figure A.1:** Measured and fitted trigger SF for HLT\_xe110\_mht\_L1XE50. The hatched band shows the  $1\sigma$  uncertainty of the fit.

### Sources of uncertainties

Two different sources of uncertainties are considered in the  $E_T^{\text{miss}}$  trigger calibration. The first one is the statistical uncertainty which is defined as the  $1\sigma$  uncertainty of the fit. In Figure A.1 this is indicated by the hatched band around the SF curve. The second one is a systematic uncertainty. It takes into account that the measured SF may deviate from the *real* SFs in the SR or  $1\mu$ -CR, because the calibration is performed inclusively in all  $b$ -jet multiplicities. To estimate the associated uncertainties, the SFs are calculated separately in a selection with  $\geq 1$   $b$ -jet, but which is otherwise identical to the single-muon measurement region. The difference with respect to the nominal SF is defined to be the systematic uncertainty, denoted as  $\sigma_{\text{sys}}$ . To be more conservative about the impact of  $\sigma_{\text{sys}}$ , the uncertainty is symmetrised, i.e. the real SF is assumed to lie within  $\text{SF} \pm 1\sigma_{\text{sys}}$ .

However, deriving the uncertainties in this way has the following shortcoming: The  $b$ -jet inclusive measurement region is dominated by  $W$ +jets events, while the SR is  $Z$ +jets and  $t\bar{t}$  dominated. On the other hand, the  $\geq 1$   $b$ -jet selection, in which the systematic uncertainties are derived, has a larger fraction of  $t\bar{t}$  events. This background composition is thus more similar to the one of the SR, so that the SF determined in the  $\geq 1$   $b$ -jet region is expected to be closer to the real SF of the SR than the nominal one. This represents another reason, why the calibration strategy was modified in the  $139 \text{ fb}^{-1}$  analysis.

## A.2 Event selection in the 139 fb<sup>-1</sup> analysis

This section describes, which event selection is applied in the measurement regions in the 139 fb<sup>-1</sup> and how the chosen selection was optimised.

The base selection, i.e. the muon-trigger and the signal muon requirements, are adopted from the previous search. Ideally, the further event selection in the measurement region should be kinematically as close as possible to the SR and 1 $\mu$ -CR and also have a similar background composition. At the same time, the data and MC statistics should be large enough to obtain reasonable fit results. Therefore, to define a suitable measurement region, it is important to understand how the different selection criteria affect the trigger SF.

First, it has been tested whether it is possible to include all jet and  $E_T^{\text{miss}}$ -related requirements of Table 7.5 (except for the  $E_T^{\text{miss}}$  cut) and still have a sufficiently large statistics. Again,  $E_T^{\text{miss, no } \mu}$  is used as  $E_T^{\text{miss}}$  proxy and also the requirement  $\geq 2$   $b$ -jets is applied. However, it has been found that only for the trigger HLT\_xe110\_pufit\_70\_L1XE55 a reliable SF measurement can be achieved. This is the  $E_T^{\text{miss}}$  trigger which has been used for all 2018 data-taking periods, corresponding to an integrated luminosity of 58.5 fb<sup>-1</sup>. Due to their much lower associated integrated luminosities, no reasonable calibration can be performed for the other triggers. Especially problematic is the calibration of HLT\_xe70\_mht and HLT\_xe90\_mht\_L1XE50 which was only used for a dataset of 3.2 fb<sup>-1</sup> and 6.1 fb<sup>-1</sup>, respectively. For these, it is even not possible to follow the approach of the 79.8 fb<sup>-1</sup> search and to calculate the SFs inclusively in all  $b$ -jet multiplicities. The reason for this are the newly introduced cuts on  $m_T^{b,\text{min}}$  and  $m_T^{b,\text{max}}$ : While the 79.8 fb<sup>-1</sup> search has only two  $E_T^{\text{miss}}$ -dependent discriminating variables besides  $E_T^{\text{miss}}$ , i.e. the requirements on  $\Delta\phi(\mathbf{E}_T^{\text{miss}}, \mathbf{j}_{1,2,3}^{\text{centr.+forw.}})$  and  $\mathcal{S}$ , the current search has two more. Like  $\mathcal{S}$ , also  $m_T^{b,\text{min}}$  and  $m_T^{b,\text{max}}$  are highly correlated with  $E_T^{\text{miss}}$ . If a cut on these is applied, then removes many low- $E_T^{\text{miss}}$  events in general. Therefore, to increase the statistics, the requirements on  $\mathcal{S}$ ,  $m_T^{b,\text{min}}$  and  $m_T^{b,\text{max}}$  are not imposed in the measurement region. It has also been validated that leaving these cuts away does not change the shape of the efficiency curves in data and MC too much. This was done by comparing the corresponding curves with and without these cuts for HLT\_xe110\_pufit\_70\_L1XE55, i.e. the only trigger with a sufficiently large luminosity to successfully measure the SF even with all event selection criteria. On the contrary, removing other selection criteria, e.g. the  $b$ -jet or  $p_T(\mathbf{j}_1, \mathbf{j}_2)$  requirements, shows a larger impact on the efficiency curves.

As explained in Section 5.4.3, the trigger efficiencies are derived in events with one  $b$ -jet, because this selection has approximately an equal contribution of  $t\bar{t}$  and  $W$ +jets. This should resemble the background composition of the SR, in which the two most important backgrounds are  $t\bar{t}$  and  $Z$ +jets. To confirm whether the SFs for  $Z$ +jets can be described by the SFs derived in  $W$ +jets events, the trigger efficiency is measured for  $Z(\rightarrow \mu^+ \mu^-)$ +jets events as a function of  $E_T^{\text{miss, no } \ell\ell}$ . This aims to mimic the trigger efficiency of  $Z(\rightarrow \nu\bar{\nu})$ +jets for given  $E_T^{\text{miss}}$  values. The event selection used is the same as in the 2 $\ell$ -CR, except that the cuts on  $E_T^{\text{miss, no } \ell\ell}$ ,  $\mathcal{S}$ ,  $m_T^{b,\text{min}}$  and  $m_T^{b,\text{max}}$  are removed. The resulting efficiency curves measured for  $Z(\rightarrow \nu\bar{\nu})$ +jets MC events are then compared with the  $W$ +jets MC efficiencies measured in the single-muon region. The results for one representative  $E_T^{\text{miss}}$  trigger are shown in Figure A.2. The shape of the efficiency curves agree well. Similar results obtained for the other  $E_T^{\text{miss}}$  triggers as well. Consequently, the SFs measured in the single-muon

region for  $W$ +jets can also describe the behaviour for  $Z$ +jets events.

For the  $1\mu$ -CR the background composition is actually better resembled by using the selection with  $\geq 2$   $b$ -jets for deriving the nominal SF. However, for simplicity as well as to have a higher statistics it was decided to just use the SFs measured for the SR also for the  $1\mu$ -CR.

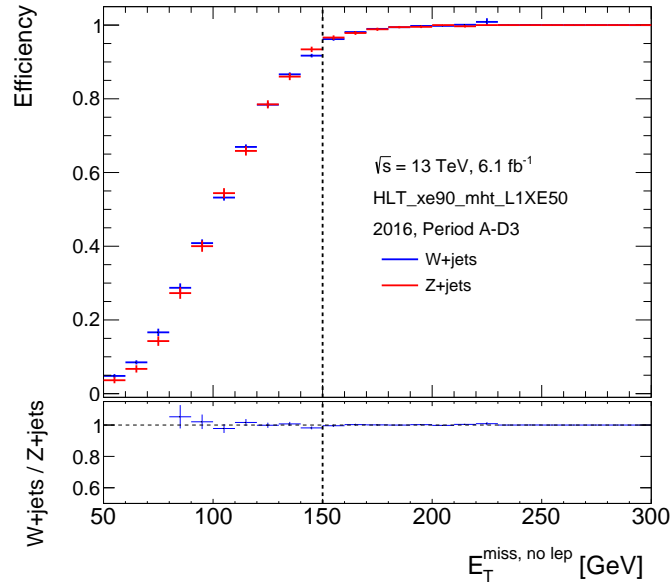


**Figure A.2:** Trigger efficiencies as a function of the offline  $E_T^{\text{miss, no } \mu} / E_T^{\text{miss, no } \ell\ell}$  measured  $W$ +jets and  $Z$ +jets events in the single-muon and dimuon measurement region, respectively, for the trigger HLT\_xe110\_pufit\_70\_L1XE55.

### A.3 Efficiencies and scale factors in the $139 \text{ fb}^{-1}$ analysis

In the following, the efficiencies and SFs derived for the different  $E_T^{\text{miss}}$  triggers in the  $139 \text{ fb}^{-1}$  analysis are summarised.

### A.3 Efficiencies and scale factors in the $139 \text{ fb}^{-1}$ analysis

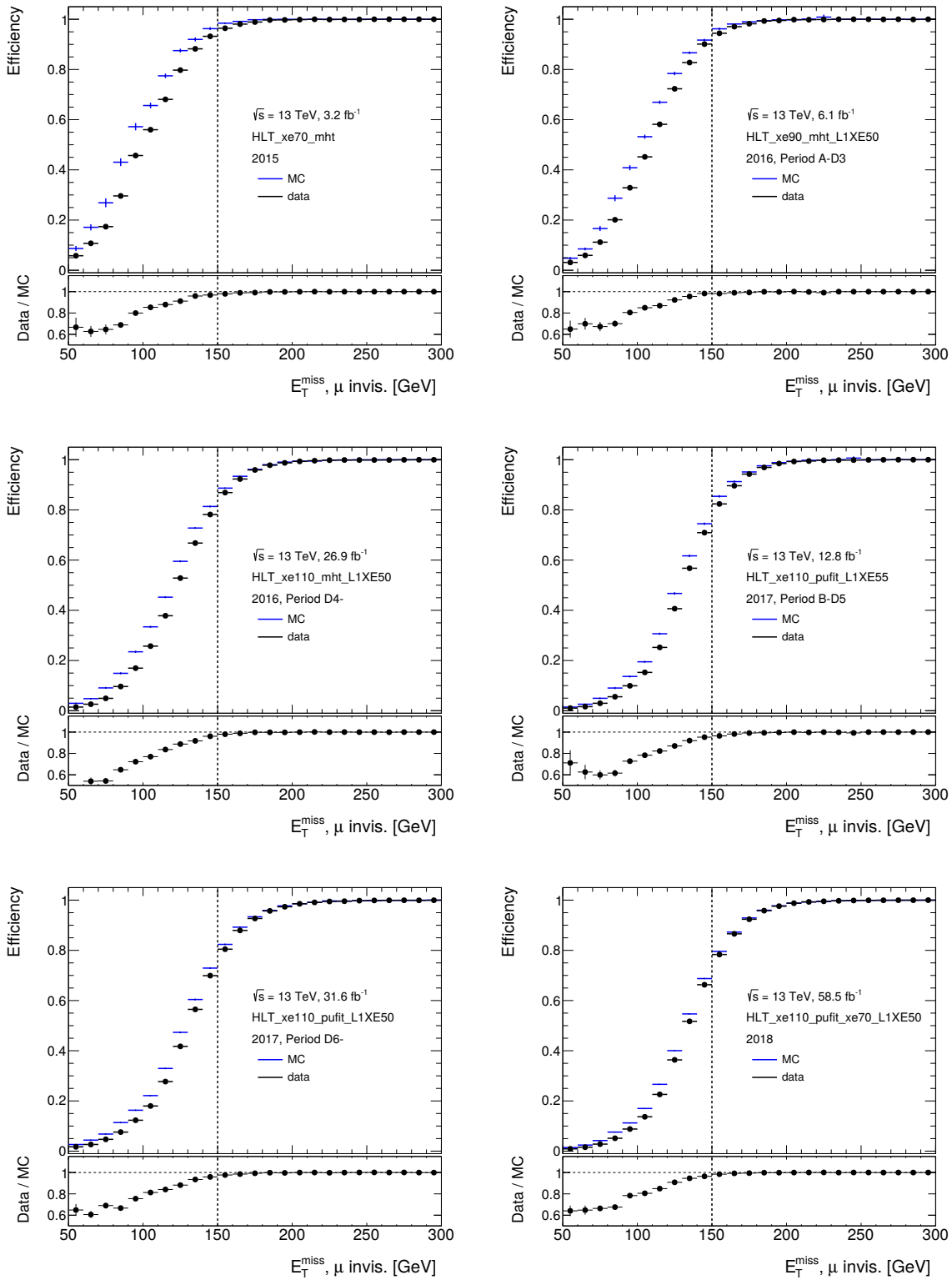


**Figure A.3:** Measured trigger efficiencies as a function of  $E_T^{\text{miss}, \text{no } \mu}$  in data and MC backgrounds for the  $E_T^{\text{miss}}$  triggers used in 2015-2018. The bottom panels show the ratio of data and MC events, i.e. the SF.

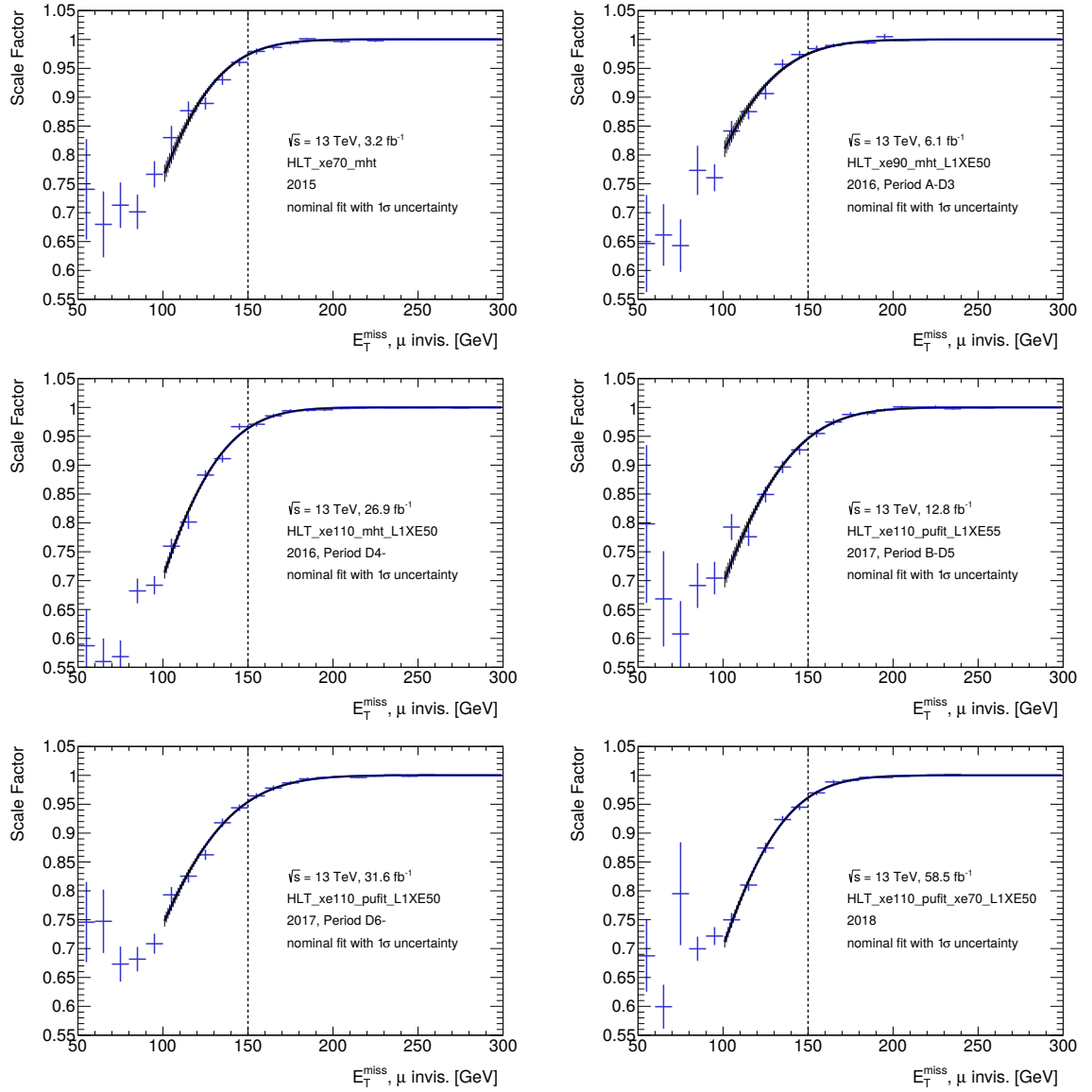


**Figure A.4:** Measured SFs as a function of  $E_T^{\text{miss}, \text{no } \mu}$  for the  $E_T^{\text{miss}}$  triggers used in 2015–2010. The SFs are derived in events with one  $b$ -tag. The hatched band shows the  $1\sigma$  fit uncertainty.

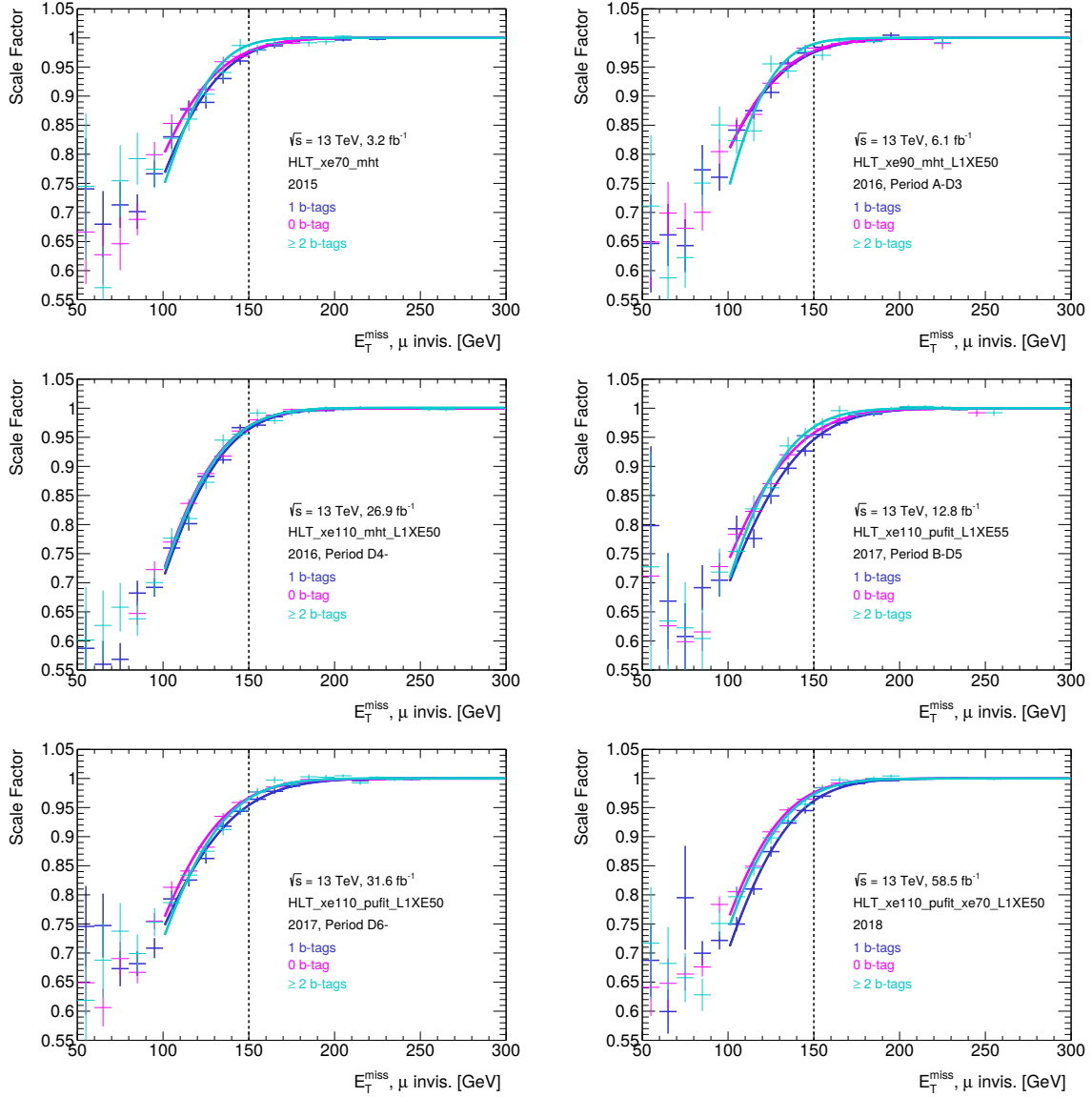


**Figure A.5:** Measured SFs as a function of  $E_T^{\text{miss}, \text{no } \mu}$  for the  $E_T^{\text{miss}}$  triggers used in 2015-2018 in events with one  $b$ -jets (blue), which corresponds to the nominal SFs, as well as for zero (pink) and two (cyan)  $b$ -jets, used to derive the systematic uncertainties.



# Appendix B

## Signal acceptance and efficiency

This chapter shows the combined acceptance and efficiency, denoted by  $A \times \epsilon$ , for the different signal models. This indicates, which fraction of the initially produced events are eventually selected in the SRs. Here,  $A$  accounts for the detector acceptance and  $\epsilon$  for the efficiency related e.g. to the trigger, the object reconstruction and the event selection of the analysis. The  $A \times \epsilon$  values are shown separately for the resolved and merged SR and are obtained by applying the full event selection of Table 7.5 to the signal samples. For the  $Z'$ -2HDM and ggF-induced 2HDM+ $a$  signals, only the results for the  $2b$  SR are shown, while for the  $b\bar{b}$ -induced signals also the  $3b+$  category is considered.

Compared to the ggF-induced 2HDM+ $a$  signals, the  $A \times \epsilon$  values for the  $b\bar{b}$ -induced signals are much lower. This is also the reason, why the sensitivity to the  $b\bar{b}$ -induced signals is much smaller than for the ggF models, as shown in Figure 7.21 and Figure 7.22. The  $b\bar{b}$ -induced signals generally have a rather low  $E_T^{\text{miss}}$  spectrum, so that they are less likely to pass the  $E_T^{\text{miss}}$  trigger and the requirement  $E_T^{\text{miss}} > 150$  GeV. This is illustrated in Figure B.5, which shows the  $E_T^{\text{miss}}$  distribution for a representative signal model from the ggF as well as the  $b\bar{b}$ -induced 2HDM+ $a$  with the same values  $m_A = 1$  TeV and  $m_a = 550$  GeV. The distributions are obtained from truth MC samples with no preselection criteria applied, except for the lepton veto and  $E_T^{\text{miss}} > 50$  GeV. The  $E_T^{\text{miss}}$  distribution of the ggF-induced signal clearly lies at higher values.

To understand the different kinematic behaviour, the production mechanisms are determined following the procedure described in Section 7.3.2. The results for the signals with  $m_A = 1.3$  TeV and  $m_a = 500$  GeV are shown in Figure B.6. For the ggF model, all signal events originate from resonant  $A$ -production, corresponding to the Feynman diagram in 2.9. On the other hand, for the  $b\bar{b}$ -induced signal the largest contributions come from the off-shell  $a \rightarrow Ah$  decay and the  $t$ -channel process, as shown in the diagrams of Figure 2.11. Similar results are also seen for models with other  $m_A$  and  $m_a$ . Consequently, the different production mechanisms are responsible for the large kinematic differences.

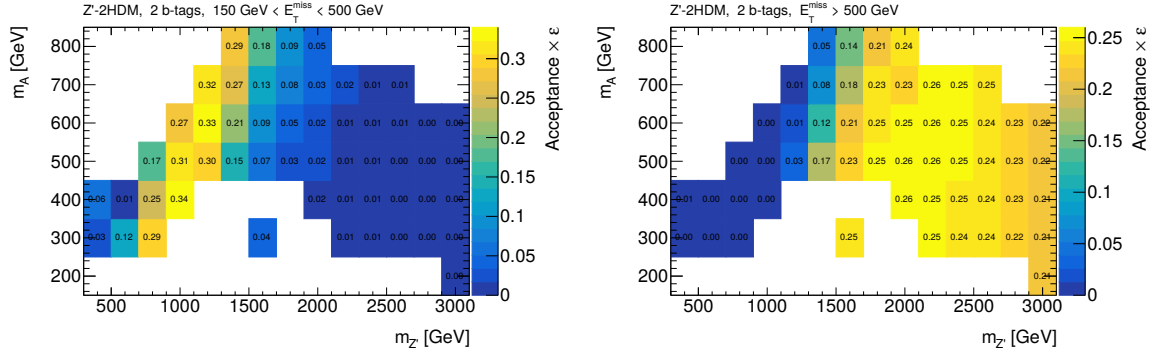


**Figure B.1:**  $A \times \epsilon$  for the  $Z'$ -2HDM signals with  $m_H = m_{H^\pm} = 300$  GeV. The left plot corresponds to the resolved SR, the right plot to th merged SR.

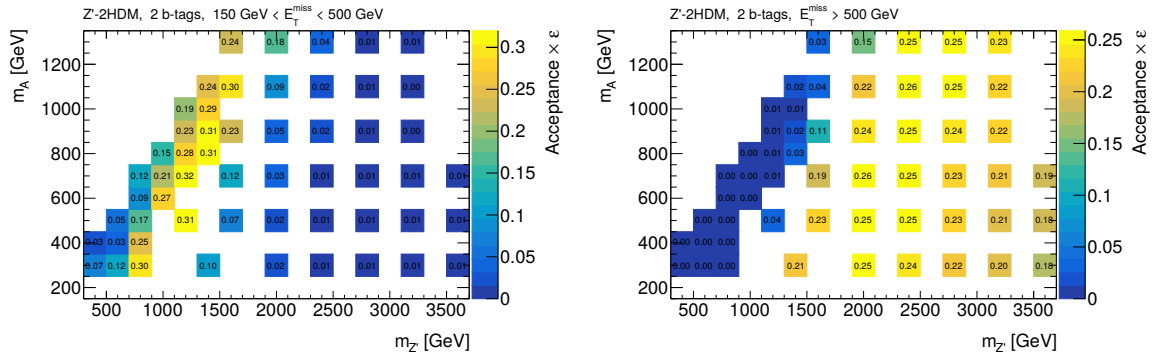


**Figure B.2:**  $A \times \epsilon$  for the  $Z'$ -2HDM signals with  $m_H = m_{H^\pm} = m_A$ . The left plot corresponds to the resolved SR, the right plot to th merged SR.

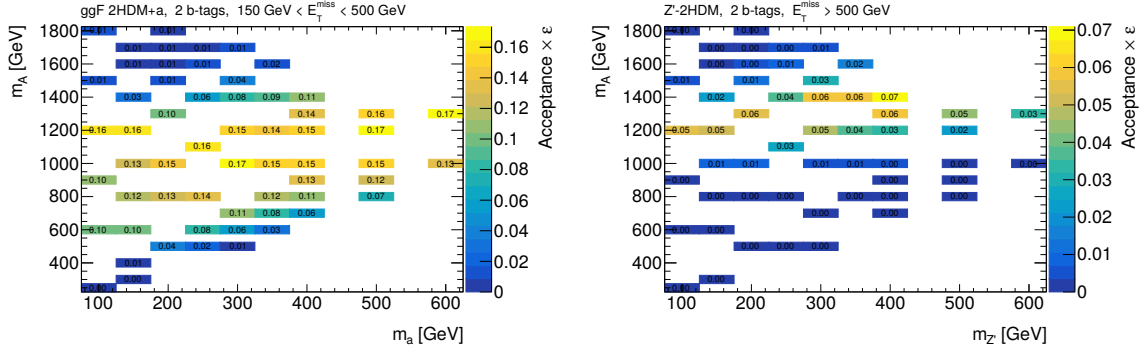


**Figure B.3:**  $A \times \epsilon$  for the ggF-induced 2HDM+ $a$  signals. The left plot corresponds to the resolved SR, the right plot to th merged SR.

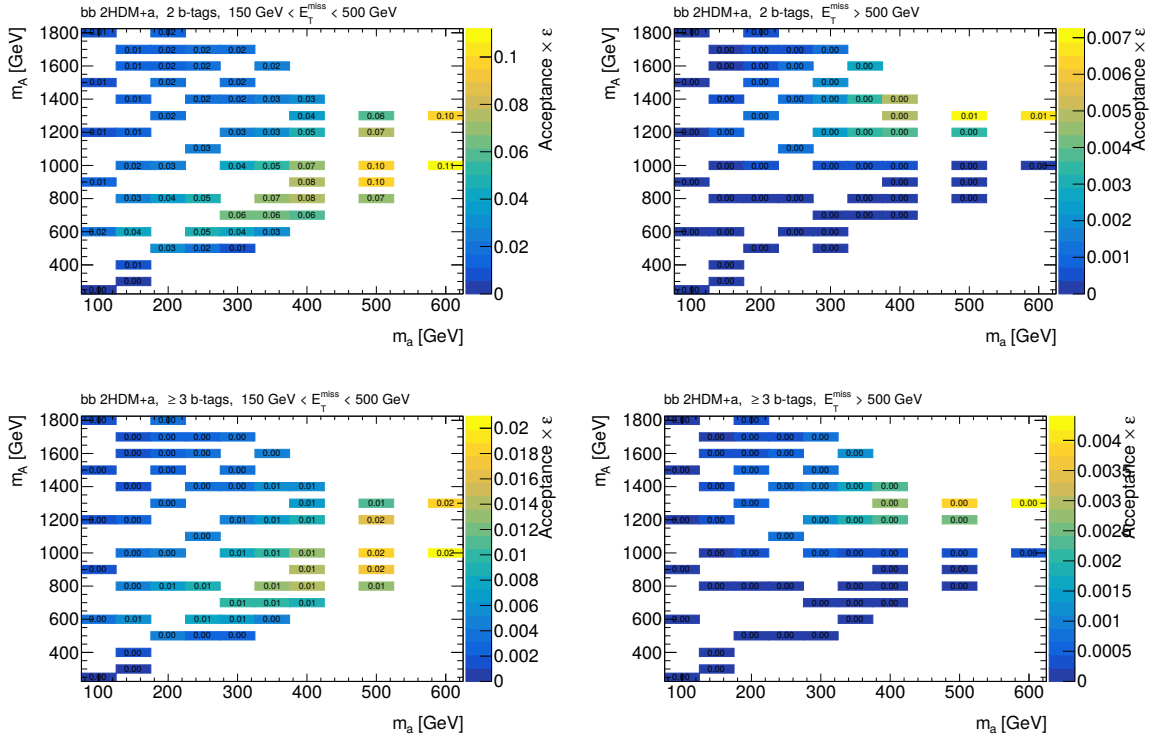


**Figure B.4:**  $A \times \epsilon$  for the ggF-induced 2HDM+ $a$  signals. The plots in the top row correspond to the  $2b$ , the ones in the bottom row to the  $3b+$  SR. The resolved SRs are shown on the left, the merged SRs on the right.

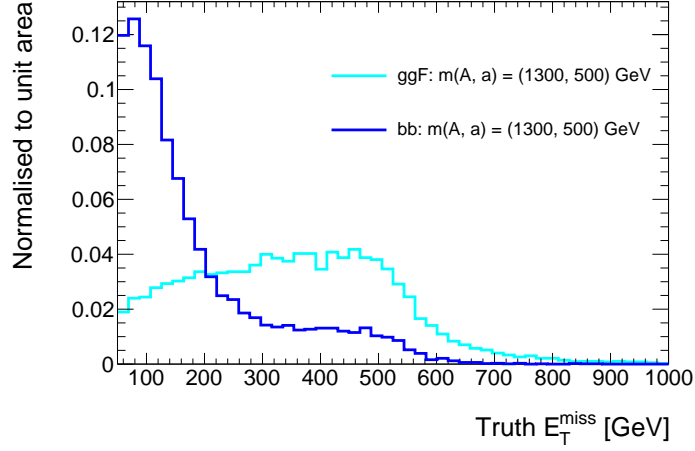


**Figure B.5:** Distribution of the truth  $E_T^{\text{miss}}$  for the ggF and  $b\bar{b}$ -induced signal models with  $m_A = 1.3$  TeV and  $m_a = 500$  GeV.

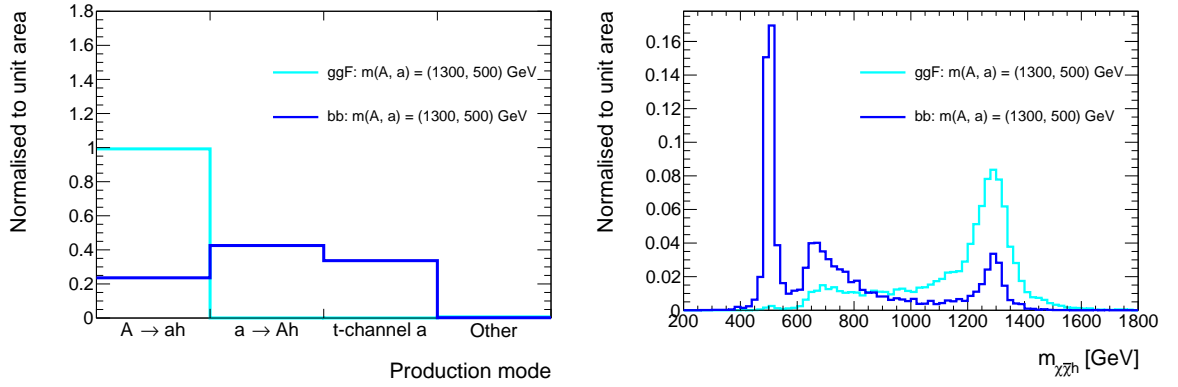


**Figure B.6:** Distribution of the truth  $E_T^{\text{miss}}$  for the ggF and  $b\bar{b}$ -induced signal models with  $m_A = 1.3$  TeV and  $m_a = 500$  GeV. The left plot shows the fractional contribution of the production modes for the ggF and  $b\bar{b}$ -induced signal models with  $m_A = 1.3$  TeV and  $m_a = 500$  GeV. The right plot shows the associated  $m_{\chi\bar{\chi}h}$  distributions, normalised to unit area. Resonant  $A$ -production causes the peak around  $m_A = 1.3$  TeV, the off-shell decay  $a \rightarrow Ah$  leads to the peak around  $m_a = 500$  GeV and the  $t$ -channel diagram leads to the broad distribution observed within  $600 \text{ GeV} < m_{\chi\bar{\chi}h} < 1$  TeV for the  $b\bar{b}$ -induced process.

# Bibliography

- [1] Planck Collaboration, *Planck 2015 results. XIII. Cosmological parameters*, *Astron. Astrophys.* **594** (2016) A13, arXiv: [1502.01589 \[astro-ph.CO\]](#).
- [2] M. Tanabashi et al., *Review of Particle Physics*, *Phys. Rev.* **D98** (2018) 030001.
- [3] D. Clowe et al., *A Direct Empirical Proof of the Existence of Dark Matter*, *The Astrophysical Journal* **648** (2006) L109.
- [4] G. Barr, R. Devenish, R. Walczak, T. Weidberg and O. U. Press, *Particle Physics in the LHC Era*, Oxford University Press, 2016, ISBN: 9780198748564.
- [5] L. Carpenter et al., *Mono-Higgs: a new collider probe of dark matter*, *Phys. Rev.* **D89** (2014) 075017, arXiv: [1312.2592 \[hep-ph\]](#).
- [6] D. de Florian et al., *Handbook of LHC Higgs Cross Sections: 4. Deciphering the Nature of the Higgs Sector*, *CERN Yellow Reports: Monographs* (2016).
- [7] ATLAS Collaboration, *Search for dark matter produced in association with a Higgs boson decaying to two bottom quarks in pp collisions at  $\sqrt{s} = 8$  TeV with the ATLAS detector*, *Phys. Rev. D* **93** (2016) 072007, arXiv: [1510.06218 \[hep-ex\]](#).
- [8] ATLAS Collaboration, *Search for dark matter in association with a Higgs boson decaying to b-quarks in pp collisions at  $\sqrt{s} = 13$  TeV with the ATLAS detector*, *Phys. Lett. B* **765** (2017) 11, arXiv: [1609.04572 \[hep-ex\]](#).
- [9] ATLAS Collaboration, *Search for Dark Matter Produced in Association with a Higgs Boson Decaying to  $b\bar{b}$  using  $36\text{ fb}^{-1}$  of pp collisions at  $\sqrt{s} = 13$  TeV with the ATLAS Detector*, *Phys. Rev. Lett.* **119** (2017) 181804, arXiv: [1707.01302 \[hep-ex\]](#).
- [10] D. Griffiths, *Introduction to Elementary Particles*, Physics textbook, Wiley, 2008, ISBN: 9783527618477.
- [11] M. Peskin and D. Schroeder, *An Introduction to Quantum Field Theory*, Advanced book program, Levant Books, 2005, ISBN: 9788187169529.
- [12] I. Brock and T. Schörner-Sadenius, *Physics at the Terascale*, Wiley, 2011, ISBN: 9783527634972.
- [13] M. Maggiore, *A Modern Introduction to Quantum Field Theory*, Oxford University Press, 2005, ISBN: 9780198520733.

- [14] ATLAS Collaboration, *Observation of a new particle in the search for the Standard Model Higgs boson with the ATLAS detector at the LHC*, *Phys. Lett. B* **716** (2012) 1, arXiv: [1207.7214 \[hep-ex\]](#).
- [15] CMS Collaboration, *Observation of a new boson at a mass of 125 GeV with the CMS experiment at the LHC*, *Phys. Lett. B* **716** (2012) 30, arXiv: [1207.7235 \[hep-ex\]](#).
- [16] ATLAS Collaboration, *Observation of  $H \rightarrow b\bar{b}$  decays and  $VH$  production with the ATLAS detector*, *Physics Letters B* **786** (2018) 59.
- [17] CMS Collaboration, *Observation of Higgs Boson Decay to Bottom Quarks*, *Physical Review Letters* **121** (2018).
- [18] M. Thomson, *Modern particle physics*, Cambridge University Press, 2013, ISBN: 978-1-107-03426-6.
- [19] K. G. Begeman, A. H. Broeils and R. H. Sanders, *Extended rotation curves of spiral galaxies: dark haloes and modified dynamics*, *Monthly Notices of the Royal Astronomical Society* **249** (1991) 523.
- [20] M. Bauer and T. Plehn, *Yet Another Introduction to Dark Matter: The Particle Physics Approach*, Lecture Notes in Physics, Springer International Publishing, 2019, ISBN: 9783030162344.
- [21] G. Bertone, D. Hooper and J. Silk, *Particle dark matter: evidence, candidates and constraints*, *Physics Reports* **405** (2005) 279.
- [22] *Homepage of the CRESST experiment*, URL: <https://www.cresst.de/>.
- [23] *Homepage of the XENON experiment*, URL: <http://www.xenon1t.org/>.
- [24] XENON Collaboration, *The XENON1T dark matter experiment*, *The European Physical Journal C* **77** (2017).
- [25] *Homepage of the IceCube experiment*, URL: <https://icecube.wisc.edu/>.
- [26] IceCube Collaboration, *First year performance of the IceCube neutrino telescope*, *Astroparticle Physics* **26** (2006) 155.
- [27] *NASA homepage of Fermi telescope*, URL: <https://fermi.gsfc.nasa.gov/>.
- [28] Fermi/LAT Collaboration, *The Large Area Telescope on the Fermi Gamma-ray Space Telescope Mission*, *The Astrophysical Journal* **697** (2009) 1071.
- [29] ATLAS Collaboration, *The ATLAS Experiment at the CERN Large Hadron Collider*, *JINST* **3** (2008) S08003.
- [30] CMS Collaboration, *The CMS experiment at the CERN LHC*, *JINST* **3** (2008) S08004.
- [31] S. P. Martin, *A Supersymmetry Primer*, *Advanced Series on Directions in High Energy Physics* (1998) 1.

- 
- [32] G. C. Branco et al., *Theory and phenomenology of two-Higgs-doublet models*, *Phys. Rept.* **516** (2012) 1, arXiv: [1106.0034 \[hep-ph\]](#).
- [33] J. F. Gunion, S. Dawson, H. E. Haber and G. L. Kane, *The Higgs hunter's guide*, vol. 80, Frontiers in Physics, Brookhaven Nat. Lab., 1989.
- [34] M. Mühlleitner, *Lecture Notes: Beyond the Standard Model Physics*, 2014, URL: [https://www.itp.kit.edu/~rauch/Teaching/WS1415\\_BSMHiggs/bsm.pdf](https://www.itp.kit.edu/~rauch/Teaching/WS1415_BSMHiggs/bsm.pdf).
- [35] *Lecture notes by S. Dawson at 2018 Maria Laach summer school*, URL: <https://www.maria-laach.tp.nt.uni-siegen.de/downloads/files/2018/Dawson-2018-3.pdf>.
- [36] ATLAS Collaboration, *Combined measurements of Higgs boson production and decay using up to 80 fb<sup>-1</sup> of proton-proton collision data at  $\sqrt{s} = 13$  TeV collected with the ATLAS experiment*, ATLAS-CONF-2018-031, 2018, URL: <https://cds.cern.ch/record/2629412>.
- [37] T. Abe et al., *LHC Dark Matter Working Group: Next-generation spin-0 dark matter models*, *Phys. Dark Univ.* (2018) 100351, arXiv: [1810.09420 \[hep-ex\]](#).
- [38] M. Misiak et al., *Estimate of  $\mathcal{B}(\bar{B} \rightarrow X_s \gamma)$  at  $O(\alpha_s^2)$* , *Phys. Rev. Lett.* **98** (2 2007) 022002.
- [39] T. Hermann, M. Misiak and M. Steinhauser,  *$\bar{B} \rightarrow X_s \gamma$  in the Two Higgs Doublet Model up to next-to-next-to-leading order in QCD*, *Journal of High Energy Physics* **2012** (2012).
- [40] M. Misiak et al., *Updated Next-to-Next-to-Leading-Order QCD Predictions for the Weak Radiative B-Meson Decays*, *Physical Review Letters* **114** (2015).
- [41] M. Misiak and M. Steinhauser, *Weak radiative decays of the B meson and bounds on  $M_{H^\pm}$  in the Two-Higgs-Doublet Model*, *The European Physical Journal C* **77** (2017).
- [42] A. Abdesselam et al., 'Measurement of the inclusive  $B \rightarrow X_{s+d} \gamma$  branching fraction, photon energy spectrum and HQE parameters', *38th International Conference on High Energy Physics*, 2016, arXiv: [1608.02344 \[hep-ex\]](#).
- [43] H. Sahoo, 'Exclusive Radiative B meson decays at Belle', *Particles and fields. Proceedings, Meeting of the Division of the American Physical Society, DPF 2009, Detroit, USA, July 26-31, 2009*, arXiv: [0910.0124 \[hep-ex\]](#).
- [44] J.-M. Gérard and M. Herquet, *Twisted Custodial Symmetry in Two-Higgs-Doublet Models*, *Physical Review Letters* **98** (2007).
- [45] ATLAS Collaboration, *Constraints on mediator-based dark matter and scalar dark energy models using  $\sqrt{s} = 13$  TeV pp collision data collected by the ATLAS detector*, *JHEP* **05** (2019) 142, arXiv: [1903.01400 \[hep-ex\]](#).
- [46] T. Plehn, *Lectures on LHC Physics*, *Lect. Notes Phys.* **844** (2012) 1, arXiv: [0910.4182 \[hep-ph\]](#).

- [47] ATLAS Collaboration, *Search for dark matter in events with missing transverse momentum and a Higgs boson decaying to two photons in pp collisions at  $\sqrt{s} = 13$  TeV with the ATLAS detector*, ATLAS-CONF-2020-054, 2020, URL: <https://cds.cern.ch/record/2743083>.
- [48] A. Berlin, T. Lin and L.-T. Wang, *Mono-Higgs Detection of Dark Matter at the LHC*, *JHEP* **06** (2014) 078, arXiv: 1402.7074 [hep-ph].
- [49] ATLAS Collaboration, *Search for Dark Matter Produced in Association with a Higgs Boson decaying to  $b\bar{b}$  at  $\sqrt{s} = 13$  TeV with the ATLAS Detector using  $79.8\text{fb}^{-1}$  of proton-proton collision data*, ATLAS-CONF-2018-039, 2018, URL: <https://cds.cern.ch/record/2632344>.
- [50] D. Abercrombie et al., *Dark Matter benchmark models for early LHC Run-2 Searches: Report of the ATLAS/CMS Dark Matter Forum*, *Physics of the Dark Universe* **27** (2020) 100371.
- [51] ATLAS Collaboration, *Combination of searches for invisible Higgs boson decays with the ATLAS experiment*, ATLAS-CONF-2020-052, 2020, URL: <http://cds.cern.ch/record/2743055>.
- [52] *Private discussion with Ulrich Haisch*, August 2020.
- [53] CMS Collaboration, *Search for dark matter produced in association with a Higgs boson decaying to a pair of bottom quarks in proton-proton collisions at  $\sqrt{s} = 13$  TeV*, *The European Physical Journal C* **79** (2019).
- [54] CMS Collaboration, *Search for heavy resonances decaying into a vector boson and a Higgs boson in final states with charged leptons, neutrinos and b quarks at  $\sqrt{s} = 13$  TeV*, *Journal of High Energy Physics* **2018** (2018).
- [55] *Talk on  $Z'$ -2HDM by Ulrich Haisch in the meeting "Topical discussion: searches with the  $h(bb)+MET$  signature"*, October 2018, URL: <https://indico.cern.ch/event/768106/contributions/3198524/attachments/1744404/2824152/Zp2HDM.pdf>.
- [56] CMS Collaboration, *Search for narrow and broad dijet resonances in proton-proton collisions at  $\sqrt{s} = 13$  TeV and constraints on dark matter mediators and other new particles*, *JHEP* **08** (2018) 130, arXiv: 1806.00843 [hep-ex].
- [57] ATLAS Collaboration, *Search for new phenomena in dijet events using  $37\text{fb}^{-1}$  of pp collision data collected at  $\sqrt{s} = 13$  TeV with the ATLAS detector*, *Phys. Rev. D* **96** (2017) 052004, arXiv: 1703.09127 [hep-ex].
- [58] ATLAS Collaboration, *Phys. Rev. Lett.* **121** (8 2018) 081801, URL: <https://link.aps.org/doi/10.1103/PhysRevLett.121.081801>.
- [59] M. Bauer, U. Haisch and F. Kahlhoefer, *Simplified dark matter models with two Higgs doublets: I. Pseudoscalar mediators*, *JHEP* **05** (2017) 138, arXiv: 1701.07427 [hep-ph].

- 
- [60] ATLAS Collaboration, *Search for Dark Matter produced in association with a Standard Model Higgs boson decaying to  $b\bar{b}$  with  $139 \text{ fb}^{-1}$  of  $pp$  collision data with the ATLAS detector*, Internal note of the ATLAS mono- $h(b\bar{b})$  analysis using  $79.8 \text{ fb}^{-1}$  of collected data, 2020, URL: <https://cds.cern.ch/record/2667406/>.
- [61] N. F. Bell, G. Busoni and I. W. Sanderson, *Loop effects in direct detection*, *Journal of Cosmology and Astroparticle Physics* **2018** (2018) 017.
- [62] L. Evans and P. Bryant, *LHC Machine*, *JINST* **3** (2008) S08001.
- [63] A. A. Alves Jr. et al., *The LHCb Detector at the LHC*, *JINST* **3** (2008) S08005.
- [64] K. Aamodt et al., *The ALICE experiment at the CERN LHC*, *JINST* **3** (2008) S08002.
- [65] *CERN webpage*, Accessed: October 2020, URL: <https://home.cern/news/news/accelerators/ls2-report-new-schedule>.
- [66] E. Mobs, *The CERN accelerator complex - 2019. Complexe des accélérateurs du CERN - 2019*, (2019), General Photo, URL: <https://cds.cern.ch/record/2684277>.
- [67] *ATLAS Luminosity public results*, <https://twiki.cern.ch/twiki/bin/view/AtlasPublic/LuminosityPublicResultsRun2>, Accessed: January 2020.
- [68] Z. Marshall, *Simulation of Pile-up in the ATLAS Experiment*, *Journal of Physics: Conference Series* **513** (2014) 022024, URL: <https://doi.org/10.1088%2F1742-6596%2F513%2F2%2F022024>.
- [69] J. Pequeno, ‘Computer generated image of the whole ATLAS detector’, 2008, URL: <https://cds.cern.ch/record/1095924>.
- [70] *Twiki of UZH: How to draw diagrams in LaTeX with TikZ*, <https://wiki.physik.uzh.ch/cms/latex:tikz>, Accessed: December 2019.
- [71] J. Pequeno, ‘Computer generated image of the ATLAS inner detector’, 2008, URL: <https://cds.cern.ch/record/1095926>.
- [72] ATLAS Collaboration, *Track Reconstruction Performance of the ATLAS Inner Detector at  $\sqrt{s} = 13 \text{ TeV}$* , ATL-PHYS-PUB-2015-018, 2015, URL: <https://cds.cern.ch/record/2037683>.
- [73] ATLAS Collaboration, *ATLAS Insertable B-Layer Technical Design Report*, ATLAS-TDR-19, 2010, URL: <https://cds.cern.ch/record/1291633>, Addendum: ATLAS-TDR-19-ADD-1, 2012, URL: <https://cds.cern.ch/record/1451888>.
- [74] G. Ripellino, *The alignment of the ATLAS Inner Detector in Run-2*, *PoS LHCP2016* (2016) 196.
- [75] B. Mindur, *ATLAS Transition Radiation Tracker (TRT): Straw tubes for tracking and particle identification at the Large Hadron Collider*, *Nucl. Instrum. Meth.* **A845** (2017) 257.

- [76] ATLAS Collaboration, *Particle Identification Performance of the ATLAS Transition Radiation Tracker*, ATLAS-CONF-2011-128, 2011, URL: <https://cds.cern.ch/record/1383793>.
- [77] J. Pequenao, 'Computer Generated image of the ATLAS calorimeter', 2008, URL: <https://cds.cern.ch/record/1095927>.
- [78] J. Pequenao, 'Computer generated image of the ATLAS Muons subsystem', 2008, URL: <https://cds.cern.ch/record/1095929>.
- [79] G. Avoni et al., *The new LUCID-2 detector for luminosity measurement and monitoring in ATLAS*, *JINST* **13** (2018) P07017.
- [80] L. Adamczyk et al., *Technical Design Report for the ATLAS Forward Proton Detector*, tech. rep. CERN-LHCC-2015-009. ATLAS-TDR-024, 2015, URL: <https://cds.cern.ch/record/2017378>.
- [81] ATLAS Collaboration, *Luminosity determination in pp collisions at  $\sqrt{s} = 13$  TeV using the ATLAS detector at the LHC*, ATLAS-CONF-2019-021, 2019, URL: <http://cds.cern.ch/record/2677054>.
- [82] S. Abdel Khalek et al., *The ALFA Roman Pot Detectors of ATLAS*, *JINST* **11** (2016) P11013, arXiv: [1609.00249](https://arxiv.org/abs/1609.00249) [[physics.ins-det](#)].
- [83] ATLAS Collaboration, *Performance of the ATLAS trigger system in 2015*, *Eur. Phys. J. C* **77** (2017) 317, arXiv: [1611.09661](https://arxiv.org/abs/1611.09661) [[hep-ex](#)].
- [84] R. Seuster, M. Elsing, G. A. Stewart and V. Tsulaia, *Status and Future Evolution of the ATLAS Offline Software*, *Journal of Physics: Conference Series* **664** (2015) 072044.
- [85] A. Buckley et al., *Implementation of the ATLAS Run 2 event data model*, *Journal of Physics: Conference Series* **664** (2015) 072045.
- [86] J. Catmore et al., *A new petabyte-scale data derivation framework for ATLAS*, *Journal of Physics: Conference Series* **664** (2015) 072007.
- [87] R. Brun and F. Rademakers, *ROOT: An object oriented data analysis framework*, *Nucl. Instrum. Meth.* **A389** (1997) 81.
- [88] *Worldwide LHC Computing Grid*, <https://wlcg-public.web.cern.ch/>, Accessed: January 2020.
- [89] A. Buckley et al., *General-purpose event generators for LHC physics*, *Phys. Rept.* **504** (2011) 145, arXiv: [1101.2599](https://arxiv.org/abs/1101.2599) [[hep-ph](#)].
- [90] R. D. Ball et al., *Parton distributions for the LHC Run II*, *JHEP* **04** (2015) 040, arXiv: [1410.8849](https://arxiv.org/abs/1410.8849) [[hep-ph](#)].
- [91] Gleisberg, T. and Höche, Stefan. and Krauss, F. and Schönherr, M. and Schumann, S. and others, *Event generation with SHERPA 1.1*, *JHEP* **02** (2009) 007, arXiv: [0811.4622](https://arxiv.org/abs/0811.4622) [[hep-ph](#)].

- 
- [92] S. Agostinelli et al., *GEANT4: A Simulation toolkit*, *Nucl. Instrum. Meth. A* **506** (2003) 250.
- [93] ATLAS Collaboration, *The ATLAS Simulation Infrastructure*, *Eur. Phys. J. C* **70** (2010) 823, arXiv: 1005.4568 [physics.ins-det].
- [94] ATLAS Collaboration, *Performance of the ATLAS track reconstruction algorithms in dense environments in LHC Run 2*, *Eur. Phys. J. C* **77** (2017) 673, arXiv: 1704.07983 [hep-ex].
- [95] R. Fruhwirth, *Application of Kalman filtering to track and vertex fitting*, *Nucl. Instrum. Meth. A* **262** (1987) 444.
- [96] ATLAS Collaboration, *Performance of the ATLAS Inner Detector Track and Vertex Reconstruction in High Pile-Up LHC Environment*, ATLAS-CONF-2012-042, 2012, URL: <https://cds.cern.ch/record/1435196>.
- [97] T. Cornelissen et al., *The new ATLAS track reconstruction (NEWT)*, *Journal of Physics: Conference Series* **119** (2008) 032014.
- [98] ATLAS Collaboration, *Reconstruction of primary vertices at the ATLAS experiment in Run 1 proton–proton collisions at the LHC*, *Eur. Phys. J. C* **77** (2017) 332, arXiv: 1611.10235 [hep-ex].
- [99] ATLAS Collaboration, *Vertex Reconstruction Performance of the ATLAS Detector at  $\sqrt{s} = 13$  TeV*, ATL-PHYS-PUB-2015-026, 2015, URL: <https://cds.cern.ch/record/2037717>.
- [100] T. Carli, K. Rabbertz and S. Schumann, *Studies of Quantum Chromodynamics at the LHC*, *The Large Hadron Collider* (2015) 139.
- [101] ATLAS Collaboration, *Topological cell clustering in the ATLAS calorimeters and its performance in LHC Run 1*, *Eur. Phys. J. C* **77** (2017) 490, arXiv: 1603.02934 [hep-ex].
- [102] ATLAS Collaboration, *Jet energy scale measurements and their systematic uncertainties in proton–proton collisions at  $\sqrt{s} = 13$  TeV with the ATLAS detector*, *Phys. Rev. D* **96** (2017) 072002, arXiv: 1703.09665 [hep-ex].
- [103] M. Cacciari, G. P. Salam and G. Soyez, *The anti- $k_t$  jet clustering algorithm*, *JHEP* **04** (2008) 063, arXiv: 0802.1189 [hep-ph].
- [104] M. Cacciari and G. P. Salam, *Pileup subtraction using jet areas*, *Phys. Lett.* **B659** (2008) 119, arXiv: 0707.1378 [hep-ph].
- [105] ATLAS Collaboration, *Jet Calibration and Systematic Uncertainties for Jets Reconstructed in the ATLAS Detector at  $\sqrt{s} = 13$  TeV*, ATL-PHYS-PUB-2015-015, 2015, URL: <https://cds.cern.ch/record/2037613>.
- [106] ATLAS Collaboration, *Performance of pile-up mitigation techniques for jets in pp collisions at  $\sqrt{s} = 8$  TeV using the ATLAS detector*, *Eur. Phys. J. C* **76** (2016) 581, arXiv: 1510.03823 [hep-ex].

- [107] ATLAS Collaboration, *Tagging and suppression of pileup jets with the ATLAS detector*, ATLAS-CONF-2014-018, 2014, URL: <https://cds.cern.ch/record/1700870>.
- [108] ATLAS Collaboration, *Jet reconstruction and performance using particle flow with the ATLAS Detector*, *Eur. Phys. J. C* **77** (2017) 466, arXiv: [1703.10485](https://arxiv.org/abs/1703.10485) [[hep-ex](#)].
- [109] ATLAS Collaboration, *Jet energy scale and resolution measured in proton-proton collisions at  $\sqrt{s} = 13$  TeV with the ATLAS detector*, (2020), arXiv: [2007.02645](https://arxiv.org/abs/2007.02645) [[hep-ex](#)].
- [110] ATLAS Collaboration, *Identification of Boosted, Hadronically-Decaying W and Z Bosons in  $\sqrt{s} = 13$  TeV Monte Carlo Simulations for ATLAS*, ATL-PHYS-PUB-2015-033, 2015, URL: <https://cds.cern.ch/record/2041461>.
- [111] D. Krohn, J. Thaler and L.-T. Wang, *Jet Trimming*, *JHEP* **02** (2010) 084, arXiv: [0912.1342](https://arxiv.org/abs/0912.1342) [[hep-ph](#)].
- [112] S. D. Ellis and D. E. Soper, *Successive combination jet algorithm for hadron collisions*, *Physical Review D* **48** (1993) 3160.
- [113] S. Catani, Y. Dokshitzer, M. Seymour and B. Webber, *Longitudinally-invariant k-clustering algorithms for hadron-hadron collisions*, *Nuclear Physics B* **406** (1993) 187, ISSN: 0550-3213.
- [114] ATLAS Collaboration, *Jet mass reconstruction with the ATLAS Detector in early Run 2 data*, ATLAS-CONF-2016-035, 2016, URL: <https://cds.cern.ch/record/2200211>.
- [115] M. Cacciari, G. P. Salam and G. Soyez, *The Catchment Area of Jets*, *JHEP* **04** (2008) 005, arXiv: [0802.1188](https://arxiv.org/abs/0802.1188) [[hep-ph](#)].
- [116] ATLAS Collaboration, *In situ calibration of large-radius jet energy and mass in 13 TeV proton-proton collisions with the ATLAS detector*, *Eur. Phys. J. C* **79** (2019) 135, arXiv: [1807.09477](https://arxiv.org/abs/1807.09477) [[hep-ex](#)].
- [117] ATLAS Collaboration, *Performance of jet substructure techniques for large-R jets in proton-proton collisions at  $\sqrt{s} = 7$  TeV using the ATLAS detector*, *JHEP* **09** (2013) 076, arXiv: [1306.4945](https://arxiv.org/abs/1306.4945) [[hep-ex](#)].
- [118] ATLAS Collaboration, *Jet Mass Resolutions in ATLAS using Run 2 Monte Carlo Simulation*, ATL-PHYS-PUB-2018-015, 2018, URL: <http://cds.cern.ch/record/2631339>.
- [119] ATLAS Collaboration, *Flavor Tagging with Track-Jets in Boosted Topologies with the ATLAS Detector*, ATL-PHYS-PUB-2014-013, 2014, URL: <https://cds.cern.ch/record/1750681>.
- [120] D. Krohn, J. Thaler and L.-T. Wang, *Jets with Variable R*, *JHEP* **06** (2009) 059, arXiv: [0903.0392](https://arxiv.org/abs/0903.0392) [[hep-ph](#)].

- 
- [121] ATLAS Collaboration, *Variable Radius, Exclusive- $k_T$ , and Center-of-Mass Subjet Reconstruction for Higgs( $\rightarrow b\bar{b}$ ) Tagging in ATLAS*, ATL-PHYS-PUB-2017-010, 2017, URL: <https://cds.cern.ch/record/2268678>.
- [122] ATLAS Collaboration, *Performance of b-jet identification in the ATLAS experiment*, *JINST* **11** (2016) P04008, arXiv: [1512.01094](https://arxiv.org/abs/1512.01094) [[hep-ex](#)].
- [123] ATLAS Collaboration, *Optimisation and performance studies of the ATLAS b-tagging algorithms for the 2017-18 LHC run*, ATL-PHYS-PUB-2017-013, 2017, URL: <https://cds.cern.ch/record/2273281>.
- [124] ATLAS Collaboration, *Expected performance of the ATLAS b-tagging algorithms in Run-2*, ATL-PHYS-PUB-2015-022, 2015, URL: <https://cds.cern.ch/record/2037697>.
- [125] ATLAS Collaboration, *ATLAS b-jet identification performance and efficiency measurement with  $t\bar{t}$  events in pp collisions at  $\sqrt{s} = 13$  TeV*, *The European Physical Journal C* **79** (2019).
- [126] ATLAS Collaboration, *Electron and photon performance measurements with the ATLAS detector using the 2015–2017 LHC proton-proton collision data*, *Journal of Instrumentation* **14** (2019) P12006.
- [127] ATLAS Collaboration, *Electron and photon energy calibration with the ATLAS detector using 2015–2016 LHC proton–proton collision data*, *JINST* **14** (2019) P03017, arXiv: [1812.03848](https://arxiv.org/abs/1812.03848) [[hep-ex](#)].
- [128] ATLAS Collaboration, *Electron reconstruction and identification in the ATLAS experiment using the 2015 and 2016 LHC proton–proton collision data at  $\sqrt{s} = 13$  TeV*, *Eur. Phys. J.* **79** (2019), ISSN: 1434-6052, arXiv: [1902.04655](https://arxiv.org/abs/1902.04655) [[hep-ex](#)].
- [129] ATLAS Collaboration, *Muon reconstruction performance of the ATLAS detector in proton–proton collision data at  $\sqrt{s} = 13$  TeV*, *Eur. Phys. J. C* **76** (2016) 292, arXiv: [1603.05598](https://arxiv.org/abs/1603.05598) [[hep-ex](#)].
- [130] ATLAS Collaboration, *Muon reconstruction and identification efficiency in ATLAS using the full Run 2 pp collision data set at  $\sqrt{s} = 13$  TeV*, ATL-CONF-2020-030, 2020, URL: <https://cds.cern.ch/record/2725736>.
- [131] ATLAS Collaboration, *Reconstruction, Energy Calibration, and Identification of Hadronically Decaying Tau Leptons in the ATLAS Experiment for Run-2 of the LHC*, ATL-PHYS-PUB-2015-045, 2015, URL: <https://cds.cern.ch/record/2064383>.
- [132] ATLAS Collaboration, *Identification of hadronic tau lepton decays using neural networks in the ATLAS experiment*, ATL-PHYS-PUB-2019-033, 2019, URL: <https://cds.cern.ch/record/2688062>.
- [133] ATLAS Collaboration, *Performance of missing transverse momentum reconstruction with the ATLAS detector using proton–proton collisions at  $\sqrt{s} = 13$  TeV*, *Eur. Phys. J. C* **78** (2018) 903, arXiv: [1802.08168](https://arxiv.org/abs/1802.08168) [[hep-ex](#)].

- [134] ATLAS Collaboration,  *$E_T^{miss}$  performance in the ATLAS detector using 2015-2016 LHC pp collisions*, ATLAS-CONF-2018-023, 2018, URL: <https://cds.cern.ch/record/2625233>.
- [135] ATLAS Collaboration, *Object-based missing transverse momentum significance in the ATLAS Detector*, ATLAS-CONF-2018-038, 2018, URL: <https://cds.cern.ch/record/2630948>.
- [136] E. Bothmann et al., *Event Generation with Sherpa 2.2*, SciPost Physics **7** (2019), arXiv: [1905.09127](https://arxiv.org/abs/1905.09127) [[hep-ph](#)].
- [137] S. Schumann and F. Krauss, *A Parton shower algorithm based on Catani-Seymour dipole factorisation*, JHEP **03** (2008) 038, arXiv: [0709.1027](https://arxiv.org/abs/0709.1027) [[hep-ph](#)].
- [138] S. Höche, F. Krauss, M. Schönherr and F. Siegert, *A critical appraisal of NLO+PS matching methods*, JHEP **09** (2012) 049, arXiv: [1111.1220](https://arxiv.org/abs/1111.1220) [[hep-ph](#)].
- [139] S. Höche, F. Krauss, M. Schönherr and F. Siegert, *QCD matrix elements + parton showers: The NLO case*, JHEP **04** (2013) 027, arXiv: [1207.5030](https://arxiv.org/abs/1207.5030) [[hep-ph](#)].
- [140] S. Catani, F. Krauss, R. Kuhn and B. R. Webber, *QCD Matrix Elements + Parton Showers*, JHEP **11** (2001) 063, arXiv: [hep-ph/0109231](https://arxiv.org/abs/hep-ph/0109231).
- [141] S. Höche, F. Krauss, S. Schumann and F. Siegert, *QCD matrix elements and truncated showers*, JHEP **05** (2009) 053, arXiv: [0903.1219](https://arxiv.org/abs/0903.1219) [[hep-ph](#)].
- [142] D. J. Lange, *The EvtGen particle decay simulation package*, Nucl. Instrum. Meth. A **462** (2001) 152.
- [143] T. Sjöstrand, S. Mrenna and P. Z. Skands, *A Brief Introduction to PYTHIA 8.1*, Comput. Phys. Commun. **178** (2008) 852, arXiv: [0710.3820](https://arxiv.org/abs/0710.3820) [[hep-ph](#)].
- [144] R. D. Ball et al., *Parton distributions with LHC data*, Nucl. Phys. **B867** (2013) 244, arXiv: [1207.1303](https://arxiv.org/abs/1207.1303) [[hep-ph](#)].
- [145] ATLAS Collaboration, *The Pythia 8 A3 tune description of ATLAS minimum bias and inelastic measurements incorporating the Donnachie-Landshoff diffractive model*, ATL-PHYS-PUB-2016-017, 2016, URL: <https://cds.cern.ch/record/2206965>.
- [146] J. Alwall et al., *The automated computation of tree-level and next-to-leading order differential cross sections, and their matching to parton shower simulations*, JHEP **07** (2014) 079, arXiv: [1405.0301](https://arxiv.org/abs/1405.0301) [[hep-ph](#)].
- [147] T. Sjöstrand et al., *An Introduction to PYTHIA 8.2*, Comput. Phys. Commun. **191** (2015) 159, arXiv: [1410.3012](https://arxiv.org/abs/1410.3012) [[hep-ph](#)].
- [148] *ATLAS Run 1 Pythia8 tunes*, ATL-PHYS-PUB-2014-021, 2014, URL: <https://cds.cern.ch/record/1966419>.

- 
- [149] R. D. Ball et al.,  
*Impact of Heavy Quark Masses on Parton Distributions and LHC Phenomenology*,  
*Nucl. Phys.* **B849** (2011) 296, arXiv: [1101.1300 \[hep-ph\]](#).
- [150] C. Anastasiou, L. Dixon, K. Melnikov and F. Petriello,  
*High-precision QCD at hadron colliders: Electroweak gauge boson rapidity distributions at next-to-next-to leading order*, *Physical Review D* **69** (2004).
- [151] S. Frixione, P. Nason and G. Ridolfi,  
*A positive-weight next-to-leading-order Monte Carlo for heavy flavour hadroproduction*,  
*JHEP* **09** (2007) 126, arXiv: [0707.3088 \[hep-ph\]](#).
- [152] P. Nason,  
*A New method for combining NLO QCD with shower Monte Carlo algorithms*,  
*JHEP* **11** (2004) 040, arXiv: [hep-ph/0409146](#).
- [153] S. Frixione, P. Nason and C. Oleari, *Matching NLO QCD computations with Parton Shower simulations: the POWHEG method*, *JHEP* **11** (2007) 070, arXiv: [0709.2092 \[hep-ph\]](#).
- [154] S. Alioli, P. Nason, C. Oleari and E. Re, *A general framework for implementing NLO calculations in shower Monte Carlo programs: the POWHEG BOX*, *JHEP* **06** (2010) 043, arXiv: [1002.2581 \[hep-ph\]](#).
- [155] M. Beneke, P. Falgari, S. Klein and C. Schwinn,  
*Hadronic top-quark pair production with NNLL threshold resummation*,  
*Nucl. Phys. B* **855** (2012) 695, arXiv: [1109.1536 \[hep-ph\]](#).
- [156] M. Cacciari, M. Czakon, M. Mangano, A. Mitov and P. Nason, *Top-pair production at hadron colliders with next-to-next-to-leading logarithmic soft-gluon resummation*, *Phys. Lett. B* **710** (2012) 612, arXiv: [1111.5869 \[hep-ph\]](#).
- [157] P. Bärnreuther, M. Czakon and A. Mitov, *Percent-Level-Precision Physics at the Tevatron: Next-to-Next-to-Leading Order QCD Corrections to  $q\bar{q} \rightarrow t\bar{t} + X$* , *Phys. Rev. Lett.* **109** (2012) 132001, arXiv: [1204.5201 \[hep-ph\]](#).
- [158] M. Czakon and A. Mitov, *NNLO corrections to top-pair production at hadron colliders: the all-fermionic scattering channels*, *JHEP* **12** (2012) 054, arXiv: [1207.0236 \[hep-ph\]](#).
- [159] M. Czakon and A. Mitov,  
*NNLO corrections to top pair production at hadron colliders: the quark-gluon reaction*,  
*JHEP* **01** (2013) 080, arXiv: [1210.6832 \[hep-ph\]](#).
- [160] M. Czakon, P. Fiedler and A. Mitov,  
*Total Top-Quark Pair-Production Cross Section at Hadron Colliders Through  $O(\alpha_S^4)$* ,  
*Phys. Rev. Lett.* **110** (2013) 252004, arXiv: [1303.6254 \[hep-ph\]](#).
- [161] M. Czakon and A. Mitov,  
*Top++: A program for the calculation of the top-pair cross-section at hadron colliders*,  
*Comput. Phys. Commun.* **185** (2014) 2930, arXiv: [1112.5675 \[hep-ph\]](#).

- [162] M. Aliev et al.,  
*HATHOR – HAdronic Top and Heavy quarks crOss section calculatoR*,  
*Comput. Phys. Commun.* **182** (2011) 1034, arXiv: [1007.1327 \[hep-ph\]](#).
- [163] P. Kant et al., *HatHor for single top-quark production: Updated predictions and uncertainty estimates for single top-quark production in hadronic collisions*,  
*Comput. Phys. Commun.* **191** (2015) 74, arXiv: [1406.4403 \[hep-ph\]](#).
- [164] ATLAS Collaboration, *Measurement of the  $Z/\gamma^*$  boson transverse momentum distribution in  $pp$  collisions at  $\sqrt{s} = 7$  TeV with the ATLAS detector*,  
*JHEP* **09** (2014) 145, arXiv: [1406.3660 \[hep-ex\]](#).
- [165] J. Pumplin et al.,  
*New generation of parton distributions with uncertainties from global QCD analysis*,  
*JHEP* **07** (2002) 012, arXiv: [hep-ph/0201195](#).
- [166] M. L. Ciccolini, S. Dittmaier and M. Kramer, *Electroweak radiative corrections to associated WH and ZH production at hadron colliders*, *Phys. Rev.* **D68** (2003) 073003, arXiv: [hep-ph/0306234 \[hep-ph\]](#).
- [167] O. Brein, A. Djouadi and R. Harlander,  
*NNLO QCD corrections to the Higgs-strahlung processes at hadron colliders*,  
*Phys. Lett.* **B579** (2004) 149, arXiv: [hep-ph/0307206 \[hep-ph\]](#).
- [168] G. Ferrera, M. Grazzini and F. Tramontano, *Associated WH production at hadron colliders: a fully exclusive QCD calculation at NNLO*,  
*Phys. Rev. Lett.* **107** (2011) 152003, arXiv: [1107.1164 \[hep-ph\]](#).
- [169] O. Brein, R. Harlander, M. Wiesemann and T. Zirke,  
*Top-Quark Mediated Effects in Hadronic Higgs-Strahlung*,  
*Eur. Phys. J.* **C72** (2012) 1868, arXiv: [1111.0761 \[hep-ph\]](#).
- [170] G. Ferrera, M. Grazzini and F. Tramontano,  
*Higher-order QCD effects for associated WH production and decay at the LHC*,  
*JHEP* **04** (2014) 039, arXiv: [1312.1669 \[hep-ph\]](#).
- [171] G. Ferrera, M. Grazzini and F. Tramontano, *Associated ZH production at hadron colliders: the fully differential NNLO QCD calculation*, *Phys. Lett.* **B740** (2015) 51, arXiv: [1407.4747 \[hep-ph\]](#).
- [172] J. M. Campbell, R. K. Ellis and C. Williams,  
*Associated production of a Higgs boson at NNLO*, *JHEP* **06** (2016) 179, arXiv: [1601.00658 \[hep-ph\]](#).
- [173] L. Altenkamp, S. Dittmaier, R. V. Harlander, H. Rzehak and T. J. E. Zirke,  
*Gluon-induced Higgs-strahlung at next-to-leading order QCD*, *JHEP* **02** (2013) 078, arXiv: [1211.5015 \[hep-ph\]](#).
- [174] R. V. Harlander, A. Kulesza, V. Theeuwes and T. Zirke,  
*Soft gluon resummation for gluon-induced Higgs Strahlung*, *JHEP* **11** (2014) 082, arXiv: [1410.0217 \[hep-ph\]](#).

- 
- [175] O. Brein, R. V. Harlander and T. J. E. Zirke, *vh@nnlo - Higgs Strahlung at hadron colliders*, *Comput. Phys. Commun.* **184** (2013) 998, arXiv: 1210.5347 [hep-ph].
- [176] ATLAS collaboration, *Performance of the missing transverse momentum triggers for the ATLAS detector during Run-2 data taking*, *JHEP* **08** (2020) 080, arXiv: 2005.09554 [hep-ex].
- [177] ATLAS Collaboration, *Performance of electron and photon triggers in ATLAS during LHC Run 2*, *The European Physical Journal C* **80** (2020).
- [178] ATLAS Collaboration, *Performance of the ATLAS muon triggers in Run 2*, *Journal of Instrumentation* **15** (2020), arXiv: 2004.13447 [hep-ex].
- [179] ATLAS Collaboration, *Muon Trigger Public Results*, accessed: July 2020, URL: <https://twiki.cern.ch/twiki/bin/view/AtlasPublic/MuonTriggerPublicResults>.
- [180] ATLAS Collaboration, *Search for Dark Matter Produced in Association with a Higgs Boson Decaying to  $b\bar{b}$  at  $\sqrt{s} = 13$  TeV with the ATLAS Detector*, Internal note of the ATLAS mono- $h(b\bar{b})$  analysis using  $36.1 \text{ fb}^{-1}$  of collected data, 2016, URL: <https://cds.cern.ch/record/2225941>.
- [181] ATLAS Collaboration, *Selection of jets produced in 13 TeV proton-proton collisions with the ATLAS detector*, ATLAS-CONF-2015-029, 2015, URL: <https://cds.cern.ch/record/2037702>.
- [182] ATLAS Collaboration, *Search for Dark Matter Produced in Association with a Higgs Boson Decaying to  $b\bar{b}$  at  $\sqrt{s} = 13$  TeV using  $79.8 \text{ fb}^{-1}$  of pp collision data with the ATLAS Detector*, Internal note of the ATLAS mono- $h(b\bar{b})$  analysis using  $79.8 \text{ fb}^{-1}$  of collected data, 2018, URL: <https://cds.cern.ch/record/2301321>.
- [183] ATLAS Collaboration, *Search for the  $b\bar{b}$  decay of the Standard Model Higgs boson in associated (W/Z)H production with the ATLAS detector*, *JHEP* **01** (2015) 069, arXiv: 1409.6212 [hep-ex].
- [184] ATLAS Collaboration, *Evidence for the  $H \rightarrow b\bar{b}$  decay with the ATLAS detector*, *JHEP* **12** (2017) 024, arXiv: 1708.03299 [hep-ex].
- [185] ATLAS Collaboration, *Flavour tagging public results: ATLAS b-jet identification performance and efficiency measurement with  $t\bar{t}$  events in pp collisions at  $\sqrt{s} = 13$  TeV*, accessed: August 2020, URL: <http://atlas.web.cern.ch/Atlas/GROUPS/PHYSICS/PLOTS/FTAG-2019-002/>.
- [186] G. Cowan, K. Cranmer, E. Gross and O. Vitells, *Asymptotic formulae for likelihood-based tests of new physics*, *The European Physical Journal C* **71** (2011).
- [187] R. J. Barlow, *Statistics: A Guide to the Use of Statistical Methods in the Physical Sciences*, Manchester physics series, Wiley, 1989.

- [188] K. Cranmer, G. Lewis, L. Moneta, A. Shibata and W. Verkerke, *HistFactory: A tool for creating statistical models for use with RooFit and RooStats*, (2012).
- [189] G. Cowan, *Statistics for Searches at the LHC*, 2013, arXiv: [1307.2487 \[hep-ex\]](#).
- [190] A. L. Read, *Presentation of search results: the  $CL_s$  technique*, *Journal of Physics G: Nuclear and Particle Physics* **28** (2002) 2693.
- [191] ATLAS Collaboration, *A method for the construction of strongly reduced representations of ATLAS experimental uncertainties and the application thereof to the jet energy scale*, ATL-PHYS-PUB-2015-014, 2015, URL: <https://cds.cern.ch/record/2037436>.
- [192] ATLAS Collaboration, *Search for Dark Matter in association with a Higgs boson decaying to b-quarks in pp collisions at  $\sqrt{s} = 13$  TeV with the ATLAS detector*, Internal note of the ATLAS mono- $h(b\bar{b})$  analysis using  $3.2 \text{ fb}^{-1}$  of collected data, 2015, URL: <https://cds.cern.ch/record/2104266>.
- [193] ATLAS Collaboration, *Observation of  $H \rightarrow b\bar{b}$  decays and  $VH$  production with the ATLAS detector*, *Phys. Lett. B* **786** (2018) 59, arXiv: [1808.08238 \[hep-ex\]](#).
- [194] ATLAS Collaboration, *Search for a scalar partner of the top quark in the jets plus missing transverse momentum final state at  $\sqrt{s} = 13$  TeV with the ATLAS detector*, *Journal of High Energy Physics* **2017** (2017).
- [195] N. Hartmann, *ahoi framework*, Accessed: July 2019, URL: <https://gitlab.com/nikoladze/ahoi>.
- [196] ATLAS Collaboration, *Formulae for Estimating Significance*, ATL-PHYS-PUB-2020-025, 2020, URL: <https://cds.cern.ch/record/2736148>.
- [197] S. Meier, *Suche nach dunkler Materie in Assoziation mit einem Higgs-Boson*, Bachelor thesis by Sophie Meier at LMU Munich, 2019, URL: [https://www.etp.physik.uni-muenchen.de/publications/bachelor/download\\_auth\\_etp/bac19\\_smeier.pdf](https://www.etp.physik.uni-muenchen.de/publications/bachelor/download_auth_etp/bac19_smeier.pdf).
- [198] ATLAS Collaboration, *Search for Dark Matter produced in association with a Standard Model Higgs boson decaying to b-quarks with  $139 \text{ fb}^1$  of pp collision data with the ATLAS detector*, (), ATLAS internal access only; paper to be published, URL: <https://cds.cern.ch/record/2740679>.
- [199] J. Butterworth et al., *PDF4LHC recommendations for LHC Run II*, *J. Phys.* **G43** (2016) 023001, arXiv: [1510.03865 \[hep-ph\]](#).
- [200] S. Hoeche and M. Schonherr, *Uncertainties in next-to-leading order plus parton shower matched simulations of inclusive jet and dijet production*, *Phys. Rev.* **D86** (2012) 094042, arXiv: [1208.2815 \[hep-ph\]](#).
- [201] M. Bahr et al., *Herwig++ Physics and Manual*, *Eur. Phys. J. C* **58** (2008) 639, arXiv: [0803.0883 \[hep-ph\]](#).

- 
- [202] J. Bellm et al., *Herwig 7.0/Herwig++ 3.0 release note*, *Eur. Phys. J. C* **76** (2016) 196, arXiv: 1512.01178 [hep-ph].
- [203] I. Brivio et al., *ALPs effective field theory and collider signatures*, *The European Physical Journal C* **77** (2017).
- [204] ATLAS Collaboration, *Search for dark matter in association with an energetic photon in pp collisions at s=13 TeV with the ATLAS detector*, 2020, URL: <https://cds.cern.ch/record/2720250>.
- [205] ATLAS Collaboration, *Search for new phenomena in events with jets and missing transverse momentum in pp collisions at  $\sqrt{s} = 13$  TeV with the ATLAS detector*, ATLAS-CONF-2020-048, 2020, URL: <http://cds.cern.ch/record/2728058>.
- [206] H. Mirkes, *Sensitivität zu axion-artigen Teilchen in Signaturen mit einem Higgs-Boson und fehlender Transversalenergie am ATLAS Experiment*, Bachelor thesis by Holger Mirkes at LMU Munich, 2020, URL: [https://www.etp.physik.uni-muenchen.de/publications/bachelor/download\\_auth\\_etp/bac20\\_hmirkes.pdf](https://www.etp.physik.uni-muenchen.de/publications/bachelor/download_auth_etp/bac20_hmirkes.pdf).
- [207] ATLAS Collaboration, *Search for an invisibly decaying Higgs boson or dark matter candidates produced in association with a Z boson in pp collisions at  $\sqrt{s} = 13$  TeV with the ATLAS detector*, *Phys. Lett. B* **776** (2018) 318, arXiv: 1708.09624 [hep-ex].
- [208] P. Pani and G. Polesello, *Dark matter production in association with a single top-quark at the LHC in a two-Higgs-doublet model with a pseudoscalar mediator*, *Physics of the Dark Universe* **21** (2018) 8.
- [209] ATLAS Collaboration, *Search for dark matter in association with a Higgs boson decaying to two photons at  $\sqrt{s} = 13$  TeV with the ATLAS detector*, *Phys. Rev. D* **96** (2017) 112004, arXiv: 1706.03948 [hep-ex].
- [210] *Webpage of HL-LHC Project*, Accessed: October 2020, URL: <https://project-hl-lhc-industry.web.cern.ch/sites/project-hl-lhc-industry.web.cern.ch/files/inline-images/HL-LHC-plan-2020-Plan-2.pdf>.
- [211] G. Apollinari, O. Brüning, T. Nakamoto and L. Rossi, *High Luminosity Large Hadron Collider HL-LHC*, *CERN Yellow Rep.* (2015) 1, ed. by G. Apollinari, I. Béjar Alonso, O. Brüning, M. Lamont and L. Rossi, arXiv: 1705.08830 [physics.acc-ph].



# Danksagung

An dieser Stelle möchte ich mich bei allen bedanken, die mich in den letzten Jahren unterstützt haben und ohne die diese Arbeit nicht möglich gewesen wäre:

- Prof. Dr. Dorothee Schaile für ihre Unterstützung und Betreuung während der letzten Jahre und dass sie es mir ermöglicht hat, meine Doktorarbeit hier zu schreiben. Vielen Dank auch dafür, dass ich dabei ein halbes Jahr am CERN verbringen und an unterschiedlichen Workshops, Schulen und Konferenzen teilnehmen durfte.
- Dr. Jeanette Lorenz für die Betreuung in den letzten sechs Jahren während meiner Bachelor-, Master- und Doktorarbeit. Ich konnte mich mit meinen Fragen immer an sie wenden, wurde sehr gut von ihr beraten und konnte bei Problemen auf ihre Hilfe bauen.
- Prof. Dr. Wolfgang Dünneweber für die Bereitschaft das Zweitgutachten zu erstellen.
- Prof. Dr. Thomas Kuhr, Prof. Dr. Andreas Burkert und Prof. Dr. Hans Böhringer für die Bereitschaft in meiner Prüfungskommission mitzuwirken.
- Allen Mitgliedern des Lehrstuhls Schaile für die Hilfsbereitschaft bei allen Fragen, die angenehme Arbeitsatmosphäre, wie auch für die vielen Aktivitäten außerhalb der Arbeitszeit. Ich habe die Zeit hier sehr genossen. Ein besonderer Dank geht an Thomas Maier und Nikolai Hartmann, die mir bei meinen vielen technischen Problemen geholfen haben, Ferdinand Krieter für die Zeit am CERN und Michael Adersberger und Michael Holzbock für die vielen auch nicht arbeitsbezogenen Gespräche.
- Johannes Junggeburth und Philipp Gadow, die mir bei vielen Analyseproblemen weitergeholfen haben und ohne die die Arbeit in den letzten Jahren bei weitem nicht so viel Spaß gemacht hätte.
- Dr. Spyridon Argyropoulos, for answering my physics and analysis questions and for providing comments on the theory part of my thesis.
- All members of the last two mono- $h(b\bar{b})$  analysis teams for the discussions, the help with any problems and for the friendly atmosphere in the team. I enjoyed the work in the analysis a lot.
- Meinen Eltern Marta und Ivo Matic wie auch meiner Schwester Ivana, die immer für mich da sind.
- Ein ganz besonderer Dank geht an meinen Freund Bernhard Flierl, der nicht nur meine Arbeit korrekturgelesen hat, sondern auch immer für mich da ist und mich in der letzten stressigen Zeit sogar noch mehr als sonst unterstützt hat.